

D5.2.2



Synthesis of the results obtained of test cases from task 5.2

Deliverable D5.2.2/D5.4 Report

Author: Jean Talandier, Andra

Reporting period: 01/06/20 – 31/05/21

Date of issue of this report: **12/08/2020**

Start date of project: **01/06/17**

Duration: 48 Months

This project receives funding from the Euratom research and training programme 2014-2018
under grant agreement No 745 942

Dissemination Level P

PU Public

REVIEW

Name	Internal/Project/External	Comments
Beacon Partners	Project internal	

DISTRIBUTION LIST

Name	Number of copies	Comments
André Jouve (EC)	Digital	
Christophe Davies (EC)	Digital	
Beacon partners	Digital	

Content

1	Introduction	6
2	Description of the model	8
2.1	UPC	8
2.2	ULG	11
2.3	CU/CTU	12
2.4	ClayTechnology - Comsol	14
2.4.1	New Comsol implementation strategy	15
2.4.2	Vapor included in water mass balance	15
2.4.3	Energy balance included	16
2.4.4	New evolution equation for the micro void ratio	16
2.4.5	New equation restricting the path dependent variable	17
2.4.6	New Febex bentonite parameter set	18
2.5	Clay Technology – Code_Bright	18
2.6	VTT/UCLM	18
2.7	ICL	20
2.7.1	Software	20
2.7.2	Mechanical model	20
2.7.3	Soil water retention (SWR) model	23
2.7.4	Hydraulic conductivity (permeability) model	23
2.8	LEI	24
2.9	Quintessa	25
2.10	EPFL	28
2.11	BGR	33
2.11.1	Heat transport model	36
2.11.2	Vapour diffusion model	36
2.11.3	Hydraulic model	36
2.11.4	Mechanical model	36
2.11.5	Coupled mass and momentum balance	37
2.11.6	Constitutive relations	37
2.11.7	Post processing	38
3	EB	39
3.1	Main feature of the test – why it is relevant for Beacon	39
3.2	UPC	39
3.2.1	Geometry and discretization	39
3.2.2	Input parameters	40
3.2.3	Initial and boundary conditions	44
3.2.4	Results/discussion	46
3.2.5	Lessons learnt	57
3.3	ULG	59
3.3.1	Geometry and discretization	59
3.3.2	Input parameters	60
3.3.3	Initial and boundary conditions	66
3.3.4	Results/discussion	72
3.3.5	Lessons learnt	81
3.4	Synthesis of results for EB – key lessons (Andra + All)	82
4	CRT	85
4.1	Main feature of the test – why it is relevant for Beacon	85
4.2	CU/CTU	85
4.2.1	Geometry and discretization	85

4.2.2	Input parameters	86
4.2.3	Initial and boundary conditions.....	88
4.2.4	Results/discussion	89
4.3	ClayTechnology – Code_Bright	99
4.3.1	Geometry and discretization	99
4.3.2	Input parameters.....	99
4.3.3	Initial and boundary conditions.....	103
4.3.4	Results/discussion	106
4.4	ICL.....	115
4.4.1	Geometry and discretization	115
4.4.2	Input parameters.....	116
4.4.3	Initial and boundary conditions.....	118
4.4.4	Results/discussion	119
4.4.5	Lessons learnt.....	122
4.5	VTT/UCLM	124
4.5.1	Modelling a slice at canister mid-height.....	124
4.5.2	Modelling the entire CRT	135
4.5.3	Lessons learnt.....	143
4.6	Synthesis of results for CRT – key lessons (Andra + All)	145
5	Febex	151
5.1	Main feature of the test – why it is relevant for Beacon	151
5.2	ICL.....	151
5.2.1	Geometry and discretization	151
5.2.2	Input parameters.....	152
5.2.3	Initial and boundary conditions.....	156
5.2.4	Results/discussion	158
5.2.5	Lessons learnt.....	163
5.3	LEI.....	165
5.3.1	Geometry and discretization	165
5.3.2	Input parameters.....	165
5.3.3	Initial and boundary conditions.....	171
5.3.4	Results/discussion	172
5.4	Quintessa.....	184
5.4.1	Geometry and discretization	184
5.4.2	Input parameters.....	185
5.4.3	Initial and boundary conditions.....	188
5.4.4	Results/discussion	189
5.5	Clay Technology - Comsol	199
5.5.1	Geometry and discretization	199
5.5.2	Input parameters.....	200
5.5.3	Initial and boundary conditions.....	202
5.5.4	Results/discussion	203
5.6	Clay Technology – Code_Bright	211
5.6.1	Geometry and discretization	211
5.6.2	Input parameters.....	212
5.6.3	Initial and boundary conditions.....	216
5.6.4	Results/discussion	217
5.7	EPFL.....	225
5.7.1	Geometry and discretization	225
5.7.2	Input parameters.....	226
5.7.3	Initial and boundary conditions.....	231
5.7.4	Results/discussion	233
5.8	BGR.....	249

Beacon

D5.2.2 – Synthesis of the results obtained of test cases from task 5.2

Dissemination level: PU

Date of issue: **15/07/2020**



5.8.1	Geometry and discretization	249
5.8.2	Input parameters	253
5.8.3	Initial and boundary conditions.....	253
5.8.4	Results/discussion	254
5.9	Synthesis of results for FEBEX – key lessons (Andra + All)	264
6	Synthesis of task 5.2.....	270
	References	272

1 Introduction

This report presents the results and analyses obtained during the task 5.2 from WP5. This task concerns the modelling of large-scale experiments performed in the Grimsel, Äspö and Mont Terri laboratory. The tests were chosen from the initial inventory made in WP2 from the Beacon project.

The motivation for the choice of those tests was that they are relevant in regards of Beacon project objectives, they have already been dismantled and they are well documented. This means that a large amount of data is available concerning material evolution during the test but also map of quantities such as water content or dry densities at the end of the tests. This type of data are very important to evaluate at the end, homogeneity of the swelling clay.

Main specificities of the tests are list below

- For two experiments FEBEX and CRT, the bentonite is submitted to both water saturation and temperature during the test.
- Febex bentonite was used for EB and FEBEX. MX-80 was used for CRT
- In EB, most of the excavation was filled with pellets mixture.
- In FEBEX and CRT, the majority of the volume was filled with compacted blocks.

The task 5.2 has been started 2 years after the beginning of the Beacon project. The idea was to use the feedback from the task 5.1 which concerned modelling of lab tests and evaluate the benefits of the developments made in WP3.

Partners involved in task 5.2 have selected one or two tests between these three. The choice of the partners are presented in Table 1-1.

Table 1-1 List of partners involved in Task 5.2 and performed tests

	EB	FEBEX	CRT
UPC	X		
ULG	X		
BGR		X	
CU-CTU			X
LEI		X	
ClayTechnology		X(1)	X(2)

ICL		X	X
EPFL		X	
Quintessa		X	
VTT/UCLM			X

In a first part, a brief description of the models used in this task is reminded. In a second part, results obtained for each test by all the partners are presented with a first analysis. A synthesis is proposed for each test indicating the lessons learned from the tests particularly in terms of the strength and weakness of the models. This will give as during task 5.1 a lot of information for the orientation of model developments in WP3.

2 Description of the model

In this paragraph, a brief description of the model used during the task 5.2 is given. The complete description of the models is presented in reports produced in D3.1. The description is mainly oriented on the specific features of the models needed for this series of tests.

2.1 UPC

UPC has used an elastoplastic double structure model. Only a summary of the main features of the model are presented here. The fabric of a bentonite can be identified as a porous medium of macroparticles (clay aggregates) formed by clay platelets (Figure 2-1). From this physical fact, several constitutive models for these geomaterials have been postulated on the hypothesis of explicit consideration of two pore levels (Gens and Alonso 1992, Alonso et al. 1999, Sanchez et al. 2005, Gens et al. 2011)

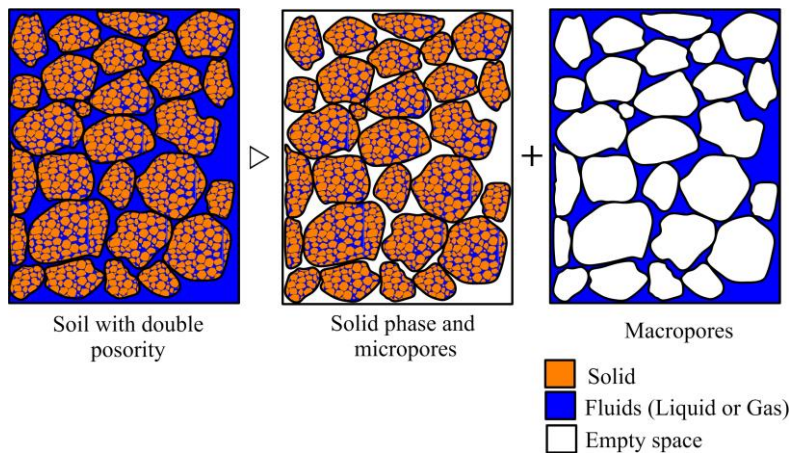


Figure 2-1 Schematic representation of the double-structure porous medium.

The porous medium consists of three phases [solid (s), liquid (L) and gas (g)] and three main components [solid (s), water (w) and air (a)]. An important difference with respect to the original formulation is that Macro and micro structural levels contain air and water in gas and liquid state.

The reference of the quantities with respect to the whole volume control, *volume fraction concept*, is needed for the HM formulation. According to the structural levels of expansive clays, it is possible to define the *micro pore volume fraction* (2.1-1) *macro pore volume fraction* (2.1-2) and *solid volume fraction* (2.1-3).

$$\bar{\phi}_{micro} = \frac{(V_{Pores})_{micro}}{V} \quad (2.1-1)$$

$$\bar{\phi}_{Macro} = \frac{(V_{Pores})_{Macro}}{V} \quad (2.1-2)$$

$$\bar{\phi}_{Solid} = \frac{(V_{Solid})_{micro}}{V} \quad (2.1-3)$$

Table 2-1 list the system of governing equations and the unknown variables associated with them. The hydraulic equilibrium between two structural levels is not assumed; that is, at each point of the domain the water potentials in the macro- and micro-structure may be different, leading to an exchange of mass of water and air between them. Water exchange will therefore be driven by suction differences alone (2.1-4).

$$\Gamma^w = \gamma(s_1 - s_2) \quad (2.1-4)$$

Table 2-1 Balance equations unknowns

Solid mass balance	$\bar{\phi}$ - Volume fraction
Water mass balance for macro-structure	P_{L2} - Liquid pressure at macro-structural level.
Water mass balance for micro-structure	P_{L1} - Liquid pressure at micro-structural level
Air mass balance for macro-structure	P_{g2} - Gas pressure at macro-structural level.
Air mass balance for micro-structure	P_{g1} - Gas pressure at micro-structural level.
Momentum balance	\dot{u} - Solid Velocity
Note: From now, we refer the micro-structural level with the subscript 1, the macro-structural level with the subscript 2 and the double-structural porous media without subscript.	

Concerning the *hydraulic constitutive laws*, the generalized Darcy's law governs liquid and gas flow. This is only formulated for the macro-structural level, due to the neglected advective fluxes in the micro-structural level.

$$\mathbf{q}_{\alpha 2} = -\frac{\mathbf{k}_2 k_{r\alpha 2}}{\mu_\alpha} (\nabla P_{\alpha 2} - \rho_{\alpha 2} \mathbf{g}) \quad (2.1-5)$$

where:

- μ_α is the fluid viscosity, $\rho_{\alpha 2}$ is the fluid density and \mathbf{g} is the gravity acceleration.

A power law defines the intrinsic permeability, which expresses the effect of degree of saturation (or suction) on global permeability (2.1-6). A dependence of intrinsic permeability on porosity is adopted (2.1-7)

$$(k_r)_\alpha = [(S_e)_\alpha]^c \quad (2.1-6)$$

$$\mathbf{k}_2 = \mathbf{k}_{o2} \exp[b(\bar{\phi}_2 - (\bar{\phi}_o)_2)] \quad (2.1-7)$$

-

The *mechanical response* of the expansive soils is accomplished by the consideration of several plastic mechanisms that can act jointly or not at different stages of the analysis depending on the direction of the stress/strain path.

$$\dot{\boldsymbol{\varepsilon}} = \dot{\boldsymbol{\varepsilon}}^e + \dot{\boldsymbol{\varepsilon}}_{\beta}^p + \dot{\boldsymbol{\varepsilon}}_{LC}^p \quad (2.1-8)$$

Table 2-2 Constitutive variables used for the double-structure model

	First constitutive variables FCV	Second constitutive variables SCV
micro-structural level	Bishop's effective stress $\boldsymbol{\sigma}'_1 = \boldsymbol{\sigma}_1 - P_{g1}\mathbf{I} + S_1s_1\mathbf{I}$	micro-suction $s_1 = \max(P_{g1} - P_{L1}, 0)$
Macro-structural level	Net stress $\boldsymbol{\sigma}''_2 = \boldsymbol{\sigma}_2 - P_{g2}\mathbf{I}$	Macro-suction $s_2 = \max(P_{g2} - P_{L1}, 0)$

where S_1 stands for liquid saturation.

Table 2-2 shows the constitutive variables for each structural level. Non-linear elasticity is used to define the fully reversible micro-structural strains. The LC plastic strains are derived from the basic BBM model (Alonso and Gens 1990). Finally, the plastic macro-structural strain induced by micro-structural effects are evaluated by:

$$d\boldsymbol{\varepsilon}_{\beta} = f_{\beta}d\bar{\boldsymbol{\varepsilon}}_1 \quad (2.1-9)$$

Two interaction functions are defined: **mc** for microstructural contraction paths (2.1-10) and **ms** for microstructural swelling paths (2.1-11).

$$f_{\beta} = \frac{\varepsilon_{vol2}^p}{\varepsilon_{vol1}} = f_{mc_1} + (f_{mc_0} - f_{mc_1})(1 - \mu_{\beta})^{n_{mc}} \quad (2.1-10)$$

$$f_{\beta} = \frac{\varepsilon_{vol2}^p}{\varepsilon_{vol1}} = f_{ms_1} + (f_{ms_0} - f_{ms_1})(1 - \mu_{\beta})^{n_{ms}} \quad (2.1-11)$$

where:

- μ_{β} is the degree of compactness related to the stress state.
- $f_{mc_0}, f_{mc_1}, f_{ms_0}, f_{ms_1}, n_{ms}$ **and** n_{mc} are model parameters.

Finally, the hardening of the whole double-structure medium is given by the evolution of the isotropic yield stress due to the plastic strains of the structural interaction (*mechanism β*) and macro-structure itself (*mechanism LC*).

$$dp_0^* = \frac{(1 + \bar{e}_2)p_0^*}{\lambda_{sat} - \kappa_2} d\varepsilon_v^p = \frac{(1 + \bar{e}_2)p_0^*}{\lambda_{sat} - \kappa_2} (d\varepsilon_{LC}^p + d\boldsymbol{\varepsilon}_{\beta}) \quad (2.1-12)$$

2.2 ULG

Mechanical model

The complexity of the coupled multiphysical and multiscale phenomena taking place during bentonite hydration is well known. The Barcelona Basic Model (BBM) (Alonso, Gens, & Josa, 1990) is able to reproduce a wide range of phenomena occurring in unsaturated soils and, due to this, it is selected as mechanical constitutive model. The model is formulated adopting net stress σ [Eq. 1] and suction s as stress variables.

$$\sigma = \sigma_T - u_a I \quad \text{Eq. 1}$$

With σ_T the total stress tensor, u_a the air pressure for $s > 0$ and I the identity tensor.

According to the BBM, under isotropic stress conditions, the variation of volumetric elastic strain is associated to changes in mean net stress p and suction s (Eq. 2). Moreover, in order to tackle the stress dependence of the swelling strain for change in suction underlined by (Dueck & Nilsson, 2010), Eq. 3 is adopted.

$$d\varepsilon_v^e = \frac{\kappa}{1+e} \frac{dp}{p} + \frac{\kappa_s}{1+e} \frac{ds}{s + u_{atm}} \quad \text{Eq. 2}$$

$$\kappa_s(p) = \kappa_{s0} * \exp(-\alpha_p * p) \quad \text{Eq. 3}$$

The evolution of the preconsolidation pressure $p_0(s)$ is modelled consistently with the concept of increasing the elastic domain with increasing suction [Eq. 4] as well as the rate of increase of the soil stiffness with suction (Eq. 5).

$$p_0(s) = p_c \left(\frac{p_0^*}{p_c} \right)^{\frac{\lambda(0)-\kappa}{\lambda(s)-\kappa}} \quad \text{Eq. 4}$$

$$\lambda(s) = \lambda(0)[(1-r) \exp(-\omega s) + r] \quad \text{Eq. 5}$$

Hydraulic model

The selected water retention model (Dieudonne, 2016) is formulated in terms of water ratio e_w [Eq. 6], which is expressed as the superposition of a contribution from the water stored in the micropores e_{wm} and a second contribution from the water contained in the macropores e_{wM} [Eq. 7]

$$e_w = S_r e \quad \text{Eq. 6}$$

$$e_w = e_{wm} + e_{wM} \quad \text{Eq. 7}$$

The model also considers the microstructure evolution occurring during saturation (Eq. 8).

$$e_m = e_{m0} + \beta_0 e_w + \beta_1 e_w^2 \quad (8)$$

Eq. 8

Therefore, global degree of saturation is obtained by the sum of the microstructural and macrostructural degrees of saturation, weighed by the corresponding volumetric fractions (Eq. 9).

$$S_r = \frac{e_w}{e} = \frac{e_m}{e} S_{rm} + \frac{e_M}{e} S_{rM} \quad \text{Eq. 9}$$

Dubinin's isotherm is adopted to describe the water retention behaviour of the microstructure, which is mainly stored by absorption [Eq. 10]. For the macrostructural water retention domain, the van Genuchten equation is selected [Eq. 11] replacing the void ratio e by macrostructural void ratio $e_M = e - e_m$. The parameter α is assumed to depend on the macrostructural void ratio representing the influence of the bentonite structure on the air-entry value [Eq. 12].

$$e_{wm}(s, e_m) = e_m \exp[-(C_{ads} s)^{n_{ads}}] \quad \text{Eq. 10}$$

$$e_{wM}(s, e) = (e - e_m) \left[1 + \left(\frac{s}{\alpha} \right)^n \right]^{-m} \quad \text{Eq. 11}$$

$$\alpha = \frac{A}{e - e_m} \quad \text{Eq. 12}$$

2.3 CU/CTU

The CU/CTU team used a hypoplastic model, implemented in the inhouse finite-element solver SIFEL. The constitutive formulation is that of Mašín (2017), which couples the effect of temperature to the hydro-mechanical hypoplastic formulation for expansive clays presented in Mašín (2013a), alongside with other improvements.

A double-structure approach (Gens and Alonso, 1992; Alonso et al., 1999) was used, accounting for experimental evidence (e.g., Pusch, 1982; Sun et al., 2018c) that expansive soils have two identifiable structural levels: a macrostructure (M), formed by the clay aggregates and the macropores, and a microstructure (m), corresponding to the internal arrangement of the aggregates, and their micropores. Mechanical (G) and hydraulic (H) behaviours at the two levels are modelled separately, and the $G - H$ coupling is realised at each level. The link between the two levels is provided by a double-structure coupling function, f_m (Mašín, 2013a, 2017), so that when $f_m = 1$ a volume change of the aggregates corresponds to an equal global volumetric response, while when $f_m = 0$ changes of volume of the aggregates occur at the expense of the macropores, without triggering a global volumetric response.

The H^M model accounts for variable saturation through a hysteretic water retention model depending on the void ratio (e) (Mašín, 2010, 2013a). The G^M model features an explicit formulation of the asymptotic state boundary surface, as well as stiffness anisotropy (Mašín, 2013b, 2014). The behaviour of the microstructure is simplified in the sense that the H^m model is assumed always fully saturated, which is a reasonable assumption for $s_t < \sim 100 \text{ MPa}$, while the mechanical behaviour (G^m) is assumed reversible and isotropic.

The model accounts for the fact that temperature (T) affects both the hydraulic and mechanical behaviours at both structural levels (Mašín, 2017, 2018). The position of the normal compression line (NCL) depends on temperature, hence the G^M model considers a parallel shift of the NCL towards lower values of void ratio as temperature increases. At the microstructural level, the effect of temperature is non-unique: it may cause shrinkage, swelling, or substantial no effect (e.g., Villar and Lloret, 2004; Romero et al., 2005; Tang et al., 2008). As for the water retention behaviour, the effect of T on H^M is assumed to depend only on changes of surface tension of water. In the microstructure, assumed saturated, temperature-induced volume changes (G^m) induce corresponding changes in water retention capacity (H^m).

The general rate formulation of the model is as follows (Mašín, 2017):

$$\dot{\sigma}^M = f_s[\mathcal{L}:(\dot{\epsilon} - f_m \dot{\epsilon}^m) + f_d \mathbf{N} \|\dot{\epsilon} - f_m \dot{\epsilon}^m\|] + f_u \mathbf{H}_s$$

where $\dot{\sigma}^M$ is the effective stress rate of the macrostructure, $\dot{\epsilon}$ is the global Euler stretching tensor, $\dot{\epsilon}^m$ is the strain rate of the microstructure, f_m is the double-structure coupling factor, \mathcal{L} and \mathbf{N} are the 4th and 2nd order hypoplastic tensors, respectively, \mathbf{H}_s controls wetting-induced collapse, and f_s , f_d , and f_u are scalar factors for barotropy, pyknotropy, and collapsible behaviour.

The model requires the following parameters to be specified.

φ_c	Macrostructural critical state friction angle
λ^*	Slope of the isotropic NCL (INCL) in $\ln(p^M/p_r) - \ln(1 + e)$ coordinates, where p^M is the macrostructural effective mean stress, and $p_r = 1 \text{ kPa}$ is a reference stress
κ^*	Macrostructural volume strain upon p^M unloading
N	Position of the INCL in $\ln(p^M/p_r) - \ln(1 + e)$ coordinates
v	Stiffness in shear
n_s	Effect of s on the position of the INCL
l_s	Effect of s on the slope of the INCL
n_T	Effect of T on the position of the INCL
l_T	Effect of T on the slope of the INCL

m	Parameter controlling how wetting-induced and heating-induced compactions are affected by the distance from the state boundary surface, and how wetting–drying and heating–cooling cycles affect e through f_m
α_s	Effect of T on the microstructural volume strain
κ_m	Effect of p^m (microstructural effective mean stress) on the microstructural volume strain
s_r	Reference value of suction for e^m
e_{r0}^m	Reference value of e^m at zero total stress, reference suction s_r , and reference temperature T_r
c_{sh}	Value of f_m in compression
e_0^M	Reference e^M at the reference air-entry value s_{e0} ;
s_{e0}	Reference air-entry value of s at e_0^M
T_r	Reference value of T
a	Effect of T on s_{e0}
b	Effect of T on s_{e0}
a_e	Ratio between air-entry and air-expulsion s values
λ_{p0}	Slope of the main drying-wetting curve in $\ln S_r^M - \ln s$ coordinates, where S_r^M is the macrostructural degree of saturation

The model is implemented in a C++ routine, which is plugged into SIFEL, an inhouse finite-element solver (Koudelka et al., 2011, 2017, 2018). SIFEL is open source and freely available (<http://mech.fsv.cvut.cz/~sifel/>).

Thermo-hydro-mechanical (THM) finite-element problems can be solved in SIFEL by two approaches: a staggered approach, in which transport and mechanical parts are solved independently and in sequence, or a fully coupled approach, in which a complete THM stiffness matrix is assembled and solved using a Newton-Raphson iterative scheme. The construction of the stiffness matrix is carried out either by approximation with the linear part of the THM hypoplastic model, or by numerical estimation of the stiffness matrix using perturbation. The Newton-Raphson scheme can be implemented in two ways: by updating the system matrix at every iteration, which makes the implementation time consuming, or by using the same system matrix for several steps, with matrix factorisation being carried out only when the matrix is updated. Various Runge-Kutta integration schemes are available, from the simple forward Euler scheme to the Runge-Kutta-Fehlberg method of the 5th order (Fehlberg, 1969).

2.4 ClayTechnology - Comsol

Below follows a description of new parts or updates of the formulation/Comsol implementation used when solving this task. Otherwise the formulation follows what was described in Åkesson et. el. (2020), Annex C

of BEACON deliverable D3.2.

2.4.1 New Comsol implementation strategy

When solving problems using the saturated formulation it was found that a monolithic solution method was numerically favourable. For the saturated formulation this was achievable using a user-defined external stress-strain routine in Comsol for the strain driven stress and an additional weak contribution of the suction driven stress defined in the Comsol solid mechanics physics framework.

When turning to unsaturated conditions the formulation grew in complexity which disabled the implementation strategy used for saturated conditions if a monolithic solution method was to be used.

Instead, in addition to the force balance, additional distributed partial differential equations were used for integration of the stress, path variable and micro void ratio. This gives a so-called mixed formulation where the mentioned variables now become new degrees of freedom (independent variables) to solve for, see Navarro et al. (2014). With the new implementation the numerically favourable monolithic solution method could be used again.

The implementation was now formulated directly within the Comsol GUI, not as before in form of a compiled and linked independent code written in C.

2.4.2 Vapor included in water mass balance

The water mass balance given below now includes a gas phase of water (vapor).

$$\frac{\partial}{\partial t} [\mu \rho_l e_\mu (1 - \phi)] + \frac{\partial}{\partial t} [{}^m \tilde{\theta}_g^w (e - e_\mu) (1 - \phi)] + \text{div}(\mu \rho_l \mathbf{q}_l) + \text{div} \mathbf{i}_g^w = \mu f_l^w + m f_g^w$$

A tilde above an entity indicates it should be seen as a function. The gas phase is assumed to be a mixture of two ideal gases, vapor and dry air ($p_g = p_g^w + p_g^a$). To define the gas phase the following have been used,

$$\begin{aligned} \tilde{\rho}_g(s, T) &= m \tilde{\theta}_g^w(s, T) + m \tilde{\theta}_g^a(s, T), \\ m \tilde{\theta}_g^w(s, T) &= \frac{M_w}{RT} \tilde{p}_g^w \text{sat}(T) \tilde{RH}(s, T), \quad m \tilde{\theta}_g^a(s, T) = \frac{M_a}{RT} (p_g - \tilde{p}_g^w \text{sat}(T) \tilde{RH}(s, T)), \\ \tilde{p}_g^w \text{sat}(T) &= 136075 \cdot 10^6 \exp\left(\frac{-5239.7}{T}\right), \quad \tilde{RH}(s, T) = \exp\left(\frac{-s M_w}{RT \mu \tilde{\rho}_l(s)}\right). \end{aligned}$$

The vapor flux \mathbf{i}_g^w is driven by a gradient in vapor mass concentration c which can be rewritten as a gradient in liquid pore pressure (or suction) and temperature,

$$\mathbf{i}_g^w = -\tilde{\mathbf{D}}(e, e_\mu, s, T) \left[\frac{\partial \tilde{c}(s, T)}{\partial s} \nabla s + \frac{\partial \tilde{c}(s, T)}{\partial T} \nabla T \right],$$

$$\tilde{c}(s, T) = \left[\frac{m_{\theta_g^w}(s, T)}{\rho_g(s, T)} \right],$$

$$\tilde{\mathbf{D}}(e, e_\mu, s, T) = \tau \phi \tilde{\rho}_g(s, T) \left(1 - \frac{e_\mu}{e} \right) D \frac{T^{2.3}}{p_g} \mathbf{1}.$$

2.4.3 Energy balance included

Comsol's built-in physics interface "Heat transfer in porous media" with an assumption of a common temperature T was utilized for adding a suitable energy balance to the formulation,

$$(\rho C_p)_{eff} \frac{\partial T}{\partial t} + {}^\mu \rho_l C_p^l \mathbf{q}_l \cdot \nabla T + \nabla \cdot \mathbf{h} = Q,$$

$$\mathbf{h} = - \left(\lambda_{dry} \left(1 - \frac{e_\mu}{e} \right) + \lambda_{sat} \frac{e_\mu}{e} \right) \nabla T,$$

$$(\rho C_p)_{eff} = (1 - \phi) \rho_s C_p^s + \phi {}^\mu \rho_l C_p^l.$$

2.4.4 New evolution equation for the micro void ratio

The evolution of micro void ratio is driven by changes in total void ratio as well as suction,

$$de_\mu = \frac{\partial e_\mu}{\partial e} de + \frac{\partial e_\mu}{\partial s} ds,$$

The void ratio driven term is taken as the contact area function,

$$\frac{\partial e_\mu}{\partial e} = \tilde{\alpha}(e, e_\mu) = \left(\frac{1 + e_\mu}{1 + e} \right)^\gamma.$$

The most recent formulation for the suction-driven term is defined differently for negative and positive suction rates, respectively.

For negative suction rates, the properties of $\partial e_\mu / \partial s$ is illustrated in the left panel of Figure 2-1. The derivative is defined so that: i) the suction decreases faster than the ψ_M -function for increasing e_μ -values; and ii) so that saturated conditions (i.e. $e_\mu = e_{tot}$) is reached precisely when $s = 0$. The first condition implies that a stress which corresponds to $f = 0$, ($\mathbf{f} = f\mathbf{1}$) will display an increasing trend. This is achieved with the condition that the s/ψ_M -ratio displays a linear decrease with an increasing e_μ -value (Figure 2-1, left panel, right graph). The introduction of this ratio (r) means that:

$$s = r\psi_M$$

Derivation the expression above with respect to e_μ results in the first relation in the equation below.

$$\frac{\partial s}{\partial e_\mu} = \frac{\partial r}{\partial e_\mu} \psi_M + r \frac{\partial \psi_M}{\partial e_\mu} = \frac{-s}{\psi_M} \frac{1}{e_{tot} - e_\mu} \psi_M + \frac{s}{\psi_M} \frac{\partial \psi_M}{\partial e_\mu}$$

This expression is obtained by identifying $\partial r / \partial e_\mu$ by a straight line from the point (e_μ, r) to point $(e_{tot}, 0)$ in Figure 2-1 (left panel, right graph), and by substituting r with s / ψ_M . Inverting the relation above gives the sought reciprocal partial derivative.

For positive suction rates, the properties of the corresponding derivative are illustrated in the right panel of Figure 2-1. The derivative is defined so that the suction value changes asymptotically towards the ψ_M -function. This implies that a stress (with $f = 0$) will display an asymptotic trend towards zero.

For this purpose, a parameter e_{step} is introduced. The derivative is defined so that a stress path in each point (e_μ, s) is directed towards the point $(e_\mu - e_{step}, \tilde{\psi}_M(e_\mu - e_{step}))$ which yields the following expression:

$$\frac{\partial e_\mu}{\partial s} = \frac{-e_{step}}{|s - \tilde{\psi}_M(e_\mu - e_{step})|}$$

Since e_{step} is constant, this means that the point of direction will change with decreasing e_μ values. The absolute value is introduced so that the derivative will yield a negative value regardless of the relative magnitude of s and Ψ_M .

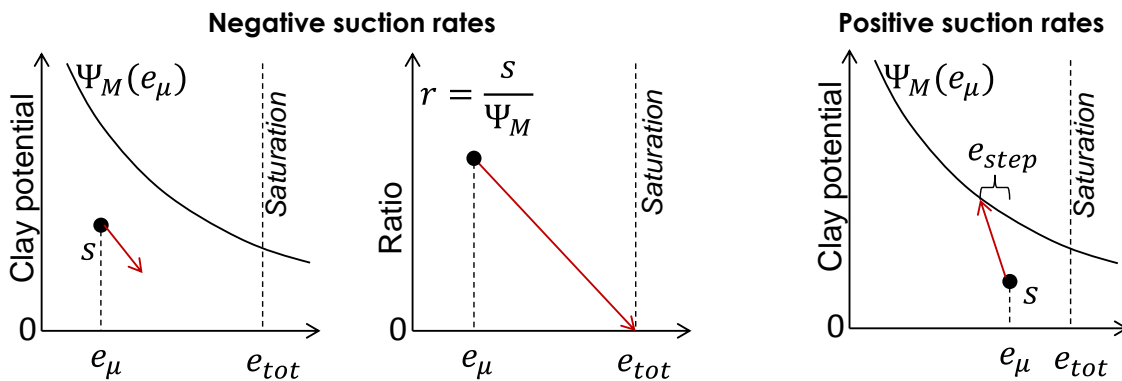


Figure 2-1. Definition of $\partial e_\mu / \partial s$. Left panel: Negative suction rates, ψ_M and s vs e_μ (left); s / ψ_M -ratio vs. e_μ (right). Right panel: Positive suction rates, ψ_M and s vs. e_μ .

2.4.5 New equation restricting the path dependent variable

The path dependent variable f is a second order tensor which may be split into a spherical and deviatoric part,

$$\mathbf{f} = \frac{1}{3} \text{tr} \mathbf{f} \mathbf{1} + \mathbf{f}^{dev} = f_p \mathbf{1} + \mathbf{f}^{dev}$$

From the deviatoric part an invariant f_q can be defined according to,

$$f_q = \sqrt{3J_2^q} \quad \text{where} \quad J_2^q = \frac{1}{2} \mathbf{f}^{dev} \cdot \mathbf{f}^{dev}.$$

A relation $f_p^2 + f_q^2 = R^2$ is set up as to obtain limiting values for \mathbf{f} in different directions. The new parameter R defines the restriction and when studying the behaviour of the model a value of 0.9 was found suitable.

2.4.6 New Febex bentonite parameter set

The clay potential function is linked to experimentally motivated swelling pressure curves, $\tilde{p}_{sw}^{high}(e_\mu)$ and $\tilde{p}_{sw}^{low}(e_\mu)$, on the format,

$$\tilde{p}_{sw}^\beta(e_\mu) = (p_{sw}^\beta)_0 \exp(c_0^\beta + c_1^\beta e_\mu + c_2^\beta e_\mu^2 + c_3^\beta e_\mu^3) \quad \text{where } \beta = \text{high, low}.$$

The *low* curve corresponds to what is measured at swelling/wetting and the *high* curve corresponds to what is measured at compression/drying, respectively. The parameter set $\{(p_{sw}^\beta)_0, c_i^\beta\}$ was calibrated so that the functions $\tilde{p}_{sw}^\beta(e_\mu)$ fitted Febex data.

The Darcy-flux is given by

$$\mathbf{q}_l = -\frac{\tilde{\kappa}(e) \left(\frac{e_\mu}{e}\right)^3}{\mu} (-\nabla s) \quad \text{where} \quad \tilde{\kappa}(e) = \kappa_0 \left(\frac{e}{e_{ref}}\right)^\beta.$$

The parameter set $\{\kappa_0, e_{ref}, \beta\}$ was calibrated as to obtain a representative fit of $\tilde{\kappa}(e)$ with respect to Febex data.

2.5 Clay Technology – Code_Bright

It was requested that Clay Technology reported the outcome from pre-existing models of the Canister Retrieval Test and the Febex Test. Short descriptions of the formulations are given in the sections where the simulations are addressed. For more information see Kristensson (2019a) and Kristensson (2019b) for CRT and Febex, respectively.

2.6 VTT/UCLM

The general framework for the coupled thermo-hydraulic-mechanical-

chemical (THMc) model developed by VTT and UCLM has been described in the BEACON Deliverable D3.1 Annex G. The use of COMSOL Multiphysics software as the implementation platform and the adopted model development and implementation strategy (Navarro et al., 2019) allow for flexible simulations also with subsets of the phenomena and processes considered in the THMc model framework. The macrostructure-microstructure mechanical coupling for wetting paths is modelled within the framework of the Barcelona Expansive Model (BExM). The mechanical part of model has been extended by the formulation proposed by (Navarro et al., 2017) allowing for chemo-mechanical coupling and for free-swelling processes.

In the CRT simulation, a hydro-mechanical (HM) coupled double porosity model (DPM) has been applied for the compacted block domains, and a HM coupled triple porosity model (TPM) has been used for the pellet fill between the wall of the deposition hole and the blocks. For the TPM (Navarro et al., 2020), a new structural level is introduced to take into account the particularities of the inter-pellet space. In the domain with a granular/pellet structure, in addition to the microstructural level, the M1 level comprises the inter-aggregate pore space inside the bentonite pellets, and the M2 level comprises the inter-pellet space. The M2 level is treated as elastic with regard to stress changes.

Given the fast imposed hydration of the inter-pellet space due to the artificial wetting, the liquid pressure in level M2, $P_{L,2}$, is taken in all the pellet fill domain as equal to the liquid pressure applied on the boundary $P_{L,ext}$. A water exchange between M1 and M2 levels is assumed to be proportional to the difference in liquid pressure between both levels.

The interface between the compacted blocks and the pellet fill has been modelled using identity pairs, a COMSOL in-built feature, ensuring continuity in the field variables across the boundary of two adjacent domains.

While the inner gap between the canister and the compacted blocks was left empty, the outer gap between the blocks and the wall of the deposition hole was filled with pellets. The bentonite buffer in the CRT was artificially wetted by pumping water through filter mats into the pellet fill. Although the exact volume cannot be quantified, water pumped into the pellet fill also likely reached the inner gap through the interfaces between the blocks, as indicated by sensor data (Börgesson et al., 2016; Kristensson & Börgesson, 2015). This was considered in the simulations and the water supply to the inner gap was stopped when the gap has been filled by swollen bentonite. The inner gap has been treated as a contact problem. In addition, the thermal effect on the CRT caused by the Temperature Buffer Test (TBT) run in the immediate neighbourhood (6 m distance between deposition hole centres) has been taken into account in the simulations in the temperature boundary conditions. Moreover, the canister was allowed to move vertically as a consequence of the bentonite swelling.

The set of state variables are the liquid pressure in the M1 level P_L , the micro void ratio e_m , the displacement field \mathbf{u} and the temperature T . For simplicity, the gas pressure P_G has not been solved for in the presented simulations and is assumed to be constant at atmospheric pressure instead on both the M1 and M2 pore space. The vapour phase, however, is included in the model. The chemical couplings have been disregarded in the simulation of the CRT. Resulting from the applied mixed method for solving the mechanical boundary value problem (Navarro et al., 2014), the net/effective stress σ , the M2 void ratio e_{M2} and the pre-consolidation pressure for zero suction p_0^* are additional state variables. The strains are treated as anisotropic. The distribution of volumetric strains into the space directions is inversely proportional to the stress in the corresponding direction. The geometry used is 2D axisymmetric. Two geometries have been considered in modelling the CRT: a slice of the buffer at canister mid-height and the entire buffer.

2.7 ICL

2.7.1 Software

The Imperial College London (ICL) team has applied the bespoke software ICSEP (Potts & Zdravkovic, 1999) in all analyses presented in this report. This is a fully thermo-hydro-mechanically (THM) coupled general-purpose geotechnical software, providing a range of advanced soil constitutive models and boundary conditions.

2.7.2 Mechanical model

The constitutive model applied in all analyses to represent the mechanical behaviour of compacted bentonite is the Imperial College Double Structure Model (ICDSM), Ghiadistri (2019), Ghiadistri et al. (2018). This is an extension of the previous single structure model (ICSSM, Georgiadis et al., 2005; Tsiampousi et al., 2013) which adopts the Barcelona Basic Modelling (BBM) framework..

The ICDSM was introduced in detail in the deliverable D.3.1. Consequently, only the part of the model that enhances the simulation of the behaviour of expansive clays, as appropriate for compacted bentonite, is presented here. Overall, the model is formulated for unsaturated clays, adopting two independent stress variables: suction, $s = u_{air} - u_w$, and net stress, $\bar{\sigma} = \sigma_{tot} - u_{air}$, with u_{air} and u_w being the air and water pressures in the pores, respectively, and σ_{tot} being the total stress. To enable smooth transition from saturated to unsaturated states and vice versa, the model also introduces an equivalent suction, $s_{eq} = s - s_{air}$, and equivalent stress, $\sigma = \bar{\sigma} + s_{air}$, where s_{air} is the air-entry value of suction for a given soil. As such, the model allows realistic values of s_{air} to be prescribed for any soil and full saturation is

reached when $s = s_{air}$. The model is further generalised in the (J, p, θ, s_{eq}) space, where J , p and θ are the invariants of the equivalent stress tensor, representing generalised deviatoric stress, mean equivalent stress and Lode's angle, respectively.

The enhancement of the ICDSM to enable the modelling of unsaturated expansive clays comprises the introduction of a double-porosity structure into the model formulation, in agreement with e.g. Gens & Alonso (1992). This formulation differentiates two levels of structure in the clay: the macro-structure, which is assumed unsaturated and mostly defined by the original ICSSM framework; and the micro-structure, assumed to be elastic, volumetric and fully saturated.

Characteristics of the micro-structure

Assuming the micro-structure to be fully saturated implies that it can be defined in terms of effective stresses, where the mean effective stress $p' = p + s_{eq}$. The assumptions that it is also volumetric and elastic imply that changes in p' result in elastic volumetric micro-strains, $\Delta\varepsilon_{v,m}^e$:

$$\Delta\varepsilon_{v,m}^e = \frac{\Delta p'}{K_m} \quad (1)$$

where the micro-structural bulk modulus, K_m , is defined as:

$$K_m = \frac{1 + e_m}{\kappa_m} p' \quad (2)$$

In the above equation e_m is the micro-structural void ratio and κ_m is the elastic compressibility parameter. For consistency, the following must be satisfied:

$$e = e_M + e_m \quad (3)$$

where e_M is the macro-structural and e the overall void ration of the material. The bulk modulus K_m is additional to the two bulk moduli associated with the macro-structure and defined by the ICSSM formulation: $K_{s,M}$, associated with equivalent suction, and $K_{p,M}$, associated with mean equivalent stress, all three defining the overall elastic soil behaviour in the double-structure formulation.

Interaction of the two levels of structure

Although the micro-structural volumetric deformation is elastic, it is assumed to contribute to the macro-structural volumetric plastic strains, $\Delta\varepsilon_{v,\beta}^p$, through an additional plastic mechanism:

$$\Delta\varepsilon_{v,\beta}^p = f_\beta \cdot \Delta\varepsilon_{v,m}^e \quad (4)$$

defined by the interaction function, f_β , between the two levels of structure. The shape of this function is dependent on whether the micro-structure swells or compresses and is defined by the following function:

$$f_{\beta} = \begin{cases} \begin{cases} c_{c1} + c_{c2} \left(\frac{p_r}{p_0} \right)^{c_{c3}} & \text{if } \frac{p_r}{p_0} \geq 0 \\ c_{c1} & \text{if } \frac{p_r}{p_0} < 0 \end{cases} & \text{micro-compression} \\ \begin{cases} c_{s1} + c_{s2} \left(1 - \frac{p_r}{p_0} \right)^{c_{s3}} & \text{if } \frac{p_r}{p_0} \geq 0 \\ c_{s1} + c_{s2} & \text{if } \frac{p_r}{p_0} < 0 \end{cases} & \text{micro-swelling} \end{cases} \quad (5)$$

in which p_r/p_0 expresses the degree of openness of the structure in terms of the distance of the current stress state, represented by p_r , from the yield surface, represented by p_0 , while c_{c1}, c_{c2}, c_{c3} and c_{s1}, c_{s2}, c_{s3} are coefficients defining the shaper of the interaction function.

Quantification of the micro-structural evolution

Finally, the ICDSM introduces the void factor, $VF = e_m/e$, to enable the quantification of the micro-structural evolution in the clay. This parameter expresses the degree of dominance of each structural level in the overall clay fabric.

All model parameters are summarised in Table 2-3, together with a list of experiments that enable parameter derivation. A double-structure formulation introduces four additional model parameters, as shown in the table.

Table 2-3 Summary of ICDSM parameters

	Parameter	Source
Input parameters for IC SSM	Parameters controlling the shape of the yield surface, α_F, μ_F	Triaxial compression; relationship between dilatancy and J/p ratio
	Parameters controlling the shape of the plastic potential surface, α_G, μ_G	Triaxial compression
	Generalized stress ratio at critical state, M_J	Triaxial compression, related to the angle of shear resistance ϕ'_{cs}
	Characteristic pressure, p_c (kPa)	Limiting confining stress at which $p_0 = p_0^* = p_c$
	Fully saturated compressibility coefficient, $\lambda(0)$	Fully saturated isotropic loading
	Elastic compressibility coefficient, κ	Fully saturated isotropic unloading
	Maximum soil stiffness parameter, r	Isotropic compression tests at constant value of suction
	Soil stiffness increase parameter, β (1/kPa)	Isotropic compression tests at constant value of suction
	Elastic compressibility coefficient for changes in suction, κ_s (kPa)	Drying test and constant confining stress
	Poisson ratio, ν	Triaxial compression test

	Plastic compressibility coefficient for changes in suction, λ_s	Drying test and constant confining stress
	Air-entry value of suction, s_{air} (kPa)	From the retention curve
	Yield value of equivalent suction, s_0 (kPa)	Usually a high value if it is not to be mobilised
Additional input parameters for IC DSM	Microstructural compressibility parameter, k_m	No direct test
	Void factor, VF	No direct test – potentially from MIP interpretation
	Coefficients for the micro swelling function, c_{s1}, c_{s2}, c_{s3}	No direct test – potentially from MIP interpretation
	Coefficients for the micro compression function, c_{c1}, c_{c2}, c_{c3}	No direct test – potentially from MIP interpretation

2.7.3 Soil water retention (SWR) model

For the analyses presented in this report, a non-hysteretic Van Genuchten-type (van Genuchten, 1980) SWR model was adopted, formulated in terms of the degree of saturation, S_r , and the matric suction (Melgarejo, 2004):

$$S_r = \left[\frac{1}{1 + [\alpha \cdot (v - 1)^\psi \cdot s_{eq}]^n} \right]^m \cdot (1 - S_{r0}) + S_{r0} \quad (6)$$

In the above equation $s_{eq} = s - s_{air}$, S_{r0} is the residual degree of saturation, while α , m and n are fitting parameters controlling the shape of the retention curve; ψ is the parameter controlling the effect of the specific volume, v .

2.7.4 Hydraulic conductivity (permeability) model

The variable permeability model (Potts & Zdravkovic, 1999; Nyambayo & Potts, 2010) adopted in all analyses assumes the permeability (hydraulic conductivity) to vary with matric suction as depicted in Figure 2-2 and expressed below:

$$\log k = \log k_{sat} - \frac{s - s_1}{s_2 - s_1} \cdot \log \frac{k_{sat}}{k_{min}} \quad (7)$$

where k_{sat} is the saturated value of permeability (m/s), k_{min} its minimum value reached after the prescribed change in matric suction from s_1 to s_2

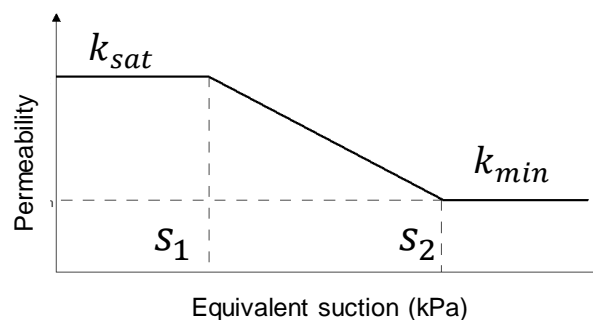


Figure 2-2 Variable permeability model

2.8 LEI

The finite element code, CODE-BRIGHT v9.3 (COuple DEformation BRIne Gas and Heat Transport) was used for numerical simulations of FEBEX experiment. The performed thermo-hydro-mechanical (THM) analysis has taken into account the following phenomena:

- Heat transport:
 - Heat conduction (Fourier's law). The dependence of thermal conductivity on porosity and degree of saturation was expressed by a variant of the geometric mean;
 - Heat advection by liquid water and water vapour flow.
- Water flow:
 - Advective flow of liquid water was described by Darcy's law. Advective flow of gaseous air was neglected - gas phase pressure considered as atmospheric and constant. Air dissolution in water was not taken into account;
 - The intrinsic permeability of bentonite depends on porosity according to Kozeny's model;
 - The retention curve for bentonite was derived from modified Van Genuchten model and for granite was derived from standard Van Genuchten model. Drying and wetting paths (hysteresis) was not taken into account;
 - The relative permeability laws for bentonite and granite was expressed by Brooks and Corey (power law) and Van Genuchten models, respectively;
 - Diffusive flow of water vapour was described by Fick's law. The effect of diffusion in the interior of a porous medium was considered by means of a coefficient of tortuosity.
- Mechanical behaviour:
 - Thermal expansion of bentonite and granite;
 - BBM thermo-elasto-plastic model (Alonso et al., 1990) for bentonite (single porosity) taking into account the variation of stress-stiffness with suction and variation of swelling potential with stresses and suction;
 - Linear elastic model for granite;
 - Excavation of disposal tunnel and buffer/heater placement.

Some simplifications in CODE_BRIGHT model were made to present FEBEX experiment:

- A homogeneous bentonite buffer was assumed disregarding the joints between the bentonite blocks and the potential gaps between rock and buffer, buffer and heater;
- Localized water entries through discontinuities (lamprophyre dikes, fractures) were not explicitly considered;

- An average mass permeability of the granite was used to describe the hydraulic property of the host rock.

2.9 Quintessa

The full description of Quintessa's coupled THM model can be found in Appendix F of Deliverable 3.1. In addition to the processes described there, vapour diffusion and additional thermal dependency of parameters have been used to model the (heated) FEBEX experiment.

The vapour transport model is based on the Philip & de Vries (1957) equation for diffusive vapour flux J [kg y^{-1}]:

$$J = -D \cdot \nabla \rho_v$$

where D is the coefficient of diffusivity [$\text{m}^2 \text{s}^{-1}$] and ρ_v is vapour density [kg m^{-3}]. Following Cleall et al. (2013), this can be expressed as:

$$J = -D_{atm} \cdot \tau_v \cdot \theta \cdot \nabla \rho_v$$

where τ is tortuosity [-], θ is porosity [-] and D_{atm} is the molecular diffusivity of vapour through air [$\text{m}^2 \text{s}^{-1}$], described by:

$$D_{atm} = 2.2 \cdot 10^{-5} \cdot \left(\frac{P_{atm}}{P_g} \right) \cdot \left(\frac{T}{T_0} \right)^{1.75}$$

where P_{atm} is atmospheric pressure [Pa], P_g is the pore gas pressure [Pa], T_0 is the reference temperature [K] and T is temperature [K]. Parameters for this model are given in Section 5.4.2.

As described in Deliverable 3.1, Quintessa's Internal Limit Model (ILM) uses an exponential curve parameterised by two constants (p_0 [MPa] and λ [-]) to represent the relationships between swelling pressure & dry density, suction & water content, and void ratio & vertical stress. This is of the form:

$$p = p_0 \cdot \exp\left(-\frac{e}{\lambda}\right)$$

where p is swelling pressure, stress or suction [MPa] and e is void ratio [-], which can be also expressed in terms of dry density or saturated water content.

In previous isothermal models developed during the Beacon project, p_0 and λ were constants calibrated to swelling pressure, water retention and oedometer data for MX-80 bentonite. For the FEBEX experiment, these parameters were re-calibrated to the equivalent data for FEBEX bentonite (see Figure 2-3 to Figure 2-5). As shown in Figure 2-5, water retention data for

FEBEX bentonite is dependent on temperature. Therefore, a linear temperature dependence for the p_0 parameter was introduced; see Section 5.4.2 for parameterisation.

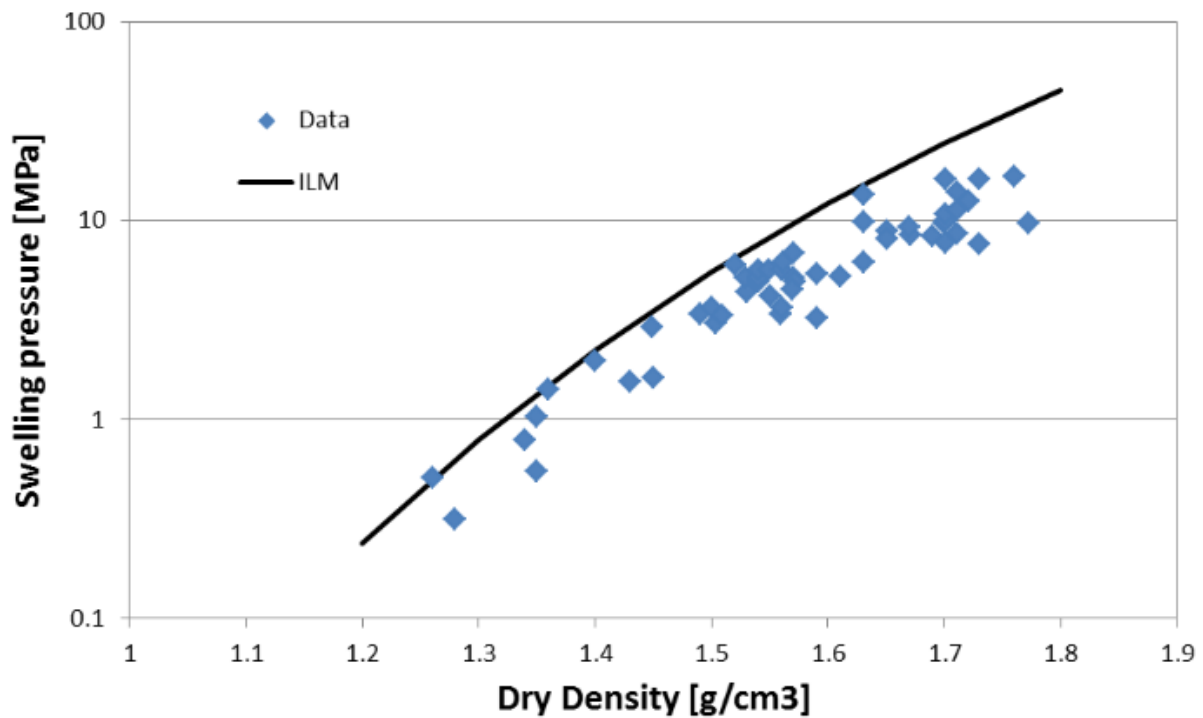


Figure 2-3: Swelling data for the FEBEX bentonite (Lloret et al., 2005) with the calibrated ILM curve.

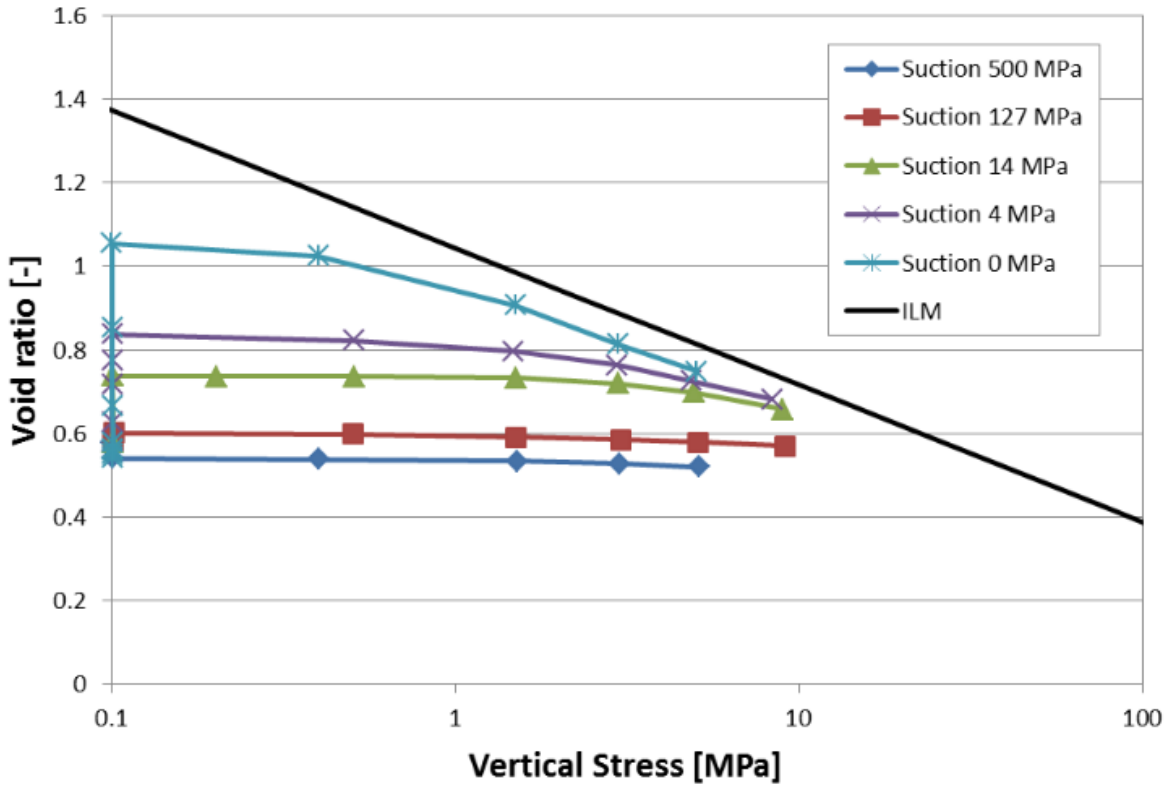


Figure 2-4: Oedometer test data for the FEBEX bentonite (Lloret et al., 2005) with the calibrated ILM curve.

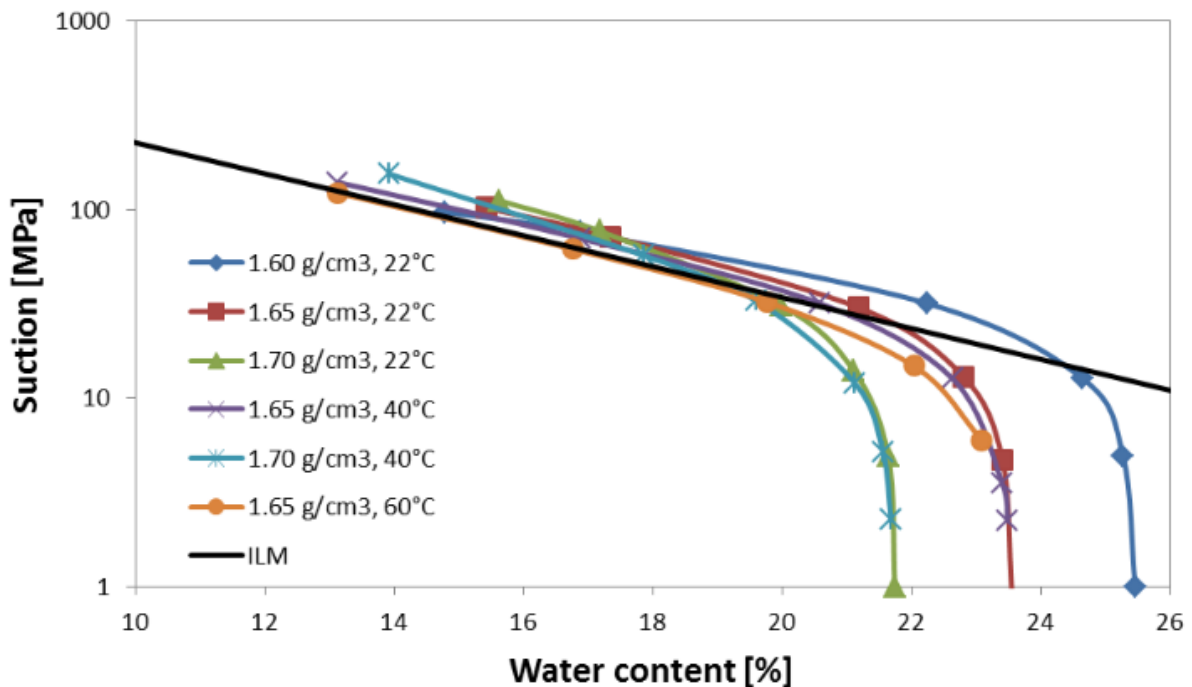


Figure 2-5: Confined water retention data for the FEBEX bentonite at different dry densities and temperatures (Lloret et al., 2005) compared with the calibrated ILM suction curve for unconfined conditions at 60°C.

Thermal expansion has also been added to the model, with temperature-dependent coefficients of linear thermal expansion (parameterised in Section 5.4.2).

Finally, a dry density dependence has been added to the definition of intrinsic permeability. Previously, a constant value of intrinsic permeability was used for simplicity. This is also parameterised in Section 5.4.2.

As in previous work, the model has been implemented in QPAC, Quintessa's general-purpose finite volume code.

2.10 EPFL

The constitutive model used by EPFL to describe the behaviour of the FEBEX bentonite is presented in the Beacon deliverable D3.2, extended to non-isothermal conditions using the thermo-elastic and thermo-plastic relationships of ACMEG-TS (Laloui and Cekerevac 2003, François and Laloui 2008; Di Donna and Laloui, 2015; Vilarrasa et al., 2017). As described in the deliverable D3.2, the model has been developed within the WP3 of the BEACON project. The complete description is planned to be reported in the deliverable D3.3 of the WP3, including its implementation in the Finite Element code Lagamine (Charlier 1987, Collin 2003) which allows the analysis of thermo-hydro-mechanical processes in porous media.

The model is formulated in the framework of the generalised effective stress, that is linked to the mechanical elastic strains, and the degree of saturation, which expresses the variation of compressibility under unsaturated conditions. A new water retention model, that takes explicitly into account the existence of adsorbed water, is used to predict the evolution of the degree of saturation with suction. The elastic domain is influenced by the stress history, the current temperature and the degree of saturation.

In particular, the model features:

- The critical state concept, based on the works of Roscoe et al. (1958)
- A non-associated flow rule and yield surface derived from thermomechanical potentials by Collins and Kelly (2002)
- Lode angle dependency of the critical state line by van Eekelen (1980) (Di Donna & Laloui, 2015)
- An effective stress framework studied by Nuth and Laloui (2008) which unifies the interpretation of unsaturated and saturated soil behaviour
- A water retention model that makes distinction between free and adsorbed water, coupled to a volume change equation for unsaturated states that allows a seamless transition between unsaturated and saturated states (Bosch et al. under review)
- Thermo-elastoplasticity framework based on ACMEG-T (Laloui and

François 2009)

The model equations are summarised in the following.

According to the theory of elasto-plasticity, an explicit distinction is made between elastic (reversible) strains and plastic (irreversible) strains:

$$d\boldsymbol{\epsilon} = d\boldsymbol{\epsilon}^e + d\boldsymbol{\epsilon}^p \quad (1)$$

where $\boldsymbol{\epsilon}$ is the total strain tensor and superscripts e , p denote elastic and plastic strains respectively. The following Bishop-type expression is used for the effective stress $\boldsymbol{\sigma}'$ (Nuth and Laloui 2008):

$$\boldsymbol{\sigma}' = \boldsymbol{\sigma} - [p_a - (p_a - p_w)S_r]\mathbf{I} \quad (2)$$

where $\boldsymbol{\sigma}$ is the total stress tensor, p_a is the pore air pressure, p_w is the pore water pressure and S_r is the degree of saturation.

The equations of the model are written in terms of the following stress invariants:

$$p' = \frac{1}{3}\text{tr}(\boldsymbol{\sigma}'), \quad q = \sqrt{3}J, \quad \sin(3\theta) = \frac{3\sqrt{3}\det \mathbf{s}}{2J^3}$$

where $\mathbf{s} = \boldsymbol{\sigma}' - p'\mathbf{I}$ and $J = \sqrt{\frac{1}{2}\text{tr}(\mathbf{s}^2)}$. Likewise, the following strain invariants are defined

$$\epsilon_v = \text{tr}(\boldsymbol{\epsilon}), \quad \epsilon_d = \sqrt{\frac{1}{3}\text{tr}(\boldsymbol{\gamma}^2)}, \quad \boldsymbol{\gamma} = \boldsymbol{\epsilon} - \frac{1}{3}\epsilon_v\mathbf{I}$$

The following elastic relationships are used:

$$d\epsilon_v^e = \frac{p'}{\kappa} dp' - \frac{1}{3}[\beta_{T0} + \beta_{T1}(T - T_r)]dT, \quad d\epsilon_d^e = \frac{9(1 - 2\nu)p'}{2(1 + \nu)\kappa} dq \quad (3)$$

Where T is the current temperature, κ and ν are elastic material parameters, T_r is a reference temperature and β_{T0} , β_{T1} are thermo-elastic parameters (Laloui and François 2009). The yield surface and flow rule derived by Collins and Kelly (2002) are used. The yield surface, f_Y in the stress space takes the following form:

$$f_Y = q^2 - M^2\Pi^2(p'_Y - p')p' = 0 \quad (4)$$

$$\Pi = \alpha + (1 - \alpha)\left(\frac{2p'}{p'_Y}\right)$$

where M is the critical stress ratio, which depends on Lode's angle, α is a material parameter, and $p'_Y = p'_Y(\epsilon_v^p, S_r, T)$ corresponds to the yield pressure. A dependency of strength on the stress path is established by taking the critical stress ratio as a function of the Lode's angle (van Eekelen, 1980; Vilarassa et al. 2017):

$$M(\theta) = a_L[1 + b_L \sin(3\theta)]^{n_L} \quad (5)$$

Where a_L and b_L are defined as:

$$a_L = \frac{M_c}{(1 + b_L)^{n_L}} \quad (6)$$

$$b_L = \frac{\left(\frac{M_c}{M_e}\right)^{1/n_L} - 1}{\left(\frac{M_c}{M_e}\right)^{1/n_L} + 1} \quad (7)$$

$$M_c = \frac{6 \sin \phi'_c}{3 - \sin \phi'_c}, \quad M_e = \frac{6 \sin \phi'_e}{3 + \sin \phi'_e} \quad (8)$$

Where ϕ'_c and ϕ'_e are the shear strength angles at failure for compression paths and extension paths respectively; and $n_L = -0.229$.

The yield pressure, p'_Y evolves with the degree of saturation (Zhou et al. 2012):

$$\frac{p'_Y}{p'_r} = \left(\frac{p'_{TY}}{p'_r}\right)^{\frac{\lambda_s - \kappa}{\lambda(S_r) - \kappa}} \quad (9)$$

Where p'_{TY} is the yield pressure at current temperature, p'_r is a reference stress, λ_s defines the elastoplastic compressibility during yielding for saturated states and $\lambda(S_r)$ is a function expressing the evolution of elastoplastic compressibility with the degree of saturation:

$$\lambda(S_r) = \lambda_s - r(\lambda_s - \kappa)(1 - S_r^\zeta)^\xi \quad (10)$$

where parameter r ($0 < r < 1$) expresses the decrease of elastoplastic compressibility from saturated to dry state ($S_r = 0$); and ζ and ξ are material parameters. A dependency of yield on temperature is introduced as (Laloui and Cekerevac 2003, Laloui and François 2009):

$$p'_{TY} = p'_{Ys} \left[1 + \gamma_T \ln \left(\frac{T}{T_r} \right) \right] \quad (11)$$

Where p'_{Ys} is the hardening variable (corresponding to the yield pressure at $S_r = 1$ and $T = T_r$) and γ_T is a material parameter.

Volumetric and deviatoric plastic strain increments are given by the flow rule:

$$d\epsilon_v^p = -d\Lambda(p' - p'_Y/2), \quad d\epsilon_a^p = -d\Lambda \frac{q}{M^2 \Pi^2} \quad (12)$$

The hardening variable, p'_{Ys} evolves according to the hardening law:

$$\frac{dp'_{Ys}}{p'_{Ys}} = \frac{d\epsilon_v^p}{\lambda_s - \kappa} \quad (13)$$

The degree of saturation is computed as the ratio between water ratio e_w (ratio of water volume with respect to volume of solids) and void ratio e , i.e. $S_r = \frac{e_w}{e}$.

The water retention model is formulated in terms of the water ratio, e_w which is divided into free water ratio, $e_{w,f}$ (volume of non-adsorbed water with respect to volume of solids) and adsorbed water, $e_{w,a}$ (volume of adsorbed water with respect to volume of solids) as $e_w = e_{w,f} + e_{w,a}$.

The evolution of free water ratio $e_{w,f}$ is modelled as:

$$e_{w,f} = (e - e_{w,a}) \left[1 + \left(a(e - e_{w,a})^b s \right)^n \right]^{1/n-1} \quad (14)$$

where n , a and b are material parameters and s stands for matric suction. $e_{w,a}$ follows a Freundlich isotherm:

$$e_{w,a} = e_{w,a}^c \left[\exp \left(- \frac{M_w}{\rho_{w,a} R T_r} s \right) \right]^{1/m} \quad (15)$$

where $\rho_{w,a}$ is the density of adsorbed water, $R = 8.314$ J/mol K, is the gas constant, M_w is the molar mass of water, $e_{w,a}^c$ is the adsorption capacity parameter, and m is a material parameter. Note that while free water ratio depends on the current void ratio, the adsorbed water ratio only depends on suction.

Specific features that make the model relevant for the FEBEX insitu test include:

- The test involved non-isothermal states. Furthermore, thermo-plasticity in FEBEX bentonite was recognised by Romero et al. (2005)
- The degree of saturation of FEBEX bentonite is sometimes computed higher than 100%, which suggests that density of adsorbed water might be above that of free water. Using the water retention model proposed, the density of adsorbed water can be considered different to that of free water
- The degree of saturation controls the hydraulic conductivity and thermal conductivity. Because it depends on the dry density, a water retention that is dependent on the void ratio is essential in order to quantitatively predict the evolution of the state of the barrier
- Drying-wetting cycles were only measured (by means of relative humidity) in the bentonite close to the heaters and starting from hygroscopic conditions. At this range of relative humidity (high suction), Lloret et al. (2003) did not observe significant hysteresis. Therefore, only the wetting branch of the water retention curve is used, and the effects of hydraulic hysteresis are going to be neglected. Nevertheless, by means of hydro-mechanical coupling, hysteresis can arise due to

irreversible deformations

At the same time, this modelling exercise was performed in order to verify the suitability of the model to analyse a full-scale test. Prior to this study, the model was verified exclusively with laboratory tests, interpreted based on an elementary volume basis. In this sense the FEBEX test allows to evaluate the capabilities of the model developed for a representative case of geological repository for high-level nuclear waste, ensuring that no spurious effects arise due, for instance, to up-scaling and arbitrary stress-paths.

The balance equations of mass, energy and momentum implemented in Lagamine are based on the compositional approach and are described in detail in Collin et al. (2002) and Collin (2003). For the sake of conciseness only the most relevant constitutive relationships will be described here.

Water flow is modelled by means of Darcy's law neglecting the gravitational forces:

$$\mathbf{q}_w = -\frac{k_{rw}\mathbf{k}_f}{\mu_w}[\text{grad}(p_w)] \quad (16)$$

Where \mathbf{q}_w is the vector of water flux, \mathbf{k}_w is the tensor of intrinsic permeability, k_{rw} is the relative permeability and μ_w is the water viscosity. Relative permeability evolves with the degree of saturation, S_r following an exponential law

$$k_{rw} = S_r^{\alpha_k} \quad (17)$$

Where k_{sat} is the permeability at saturated state, and α_k is a material parameter. In the present case it will be considered that the permeability tensor is isotropic, i.e.:

$$\mathbf{k}_f = \mathbf{I}k_f \quad (18)$$

The influence of deformation on the intrinsic permeability is taken into account by means of the Kozeny-Karman formula:

$$k_f = k_{f,0} \frac{(1 - n_0)^M}{n_0^N} \frac{n^N}{(1 - n)^M} \quad (19)$$

Where $k_{f,0}$ is the initial intrinsic permeability, n stands for porosity, n_0 is the initial porosity and M and N are material parameters.

The effect of temperature on water is important because it controls the change from liquid phase to gas phase in the form of vapor. Vapor in the porous medium is supposed to be in thermodynamic equilibrium with liquid water, thus using Kelvin-Laplace's law as the definition of relative humidity, the following relationship is obtained:

$$\rho_v = \exp \left[\frac{(p_w - p_g)M_v}{RT\rho_w} \right] \rho_{v,0} \quad (20)$$

Where M_v is the gas constant of water vapour, and $\rho_{v,0}$ is the saturated vapor density, that is dependent on temperature. Applying Dalton's law $p_g = p_a + p_v$, where p_g is the gas pressure (mixture of air and vapor) and p_v is the vapor pressure, the overall air density is:

$$\rho_a = \frac{p_g M_a}{RT} - \frac{\rho_v R_v}{R_a} \quad (21)$$

This relationship is used in the vapor diffusion law that is based on Fick's law in a porous medium:

$$\mathbf{i}_v = n(1 - S_r)\tau D \rho_g \text{grad} \left(\frac{\rho_a}{\rho_g} \right) = -\mathbf{i}_a \quad (22)$$

where \mathbf{i}_v is the vapor flow, D is the diffusion coefficient and τ the tortuosity. Heat transport is governed by both conduction and convection:

$$\mathbf{f}_T = -\Gamma \text{grad}(T) + [c_{p,w}\rho_w \mathbf{f}_w + c_{p,a}(\mathbf{i}_a + \rho_a \mathbf{f}_g) + c_{p,v}(\mathbf{i}_v + \rho_v \mathbf{f}_g)](T - T_0) \quad (23)$$

where Γ is the thermal conductivity of the mixture and $c_{p,i}$ corresponds to the heat capacity of the phase i . Γ is either considered as a function of the volume ratios of solid, liquid water and gas phases, or a specific function for the material.

2.11 BGR

The modelling of the coupled THM processes taking place in bentonite barrier of the FEBEX experiment was performed using the open source simulation software OpenGeoSys-5 (OGS5). OGS5 is a free multiplatform scientific modelling package for coupled thermo-hydro-mechanical-chemical processes in fractured and porous media (Kolditz et al. 2012). The coupled hydromechanical model used in the simulations of three test cases in step 1 of work package 5 was extended to consider temperature effects for the simulation of the FEBEX experiment. The coupled model is explained in the following sections

Symbols

$c_p^w \left(\frac{J}{kg \cdot K} \right)$: specific heat capacity of the water phase

$c_p^s \left(\frac{J}{kg.K} \right)$: specific heat capacity of the solid phase

\underline{C} : Stiffness tensor

$D^{pv} \left(\frac{m^2}{s.Pa} \right)$: pressure diffusion coefficient

$D^{Tv} \left(\frac{m^2}{s.K} \right)$: temperature diffusion coefficient

$D^v \left(\frac{m^2}{s} \right)$: binary diffusion coefficient

$\mathbf{g} \left(\frac{m}{s^2} \right)$: gravitational acceleration vector

RH (-): relative humidity

$\mathbf{I}(-)$: identity tensor

$\mathbf{J}^w \left(\frac{kg}{m^2.s} \right)$: mass flux of the water phase

$\mathbf{J}^v \left(\frac{kg}{m^2.s} \right)$: mass flux of the vapour phase

$K^w (Pa)$: compressibility of the water

$K^s (Pa)$: compressibility of the solid phase

$K^{skel} (Pa)$: compressibility of the porous skeleton

$\mathbf{k} (m^2)$: intrinsic permeability tensor

$k_{rel,w} (-)$: relative permeability of the water phase

$M_v \left(\frac{m^3}{mol} \right)$: molar volume

m: van Genuchten parameter

n: van Genuchten parameter

$p^w (Pa)$: pressure of the water phase

Q_T : heat source and sink

$R \left(\frac{J}{kg.K} \right)$: specific gas constant

S^g (-): saturation of the gas phase

S^w (-): saturation of the water phase

t (s) : time

T (K): temperature

\mathbf{u} (m): displacement field vector

α_{Biot} (-): Biot coefficient

$\beta_T^w \left(\frac{1}{K} \right)$: volumetric thermal expansion coefficient of the water phase

$\beta_T^s \left(\frac{1}{K} \right)$: volumetric thermal expansion coefficient of the solid phase

$\boldsymbol{\varepsilon}$ (-): strain tensor

$\rho^w \left(\frac{kg}{m^3} \right)$: density of the water phase

$\rho^s \left(\frac{kg}{m^3} \right)$: density of the solid phase

$\rho^{vs} \left(\frac{kg}{m^3} \right)$: saturated vapour density

$\rho^v \left(\frac{kg}{m^3} \right)$: vapour density

ϕ (-): porosity

$\lambda_m \left(\frac{W}{m.K} \right)$: thermal conductivity tensor of the medium

Θ_v (-): volumetric water content

$\mu \left(\frac{kg}{m \cdot s} \right)$: dynamic viscosity

τ (-): tortuosity

$\boldsymbol{\sigma}_{\text{tot}}$ (Pa): total stress tensor

$\boldsymbol{\sigma}_{\text{eff}}$ (Pa): effective stress tensor

$\boldsymbol{\sigma}_{\text{swell}}$ (Pa): swelling stress tensor

2.11.1 Heat transport model

The heat transport model considers transport in the liquid and solid phases only. Heat transport in the gas phase is neglected consistent with the Richards' approximation (Richards 1931) used for the liquid phase. The equation is given by

$$\left((1-\phi)\rho^s c_p^s + \phi S^w \rho^w c_p^w \right) \frac{\partial T}{\partial t} - \nabla \cdot (\lambda_m \nabla T) + c_p^w \mathbf{J}^w \nabla T + Q_T = 0 \quad (0.0.1)$$

The influence of the temperature on the hydraulic and the mechanical model is defined through the vapour diffusion model and the thermal expansion models respectively. These are elaborated in the following sections. The influence of the mechanical model on the temperature is neglected (weak coupling assumption). The liquid phase influences the heat transport through advection and conduction and the solid phase only through conduction.

2.11.2 Vapour diffusion model

To consider the effect of the temperature on the hydraulics in the form of vapour transport, the vapour diffusion model is used (Philip und Vries 1957; Rutqvist et al. 2001). This model gives the vapour mass flux as a function of the pressure and temperature gradients, given by

$$\mathbf{J}^v = -\rho^w \left(\mathbf{D}^{pv} \nabla p^w - \mathbf{D}^{Tv} \nabla T \right) \quad (0.0.2)$$

where the pressure diffusion coefficient, the temperature diffusion coefficient and the binary diffusion coefficient respectively are defined as:

$$\mathbf{D}^{Tv} = D^v \left(h_{rel} \frac{\partial \rho^{vS}}{\partial T} - \frac{\rho^v p^w}{\rho^w RT^2} \right) \quad (0.0.3)$$

$$\mathbf{D}^{pv} = \frac{D^v \rho^v}{\rho^w RT} \quad (0.0.4)$$

$$D^v = \tau \cdot S^g \cdot \phi \cdot 2.16 \cdot 10^{-5} \cdot (T / 273.15)^{1.8} \quad (0.0.5)$$

2.11.3 Hydraulic model

The flow of water is modelled with the multiphase flow formulation of Darcy's law. When the Richards' approximation is applied, the hydraulic model considers only the fluxes of water (0.0.6). Gravitational force along with other body forces were neglected for the simulation and the equations are also adapted to reflect this modelling decision.

$$\mathbf{J}^w = -\rho^w k_{rel,w} \frac{\mathbf{k}}{\mu} (\nabla p^w) \quad (0.0.6)$$

2.11.4 Mechanical model

The total stresses of the solid phase is decomposed into the effective stresses

and the respective contributions from the hydromechanical coupling, the swelling term and the thermal expansion term, given by

$$\boldsymbol{\sigma}_{\text{tot}} = \left(\boldsymbol{\sigma}_{\text{eff}} - \alpha_{\text{Biot}} S^w p^w \mathbf{I} - \Delta \boldsymbol{\sigma}_{\text{swell}} - \underline{\mathbf{C}} : \mathbf{I} \beta_T^s \Delta T \right) \quad (0.0.7)$$

The swelling stress increment is a function of the saturation increment and is given by

$$\Delta \boldsymbol{\sigma}_{\text{swell}} = -\sigma_{\text{swell}}^{\text{max}} \mathbf{I} \Delta S^w \quad (0.0.8)$$

The effective stresses are given by a linear elastic model

$$\boldsymbol{\sigma}_{\text{eff}} = \underline{\mathbf{C}} : \boldsymbol{\varepsilon} \quad (0.0.9)$$

2.11.5 Coupled mass and momentum balance

The coupled mass balance of water is formulated considering hydromechanical and thermal effects.

$$\begin{aligned} & \phi \left(\frac{\rho^w - \rho^v}{\rho^w} \right) \frac{\partial S^w}{\partial t} + S^w \left(\frac{\phi}{K^w} + \frac{\alpha_{\text{Biot}} - \phi}{K^s} \right) \frac{\partial p^w}{\partial t} \\ & + \nabla \cdot (\mathbf{J}^w + \mathbf{J}^v) / \rho^w + S^w \alpha_{\text{Biot}} \nabla \cdot \frac{\partial \mathbf{u}}{\partial t} \\ & + \phi \frac{1 - S^w}{\rho^w} \left[\left(h_{\text{rel}} \frac{\partial \rho^{vs}}{\partial T} + \frac{\rho^w p^w}{RT^2} \right) \frac{\partial T}{\partial t} + \frac{\rho^v}{\rho^w RT} \frac{\partial S^w}{\partial t} \right] \\ & - \left(\phi S^w \beta_T^w + (\alpha_{\text{Biot}} - \phi) \beta_T^s \right) \frac{\partial T}{\partial t} = 0 \end{aligned} \quad (0.0.10)$$

This model is solved using the staggered coupled scheme in which the thermal and hydraulic processes are iterated for a minimum of 2 and a maximum of 5 iterations. This is then coupled to the mechanical model and iterated again for a maximum of ten iterations.

The coupled momentum balance equation without sources or sinks and without the influence of body forces is given by

$$\nabla \cdot \left(\underline{\mathbf{C}} : \boldsymbol{\varepsilon} - \alpha_{\text{Biot}} S^w p^w \mathbf{I} - \Delta \boldsymbol{\sigma}_{\text{swell}} - \underline{\mathbf{C}} : \mathbf{I} \beta_T^s \Delta T \right) = \mathbf{0} \quad (0.0.11)$$

2.11.6 Constitutive relations

The capillary-pressure-saturation relationship is given by the standard van Genuchten curve and the relative permeability is a cubic function of the saturation of the water phase

$$S_{\text{eff}} = \frac{S^w - S_{\text{res}}^w}{1 - S_{\text{res}}^w} = \left(1 + (\alpha p_c)^n\right)^m$$

$$p_c = \begin{cases} 0 & S^w > S_{\text{max}}^w \\ \frac{\rho^w g}{\alpha} \left(S_{\text{eff}}^{\frac{1}{m}} - 1\right)^{\frac{1}{n}} & S_{\text{res}}^w < S^w < S_{\text{max}}^w \\ p_{c, \text{max}} & S^w < S_{\text{res}}^w \end{cases} \quad (0.0.12)$$

$$m = 1 - \frac{1}{n}$$

$$k_{\text{rel}}^w = (S^w)^3 \quad (0.0.13)$$

The modified van Genuchten function defined in the specification document is not used in the simulations and is currently being considered for development under WP3.

2.11.7 Post processing

The relative humidity is given by the Kelvin equation:

$$h_{\text{rel}} = e^{\frac{p_c M_v}{\rho_w R T}} \quad (0.0.14)$$

The volumetric water content is given by

$$\Theta_v = \phi \cdot S^w \quad (0.0.15)$$

These values are calculated in the post-processing step.

3 EB

3.1 Main feature of the test – why it is relevant for Beacon

Engineered Barrier Emplacement Experiment (EB experiment), is a long-term experiment that was dismantled after almost eleven years of operation. The experiment was carried out in a gallery excavated in the Opalinus clay of the Mont Terri Underground Research Laboratory. The EB experiment was designed in order to demonstrate a new emplacement technique of the bentonite barrier according to the Swiss concept and to represent the saturation phase under isothermal conditions.

This test is relevant for the Beacon project mainly due to the presence of initial heterogeneities in the system. A high difference is introduced in the initial dry density due to the presence of compacted block located below the canister (~1.7 Mg/m³) and granular bentonite used to fill the complementary part of the tunnel (~1.35Mg/m³). The hydration system and the natural water supplied contributed also to introduce differential swelling within the bentonite.

Post-mortem analysis shown residual gradients of properties in the bentonite. The challenge for the models was to reproduce the transient phase corresponding to water saturation and the final state with particular distributions of dry density or water content. An identification of main processes and/or parameters that lead to a (low) heterogeneous state was a part of this exercise.

3.2 UPC

3.2.1 Geometry and discretization

A 2-D plane strain geometry, 40 m wide and 80 m high, has been selected to represent the modelled domain, in which the symmetry of the cross section of the EB experiment has been taken into account. The domain has been spatially discretized by means of a finite element mesh composed of quadrilateral elements, is illustrated in Figure 3-1. The tunnel was excavated 160 days before the emplacement of the bentonite barrier. The tunnel has a horseshoe shaped cross section 3.00 m wide and 2.65 m high. The EDZ was modelled as a material with the same hydro-mechanical properties of the intact Opalinus Clay except for its initial porosity, water permeability and air entry suction. A width of 5.0 cm has been assumed for the EDZ. Geotextile material around the canister, between adjacent compacted block layers and at the concrete base – buffer interface has also been modelled as a very thin layer of finite elements with high porosity and water permeability.

The forced re-saturation of the barrier was achieved by the conception and built of a hydration system composed of 37 injection tubes arranged in a three-layer configuration so that the test duration could be reduced to a reasonable period of time. Due to the symmetry of the modelled geometry,

19 such points are included in the mesh, as it can be seen in Figure 3-1.

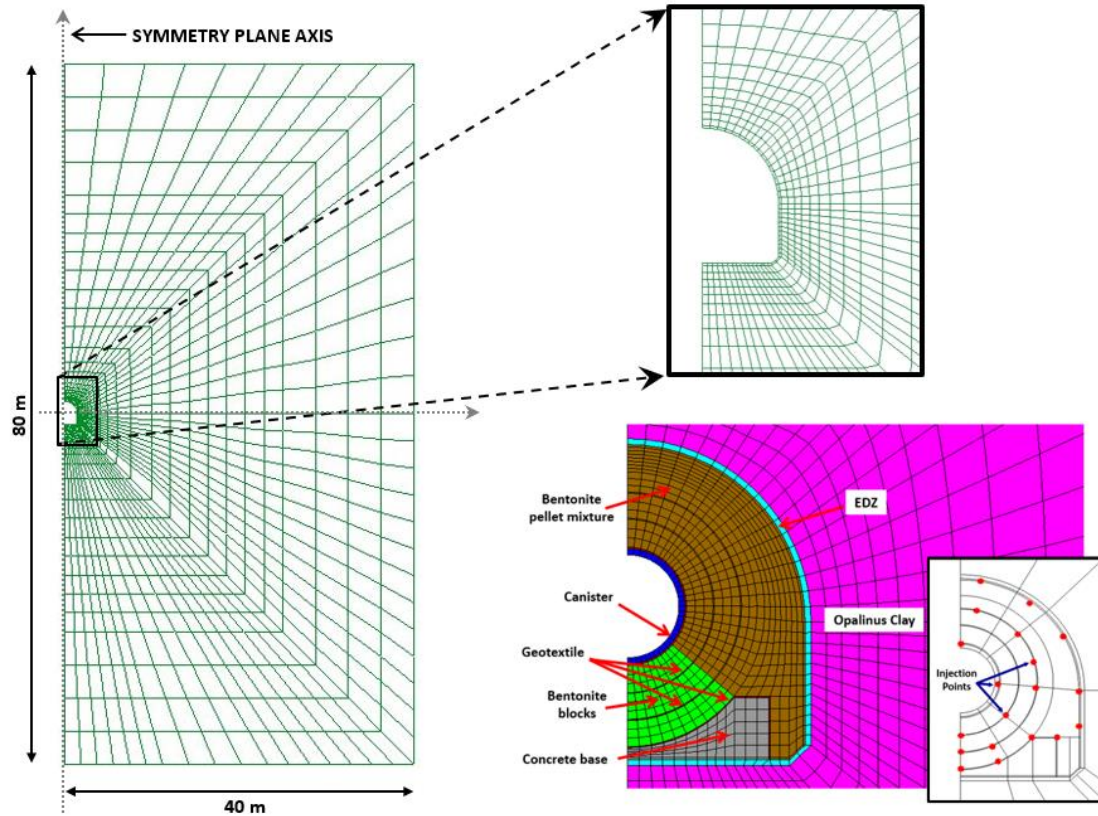


Figure 3-1 FE mesh for the modelled domain of the EB test (left), with a detailed view of the EB niche site (top right), the emplaced barrier and the distribution of the injection points (bottom right).

3.2.2 Input parameters

Most of the parameters for the bentonite pellet mixture have been derived from the numerical modelling of wetting-drying tests at constant vertical load and wetting at constant volume carried out by *Hoffman (2005)* on granular mixtures with dry density values between 1.30 and 1.90 Mg/m³. The model parameters for the compacted bentonite blocks were calibrated from the experimental studies performed during the *FEBEX Project (ENRESA, 2000)* and from previous simulations of the EB experiment (*Alonso & Hoffmann, 2007*) and of a mock-up test made of *FEBEX* bentonite blocks (*Sánchez & Gens, 2006*). The parameters used for the intact and the excavation-disturbed Opalinus Clay were collected from the literature and from the modelling of an *in-situ* heating experiment, the HE-E test carried out at Mont Terri (*Gaus et al., 2014; Gens & Vasconcelos, 2018*).

A modified form of the van Genuchten law has been used to model the soil-water retention curves of the porous media, as follows:

$$S_w = S_{w,r} + (S_{w,max} - S_{w,r}) \left(1 + \left(\frac{S}{P} \right)^{1/(1-\lambda_{rc})} \right)^{-\lambda_{rc}} \left(1 - \frac{S}{P_s} \right)^{\lambda_s} \quad (3.2-01)$$

where $S_{w,0}$, $S_{w,max}$ are the residual and the maximum water saturation, respectively; P is a material parameter ($P = P_0 \frac{\sigma_{ts}}{\sigma_{ts0}}$) related to the air entry value and λ_{rc} , P_s and λ_s are model parameters. The retention curve for the granular bentonite material was selected from the experimental data provided by *Hoffman et al. (2007)* testing samples with a dry density between 1.30 Mg/m³ and 1.50 Mg/m³. The average dry density of the granular bentonite mixture in the EB experiment was reported to be about 1.36 Mg/m³ and, therefore, lies in the experimental range. In the case of the compacted blocks, the parameters for the retention curve were obtained from wetting paths performed on confined compacted samples of *FEBEX* bentonite with dry densities varying between 1.60 – 1.75 Mg/m³ (*ENRESA, 2000*). The adopted water retention curves for bentonite pellets and blocks, together with some experimental data, are shown in Figure 3-2.

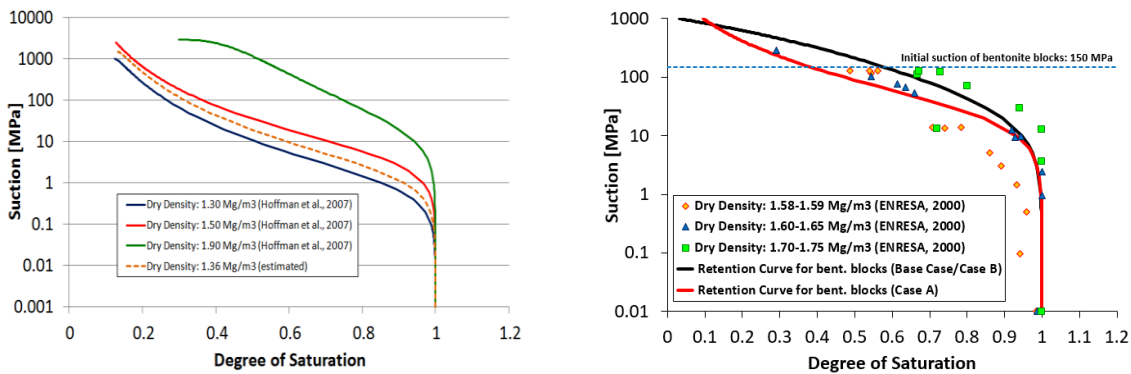


Figure 3-2 Water retention curves for the bentonite pellets (left) and for the bentonite blocks (right).

Another important feature that affects the hydration of clay barriers is the evolution of the water permeability as the water content increases. In fact, the swelling of the bentonite leads to a progressive reduction in macroporosity when such materials are saturated, which may produce a marked reduction in the intrinsic permeability. The water permeability is a material property that depends primarily on the pore structure but also on the saturation state of the porous medium. Such dependencies have been considered in the numerical simulations through the empirical Kozeny's law, expressed as

$$k = k_0 \frac{\phi^3}{(1 - \phi)^2} \frac{(1 - \phi_0)^2}{\phi_0^3} \quad (3.2-02)$$

and by means of an empirical power function of the effective degree of

saturation ($S_{w,e}$)

$$k_{rw} = A(S_{w,e})^{\lambda_{rp}} = A \left(\frac{S_w - S_{w,r}}{S_{w,max} - S_{w,r}} \right)^{\lambda_{rp}} \quad (3.2-03)$$

where \mathbf{k} is the current intrinsic permeability tensor; \mathbf{k}_0 is the intrinsic permeability at a reference porosity (ϕ_0); k_{rw} is the relative permeability factor that accounts for the impact of the state of saturation on the permeability and A and λ_{rp} are model parameters. It is assumed that the advective water flow only occurs through the larger pores, which implies that macro-porosity should be the input parameter in Equation (3.2-02) when the double-porosity approach is used. Initial macro-porosity (ϕ_0^M) values of 0.177 and 0.08 have been used, in the calculations, for the granular bentonite and for the compacted bentonite blocks, respectively. The main hydraulic properties employed in the numerical calculations are summarized in Table 3-1.

Table 3-1 Hydraulic parameters for the host rock and the bentonite buffers

		Opalinus (Intact)	Clay	Opalinus (EDZ)	Clay	Granular Bentonite Mixture	Bentonite Blocks
P_0 [MPa] Curve)	(Ref.	18.0		9.00		1.70	28.0
σ_{ts0} [N/m] Curve)	(Ref.	7.20e-02		7.20e-02		7.20e-02	7.20e-02
λ_{rc} Curve)	(Ref.	0.40		0.40		0.217	0.180*
P_s [MPa] Curve)	(Ref.	1.0e27		1.0e27		1500	1100*
λ_s Curve)	(Ref.	0.00		0.00		0.02	1.10*
$S_{w,r} - S_{w,max}$		0.07 – 1.00		0.001 – 1.00		0.001 – 1.00	0.00 – 1.00
Intrinsic Permeab. [m ²]		1.0e-20		5.0e-20		1.0e-16	1.9e-21
Reference Porosity, ϕ_0		0.12		0.14		0.177 (macro)	0.08 (macro)
Shape Parameter, A		1.0		1.0		1.0	1.0
Shape Parameter, λ_{rp}		3.0		3.0		1.9	3.0

* Model parameters of the retention curve for the bentonite blocks (Case A): $\lambda_{rc} = 0.32$; $P_s = 1.0e27$ MPa; $\lambda_s = 0.00$

An elasto-plastic framework formulated in terms of two distinct and overlapping porous media (microstructure and macrostructure) has been used for modelling the mechanical behaviour of the compacted bentonite blocks and the granular pelletized material in the clay barrier. It has been assumed that the mechanical response of the Opalinus Clay (the host rock) and the concrete bed on which the bentonite blocks lie can be adequately

reproduced by elastic constitutive models. The relevant mechanical parameters used in the simulations are given from Table 3.2-2 to Table 3.2-4.

Table 3.2-2: Mechanical parameters of the double-porosity model (for the buffers)

	Granular Bentonite Mixture	Bentonite Blocks
Elastic stiffness (macro) for changes in mean stress, κ^M	0.06	0.02
Elastic stiffness (micro) for changes in mean stress, κ^m	0.04	0.04
Elastic stiffness for changes in macro suction, κ_s^M	0.001	0.001
Poisson's ratio, ν	0.4	0.4
Slope of the virgin loading line, $\lambda(0)$ (BBM)	0.17	0.18
Coeff. for the change in cohesion with suction, r (BBM)	0.62	0.75
Coeff. for the change in cohesion with suction, β [MPa ⁻¹] (BBM)	0.02	0.05
Reference pressure, p^c [MPa] (BBM)	0.075	0.10
Coeff. for the increase of tensile strength with suction, k_s (BBM)	0.10	0.10
Cohesion for suction equal to zero, p_{s0} [MPa] (BBM)	0.10	0.10
Slope of the critical line, M (BBM)	1.5	1.5
Pre-consolidation pressure, p_0^* [MPa] (BBM)	1.0	14
Initial (total) porosity, ϕ_0	0.390	0.487
Initial micro-porosity, ϕ_0^m	0.310	0.310

Table 3.2-3: Parameters for the micro-macro interaction functions (for the buffers)

	f_{SD0}	f_{SD1}	n_{SD}	f_{SI0}	f_{SI1}	n_{SI}
Base Case/Case A (pellets & blocks)	-0.1	1.7	3.0	-0.1	1.5	0.2
Case B – Var01 (blocks)	-0.1	2.0	3.0	-0.1	2.0	0.2
Case B – Var02 (blocks)	-0.1	0.1	3.0	-0.1	0.1	0.2

Table 3.2-4: Elastic properties for the Opalinus Clay and the concrete base

	Opalinus (Intact)	Clay	Opalinus (EDZ)	Clay	Concrete Base
Young modulus, E [MPa]	3.0e05		3.0e05		3.0e05
Poisson's ratio, ν	0.30		0.30		0.30

3.2.3 Initial and boundary conditions

The numerical modelling of the EB experiment has been performed in two main steps. The first step corresponds to the construction of the tunnel where the *in-situ* test was carried out and the subsequent emplacement of the experiment, while the second step simulates the hydration of the barrier.

In the host rock near the test zone, the initial pore water pressure has been set to 1.0 MPa and the initial stress state has been assumed anisotropic, with a vertical stress value of 6.0 MPa and a horizontal stress component of 4.8 MPa. A linearly increasing distribution of in situ stresses and pore pressures (due to gravity) has been assumed.

The excavation of the niche of the EB experiment has been simulated by reducing to zero the total stresses on the boundary representing the tunnel wall. A constant suction of 10.0 MPa, corresponding to a RH of 93%, has been prescribed on that surface. The modelled geometry together with the initial and the boundary conditions in the Opalinus Clay, before and after the tunnel excavation, are shown in Figure 3-3.

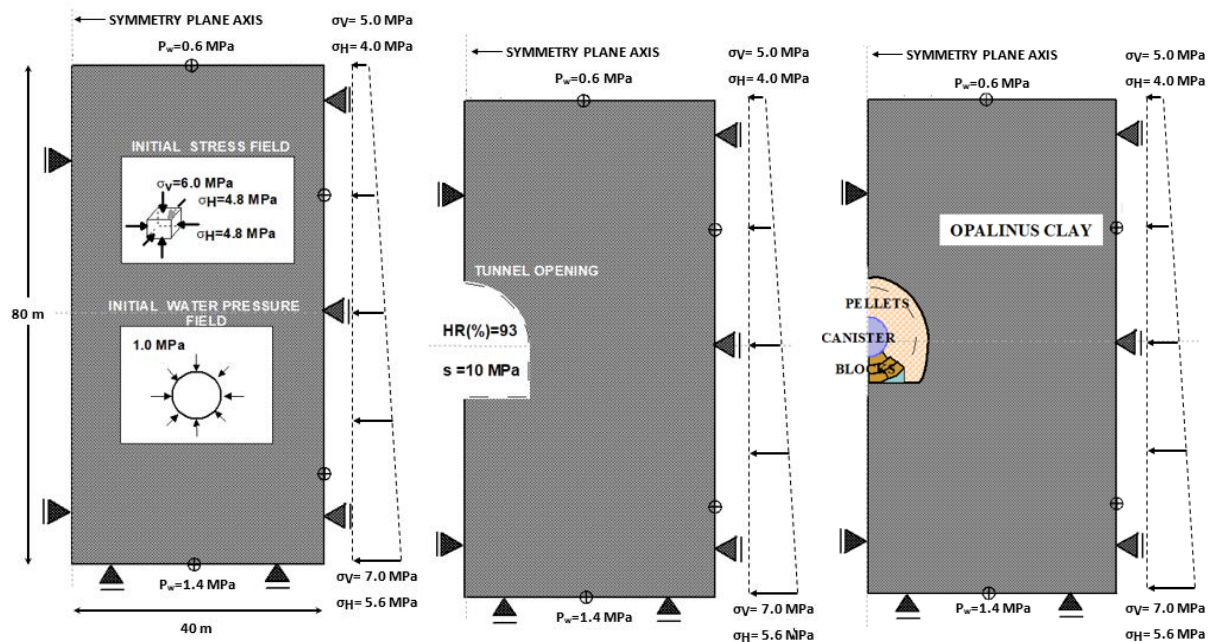


Figure 3-3 Geometry, initial and/or boundary conditions prior to the excavation (left), tunnel excavation (centre), and barrier installation (right).

The emplacement of the various components of the EB experiment took place 160 days after the opening of the niche. The construction of the rounded concrete base and the bed of bentonite blocks, the emplacement of the 0.97 m diameter metallic canister, the installation of the hydration system and the sensors and the emplacement of the granular bentonite backfill have been modelled in a single step, assuming that all such operations have occurred simultaneously and instantaneously. However, the period of time between the end of the tunnel construction and the beginning of artificial hydration has been taken into account. Suction values of 300 MPa and 150 MPa have been set to represent the initial hydraulic conditions of the pellets and of the compacted bentonite blocks, respectively. The initial stress state for the bentonite-based materials has been assumed isotropic with a value of 0.30 MPa. Figure 3-4 shows a cross-section and a longitudinal view of the experiment.

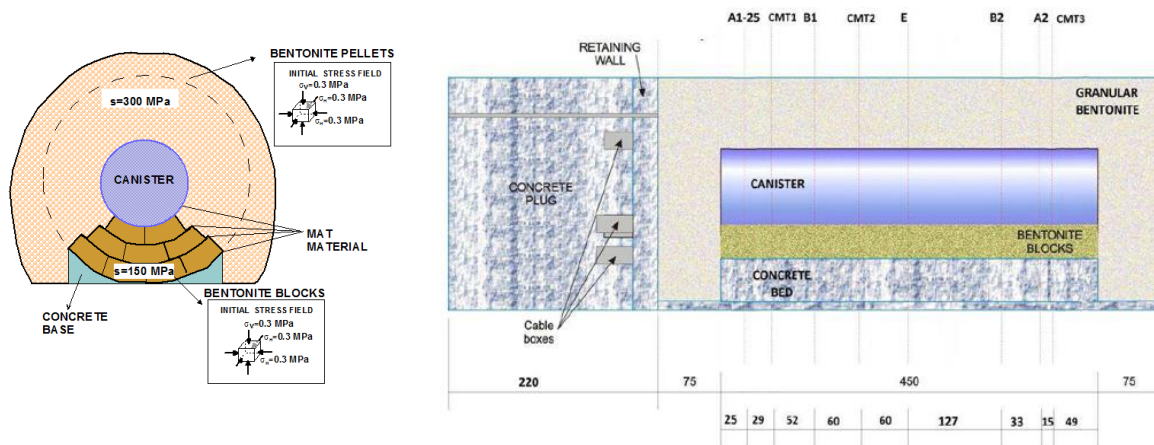


Figure 3-4 Cross-section (left) and longitudinal view (right) of the EB experiment.

The re-saturation of the barrier has been reproduced considering all the relevant episodes of the hydration conditions that took place during the EB experiment. The water injection began on May 6th, 2002 and continued until June 18th, 2007. The forced hydration started with the injection of 6.7 m³ of water over a period of two days. Such a flux boundary condition has been simulated by prescribing a flow rate of 0.033 m³/meter/day in each injection point. After that, the injection of water was discontinued for the following 126 days (due to a water leak coming from the barrier), after which automatic injection of water was started. For this stage, water has been injected into the barrier by prescribing a water pressure that varies, in time, according to the observed injection pressure evolution shown in Figure 3-5. For modelling purposes, the black continuous line represents the water pressure boundary conditions applied at each injection point. This phase covered a period of 1741 days (from September 11th, 2002 to June 18th, 2007). After June 18th, 2007, the water injection valve was closed and the hydration system no longer provided water to the bentonite buffer. Therefore, a no flux condition at the injection points was prescribed and only natural hydration from the rock

remained.

Aitemin

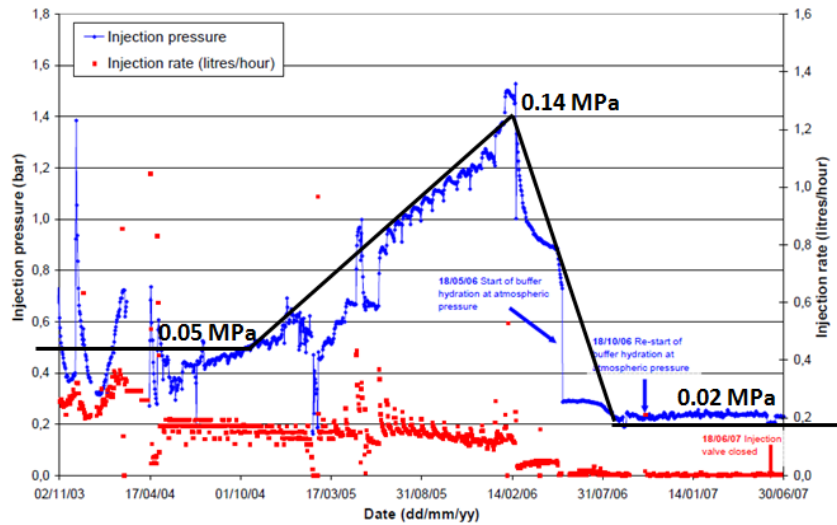


Figure 3-5 History of the injection rate and injection pressure from the start of automatic injection (AITEMIN, 2013). The injection pressure history was simplified in the calculations and it is represented by the black continuous line.

The dismantling of the hydrated engineered barrier took place between October 23rd, 2012 and January 29th, 2013. During dismantling, several samples were extracted from the pellet mixture and from the compacted blocks in order to evaluate the final state of the barrier. Dismantling has not been specifically simulated but the computed state of the barrier at the end of the experiment has been compared with measurements performed on samples taken during dismantling.

3.2.4 Results/discussion

The model results have been compared to the measurements provided by the system of sensors installed in the bentonite buffers and in the near field of the EB experiment. In the plots, the model results are represented by either full or dotted lines while symbols refer to test observations. Data from Relative Humidity (RH) sensors (in the rock and the buffer), displacement sensors (canister and rock), piezometers (rock) and total pressure cells (buffer) were recorded until January 14th, 2013, over 10 years after the beginning of the hydration of the barrier. In addition, the spatial distributions of water content and dry density (related to porosity) in the tunnel sections in which samples were taken during barrier dismantling have also been compared with the modelling results. In the numerical analyses, time has been referenced to the beginning of the hydration experiment (May 6th, 2002).

The Base Case

The progress of hydration in the clay barrier was evaluated by the measurements provided by the RH sensors installed in cross sections A1 and A2 (in the host rock) and B1 and B2 (in the bentonite barrier). The first days of artificial hydration (when a volume of about 6.7 m³ of water was injected into the barrier) resulted in a fast reduction in suction (i.e. an increase in RH), especially for those sensors located inside the compacted blocks (sensors WB13 and WB14 in section B1 and WB23 and WB24 in section B2). It can also be noted that the local re-saturation in the granular bentonite mixture occurred later in comparison with the re-saturation of the blocks. It could be a consequence of the drier initial state of the bentonite pellets. Furthermore, the different rates of hydration in the mass of pellets measured by the RH sensors in sections B1 and B2 indicated that the re-saturation of the barrier was not uniform throughout its length and height. This observation probably reflects the artificial hydration strategy adopted in the EB experiment, in which water was progressively injected from the bottom to the top and from the front to the end of the tunnel. In contrast, the volume of host rock around the excavated tunnel recorded a slight desaturation due to the ventilation of the tunnel for 160 days, between the tunnel opening and the EB construction. However, it became saturated again during the first stages of the EB hydration experiment. All these features can be observed in the graphs plotted in Figure 3-6 and Figure 3-7 together with the model results (as full lines). The evolution of the matric suction in such graphs has been obtained by means of the psychrometric law that relates relative humidity to total suction and assuming that the osmotic suction may be neglected.

Regarding the modelling of the hydration experiment, the relatively large volume of water injected in the barrier during the first phase of hydration could explain the faster re-saturation of the mass of pellets predicted by the model. In reality, water losses through the host rock and the concrete plug were reported, which implies that the actual volume of water inside the clay barrier after the first phase of hydration was unknown and very likely less than the nominal volume of 6.7 m³ for this phase. However, this amount of water has been injected, in the calculations, during the first hydration step. In the case of bentonite blocks, the model predictions appear to fit better the measured RH data. During the hydration experiment, an intriguing desaturation episode followed by a fast re-saturation was registered on a pair of sensors located in the host rock, in the vicinity of the upper section of the EB and close to the rock-pellets interface (sensor WB0_01 in section A1 and WB23_01 in section A2). This marked drop in RH could be a consequence of the natural hydration of the barrier (water flux from the rock to the EB) enhanced by the rock damage generated during the tunnel opening. Although this event was not precisely predicted by the model the numerical results at those sensor locations close to the tunnel (sensors WB0_01 and WB1_01 in section A1 and WB23_01 and WB24_01 in section A2) have showed a slight reduction in RH followed by a complete re-saturation of these zones as the granular bentonite mixture also approaches saturation.

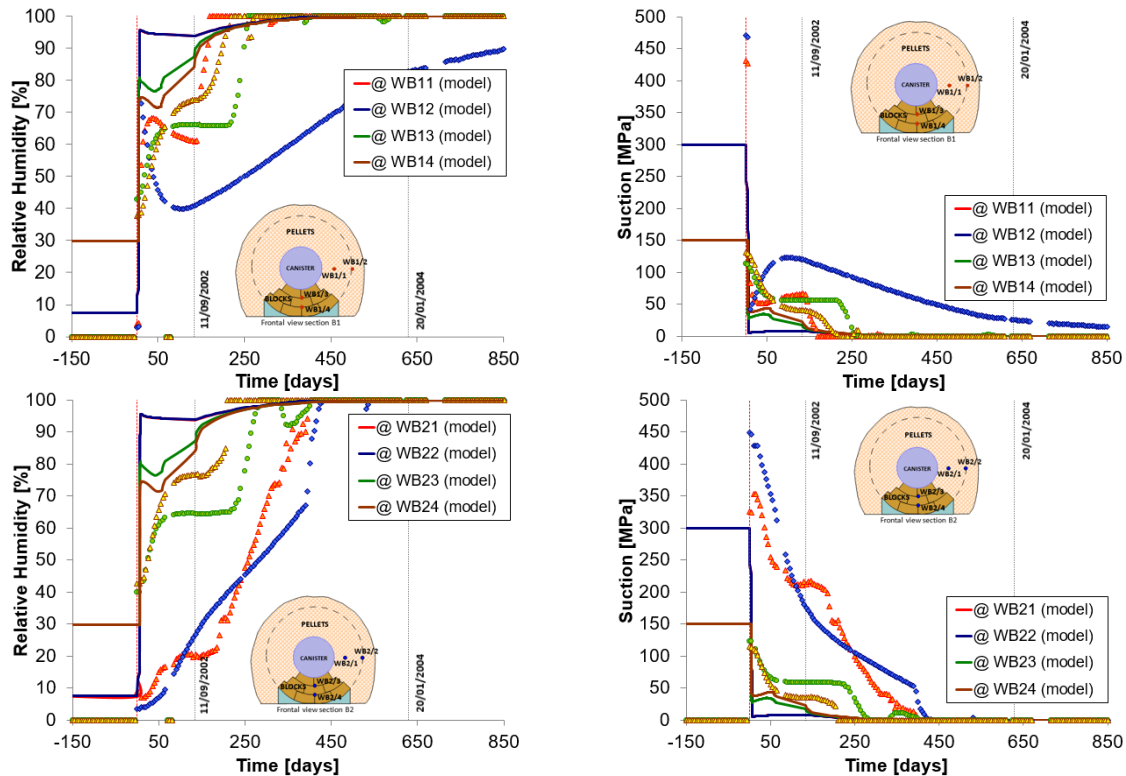


Figure 3-6 Evolution of RH (left) and suction (right) inside the buffer material for sensors in the instrumented section B1 (top) and B2 (bottom). Computed results and observations.

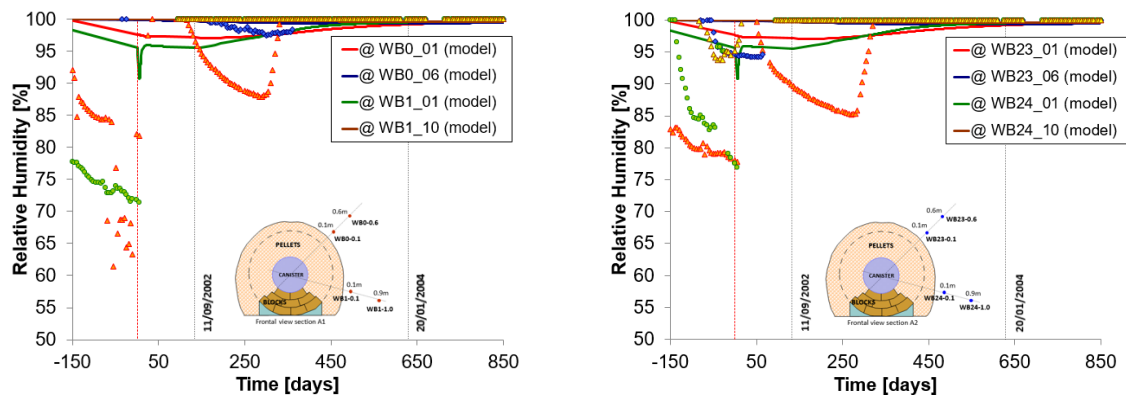


Figure 3-7 Computed and measured RH in the rock for sensors in the instrumented section A1 (left) and A2 (right).

The evolution of the pore water pressure in the near field of the EB experiment was monitored by 20 sensors distributed along four tunnel sections: B1 (6 sensors), B2 (6 sensors), C1 (4 sensors) and C2 (4 sensors). A good agreement between the *in situ* measurements and model calculations can be noted in Figure 3-8 to Figure 3-10. They confirm the tendency shown by the RH sensors installed in the Opalinus Clay that indicate an almost saturated state of the host rock in the vicinity of the experiment site. The drainage effect of the tunnel excavation, the reduction in the liquid pressure in the early stages of the hydration test due to the water flow towards the clay barrier and the

tendency to recover the pore pressure to values above the atmospheric pressure have been reproduced satisfactorily by the numerical model.

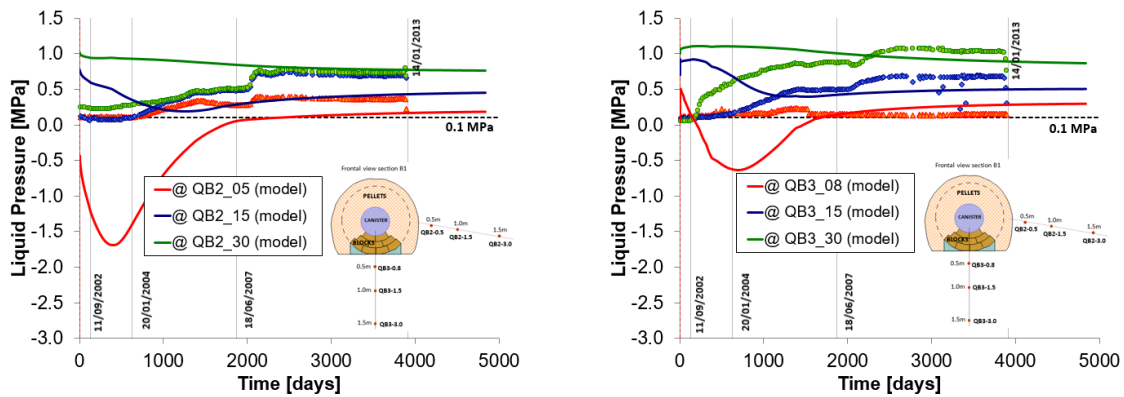


Figure 3-8 Evolution of the pore water pressure in the near field of the EB experiment (Section B1). Computed results and observations

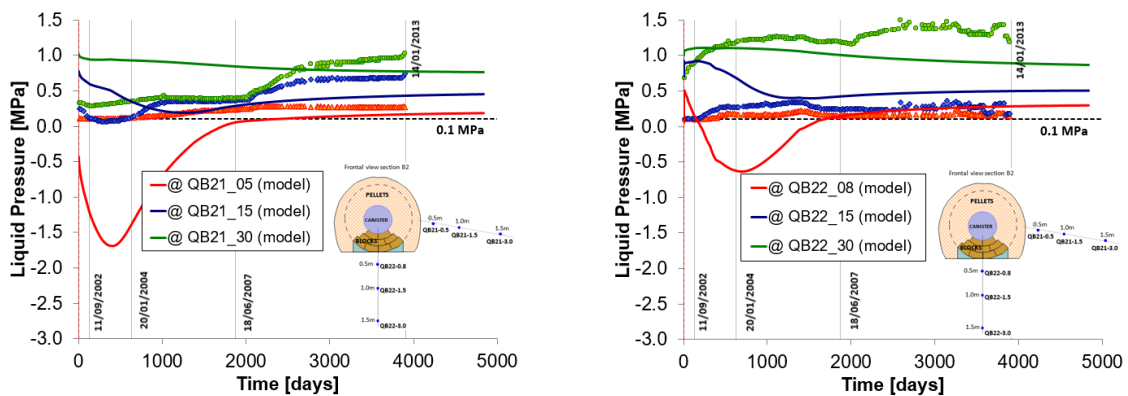


Figure 3-9 Evolution of the pore water pressure in the near field of the EB experiment (Section B2). Computed results and observations

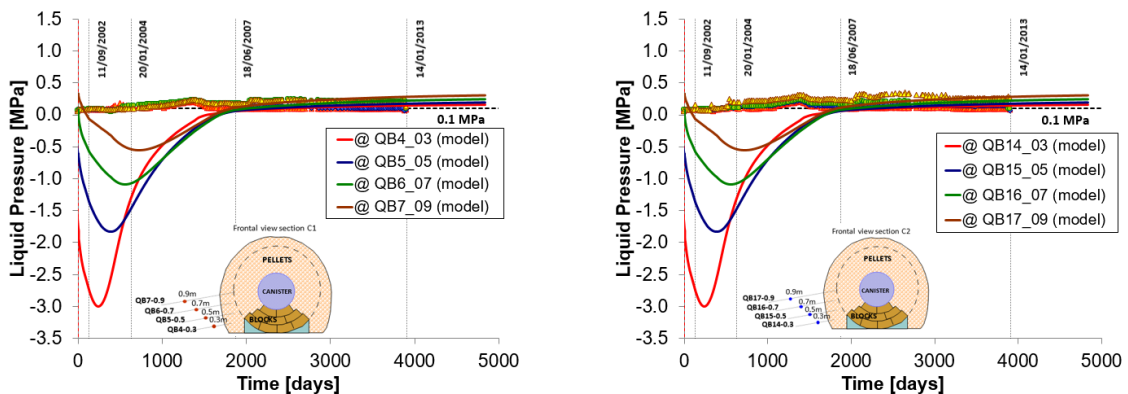


Figure 3-10 Evolution of the pore water pressure in the host rock. Section C1 (left) and C2 (right). Computed results and observations

Horizontal and vertical movements of the canister due to the buffer hydration were measured by extensometers emplaced in tunnel sections close to the ends of the canister (sections A1 and A2). The measured and computed horizontal and vertical displacements of the canister are shown in Figure 3-11, in which positive values for the vertical displacements should be interpreted as a rise of the canister. In section A1 (sensors EA11 and EA12) an upward

displacement of around 10 mm and a left to right horizontal displacement of 6 mm were recorded while in section A2 (sensors EA21 and EA22) a maximum upward displacement of 8 mm and a maximum right to left displacement of about 17 mm were measured during the hydration test. Those movements could be related to differences in the dry density of the mass of pellets around the canister, to the higher initial density of compacted blocks with respect to the bentonite pellets and to a non-symmetrical hydration pattern. Naturally, due to the assumption of material and geometrical symmetries for the model domain, a zero horizontal displacement of the canister results from the numerical modelling. It can also be noted that the model results clearly overestimate the vertical displacements of the canister.

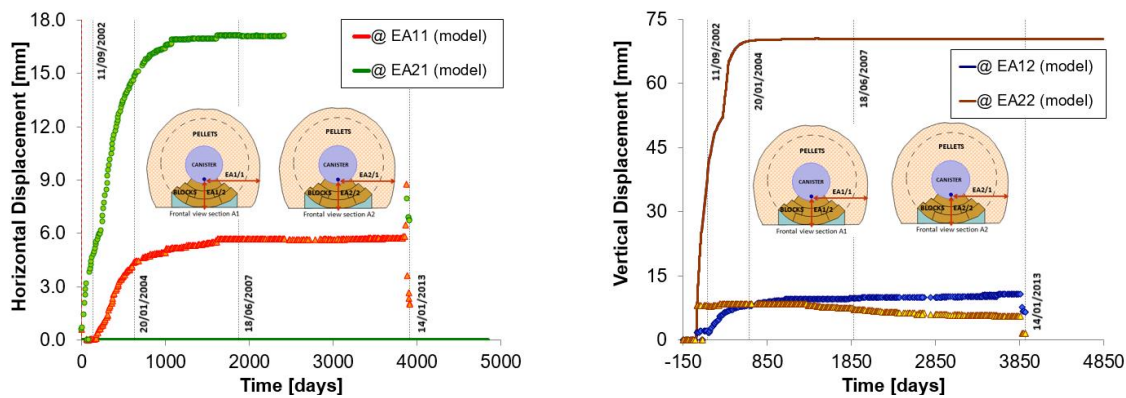


Figure 3-11 Evolution of the horizontal (left) and the vertical (right) movement of the canister during the hydration experiment. Computed results and observations

The total pressure cells installed in section E recorded a gradual increase of the swelling stresses until reaching values in the range of 1.5-2.2 MPa at the beginning of the dismantling operation. The evolutions of those stresses are plotted in Figure 3-12 (for the 4 cells around the canister) and Figure 3-13 (for the 4 cells installed on the tunnel wall) together with model results. In general, the values obtained from the calculations are close (although slightly higher) to the measurements recorded by the pressure cells. Moreover, it can be noted that the maximum total pressure was registered in sensors on the top of canister (PE1) and under the compacted blocks (PE6). Such higher values could be a consequence of the higher swelling potential of the compacted blocks (in comparison to the mass of pellets) and due to the larger pressure exerted by the expanded bentonite blocks on points immediately above and below them.

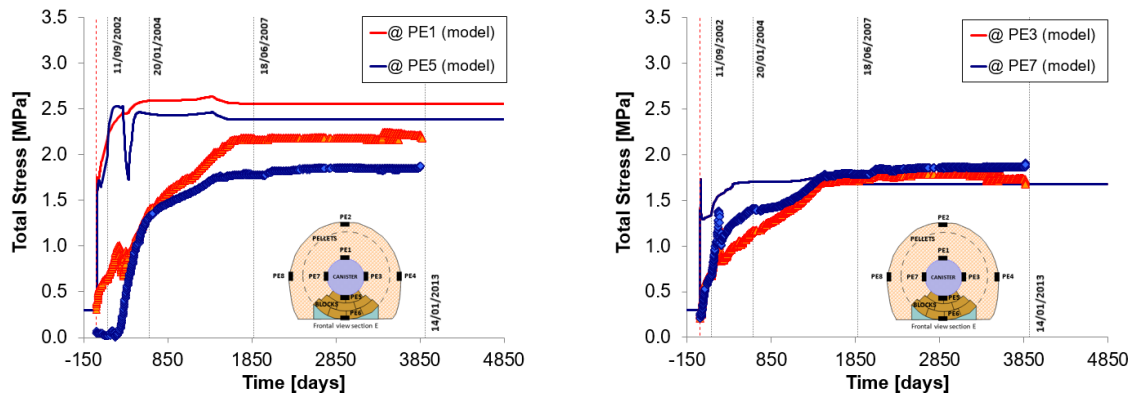


Figure 3-12 Evolution of the vertical (left) and the horizontal (right) hydration-induced compressive stresses acting on the canister. Computed results and observations

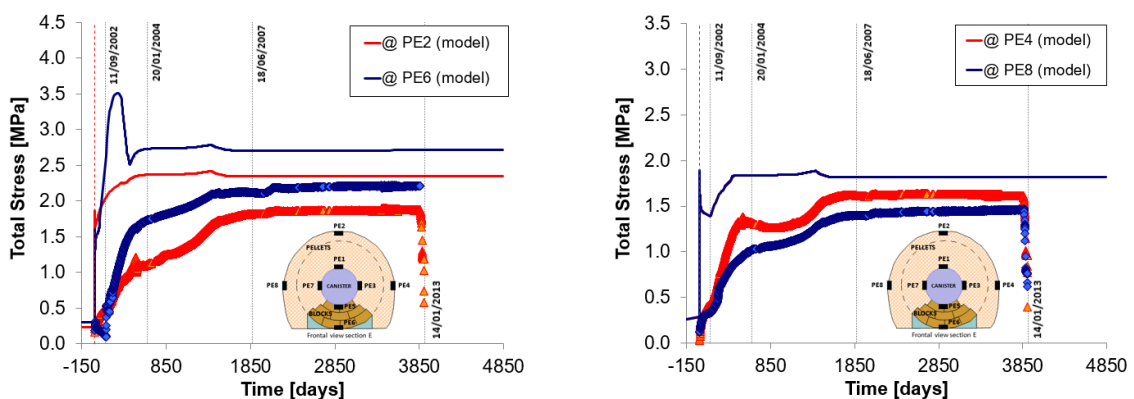


Figure 3-13 Evolution of the vertical (left) and the horizontal (right) hydration-induced compressive stresses acting on the tunnel wall. Computed results and observations

As indicated previously, the sampling performed during the dismantling of the EB test has provided additional information about the final state of the buffer. Thus, the determination, in laboratory, of the water content and the dry density along several radial profiles in selected sampling sections gave a direct insight into the spatial distribution of such variables throughout the bentonite barrier. Figure 3-14 shows the spatial distribution of the degree of saturation in sections A1-25 and E together with the radial profiles of saturation computed by the model at the time of the dismantling operations (January, 2013). All the distances have been taken from the canister surface. The good agreement between experimental and modelling data indicates that the buffer was almost fully-saturated at the end of the hydration test; the actual degree of saturation ranged between 95% and 100% in most sampling points.

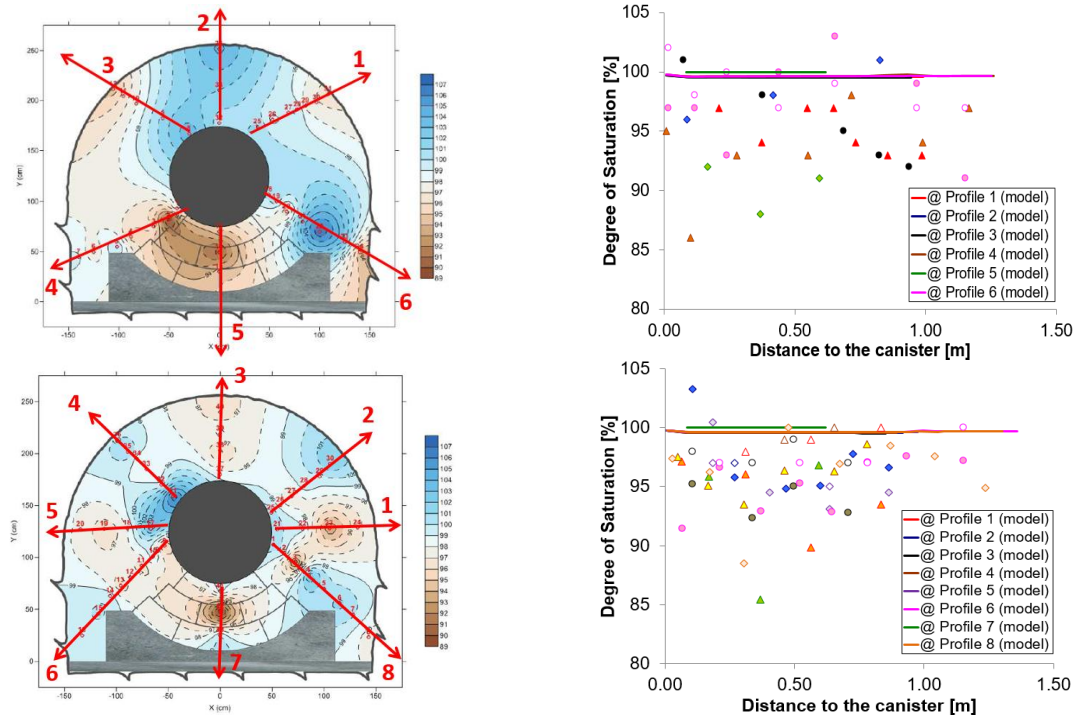


Figure 3-14 Distributions of degree of saturation along radial profiles located in the sampling sections A1-25 (top) and E (bottom). Computed results and observations.

The dry density measurements revealed a highly dense state of the mass of pellets located in the upper portion of the bentonite barrier and a considerable reduction in the dry density of the compacted blocks. The pronounced volumetric expansion of the blocks led to the vertical movement of the metallic container and to an increment in the confining stresses acting on the mass of pellets positioned above the canister. Dry density (ρ_{dry}) and total porosity (ϕ) are of course related by the following expression:

$$\rho_{dry} = \rho_s(1 - \phi) \quad (3-04)$$

where ρ_s is the solid grain density.

The observed vertical homogenization of dry density has been reproduced satisfactorily by the model, as shown in Figure 3-15, where the dry density evolution at four sampling points in section E have been plotted. Two of those selected points were in the part of the buffer above the canister (samples B-S-E_037 and B-S-E_040) while the other two were located inside the bentonite blocks (samples B-S-E_041 and B-S-E_043). Furthermore, several radial profiles of dry density have also been plotted for the sampling sections A1-25 (in Figure 3-16) and E (in Figure 3-17). It can be noted that the modelling provides a satisfactory quantitative prediction of the density state in the pellet region. However, the final dry density of the bentonite blocks (Profile 5 in Figure 3-16 and Profile 7 in Figure 3-17) has been somewhat overestimated in the numerical calculations. It is important to recall that, initially, the compacted blocks had a much higher dry density value than the pellets that were

emplaced by means of an auger system without any compaction. The initial average dry density of pellets was about 1.36 Mg/m³ while the dry density of the bentonite blocks had an initial value around 1.70 Mg/m³.

It is also worth noting that the very low dry density measured at the lower corners of the section is not reproduced by the model. However, it is likely that this specific feature reflects simply the heterogeneity of the initial emplacement density distribution; the reduced space between the Opalinus clay and the concrete bed probably made it difficult to properly backfill that zone. The model assumes initial granular bentonite homogeneity and, therefore, it is not be able to account for the effects of emplacement heterogeneity.

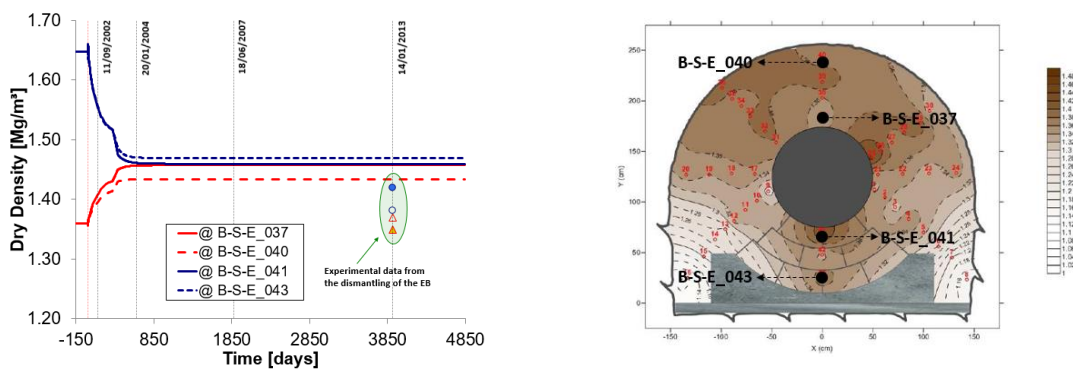


Figure 3-15 Computed evolutions of dry density inside the pellet mixture (B-S-E_037 and B-S-E_040) and in the compacted blocks (B-S-E_041 and B-S-E_043) in the sampling section E.

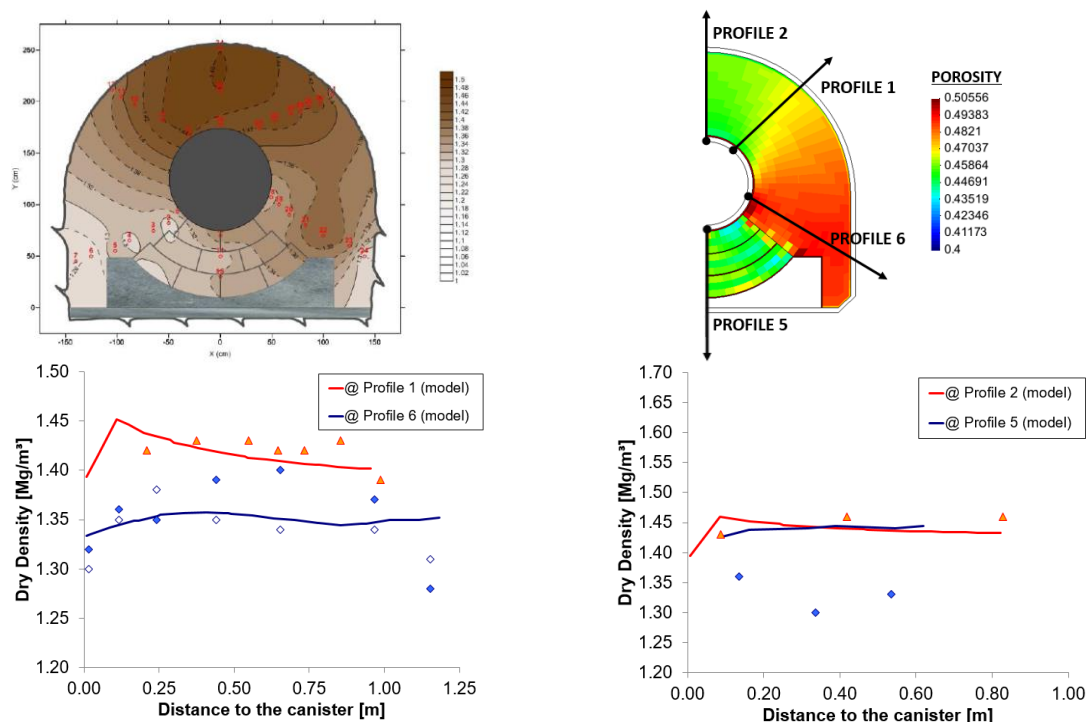


Figure 3-16 Spatial distribution (top) and radial profiles (bottom) of dry density in the

sampling section A1-25. Computed results and observations

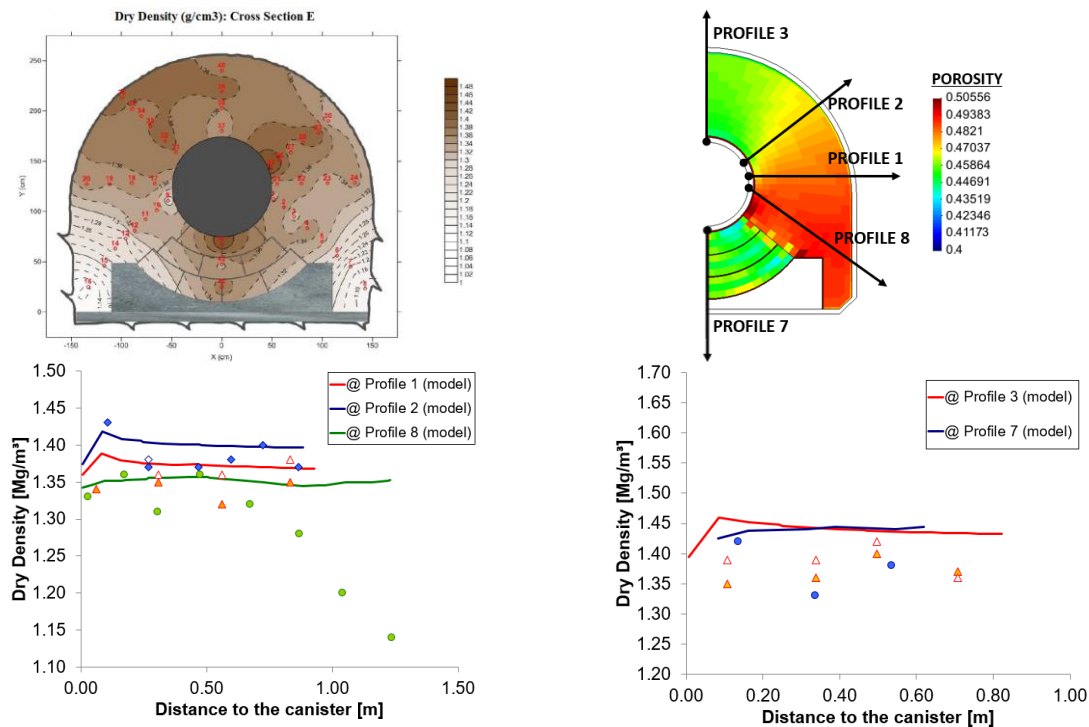


Figure 3-17 Spatial distribution (top) and radial profiles (bottom) of dry density in the sampling section E. Computed results and observations

Additional Analyses

In order to understand better the behaviour of the experiment and the results of the numerical modelling, a number of additional calculations have been performed. The following are reported here:

- Case A: the hydraulic response of the compacted blocks has been simulated using a different retention curve (see Figure 3-2 and Table 3.2-1) obtained from wetting paths under isochoric conditions in samples with initial dry densities in the range 1.60-1.65 Mg/m³. All the other constitutive parameters adopted in the Base Case for the bentonite blocks have remained unchanged.
- Case B: Two analyses (Case B-Var01 and Case B-Var02) have been performed using two alternative sets of interaction functions between micro and macro levels. The functions are plotted in Figure Figure 3-18 and the corresponding model parameters are shown in Table 3.2-3. The interaction functions for the pellets have remained unchanged.

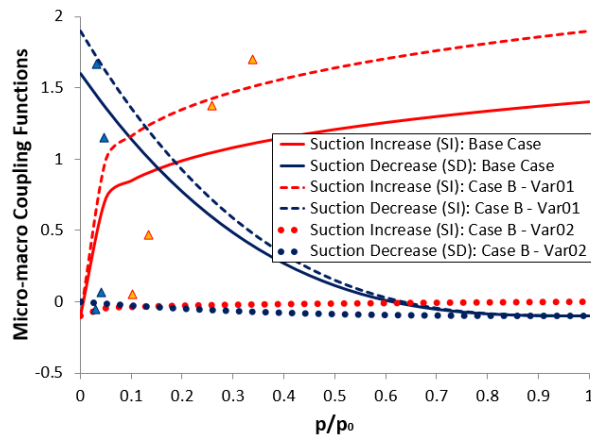


Figure 3-18 Alternative micro-macro interaction functions for the compacted bentonite blocks.

The more relevant model results arising from these additional calculations are shown in Figure 3-19 to Figure 3-21. In Figure 3-19, the evolution of the dry density for a pair of points close to the canister (in sampling section E) is presented for Cases A and B. The model predictions for the spatial distribution of the dry density along all the radial sampling profiles located above (up) and below (down) the canister are plotted in Figure 3-20 (for Case A) and Figure 3-21 (for Case B). The first feature to highlight from such analyses is that the swelling behaviour of the blocks is probably one of the key factors affecting the final density configuration within the bentonite barrier. The vertical homogenised state of the re-saturated barrier (in terms of dry density) observed during dismantling can be only reproduced by the model if the bentonite blocks are allowed to swell considerably. In that respect, the changes in the initial water content and in the re-saturation conditions of the compacted blocks (Case A) seem to have more impact on the homogenization of the barrier than the mechanical interaction between micro and macro structural levels (Case B). In fact, the drier initial state of the blocks in Case A implies that the volume of water required for such materials to reach saturation is larger in this case than in the Base Case. Consequently, the total swelling deformations of blocks are also larger for Case A. On the other hand, the amount of water required to re-saturate the bentonite blocks is the same for both Case B and the Base Case. Furthermore, the reduction in dry density of the compacted blocks during hydration is lower for the Case B-Var02, because the changes in the macro fabric of the blocks due to the swelling of microstructure are smaller in this case (as reflected in the interaction functions of Figure 3-18).

The model predictions of the vertical canister rise given by each modelling case (Base Case, Case A and Case B) are shown in Figure 3-22. Naturally, there is a direct relationship between the magnitude of the upward movement of the canister and the reduction in the dry density of the bentonite blocks supporting it. However, it can be noted that all the analyses performed overestimate the vertical movement measured by the

extensometers. In fact, the large density changes in the samples taken from the blocks during the dismantling phase are not consistent with the measured lift of the canister, suggesting that the measurement of the vertical displacement of the canister may have been in error.

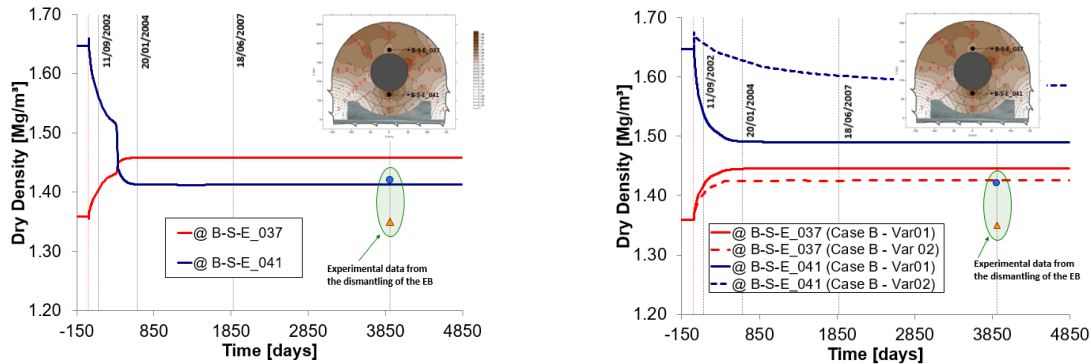


Figure 3-19 Computed evolutions of dry density inside the pellet mixture (B-S-E_037) and in the compacted blocks (B-S-E_041) for the Case A (left) and the Case B (right).

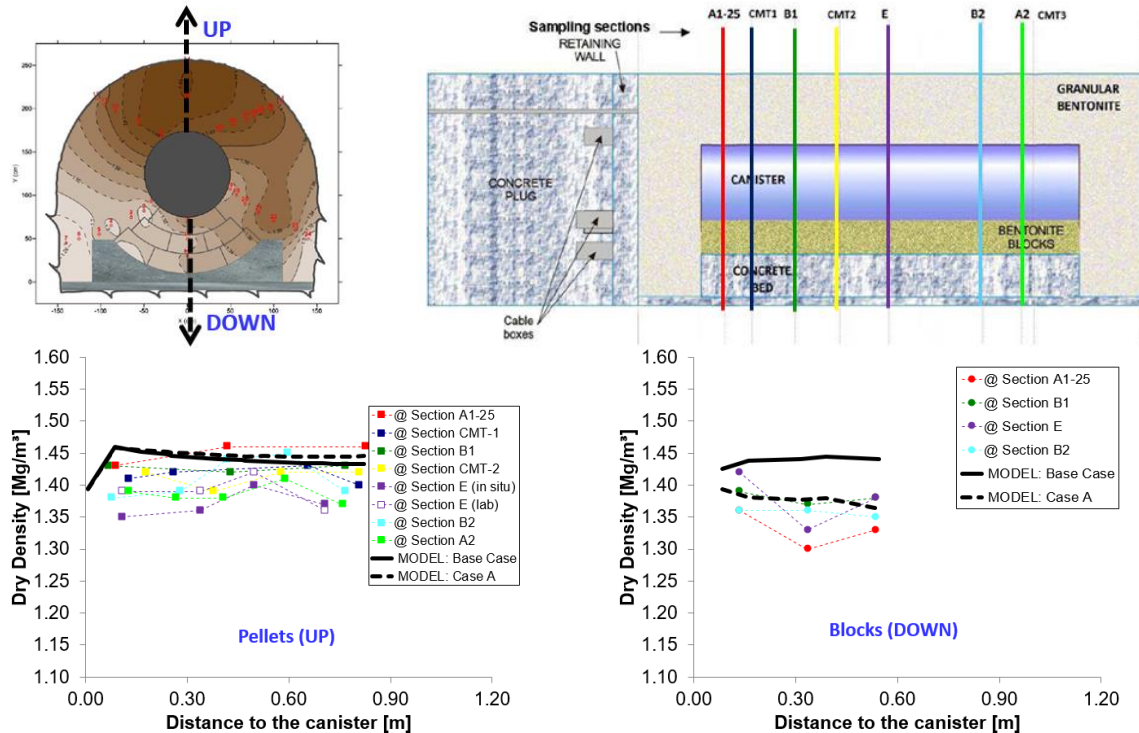


Figure 3-20 Radial profiles of dry density, in all the sampling sections, for points located in the upper section of the barrier (left) and inside the compacted blocks (right) : Base Case vs. Case A. Symbols correspond to observations.

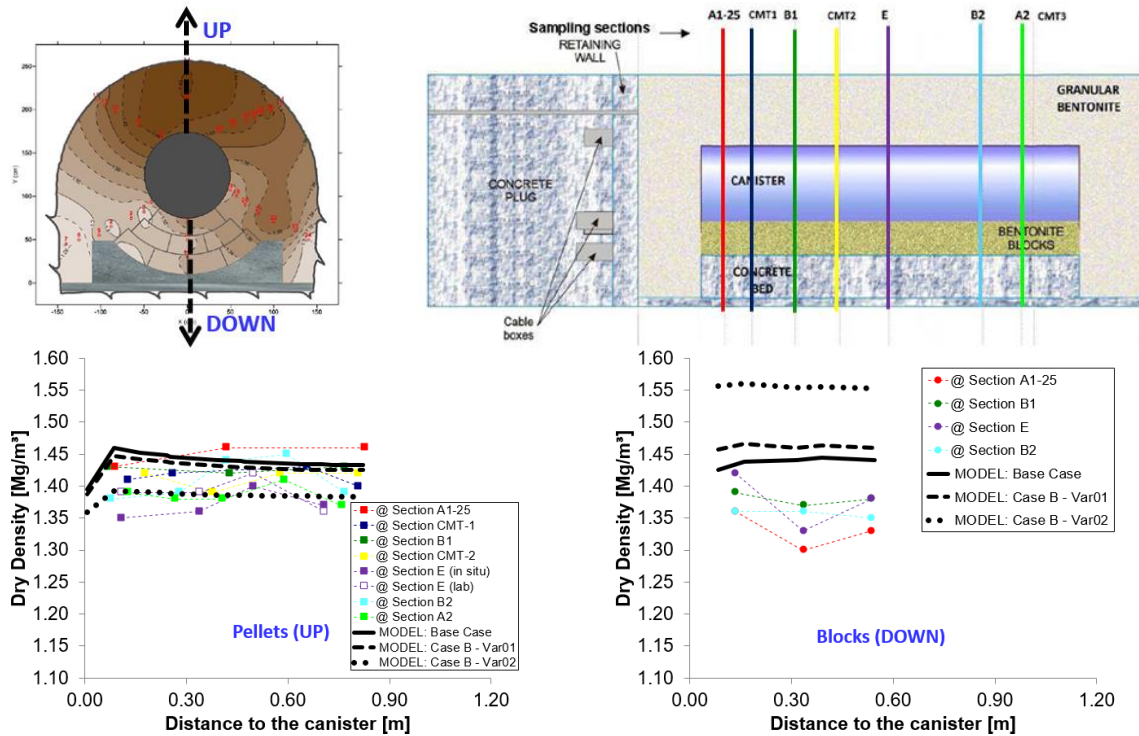


Figure 3-21 Radial profiles of dry density, in all the sampling sections, for points located in the upper section of the barrier (left) and inside the compacted blocks (right) : Base Case vs. Case B. Symbols correspond to observations.

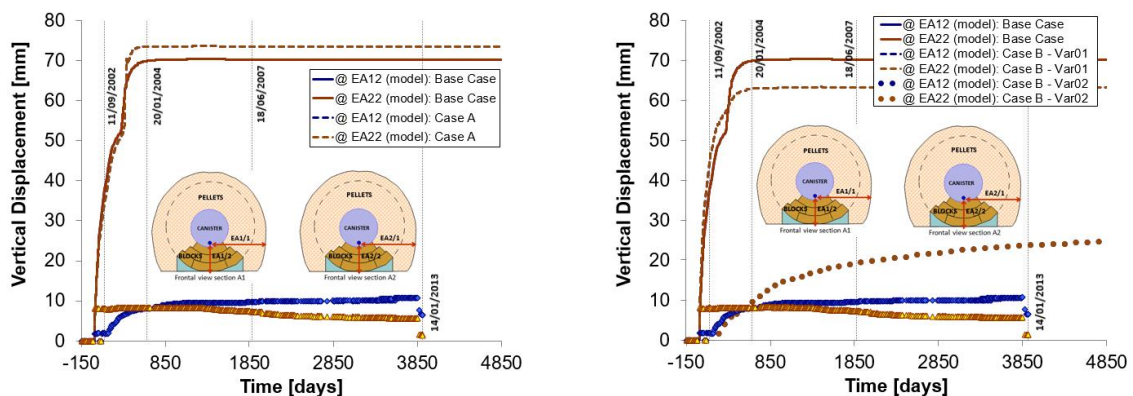


Figure 3-22 Comparison of the model predictions for the canister vertical displacement: Base Case vs. Case A (left) and Base Case vs. Case B (right). Symbols correspond to observations.

3.2.5 Lessons learnt

The UPC team used a double porosity constitutive model to represent the mechanical behaviour of pellets and blocks. Naturally, the partition between micro and macro porosity was different for the two bentonite materials. The interaction between the two porosity levels was defined by means of interaction functions.

The UPC numerical model reproduced well the trend and the magnitude of the measured quantities during the transient phase although the lack of close hydration control of the test during the saturation phase prevents a more

precise examination of the model performance during hydration. The comparison with the final state of the barrier provides more discriminating information in a matter that is very much aligned with the aims of the project. The more relevant observation obtained in the dismantling of the test was the homogenization of the dry density of blocks and pellets along a vertical section. This homogenization has been observed in all the sections sampled. The UPC numerical model was successful in reproducing this full homogenization. The dry density distribution is also well captured in the rest of the section with the exception of the very low density observed at the bottom corners that are clearly the result of initial placement heterogeneity. Therefore, the double porosity model appears very suitable to simulate the mechanical behaviour of bentonite compacted blocks, bentonite pellets and their combination in a single section. Consequently, and based on the results of this analysis, the general structure of the model does not seem to require major developments at this stage. Additional analyses have shown the significance of the interaction functions of the model. In this respect, a possible limitation of the model is the potential difficulty of determining experimentally the precise shape and magnitude of the interaction functions. More work may be required on this issue. Additional analyses have also shown the sensitivity of the results to the assumed retention curve. This outcome points towards the need to determine this curve very precisely rather than the need for a different water retention model.

3.3 ULG

3.3.1 Geometry and discretization

The EB configuration consists in a horse-shoe shape excavation, 2.65 m high and 2.9 m large. In this modelling strategy, plane strain conditions are taken into account and only half domain is considered, with a vertical symmetry axis coinciding with the plane cutting the buffer at the centre. Given the 2-D geometry of the problem, only one cross section is modelled and the results are relative to that representative section.

The current modelling strategies have to be considered as analyses, in which simplified hypotheses are taken into account. Therefore, the Opalinus clay and the tunnel excavation phase are not considered and the buffer hydration takes place directly. It is considered that the water exchanges between the buffer and the OPA does not play a major role. Gravity is not taken into consideration either, its driving force is assumed to be much lower with respect to the suction one.

The concrete bed can be considered as a very rigid element, representing a mechanical constraint for the bentonite materials and a possible hydration source and path for saturation.

It is decided to model the interaction between the bentonite-based materials and concrete bed via an interface element at its place (Figure 3-23). With such a strategy, the bentonite elements can slide in the tangential direction of the interface so that possible shear and tensile stresses, which would occur with a sticking contact with a very rigid concrete bed, are avoided. The used interface element is described in (Gramegna & Charier, 2019).

The choice to consider only the bentonite components has been made in order to focus only on the processes taking place during the artificial hydration, neglecting the interactions with the surrounding elements (i.e. host-rock and concrete bed).

The driving force of the bentonite buffer evolution is the water intake. However, the experimental conditions are not easy to understand. During a first short phase, a quick hydration is applied, but some leakage is observed. As the water is injected through tubes with opening, it is very concentrated, but the exact repartition in the whole domain is not known. For these reasons, it is decided to inject a reasonable volume of water, following a time history and a spatial repartition as credible as possible, but without trying to reproduce all the experimental hydration complexity. The developed strategy will be much detailed further in the report.

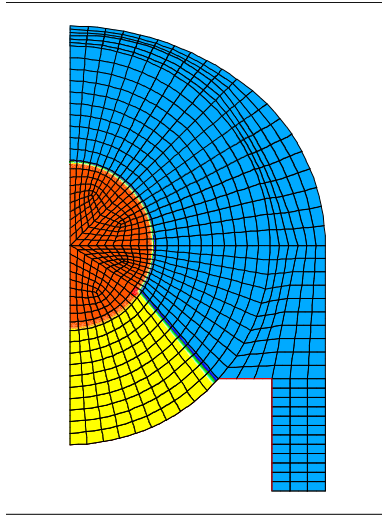


Figure 3-23: FE mesh of the modelled domain of the EB test.

The mesh consists in 1532 8-noded iso-parametric elements. The 8-noded iso-parametric elements represent the canister, the bentonite blocks, the bentonite pellet mixture and the SUCHT elements allowing the application of the uniform flux on the bentonite surface. This modelling strategy considers also 25 2-noded iso-parametric elements representing the interface itself. Table 3-2 reports the number of element of the mesh.

Table 3-2 Number of elements of each component of the EB modelled test.

	Number of elements
Canister	300
Interface element	25
Bentonite blocks	100
Bentonite pellet mixture	516
Sucht	616
Total	1557

3.3.2 Input parameters

Canister

The mechanical behaviour of the canister used in the numerical simulation is considered as linear elastic. The input mechanical parameters are presented (Table 3-3).

Table 3-3: Mechanical parameter selected for the canister.

	Young modulus	Poisson ratio
	E	ν
	[GPa]	[-]

Concerning the hydraulic constitutive behaviour of the canister, it is considered impermeable. This component does not provide water to the buffer, there is not water exchange.

Interface element

An interface element is modelled in order to reproduce a displacement constraint for the bentonite in the normal direction at the place of the concrete bed. For further details concerning the interface element, refer to (Cerfontaine, Dieudonne, Radu, Collin, & Charlier, 2015).

The longitudinal and transversal transmittivity is set equal to 1×10^{-99} (i.e. there is no water exchange between the interface and the bentonite).

In this modelling strategy, the total stress formulation is selected for the mechanical constitutive model of the interface element. The reason of the use of the total stress formulation instead of the effective stress one is explained.

A typical effective stress formulation reads:

$$\sigma = \sigma' - p \tag{Eq. 3.1}$$

Where p can represent the suction or the pore water pressure. Therefore, when there is negative pore water pressure (i.e. suction), the “effective” stress is higher with respect to the total one. The Mohr Coulomb criterion implemented for the interface element reads:

$$\tau \leq p_N \tan\phi + c \tag{Eq. 3.2}$$

Consequentially, when the effective stress formulation is used in an un-saturated state, the interface presents a certain resistance, which is proportional to the suction value in the corresponding element.

Therefore, the suction in the interface would be high and would cause a high resistance to the sliding. For instance, considering a suction equal to 66 MPa multiplied by the friction coefficient 0.05, it could give a resistance equal to 3.3 MPa (still higher than the developed swelling pressure in the simulation).

Table 3-4: Interface mechanical properties.

Penalty coefficient in the normal direction	K_t	[-]	10^8
Penalty coefficient in the longitudinal direction	K_l	[-]	10^8
Friction angle	ϕ	[°]	14

Friction coefficient	μ	[-]	0.250
Cohesion	c'	[MPa]	0

Bentonite blocks and pellet mixture

The Barcelona Basic Model (**Alonso, Gens, & Josa, 1990**) is adopted to model the mechanical behaviour of the bentonite Febex blocks and pellet mixture. The mechanical parameters for the Febex blocks compacted to a dry density $\rho_d=1.7 \text{ cm/g}^3$ (Table 3-5) are calibrated in (**Dieudonne, 2016**) in order to reproduce the experimental results obtained by (**Lloret, Villar, & Pintado, 2002**).

Table 3-5: Mechanical parameters selected for the bentonite Febex blocks and pellets mixture.

			Blocks	Blocks (1 rows of elements at the boundary with pellets)	Pellets mixture
ρ_d	[g/cm ³]	Dry density	1.70	1.70	1.35
κ	[-]	Elastic compressibility coefficient for changes in mean net stress	0.008	0.008	0.074
κ_s	[-]	Elastic compressibility coefficient for changes in suction	0.075	0.075	0.075
α_p	[-]	Parameter controlling the stress dependency of the swelling strain for change in suction	4.4×10^{-8}	4.4×10^{-8}	3×10^{-6}
p_{0^*}	[MPa]	Preconsolidation pressure for saturated state	0.40	0.40	0.65
p_c	[MPa]	Reference pressure controlling the shape of the LC curve	0.02	0.02	0.325
$\lambda(0)$	[-]	Slope of the saturated virgin consolidation line	0.12	0.12	0.20
r	[-]	Parameter defining the minimum soil compressibility	0.55	0.55	0.70
ω	[MPa ⁻¹]	Parameter controlling the soil stiffness	0.25	0.25	0.008
$c(0)$	[MPa]	Cohesion in saturated conditions	0	1	0
k	[-]	Parameter controlling the increase of cohesion for increase in suction	0.0046	0.046	0.0046
ϕ	[°]	Friction angle	26	26	26

Since the softening problems occurred in preliminary simulations, only at the interface with the pellets mixture, it was decided to modify the cohesion and the parameter k (parameter controlling the increase of cohesion for increase in suction) for one row of elements in the compacted blocks domain at the boundary with the pellets mixture. The yielding surface for these elements results in a much larger ellipse with respect to the reference one (Figure 3-24 & Figure 3-25).

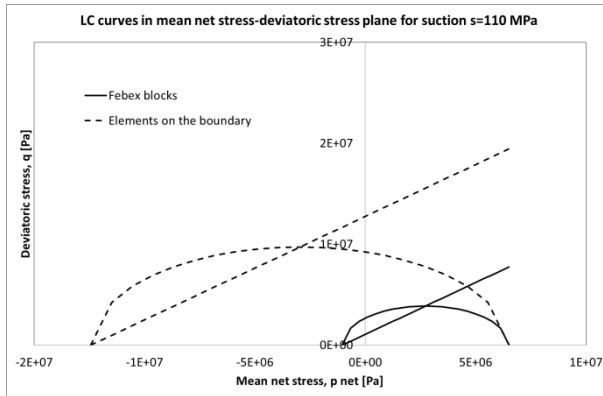


Figure 3-24 Modelled yielding surfaces in the q-p plane for suction $s=110$ MPa.

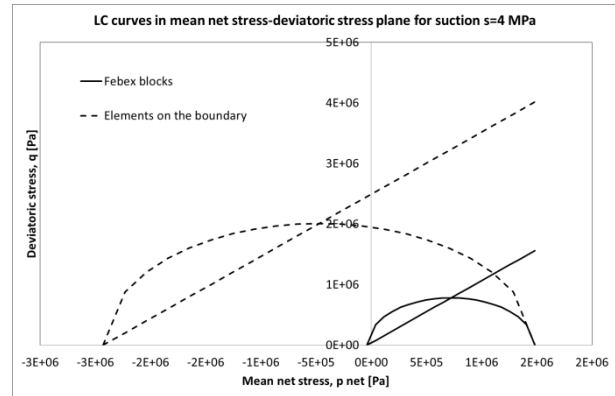


Figure 3-25 Modelled yielding surfaces in the q-p plane for suction $s=4$ MPa.

Since the Barcelona Basic Model overestimates the swelling pressure when low level of suction is reached, the following formulation is adopted in order to overcome this limitation (Eq. 3.3):

$$\kappa_s(p) = \kappa_{s0} * \exp(-\alpha_p * p) \quad \text{Eq. 3.3}$$

The parameter α_p is calibrated in order to reproduce the experimental data Figure 3-26.

The numerical results concerning the compacted blocks material (Figure 3-27) reproduce quite well the maximum value of swelling pressure equal to 8.2 MPa and the full-saturation time. The numerical simulation suggests a value of mean permeability of the material compacted to this dry density equal to $K_w=1 \times 10^{-21} \text{ m}^2$.

Figure 3-28 shows the stress path in the mean net stress – suction plane for the numerical simulation performed to reproduce the results proposed by (Villar, 2008). It is possible to observe that the stress increases in the elastic domain until point A (Figure 3-27 and Figure 3-28). Then, there is a further increase until point B in the plastic domain. After this point, a stress drop occurs until point C, which follows the plastic surface. A further increase of stress is observed until stabilisation at point D.

The mechanical parameters for the Febex pellet mixture of $\rho_d=1.35 \text{ g/cm}^3$ are selected in agreement with (Hoffman, Alonso, & Romero, 2007). Selected values are reported in Table 3-5.

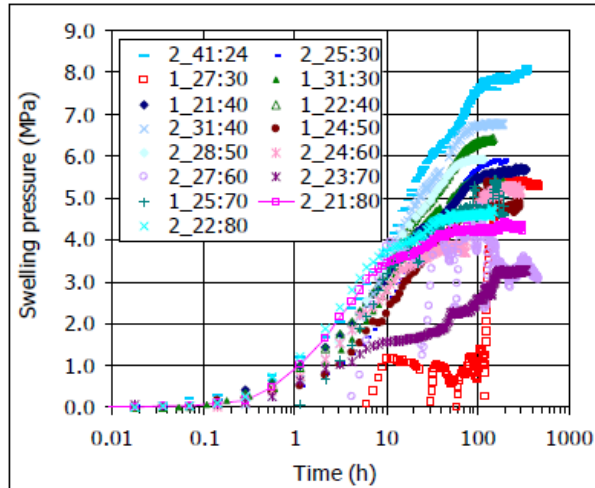


Figure 3-26: Evolution of swelling pressure in infiltration tests performed at different temperatures (indicated in °C after the test reference) in FEBEX samples compacted at nominal dry density 1.7 g/cm³ obtained in (Villar, 2008).

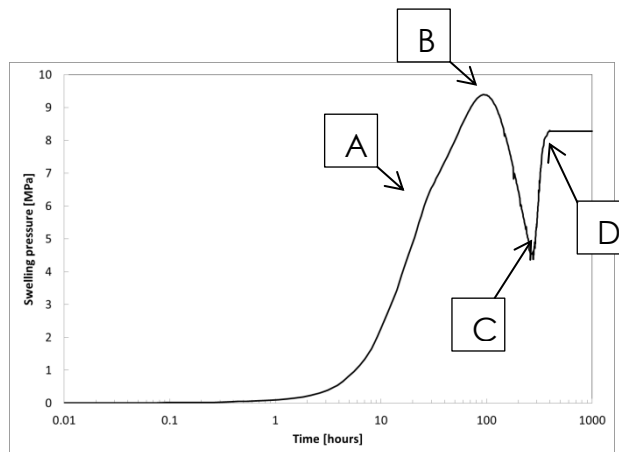


Figure 3-27: Numerical results for the modelling of the experimental campaign presented in (Villar, 2008).

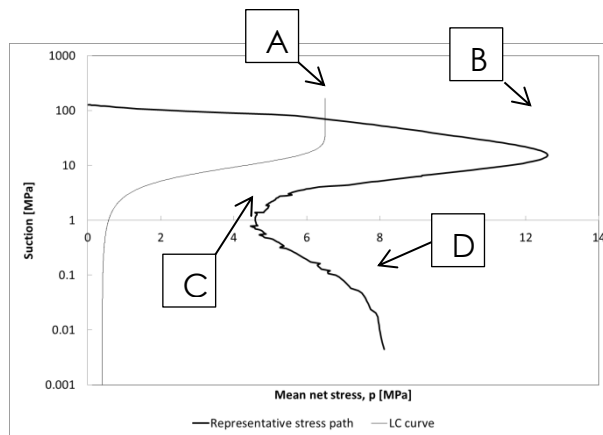


Figure 3-28: Stress path in mean net stress – suction plane for the numerical modelling of the experimental campaign presented in (Villar, 2008) (logarithmic scale for suction).

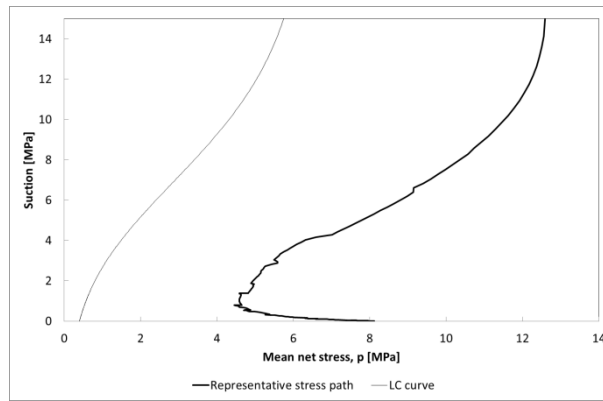


Figure 3-29: Stress path in mean net stress – suction plane for the numerical modelling of the experimental campaign presented in (Villar, 2008) (linear scale for suction).

For the hydraulic behaviour of both materials, the double porosity formulation with microstructure evolution and dry density dependence proposed and calibrated by (Dieudonne, 2016) is selected. The hydraulic parameters and the obtained water retention curve in constant volume conditions are presented respectively in Table 3-6 and Figure 3-30.

Table 3-6 Parameters of the water retention curve model.

e_{m0}	[-]	Microstructural void ratio for the dry material	0.35
β_0	[-]	Parameters quantifying the swelling potential of the aggregates	0.15
β_1	[-]		0.35
C_{ads}	[MPa ⁻¹]	Parameter associated to the desaturation rate of the soil	0.0028
n_{ads}	[-]	Parameter controlling the WRC curvature in the high suction range	0.78
n	[-]	Material parameters	3
m	[-]		0.15
A	[MPa]	Parameter controlling the dependence of the air-entry pressure on the macrostructural void ratio	0.24

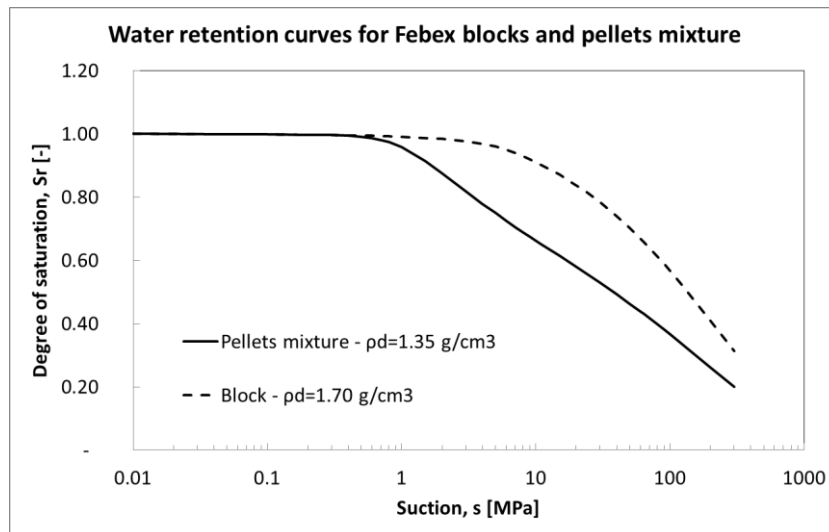


Figure 3-30: Water retention curves for constant volume conditions predicted by (Dieudonne, 2016) for Febex bentonite of $\rho_d=1.7 \text{ cm}^3/\text{g}$ and $\rho_d=1.35 \text{ g}/\text{cm}^3$.

Experimental results (Hoffman, Alonso, & Romero, 2007) underline how the permeability of this pellet mixture strongly changes during hydration. However, in this modelling strategy a mean permeability value equal to $K_w=1 \cdot 10^{-15} \text{ m}^2$ is selected, meaning probably an overestimation for a long period, after the first hydration phase. This means that hydraulic equilibrium would arrive early. The hydration strategy implies that this shouldn't greatly affect the numerical results.

3.3.3 Initial and boundary conditions

The presented numerical modelling of EB considers only the artificial hydration phase of the barrier.

A horizontal zero-displacement condition is imposed on the vertical boundary on the symmetry axis and the straight right side of the domain. On the curved area of the excavation the displacement is equal to zero in both vertical and horizontal direction. This means that no sliding can occur in this zone. On the interface, which is defined on the lower boundary of the domain, the bentonite can slide during the deformation (Figure 3-32).

The pellets mixture presents an initial suction equal $s=300 \text{ MPa}$ and a corresponding initial saturation $S_r=18\%$, whereas the blocks report a value equal to 120 MPa and an initial saturation $S_r=53\%$. The initial stress is equal to zero.

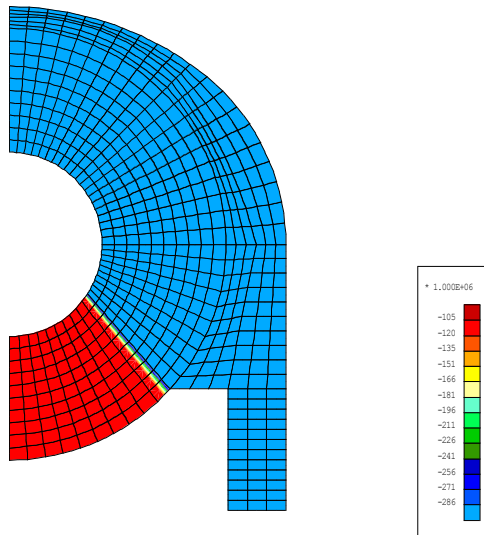


Figure 3-31: Pore water pressure initial conditions in the barrier [Pa].

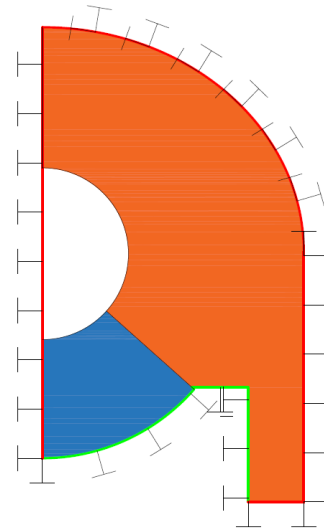


Figure 3-32: Displacement boundary conditions.

The re-saturation of the barrier has been modelled considering the hypothesis of a uniform surface hydration of the buffer with imposed injection rate (neglecting the system of tubes and the geotextile). The experimental water intake records of the barrier and the numerical ones are represented in Figure 3-33.

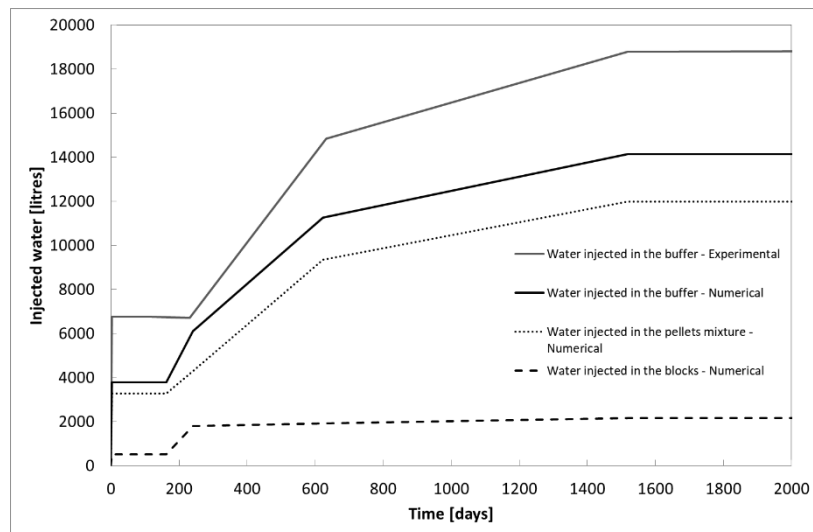


Figure 3-33: Experimental and numerical water intake time evolution.

In order to justify the following numerical modelling a number of considerations have to be presented.

Let us consider the length of the tunnel composed only by cross sections as the one depicted in Figure 3-34.

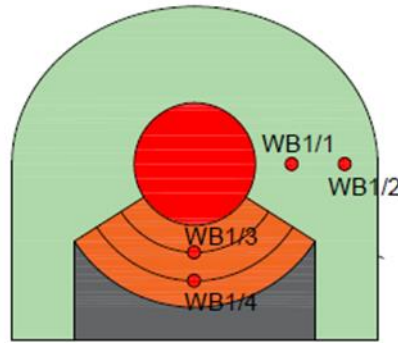


Figure 3-34 example of cross section of the analysed barrier.

With this configuration the total volume of pellets mixture is equal to 25.86 m³ (in (Talandier, 2019) a volume equal to 28.4 m³ was reported) and the total volume of the compacted blocks equal to 6.33 m³ (**Eq. 3.4**).

$$V[m^3] = A[m^2] \times L[m] \quad \begin{aligned} V_{tot,pellets} &= 4.31 \text{ m}^2 \times 6 \text{ m} = 25.86 \text{ m}^3 \\ V_{tot,blocks} &= 1.055 \text{ m}^2 \times 6 \text{ m} = 6.33 \text{ m}^3 \end{aligned} \quad \text{Eq. 3.4}$$

The pellets represent the 80% of the total volume to be hydrated, whereas the blocks the 20%.

The water content, dry density and saturation degree of the pellet mixture are equal to $w=4.17\%$, $\rho_d=1.35 \text{ Mg/m}^3$ and $S_r=11.27\%$, whereas for the compacted blocks $w=11.55\%$, $\rho_d=1.70 \text{ Mg/m}^3$ and $S_r=53\%$ (**Eq. 3.5**).

$$S_r[-] = \frac{w[-]}{\frac{1}{\rho_d \left[\frac{Mg}{m^3}\right]} - \frac{1}{\rho_s \left[\frac{Mg}{m^3}\right]}} \quad \begin{aligned} S_{r,pellets} &= \frac{0.0417}{\frac{1}{1.35 \left[\frac{Mg}{m^3}\right]} - \frac{1}{2.7 \left[\frac{Mg}{m^3}\right]}} = 0.1127 [-] \\ S_{r,blocks} &= \frac{0.1155}{\frac{1}{1.7 \left[\frac{Mg}{m^3}\right]} - \frac{1}{2.7 \left[\frac{Mg}{m^3}\right]}} = 0.53 [-] \end{aligned} \quad \text{Eq. 3.5}$$

Firstly the porosity is computed (Eq. 3.6). Via the porosity, the total volume of void is obtained (**Eq. 3.7**). Finally, the saturation represents the volume of water on the volume of voids (**Eq. 3.8**).

At the initial state, the volumes of water in the pellets mixtures and in the blocks are respectively equal to 1.46 m³ and 1.24 m³.

$n[-] = 1 - \frac{\rho_d \left[\frac{Mg}{m^3} \right]}{\rho_s \left[\frac{Mg}{m^3} \right]} = \frac{V_V[m^3]}{V_{TOT}[m^3]}$	$n_{pellets} = 1 - \frac{1.35 \left[\frac{Mg}{m^3} \right]}{2.7 \left[\frac{Mg}{m^3} \right]} = 0.5 [-]$ $n_{blocks} = 1 - \frac{1.7 \left[\frac{Mg}{m^3} \right]}{2.7 \left[\frac{Mg}{m^3} \right]} = 0.37 [-]$	Eq. 3.6
$V_v[m^3] = n[-] * V_{TOT}[m^3]$	$V_{v,pellets} = 0.5 * 25.86 [m^3] = 12.93 [m^3]$ $V_{v,blocks} = 0.37 * 6.33 [m^3] = 2.3421 [m^3]$	Eq. 3.7
$S_r[-] = \frac{V_w[m^3]}{V_V[m^3]} \rightarrow V_w[m^3]$ $= S_r[-] \times V_V[m^3]$	$V_{w,pellets} = 0.1127 \times 12.93 [m^3] = 1.46 [m^3]$ $V_{w,blocks} = 0.53 \times 2.3421 [m^3] = 1.24 [m^3]$	Eq. 3.8

Let us consider the first hydration phase with the water injection of 6.7 m³ in 2 days. Let us consider that the material is uniformly hydrated, so that the 80% of 6.7 m³ of water will go into the pellets and the 20% in the compacted blocks and let us compute the degree of saturation for the two components, which is 52.7% for the pellets and 110% for the compacted blocks (**Eq. 3.9**). The value of 110% is reasonable because this is not the case of a constant volume hydration but during wetting the material swells, therefore the dry density decreases and the volume of voids increases.

$$S_r[-] = \frac{V_w[m^3]}{V_V[m^3]} \quad \begin{aligned} S_{r,pellets}[-] &= \frac{1.46 [m^3] + 0.80 * 6.7 [m^3]}{12.93 [m^3]} = 0.527 \\ S_{r,blocks}[-] &= \frac{1.24 [m^3] + 0.20 * 6.7 [m^3]}{2.3421 [m^3]} = 1.10 \end{aligned} \quad \text{Eq. 3.9}$$

The water volume required to fully saturate the buffer can be calculated in a first approximation with **Eq. 3.10**. Finally, it can be assumed that the total volume of water needed to obtain the total saturation of the buffer is equal to 12 m³.

$$V_w[m^3] = (1 - S_r[-]) * V_V[m^3] \quad V_w[m^3] = (1 - 0.527) * 12.93 [m^3] = 6.12 [m^3] \quad \text{Eq. 3.10}$$

However, it is worth to note that after the first injection phase the suction level in the compacted bentonite blocks does not reach a value corresponding to an almost saturated state (experimental measurements show values ranging between 40 and 60 MPa). Moreover, leakage was observed during the injection. Consequentially, it can be assumed that, during the first injection phase, only a percentage equal to the 8% of 6.7 m³ of water is injected in the blocks with a uniform water flux equal to 0.00045 l*m²*m*s⁻¹ (~500 litres in 2 days in a surface of 1.055 m² times a length of 6 m, Figure 3-33). This amount of water has been compared with the available experimental suction

measurements.

After the natural re-distribution phase of water, a uniform water flux has been set in the bentonite compacted blocks equal to $0.0000324 \text{ l}\cdot\text{m}^2\cdot\text{m}\cdot\text{s}^{-1}$ between the 163rd and 240th day of the simulation time. This value of flux was selected in order to reproduce the experimental suction decrease at this location. Finally a flux equal to $5.2\cdot 10^{-7} \text{ l}\cdot\text{m}^2\cdot\text{m}\cdot\text{s}^{-1}$ between the 240th and 1517th day was imposed in order to obtain a final pore pressure value approximately equal to 2kPa.

The total water amount injected uniformly in the volume of the bentonite compacted blocks resulted equal to 2193 litres considering a surface of 1.055 m² times a length of 6 m.

With respect to the pellets mixture, the initial flux was selected in order to consider the leakage experimentally observed. Despite it was not possible to precisely quantify this water loss, it was assumed equal to $\approx 2 \text{ m}^3$. The uniform flux imposed in the first injection phase was then set equal to $7.2\cdot 10^{-4} \text{ l}\cdot\text{m}^2\cdot\text{m}\cdot\text{s}^{-1}$ with a total water amount injected in the pellet mixture in the first 2 days equal to ≈ 3300 litres (in a surface of 4.30 m² times a length of 6 m, Figure 3-33). After the natural re-distribution phase, in order to reproduce the experimental injection rate, fluxes equal to $5.8\cdot 10^{-6} \text{ l}\cdot\text{m}^2\cdot\text{m}\cdot\text{s}^{-1}$ between 163rd and 623rd day of the simulation time and $1.30\cdot 10^{-6} \text{ l}\cdot\text{m}^2\cdot\text{m}\cdot\text{s}^{-1}$ between 623rd and 1517th day, with a total water amount injected in the pellets mixture equal to ≈ 11800 litres. The final total water amount injected in the buffer is equal to 14040 litres and not equal to 18750 litres as the experimental measurements suggest. This discrepancy corresponds to the fact that the system which is modelled in this numerical strategy is closed and does not consider water exchange with the surrounding components. On the other hand, it is not negligible that during the EB experiment, it was not possible to carefully control the water injection. The available experimental data correspond to the injection of water in the entire system (i.e. bentonite components, concrete bed and plug, host-rock...), in which it can be easily demonstrated (also from post-mortem analyses) that the hydration process takes place in a non-uniform way due to the non-controllable hydration system but also due to the non-controllable heterogeneity of the buffer itself (which for example presents heterogeneous dry density distribution). These two last occurrences will be better explained and analysed in further analyses coming in the following.

Finally, considering all the difficulties involved in the EB experiment, despite the simplicity of the hypothesis of uniform surface hydration, it can be concluded that it is a useful strategy to put emphasis on a number of phenomena occurring during the hydration and avoiding several complications.

The following analysis offers 3 cases with different initial and boundary conditions both for the dry density distribution in the pellets mixture and for the hydration:

- **Case 1** (reference case). This modelling strategy presents uniform dry density distribution with an initial value equal to $\rho_d=1.35 \text{ cm/g}^3$ and

- uniform hydration in the pellets mixture (Figure 3-33 & Figure 3-35);
- **Case 2** concerns a case in which a non-uniform dry density distribution in the pellets mixture is assumed ($\rho_d=1.28 \text{ cm/g}^3$ for the red zones in Figure 3-36 and $\rho_d=1.36 \text{ cm/g}^3$ for the yellow ones) in order to simulate the non-homogeneous initial state due to the mixture emplacement and hydration evolution equal to Case 1 (Figure 3-33);
- **Case 3** presents uniform dry density distribution with an initial value equal to $\rho_d=1.35 \text{ cm/g}^3$ and non-uniform hydration distribution in the pellets mixture (Figure 3-37 & Figure 3-38). In this case, the total water amount injected in the pellets mixture is the same as the other cases but differently distributed. Since the permeability $K_w=1*10^{-15} \text{ m}^2$ is supposed to be quite high to observe the consequences of this modelling strategy, after the first injection phase it is modified to $K_w=1*10^{-18} \text{ m}^2$.

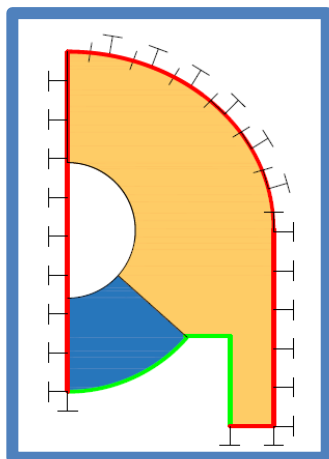


Figure 3-35 Configuration Case 1 (reference case).

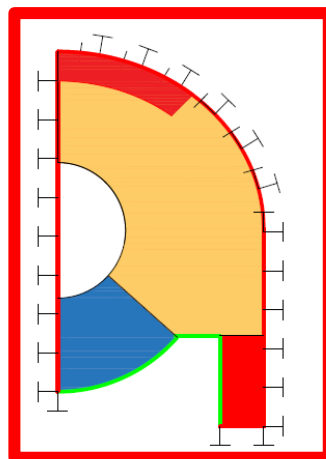


Figure 3-36 Configuration Case 2 (non-uniform dry density distribution).

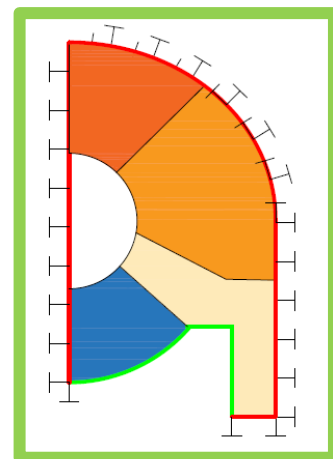


Figure 3-37 Configuration Case 3 (non-uniform hydration evolution).

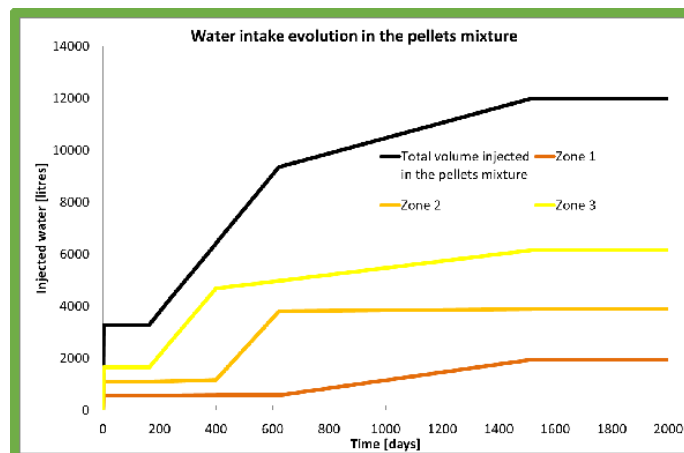


Figure 3-38 Water intake time evolution in the different zones in the pellets mixture

3.3.4 Results/discussion

To monitor the relative humidity, temperature, pore and total pressure and displacements, sensors were installed in different sections along the niche (instrumented sections in Figure 3-39). The idea was to be able to monitor buffer evolution and also the rock mass evolution around the niche. So, several types of sensors were installed. For instance, in the buffer there could be found:

- 8 Capacitive humidity sensors in sections B1 and B2;
- 8 Total pressure cells in section E;
- Extensometers in sections A1 and A2 (for canister displacements);

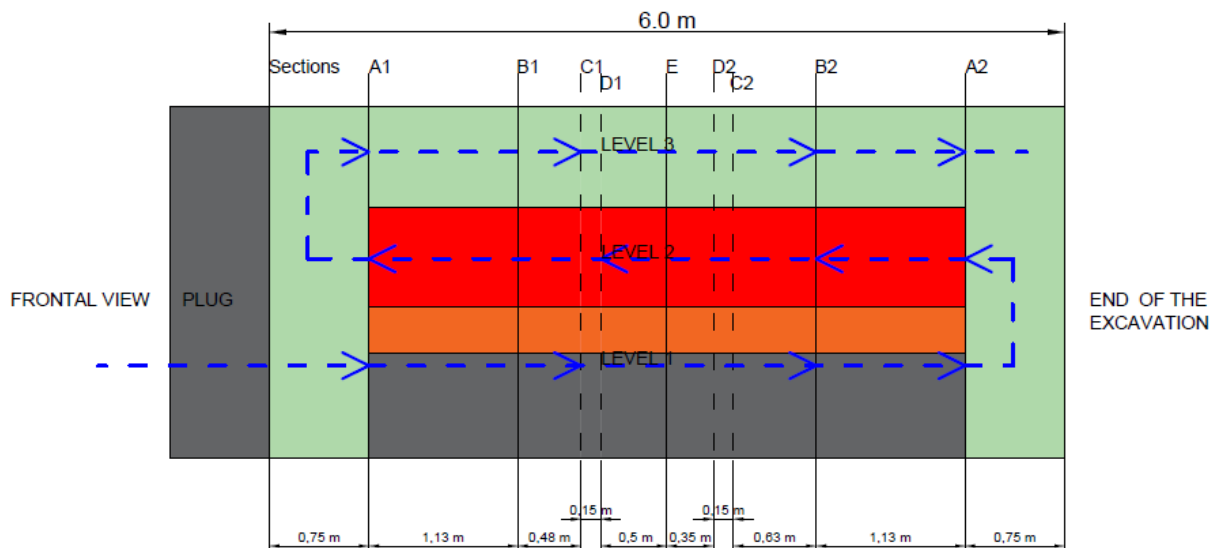


Figure 3-39: Longitudinal section of the barrier.

8 relative humidity sensors were placed into the buffer, 4 in section B1 and 4 in section B2 (Figure 3-39) respectively. Section B1 and section B2 are far 1.90 m and 4.20 m from frontal view of the excavation and so from the hydration system “beginning” and 2.26 m distant one from each other.

Figure 3-40 and Figure 3-41 report the suction evolution of the measurements point placed in the compacted blocks and the pellets mixture respectively for section B1 and B2. At their initial states, the pellets mixture presents a relative humidity equal to 4% (approximately equal to 500 MPa of suction), whereas the compacted blocks present a relative humidity equal to 40% (suction $s=150$ MPa).

The first hydration phase consists in the injection at high pore-water pressure of a considerable quantity of water in 2 days, 6 days after the seal emplacement.

In section B1 (Figure 3-41), the suction in the pellets mixture immediately decreases. This means that a remarkable quantity of water arrives in this location.

This occurrence is not consistent with the hydration system design. The hydration occurs from the bottom, so the points to be immediately hydrated are the ones located in the compacted blocks (level 1, firstly WB13 and WB14 and then WB23 and WB24). Successively, the hydrations continues on level 2, from the end of excavation toward the concrete plug (therefore WB21 and WB22 first and successively WB11 and WB12). Contrarily, it can be observed that the points in which the suction immediately decreases are WB11 and WB12, those ones should be the last to get full saturation. The suction decreases from 500 MPa to 50 MPa. Successively, the suction increases probably due to water redistribution inside the sealing. For point WB11 the full saturation occurs after 900 days whereas for point WB11 after 170 days, i.e. just after the beginning of the second injection phase (the one in which the pore water pressure is fixed, starting 130 days after the backfill emplacement). For points WB13 and WB14, the suction decreases slowly and similarly. There is a first phase, just after the 6.7 m³ injection, in which the suction decreases until the 100th day. Then the suction stabilises to an almost steady value and it decreases again when the second hydration phase begins (130th day after the backfill emplacement). The full saturation of these locations occurs approximately after 200 days since the emplacement. Point WB13 saturates slightly later with respect to point WB14 (probably because of gravity effect). However, despite point WB13 and WB14 present suction≈0, the whole assembly of the compacted blocks is far from hydration. In this context, it is worth to mention two things: the first one is that the sensors are immersed into the mat layers (preferential pathway for water) between the blocks (where water is injected). The second is that the compacted blocks present a dry density $\rho_d=1.7 \text{ Mg/m}^3$, with an intrinsic permeability $K_w\approx 1\times 10^{-21} \text{ m}^2$. Therefore, in order to obtain the full saturation of the blocks assembly larger time is needed and surely the full saturation does not occur in the first 2 days of hydration as discussed in the previous paragraph.

As already remarked, during the first injection of 6.7 m³, the hydration system fails and this could represent the reason why points WB11 and WB12 present such different full-saturation time despite they are at the same level and they should be hydrated simultaneously. The reason could also be related to the different proximity to the water injection points. However, the experimental suction measurements recorded in the pellets mixture do not seem to be reliable.

Concerning section B2, for WB21 and WB22 (pellets), the suction does not decrease immediately as observed for section B1. The hydration is slower with respect to WB11 and WB12. In WB21, the suction decreases slightly after the first injection then it reaches the steady state until the second injection (130 days after the emplacement). The full saturation is reached after 400 days. For WB22, the suction decreases continuously until the 400th day in which the

suction starts to decrease faster. For the points WB23 and WB24 located between the compacted blocks, the trend is actually the same with respect to WB13 and WB14.

The numerical results are able to well reproduce the experimental data. The water injection in the compacted blocks has been calibrated in order to reproduce the average experimental suction decrease in the compacted blocks. The numerical suction decrease in the pellets mixture reports a value in between the experimental measurements, testifying the fact that the pellets mixture presents in reality a permeability that allows an immediate and almost uniform water distribution.

The numerical measurements points in the compacted blocks and in the pellets mixture present the same suction time evolution due to the adopted uniform hydration strategy, which allows reducing the importance of the permeability in the strong hydro-mechanical couplings taking place during the hydration of a bentonite buffer.

The numerical measurements points in the compacted blocks (WB3 & WB4) and in the pellets mixture (WB1 & WB2) present the same suction time evolution due to the adopted uniform hydration strategy, which allows reducing the importance of the permeability in the strong hydro-mechanical couplings taking place during the hydration of a bentonite buffer. However, it is worth to note that the 3 strategies do not differ one from the other, neither case 3 (non-uniform hydration in the pellets mixture). The suction decrease is only slightly delayed.

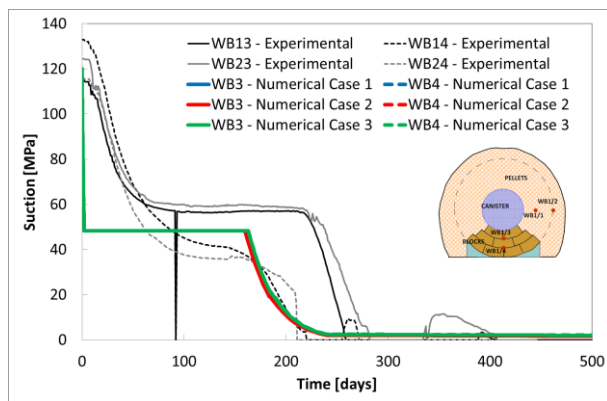


Figure 3-40 Suction time evolution of sensors located in the compacted blocks. Comparison experimental VS numerical.

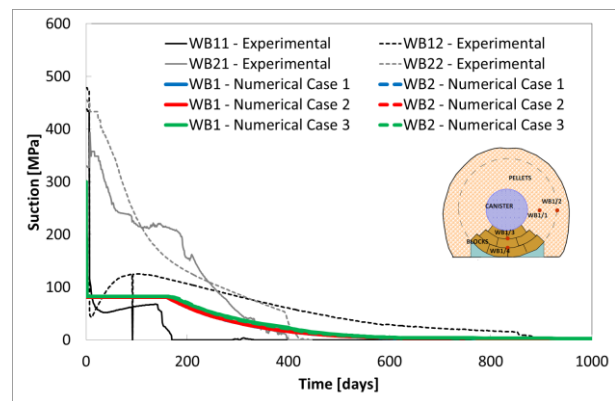


Figure 3-41 Suction time evolution of sensors located in the pellets mixture. Comparison experimental VS numerical.

8 total pressure cells are located in section E (Figure 3-39). Section E is placed just in the middle between section B1 and section B2. Figure 3-42 and Figure 3-43 analyses the vertical total pressure measurements, whereas Figure 3-44 the horizontal total pressure measurements. From a general point of view, it can be observed that all the total pressures stabilises after 1500 days since the emplacement of the sealing. Therefore, it can be assumed that the backfill is fully saturated at this stage (and not when the RH sensors detect full saturation). However, as depicted in Figure 3-33, there is still water injection at

low pore-water pressure (0.02 MPa kept constant for approximately one year).

The numerical results are able to well reproduce the non-monotonic increase of the swelling pressure in the buffer but not the final value. However, the final pressures are underestimated of half of the measured ones.

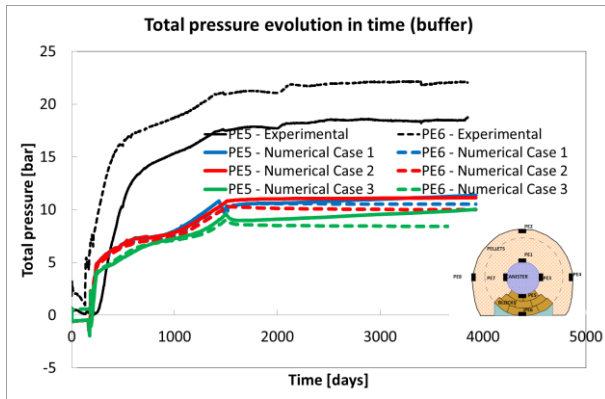


Figure 3-42: Vertical total stress time evolution for sensors PE5 and PE6. Comparison experimental VS numerical.

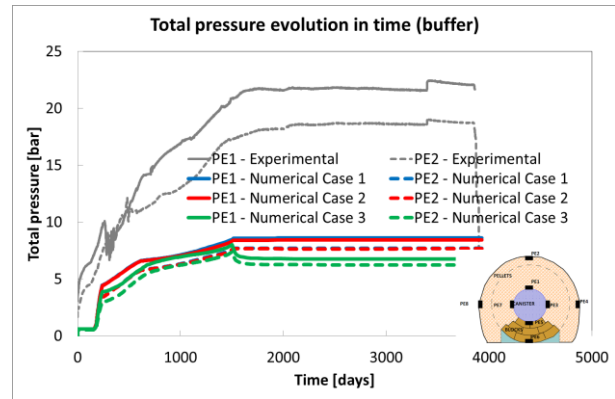


Figure 3-43: Vertical total stress time evolution for sensors PE1 and PE2. Comparison experimental VS numerical.

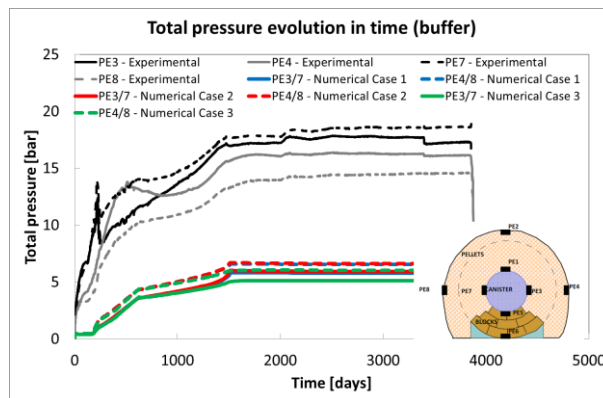


Figure 3-44: Horizontal total stress time evolution for sensors PE3, PE4, PE7 and PE8. Comparison experimental VS numerical.

Extensometers are located in sections A1 and A2 (for canister displacements). Despite the apparent symmetry of the configuration, horizontal displacements of the order of 6 mm (section A1) and 18 mm (section A2) are detected (Figure 3-45 and Figure 3-46).

The vertical displacements are 9 mm (section A1) and 7 mm (section A2). The numerical results do not provide any horizontal displacement of the canister because symmetry conditions are assumed (Figure 3-45). The vertical displacement reproduces similar behaviour with respect to the experimental one: there is a quick increase of vertical displacement due to the first injection phase followed by a steady state due to the natural water redistribution then a second increase during the second injection phase and final stabilisation

(Figure 3-46). However, it seems that the whole 3D displacement history of the canister is impossible to model with a 2D symmetric model.

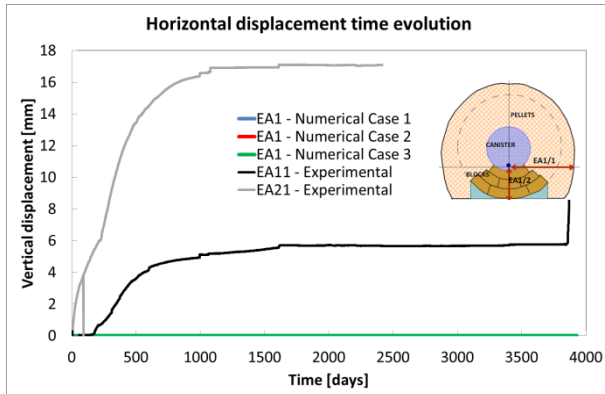


Figure 3-45: Horizontal displacement time evolution of extensometer located in the canister. Comparison experimental VS numerical

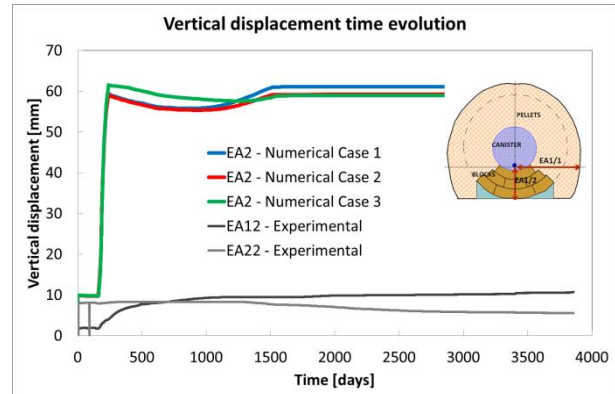


Figure 3-46: Vertical displacement time evolution of extensometer located in the canister. Comparison experimental VS numerical

Figure 3-47 reports the dry density distribution at dismantling in section A1. The initial dry density of the compacted blocks is $\rho_d=1.70 \text{ Mg/m}^3$, whereas experimental measurements underline a final dry density ranging between 1.2 Mg/m^3 and 1.3 Mg/m^3 . Some conclusions can be given:

- The swelling deformation occurs mainly in the horizontal direction. If the swelling deformation proceeds in the vertical direction only, in order to obtain an average dry density equal to 1.25 Mg/m^3 a vertical deformation equal to the 30% would have been needed in the blocks. This means that considering a vertical thickness of the compacted blocks assembly approximately equal to 60 cm, so a vertical displacement in the canister equal to 25 cm (which is not the case) and so the extensometers do not provide reliable results.
- In the case that the extensometers work properly, the swelling occurs also significantly in the horizontal direction. This may be due to the upper pellets mixture, which may represent a certain constraint for the compacted blocks in the swelling during the hydration. An initial or induced heterogeneity would also explain the horizontal displacement. However, the high level of heterogeneity in the buffer may possibly lead to a non-simultaneous hydration due to a hydration system failure or inefficiency in the casting phase (i.e. non uniform initial dry density distribution).

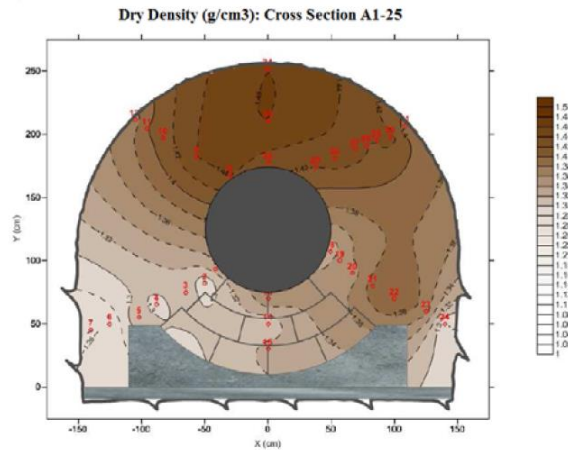


Figure 3-47: Experimental dry density distribution in section A1-25 at the end of the test.

From Figure 3-48 to Figure 3-51 the dry density distribution and the final deformed configuration are reported. The model predicts a very small variation of dry density after the first injection phase (Figure 3-48), relevant modifications are obtained with a strong decrease on dry density in the blocks and a strong increase in the upper pellets mixture. Also in the portion of pellets mixture placed on the lateral side of the concrete bed there is a decrease in dry density. In the final state (Figure 3-50), the dry density of the blocks is lower than the dry density of the upper pellets mixture with a further decrease also in the lateral side material. The deformation of the buffer occurs mainly in the vertical direction but the model allows also a horizontal swelling thanks to the interface element (Figure 3-51).

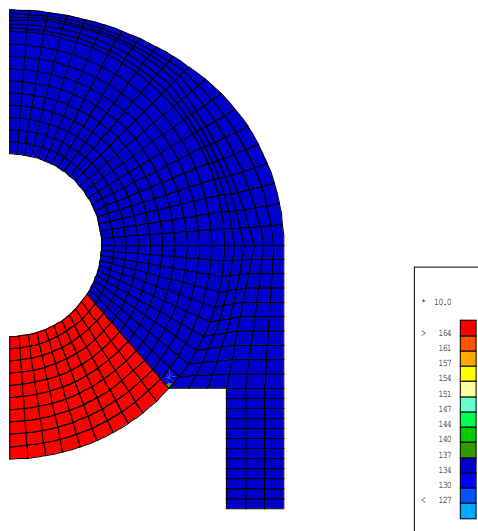


Figure 3-48 Dry density distribution after the first injection phase (case 1) (day 2 of the simulation time) [min-max value in the legend 1300 kg/m³ and 1700 kg/m³].

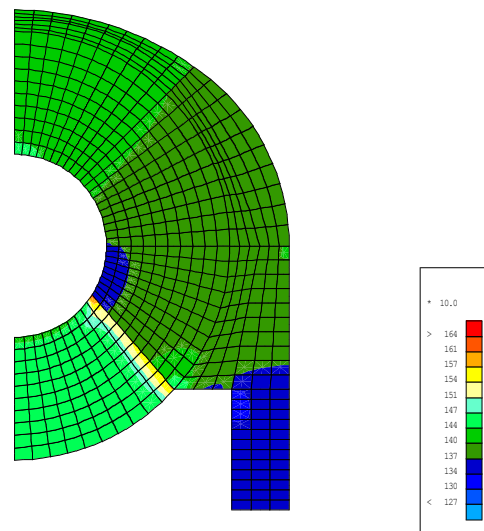


Figure 3-49 Dry density distribution during the second injection phase (case 1) (day 240 of the simulation time) [min-max value in the legend 1300 kg/m³ and 1700 kg/m³].

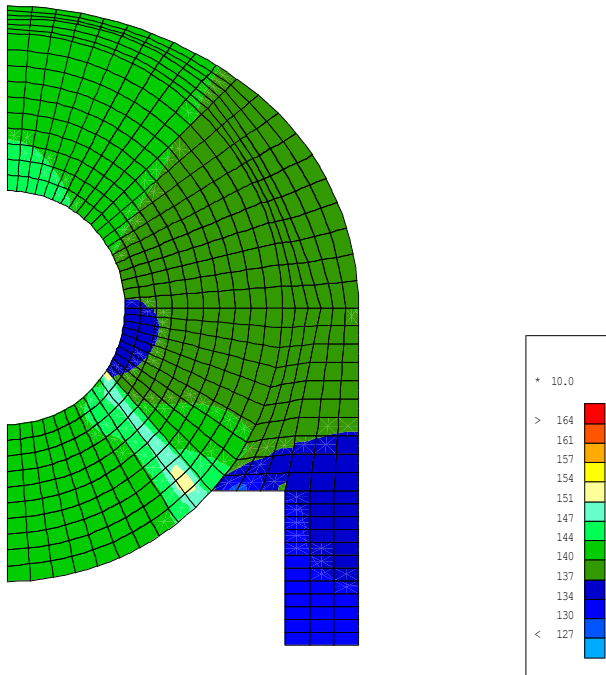


Figure 3-50: Dry density distribution at the end of the experiment (case 1) (day 3929 of the simulation time) [min-max value in the legend 1300 kg/m³ and 1700 kg/m³].

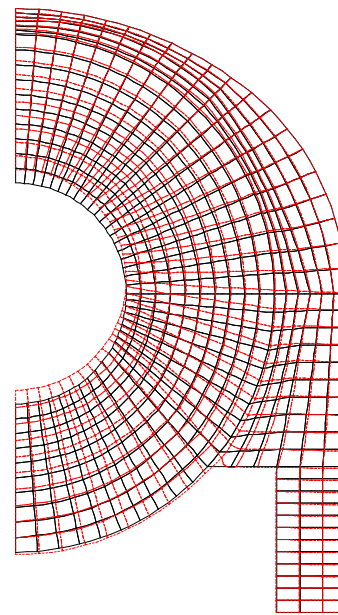


Figure 3-51: Deformed configuration at the end of the simulation (case 1) (day 3929 of the simulation time).

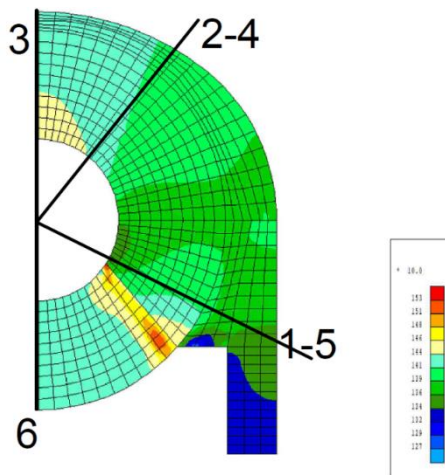


Figure 3-52 Numerical final dry density distribution (case 1) [min-max value in the legend 1280 kg/m³ and 1550 kg/m³].

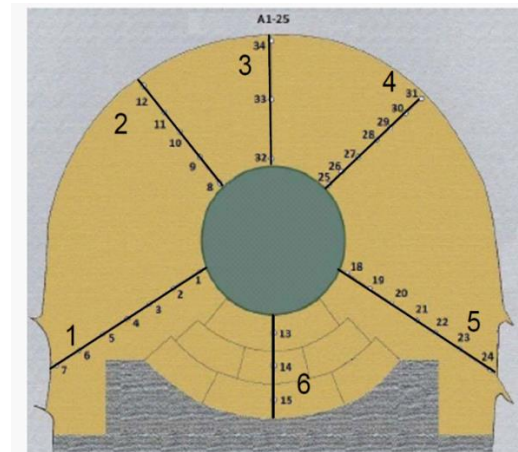


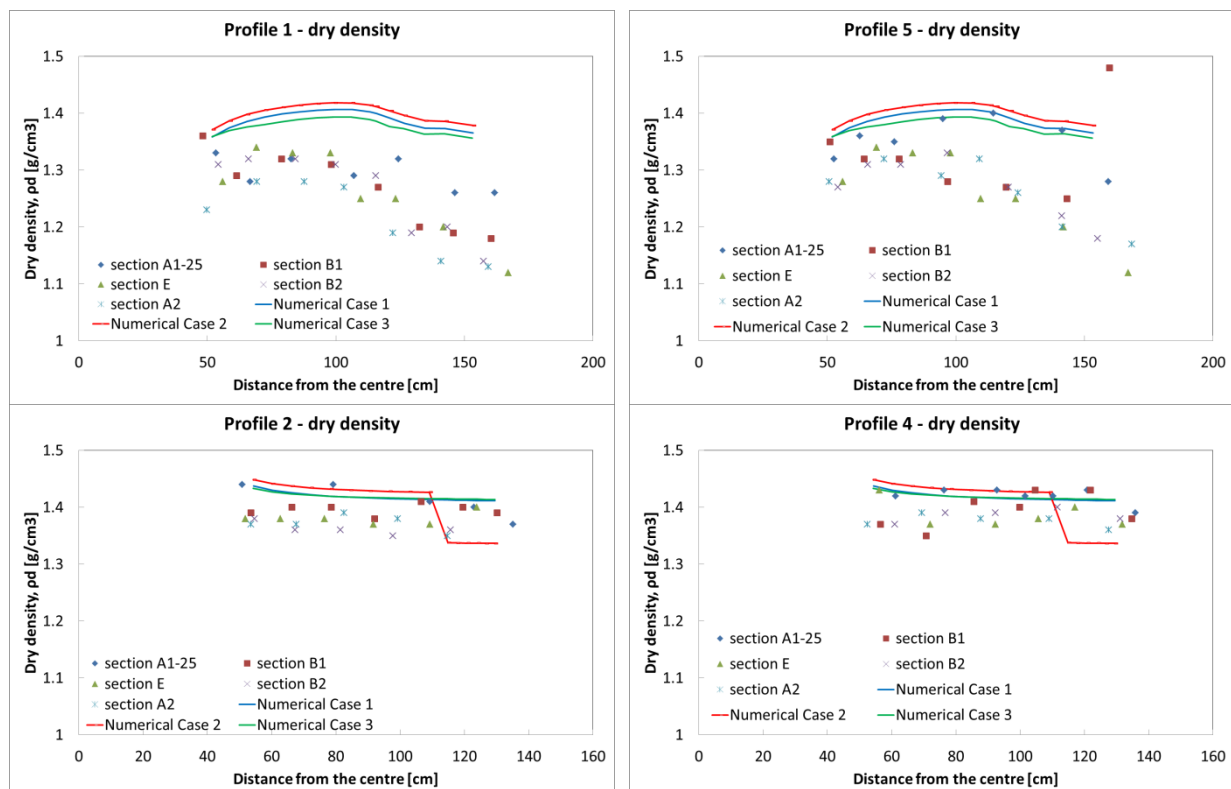
Figure 3-53 Profiles reference.

Post-mortem analyses on water content (Figure 3-55) and dry density (Figure 3-54) in a number of sections (Figure 3-39) allowed the determination of the spatial distribution of these quantities. All the distances in the following plots

refer to the centre of the canister.

The final computed dry density state is reported (Figure 3-52 and Figure 3-54). the model is able to well reproduce the final state of the barrier, in which the compacted blocks (presenting an initial state of $\rho_d=1.7 \text{ g/cm}^3$) swell up to a dry density equal to $\rho_d \approx 1.4 \text{ g/cm}^3$ (profile 6) compacting the upper pellets material (initial $\rho_d=1.35 \text{ g/cm}^3$) to a dry density equal $\rho_d \approx 1.45 \text{ g/cm}^3$ (profile 3). Despite the simplicity of the numerical strategy, which considers a uniform initial state, the non-uniform final dry density distribution is well reproduced in all the directions, apart from profile 1 and 5. At this location the numerical predictions overestimate the final dry density distribution. However, it is not negligible that the initial state of the barrier, in which the dry density distribution of the pellets material is far from being uniform and homogeneous, and the hydration system play a relevant role in its final state. Indeed, it can be noticed that case 2, which accounts a non-uniform initial dry density distribution, preserves the discontinuity until the full saturation (Profiles 2, 4 and 3, Figure 3-54).

Moreover, it is worth to say that the imposed boundary conditions (i.e. closed system in which the overall bentonite volume cannot vary) do not allow better dry density estimation, especially because of the 3D phenomena taking place during the hydration through the axis of the buffer.



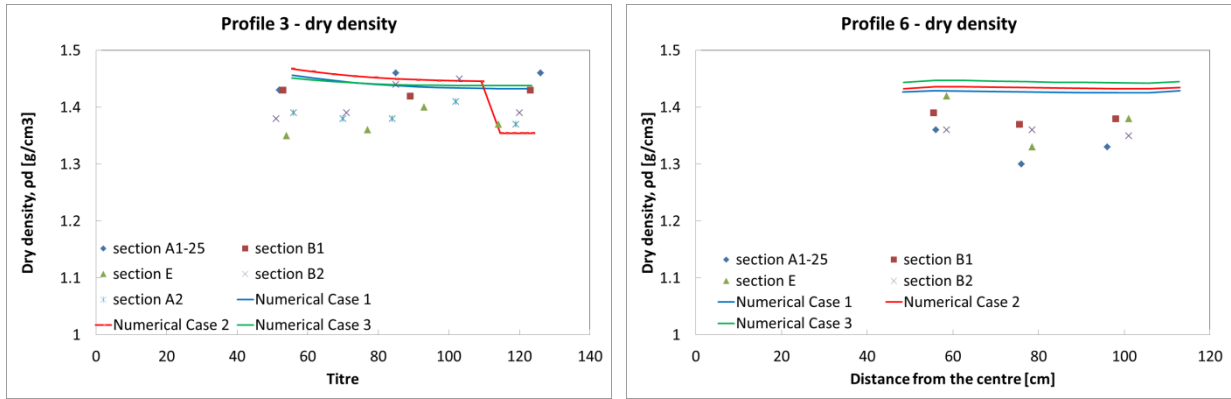


Figure 3-54 Dry density profiles. Comparison experimental vs numerical final states.

The numerical strategy imposes the full saturation of the barrier, however, the numerical results reproduce remarkably well the water content distribution for each of the analysed radii (Figure 3-55).

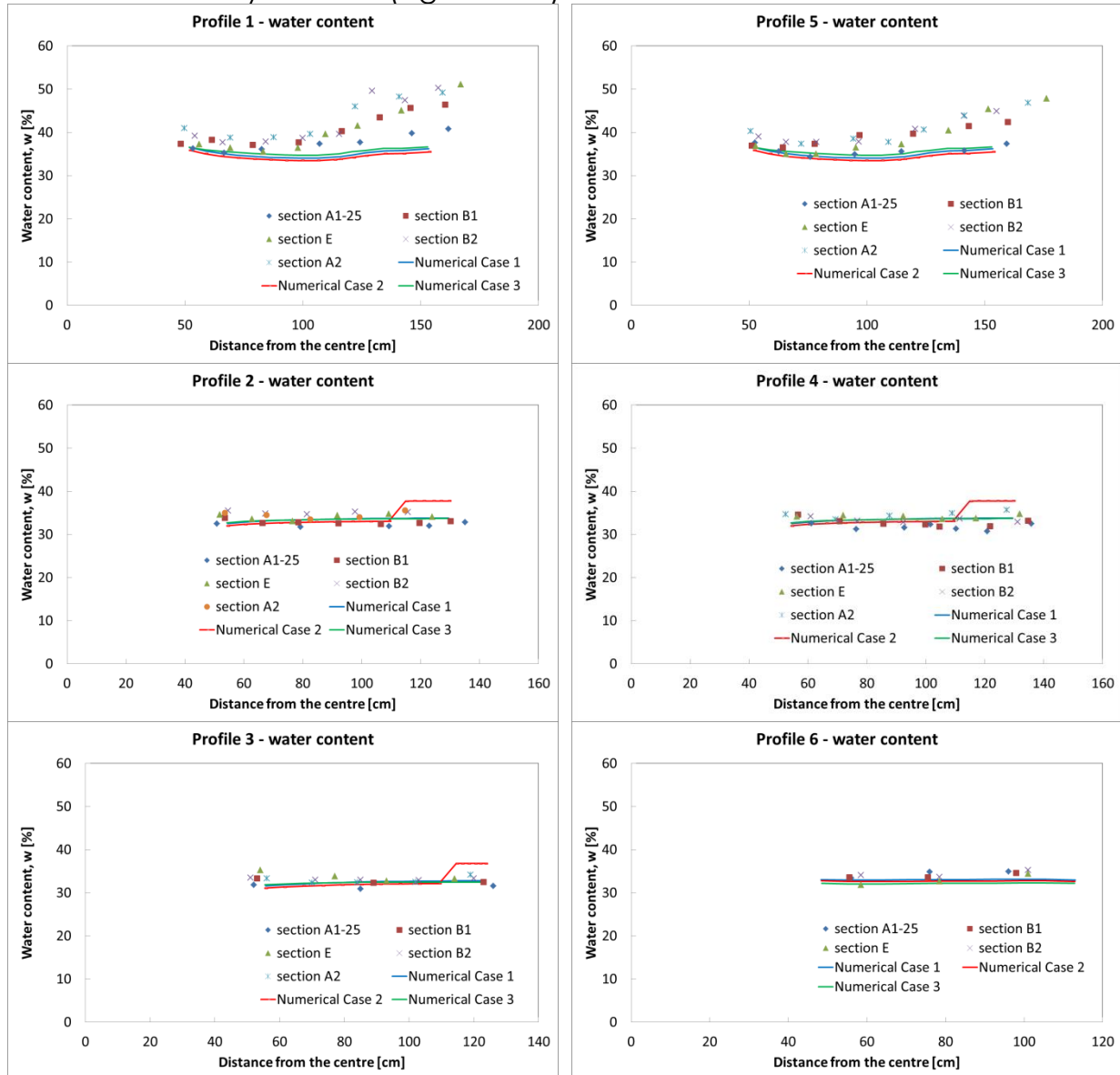


Figure 3-55: Water content profiles. Comparison experimental vs numerical final states.

3.3.5 Lessons learnt

The hydro-mechanical model implemented in the University of Liege has been adopted to model the large scale test EB. The numerical strategy considers a uniform surface hydration of a symmetric plane strain domain, which allows a simplified analysis of the complex phenomena occurring during saturation.

The imposed hydraulic boundary conditions allow the reproduction of the suction decrease recorded by the relative humidity sensors placed inside the buffer in section B1 and B2.

With respect to the total pressure sensors placed in section E, the BBM is able

to to satisfactorily reproduce the non-monothonic time evolution of the total swelling pressure (despite the obtained values are lower than the recorded ones).

Since the model considers a vertical symmetry axis, it is not possible to obtain the horizontal displacement of the canister recorded by the extensometers placed in sections A1 and A2. The numerical vertical displacement results 6 times larger than the experimental one.

The post-mortem analysis results have been compared with the numerical ones, underlining remarkable similarities between the two final states. The numerical results of dry density and water content are located in a good range of the variability of the experimental results, being able to reproduce the heterogeneous final state of the barrier (starting from a homogeneous state).

This occurrence is useful to detect the loosest zones in which the permeability can be higher and where leakage can take place, providing good indications for the safeness assessment.

Moreover, it was demonstrated that when a small heterogeneity is considered in the initial state, it is preserved until the full-saturation stage. Consequentially, it can be assumed that the model allows considering increasing complexity configurations providing good results.

Concerning the modelling tools:

- The constitutive law for the bentonite has allowed an excellent simulation of the observed final densities. It is much difficult to analyse the transient aspects, as few experimental results exist and they are largely scattered. The measured stresses were not well reproduced and this will be analysed in the future considering lab scale experiments with layers of different densities. Large deviatoric strains could be less well calibrated.

A frictional interface model has been used and was mandatory considering the large strains in the compacted bentonite blocks, with large displacements at the boundary. A sticking contact would induce too large deviatoric stresses in the bentonite blocks.

3.4 Synthesis of results for EB – key lessons (Andra + All)

The approach retained by UPC and ULG is to perform simulation on a 2D vertical plan defined perpendicularly to the axis of the tunnel considering or not the host rock. The results obtained by the two partners are in good agreement with the measures. The trend and the amplitude of the measured quantities are in most cases well reproduced. As it was foreseeable, all the measures could not be reproduced with the same accuracy, especially during the transient phase.

As it was observed in most test cases performed in Beacon project, the

transient phase is sometimes difficult to handle with the models. This is amplified in this large scale test due to additional complexity induces by the boundary and initial conditions and the organisation of the water inflow. An example of results is proposed on Figure 3-56 for total pressure at several location. Due to the fact that only half domain has been represented for symmetrical reason, the model supposes that PE3/PE4 are identical to PE7/PE8.

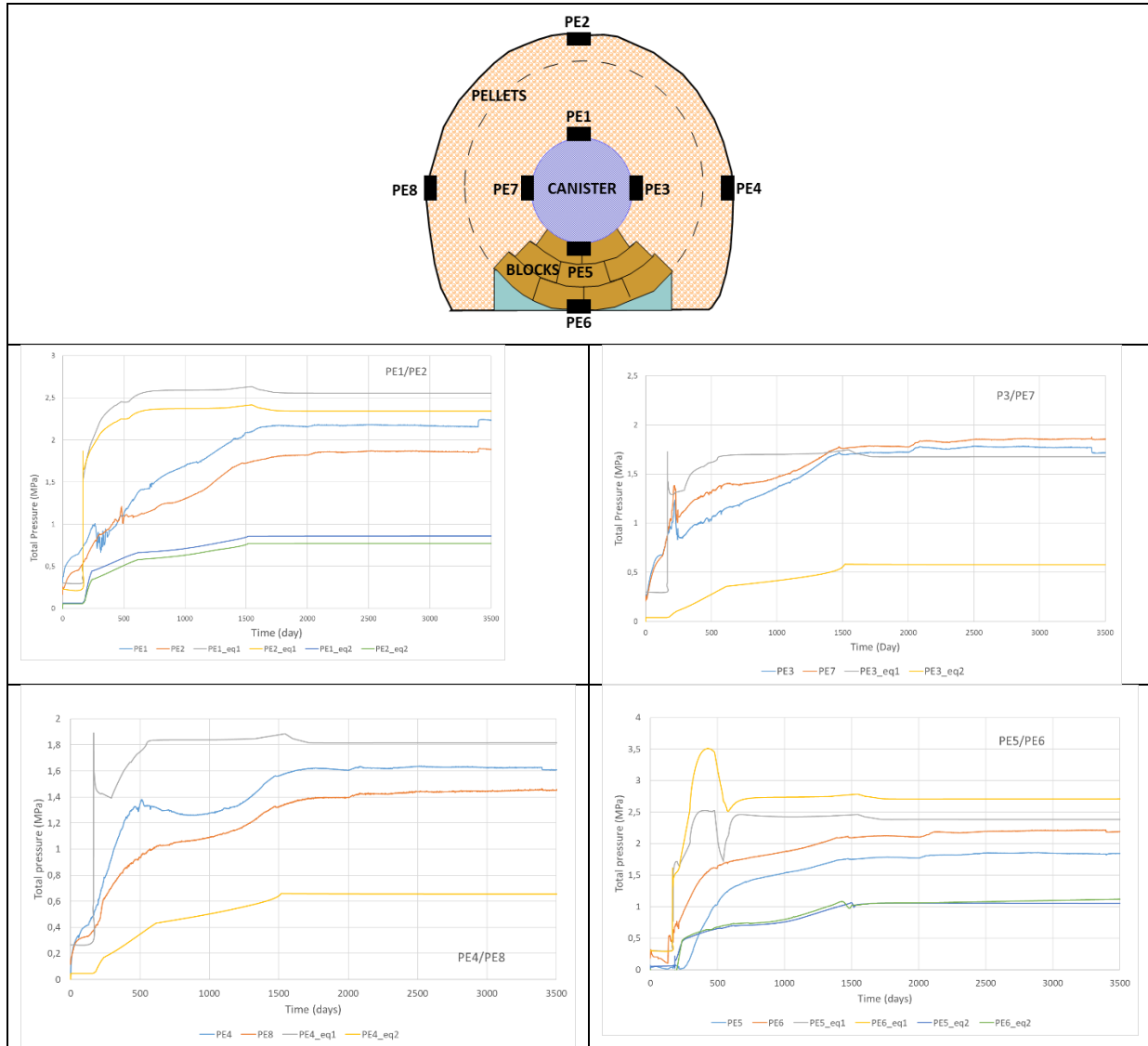


Figure 3-56 Evolution of total pressure at different locations – comparison between the numerical results and the measurements

It is interesting to observe that comparison between the results obtained at the end of the simulation and the post mortem analysis shows that the numerical results are mostly in a good range (Figure 3-57). It can be considered that the characteristic times and the final state are well approached by the two models. This is important an important point in terms of prediction of such complex structure.

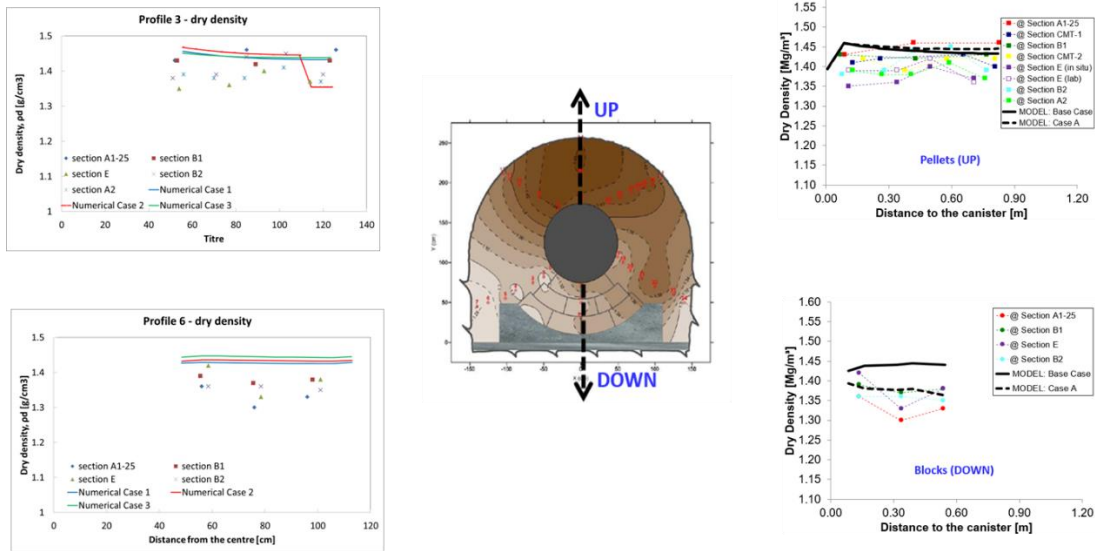


Figure 3-57 Dry density profiles below and above the canister – comparison between the numerical results and the measurements

The approach followed by the two teams to improve the results brings elements of understanding regarding the importance of modelling choices. UPC has chosen to modify some key parameters for the evolution of bentonites. They used different retention curves for bentonite and modified the interaction functions between the micro and macro scales. ULG proposed some modification in the hydration scheme and several distribution of dry density in the pellets mixture to simulate the non-homogeneous initial state due to the mixture emplacement.

This highlights the important role of the interaction functions on the results and specially to estimate the variation of these quantities during the transient phase. On the other hand, introducing a distribution of dry density of bentonite in the initial state or modification of the hydration scheme lead only to slight differences in the results. As anticipated in the previous task (task 5.1), the management of the interaction between the micro and the macro scales is one of the key point to model bentonite evolution.

4 CRT

4.1 Main feature of the test – why it is relevant for Beacon

Canister Retrieval Test (CRT) is a project that was initiated by SKB at Äspö Hard Rock Laboratory. The Canister Retrieval Test was a full-scale field experiment simulating a deposition hole in a high level radioactive waste repository of KBS-3V. It was designed to demonstrate the ability to retrieve a deposited canister at full buffer saturation. This in-situ experiment was carried out from 1999 to 2006. The experiment consisted of a cylindrical deposition hole hosting a canister encapsulated in clay buffer. Cables attached between the host rock and a plug on top of the buffer retained the buffer vertically and simulated the reaction force of a tunnel backfill. The canister was equipped with heaters to simulate the thermal activity of nuclear waste and strips of plastic filter were installed at the deposition provide a controllable simulated groundwater inflow. CRT was dismantled after 5 years of heating and artificial hydration.

The canister was surrounded by rings made by compacted bentonite. The gap between the host rock and the compacted bentonite was filled with pellets. The interfaces and pellets mixture could introduce low-density zones in the structure. They will have a role in the bentonite evolution and final state in terms of distribution of properties (dry density, water content...). This kind of situation is relevant for Beacon project to explore the consequences of unavoidable initial disturbance on the expected function of such barrier.

4.2 CU/CTU

4.2.1 Geometry and discretization

The CU/CTU team constructed a finite-element geometry in SIFEL according to the specifications of the CRT reference case (deliverable D.5.2.1§4.6), i.e. the entire buffer was simulated. Rotational symmetry was assumed, so that the simulation could be carried out in axisymmetric mode. The resulting finite-element mesh had rectangular elements with ~2 cm side and secondary nodes (>5000 nodes, >1500 elements). Four different regions – and material types/characteristics – were used, corresponding to the ring-shaped bentonite blocks, the cylinder-shaped bentonite blocks, the bentonite bricks, and the bentonite pellets loosely installed in the outer gap, between the blocks and the host rock (Figure 4-1). The prescribed inner gap, between the ring-shaped blocks and the cannister was not considered in the simulation. To simulate the anchors holding the plug on top of the cylinder-shaped blocks, a spring element was introduced with appropriate stiffness, so as to simulate the volume increase of the bentonite during the experiment.

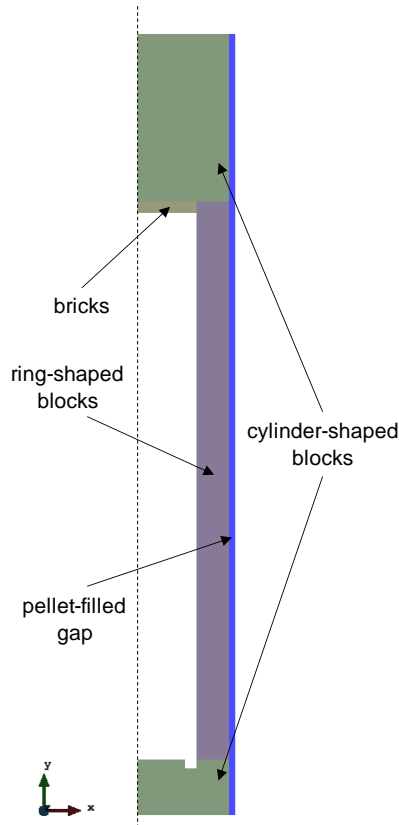


Figure 4-1: Scheme of the numerical model in SIFEL with indication of the materials. The dashed line indicates the axis of rotational symmetry.

4.2.2 Input parameters

The model parameters were calibrated from experimental results relative to the MX-80 bentonite. Experiments on the Czech B75 bentonite were also used, as it was shown that its behaviour is reasonably similar to that of the MX-80 bentonite. All data, calibration procedures and results can be found in published works (Mašín, 2013a, 2017; Janda and Mašín, 2017; Sun et al., 2018a, 2018b, 2018c; Hausmannová and Vašíček, 2014; Tang and Cui, 2005; Tang et al., 2008).

More specifically, Sun et al. (2018c) performed water adsorption tests under free-swelling at room temperature using B75 bentonite powder. The material was compacted uniaxially to various values of dry density. The compacted samples were then oven-dried to induce high values of suction; then, the vapour equilibrium technique was used for water adsorption, in sealed containers in a temperature-controlled room at 20 °C. Saturated saline solutions were used to control the relative humidity, producing suction values of 3-300 MPa. Hausmannová and Vašíček (2014) performed swelling pressure and hydraulic conductivity tests on B75 bentonite samples, compacted at room humidity at various values of dry density. The compacted samples were then transferred to an experimental device capable of measuring the hydraulic conductivity and swelling pressure simultaneously. During the experiments, water injection pressures of 1-6 MPa were applied, resulting in

hydraulic gradients of 5000-30000. The inflow and the force exerted by the sample on the top plate were monitored. Sun et al. (2018b) performed constant-load swelling tests at room temperature, using compacted B75 bentonite samples that were progressively loaded and then wetted. Afterwards, oedometric compression tests on the saturated samples were also carried out. Water adsorption–desorption tests under free swelling at various temperatures were carried out by Tang and Cui (2005) on samples of MX-80 bentonite. Tang et al. (2008) also used MX-80 bentonite to perform heating-cooling isotropic compression tests under net stress up to 5 MPa, suction up to 139 MPa, and temperature in the range 25-80 °C.

The calibration of most of the THM hypoplastic model parameters was performed using the element test driver TRIAX. Reasonable values of φ_c and ν were assumed, and the reference values s_r , e_0^M , and T_r were chosen to be in the range relevant to the experiments. In fact, these values can be selected arbitrarily, together with e_{r0}^m , which can be adjusted to optimise the water retention behaviour. The parameter κ_m was chosen so as the swelling behaviour could be predicted. The results of isotropic compression tests on MX-80 bentonite were used to calibrate the parameters of the basic hypoplastic model λ^* and κ^* (Mašín, 2013a); then, N , n_s , n_T , and l_T were corrected to predict the INCL correctly, as well as of heating-induced volume changes. The parameter α_s was calibrated from heating tests under high suction, while s_{e0} and a_e , having little effect on the behaviour under high suction, were simply assumed. The values of a and b also were assumed under the simplification that the effect of T on water retention capacity is caused only by changes of surface tension of water (Mašín, 2017).

The values of the single-element parameters (hypoplastic model parameters) used in the CRT simulation are reported in **Table 4-1**. As for the macroscopic parameters (finite-element model parameters), these are reported in **Table 4-2**. A Lewis and Schrefler's model with mechanical coupling (simplified two-phase transport, i.e. neglecting transport through gas) was implemented.

Table 4-1: Values of the parameters of the THM hypoplastic model for the bentonite.

Parameter	Unit	Value
φ_c	°	25
λ^*	–	0.130
κ^*	–	0.060
N	–	1.73
ν	–	0.25
n_s	–	0.012
l_s	–	-0.0050
n_T	–	-0.07
l_T	–	0
m	–	1
α_s	1/K	0.00015
κ_m	–	0.07
s_r	kPa	2,000
e_{r0}^m	–	0.45

c_{sh}	–	0.002
s_{e0}	<i>kPa</i>	2,700
e_0^M	–	0.50
T_r	<i>K</i>	293
a	<i>N/m</i>	0.118
b	<i>N/(mK)</i>	-0.000154
a_e	–	1.00
λ_{p0}	–	0.7

Table 4-2: Values of the parameters of the finite-element model for the bentonite.

Parameter	Unit	Value
compressible grains		yes
Biot's constant	–	1
E_{solid}	<i>MPa</i>	2.2
n_0	–	0.36–0.49*
$k_{intr,0}$	<i>m²</i>	$2 \cdot 10^{-19}$ **
$\beta_{s,0}$	<i>1/K</i>	10^{-7}
$\rho_{s,0}$	<i>kg m⁻³</i>	1000-1700*
$c_{p,s,0}$	<i>J/(kg K)</i>	830
λ_{dry}	<i>W/(m K)</i>	0.4
λ_{wet}	<i>W/(m K)</i>	1.3
$S_{r,dry}$	–	0.01
$S_{r,wet}$	–	1

* according to the specifications. ** the permeability of the pellet-filled gap was assumed to be 10 times this value

4.2.3 Initial and boundary conditions

The initial conditions were assigned to the model according to the specifications that were provided, as reported in **Table 4-3**. The only adjustment that had to be made concerned the porosity of the pellet-filled gap. In fact, while the pellets themselves were made of well-compacted bentonite, they were installed in the gap loosely, resulting in an overall very low dry density and hence high porosity. The model does not feature a third level of structure to account for the pellets-macropore structure; instead, an equivalent double-structure homogeneous material is considered. The chosen value of porosity ($n = 0.49$) was found through preliminary testing to be the maximum allowed by the THM hypoplastic model to run successfully. Obviously, this introduced some differences compared to the experiments, as the dry mass of the pellets is overestimated, with resulting overestimation of the possible swelling of the layer.

Table 4-3: Initial conditions.

Region	Type of process		
	Thermal	Hydraulic	Mechanical
Cylinder-shaped bentonite blocks	$T = 20 \text{ }^\circ\text{C}$	$S_r = 0.751$	$\sigma = 0 \text{ MPa}, n = 0.39$
Ring-shaped bentonite blocks	$T = 20 \text{ }^\circ\text{C}$	$S_r = 0.859$	$\sigma = 0 \text{ MPa}, n = 0.36$
Pellet-filled gap	$T = 20 \text{ }^\circ\text{C}$	$S_r = 0.895$	$\sigma = 0 \text{ MPa}, n = 0.49^*$
Bentonite bricks	$T = 20 \text{ }^\circ\text{C}$	$S_r = 0.637$	$\sigma = 0 \text{ MPa}, n = 0.42$

* the value in the specifications was $n = 0.64$, but it could not be used in the model.

As for the boundary conditions, the water pressure protocol, provided in the specifications, was used as the hydraulic boundary condition (**Table 4-4**), while the heater power protocol was not used as the thermal boundary condition. Instead, experimental values of some of the temperature sensors were used to set the thermal boundaries at the interfaces with the cannister and with the host rock (**Figure 4-2**). This solution was preferred as it was simpler to implement than by setting an energy flux.

Table 4-4: Hydraulic boundary condition assigned to the outer boundary (pellet-filled gap).

Day	Water pressure (MPa)	Comment
0	0	
679	0	Gradual increase of pressure
714	0.8	Final value after the increase
770	0.1	
805	0.4	
819	0.8	
1598	0	
1877	0	Air flushed (end of simulation)

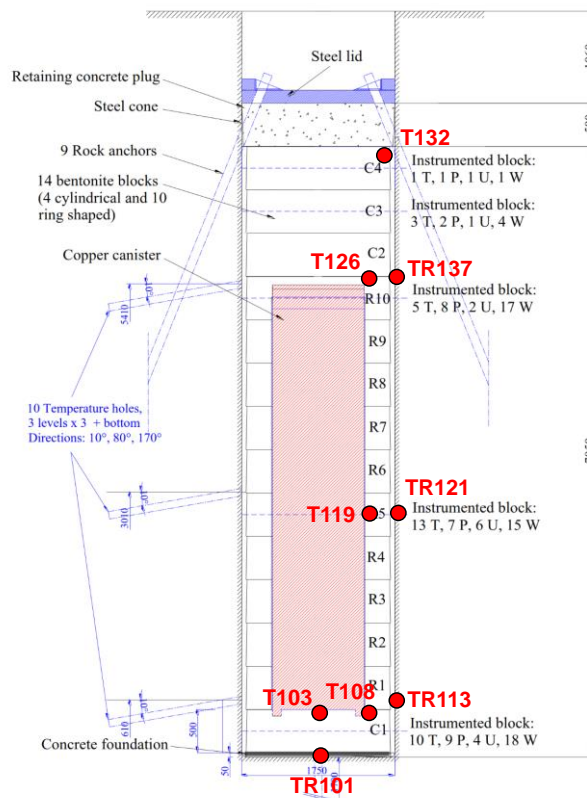


Figure 4-2: Locations of the temperature sensors used to set the thermal boundary conditions.

4.2.4 Results/discussion

In general, the numerical simulation was rather smooth, with only some adjustments in the solver parameters to ensure better and faster convergence of the iterative processes. A time step up to 1 day could be

used, ensuring completion of the 1877 days-long simulation in 12-24 hours on a 12-core desktop computer. Some challenges were brought by the spring element simulating the anchors, which in some cases caused numerical convergence issues. However, it was found that the value of the stiffness and hence the swelling allowed could be changed in a reasonable range without causing significant changes in the results, but at the same time improving the numerical performance significantly.

Some key results are reported in the charts below (Figure 4-3, Figure 4-4, Figure 4-5), where trends of simulated values are compared with experimentally measured quantities (swelling pressure, suction, temperature) at various locations within the modelled domain. In addition, the evolution of degree of saturation and dry density at various locations, as well as water content and dry density profiles in selected cross sections are shown (Figure 4-6, Figure 4-7). In Figure 4-8, the vertical displacement at the top is also shown.

The results of the simulation are generally in good agreement with the experimentally measured quantities. The trend of swelling pressure development (Figure 4-3) is well captured, both in terms of temporal evolution (shape of the curve over time) and absolute values. This suggests that the swelling parameters of the bentonite, as well as the hydraulic conductivity were calibrated reasonably well. Nonetheless, the sensors in the experiment seem to have been much more responsive to changes in the hydraulic and thermal boundaries than the numerical simulation, where these signals are almost completely damped at the monitored locations, resulting in rather smooth curves. With reference to the results in R5 (2.75 m above the bottom of the domain, i.e. at mid-height of the cannister), it can also be seen that, while the simulation provides similar values of swelling pressure along the cross section at the end of the experiment (~4.5 MPa), the experimentally measured values decrease significantly from the inner to the outer boundary. This suggests that the thermal (inner) boundary exerted a stronger control than the hydraulic (outer) boundary on the development of swelling pressures, whereas the numerical model shows more or less equal importance of the two boundaries.

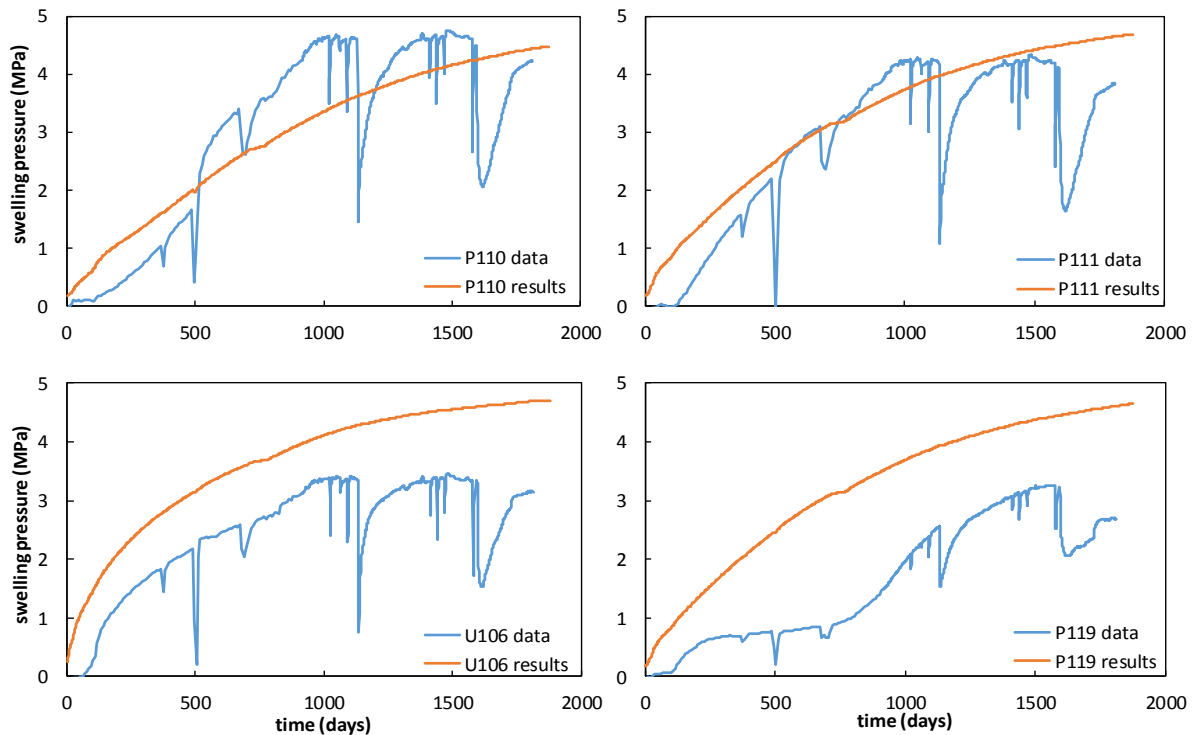


Figure 4-3: Simulated (results) and experimental (data) values of swelling pressure at four locations in the simulated domain. The sensors P110, P111, and U106 were located in the ring-shaped bentonite block n.5 (R5), at 2.75 m of height from the bottom of the domain, at radii 0.585, 0.685, and 0.785 m, respectively; P119 was located in the ring-shaped bentonite block n.10 (R10), at 5.25 m of height from the bottom of the domain, at 0.685 m radius.

As for the trend of suction (Figure 4-4), the model captures it reasonably, albeit with a general overestimation of the values. Possibly, the actual air-entry value of the used bentonite was lower than that considered in the simulations (2.7 MPa), or the hydraulic conductivity was somewhat underestimated. It is worth noting, however, that improving the fit with the suction measurements through fine-tuning of the calibrated parameters would have probably resulted in a worse fit with the swelling pressures (Figure 4-3).

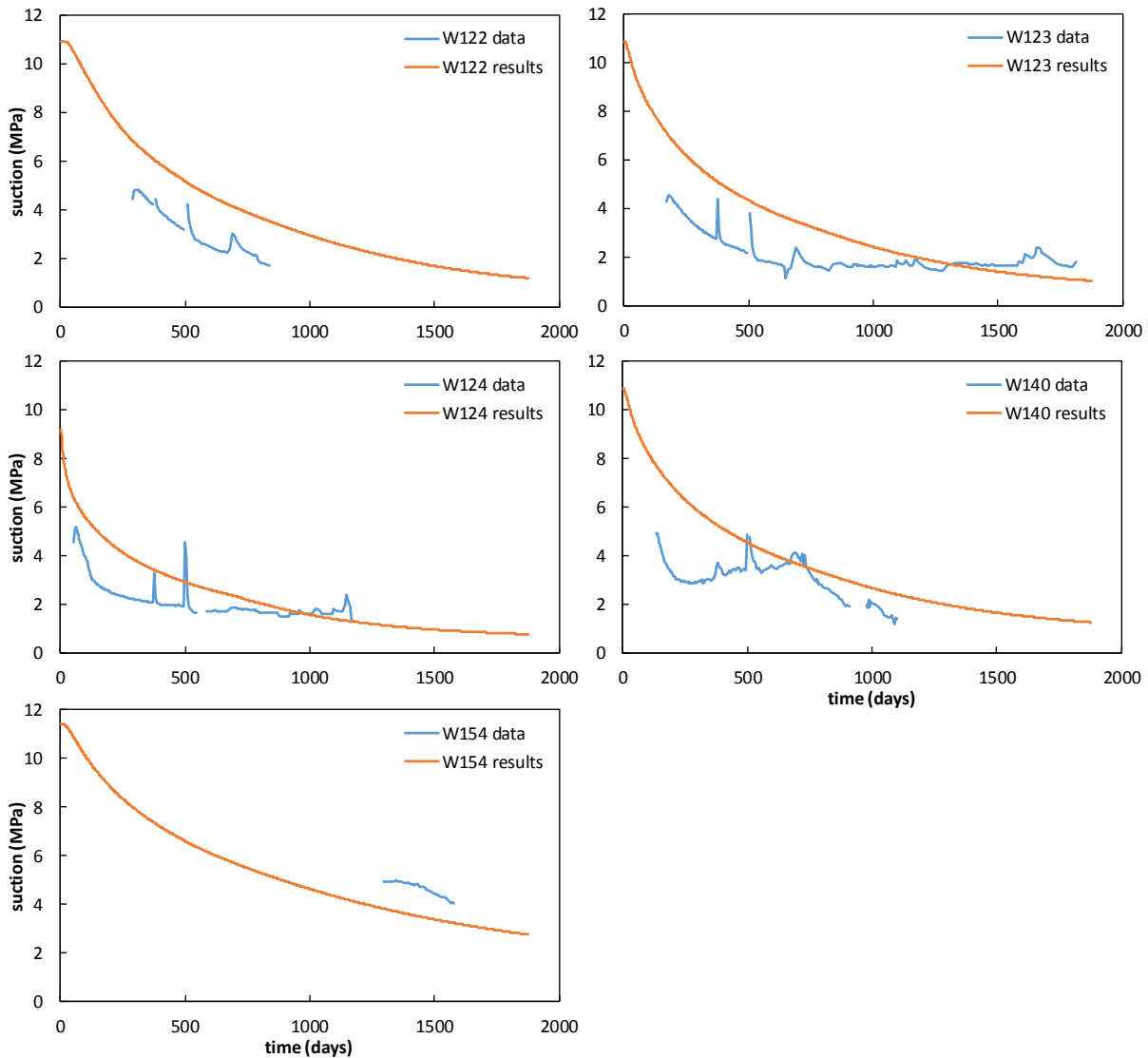


Figure 4-4: Simulated (results) and experimental (data) values of suction at five locations in the simulated domain. The sensors W122, W123, and W124 were located in the ring-shaped bentonite block n.5 (R5), at 2.75 m of height from the bottom of the domain, at radii 0.585, 0.685, and 0.785 m, respectively; W140 was located in the ring-shaped bentonite block n.10 (R10), at 5.25 m of height from the bottom of the domain, at 0.685 m radius; W154 was located in the cylinder-shaped bentonite block n.3 (C3), at 6.25 m of height from the bottom of the domain, at 0.585 m radius.

In Figure 4-5, the simulated and measured trends of temperature are compared. The fit is generally very good, which is an expected result since the thermal boundary was assigned in terms of temperatures at the boundaries rather than as an energy flux. Nonetheless, it can be seen from the figure that the model underestimated the temperatures by some degrees in C3, above the cannister, close to the outer boundary.

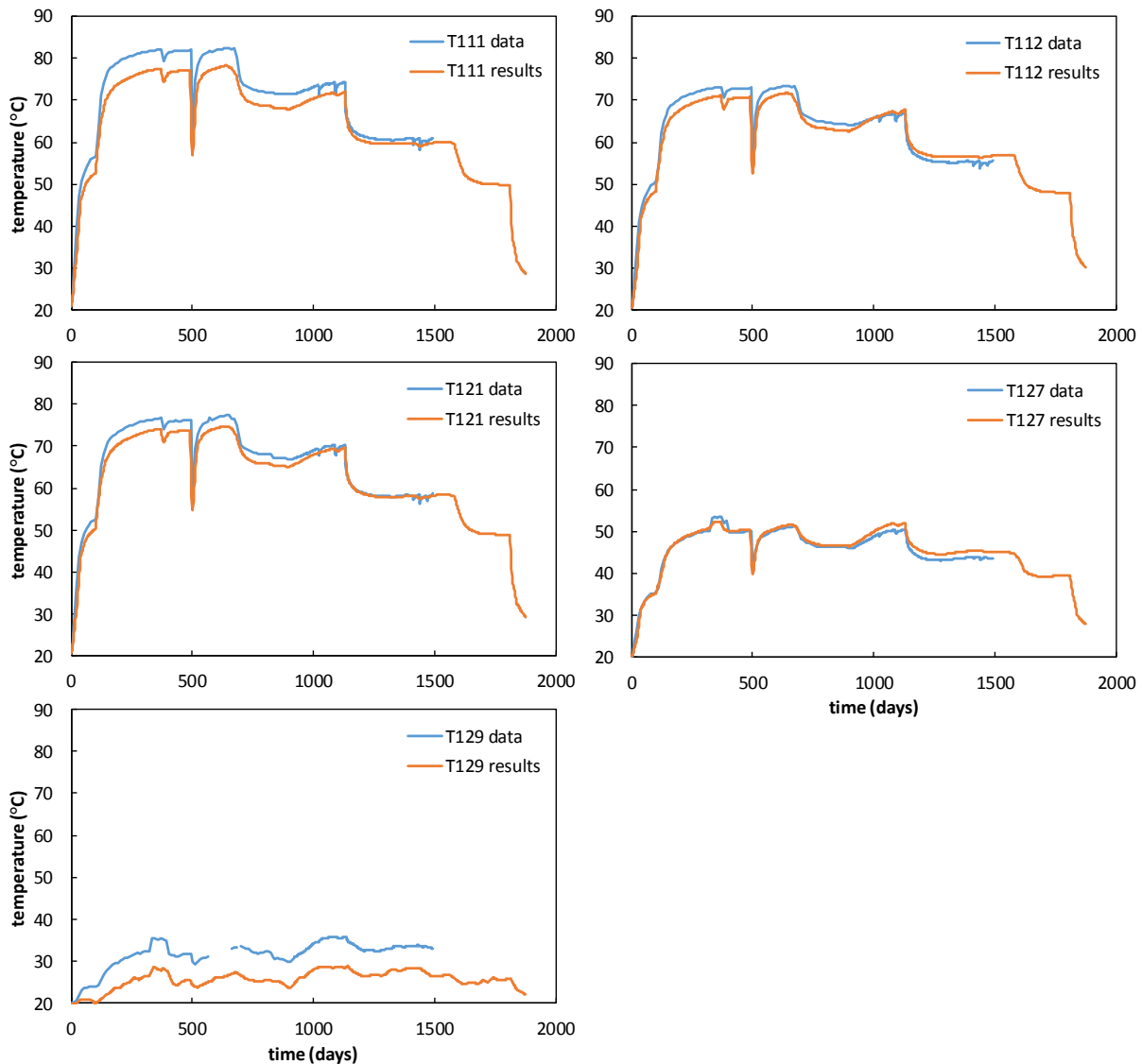


Figure 4-5: Simulated (results) and experimental (data) values of temperature at five locations in the simulated domain. The sensors T111, T112, and T121 were located in the ring-shaped bentonite block n.5 (R5), at 2.75 m of height from the bottom of the domain, at radii 0.635, 0.735, and 0.685 m, respectively; T127 was located in the ring-shaped bentonite block n.10 (R10), at 5.25 m of height from the bottom of the domain, at 0.685 m radius; T129 was located in the cylinder-shaped bentonite block n.3 (C3), at 6.25 m of height from the bottom of the domain, at 0.785 m radius.

The plots in Figure 4-6 and Figure 4-7 show the temporal evolution of degree of saturation, water content, and dry density in some well-instrumented cross sections (i.e. R5, R10, and C3). It can be seen clearly (Figure 4-6) how the saturation of the bentonite proceeded from the outer boundary towards the centre. It can also be noticed that the dry density generally decreased over time, consistently with the slight volume increase of the domain (at the expenses of a compression of the pellet-filled layer and a slight swelling of the top cap. However, in the innermost regions the dry density increased at first, as an effect of the compression caused by the expansion of the outer regions, and began to decrease only in a later stage.

The model does not show much homogenization of the bentonite (Figure 4-7). While most of the domain reaches saturation or near-saturation by the end of the simulation, the dry density crystallises during the last year of simulation (note the small differences between the values at 1400 days and those at 1877 days) while significant gradients are still present. The case of section C3 is rather emblematic, as it shows that the differences in dry density along the section remained almost unchanged throughout the simulation. In this respect, the model underestimates the homogenization which, even though it was incomplete, it did take place in a more significant way in the actual experiment.

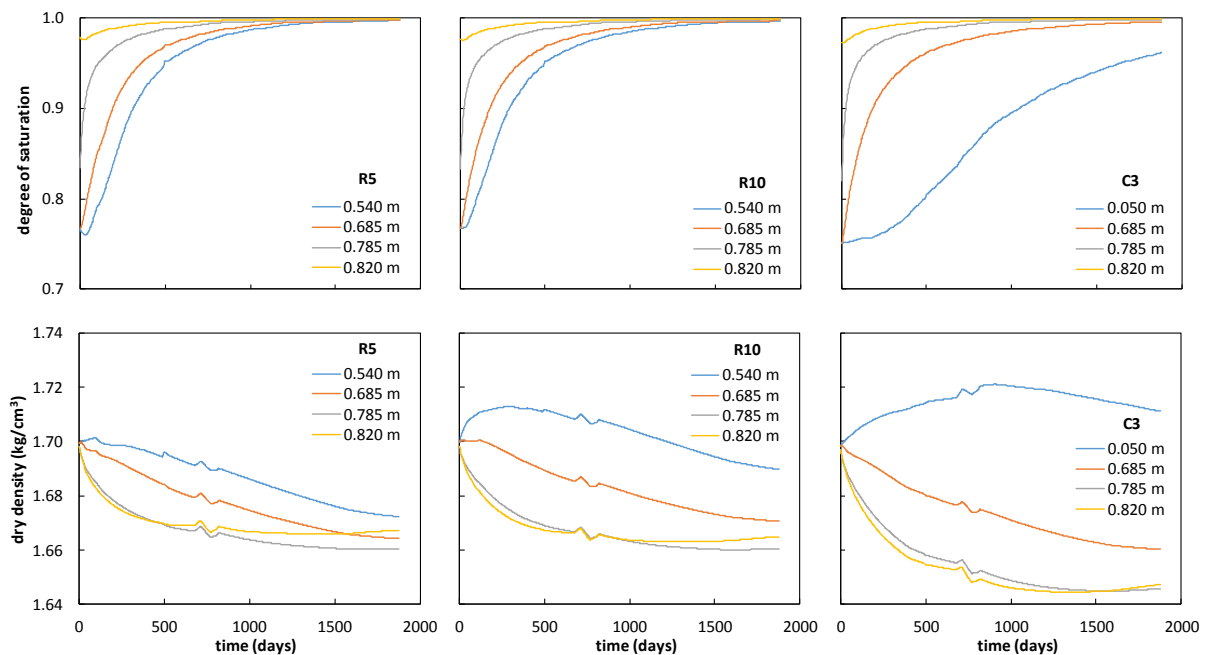


Figure 4-6: Simulated values of degree of saturation (top) and dry density (bottom) over time in three sections of the experimental domain (R5 – 2.75 m, R10 – 5.25 m, C3 – 6.25 m from the bottom) at various radial distances from the centre.

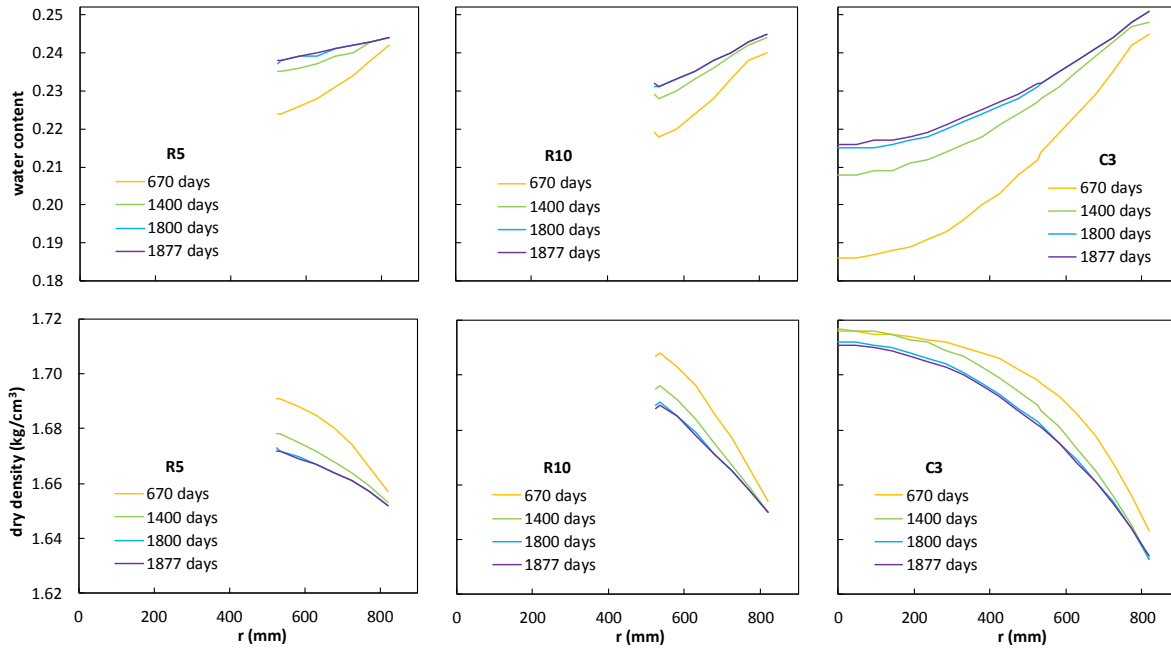


Figure 4-7: Simulated values of water content (top) and dry density (bottom) across three sections of the experimental domain (R5 – 2.75 m, R10 – 5.25 m, C3 – 6.25 m from the bottom) at various times during the simulation.

Concerning the vertical displacement recorded at the top of the domain, in response to the finite value of stiffness of the anchors, the result of the simulation shown in Figure 4-8 can be considered acceptable. However, while the magnitude of the displacement is well captured, the same cannot be said for the trend, which appears more regular in the experiments than in the simulation. The latter, in fact, shows a faster progression of the displacements initially, followed by a very slow increase. In the model, a linear spring was used; the linearity of the behaviour of the actual anchors was demonstrated by plotting the displacements together with the recorded forces. Therefore, the different trend observed in the simulation compared with the experiment must be attributed the behaviour of the bentonite (possibly to the insufficient homogenization achieved during saturation), or to simplifications (higher initial dry density of the pellet-filled gap, resulting in somewhat higher initial stiffness of the domain; absence of the inner gap between the cannister and the bentonite blocks).

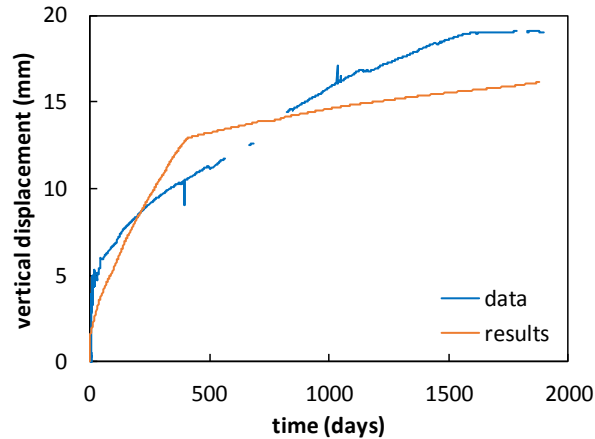


Figure 4-8: Vertical displacement at the top of the domain due to the finite value of stiffness of the anchors: experimental data vs. numerical simulation results.

In order to obtain some insight into the sensitivity of the numerical model to some of the parameters, additional simulations were carried out. In particular, it was decided to explore three values of air-entry value (s_{e0} parameter in the hypoplastic models), i.e. 1, 2.7, and 6 MPa. The intrinsic permeability of the bentonite blocks and bricks was changed in the range $0.5-10 \cdot 10^{-19} \text{ m}^2$, keeping a ratio of 10 between the (equivalent) permeability of the pellet-filled gap and that of the blocks. The stiffness of the anchors also was changed, as it was found that it can affect the convergence and success of the simulation even though it does not affect the results in terms of swelling pressures and suctions significantly. Most of the successful simulations were obtained using comparatively high values of stiffness, corresponding to very little swelling of the top cap. On the other hand, more realistic values, providing values of swelling in line with the experimental result, often resulted in numerical issues, that are being addressed in current work. An overview of all the simulations that were conducted is provided in Figure 4-9, which shows all the successful simulations (100% on the horizontal axis), as well as all the simulations that were interrupted at some point due to numerical issues.

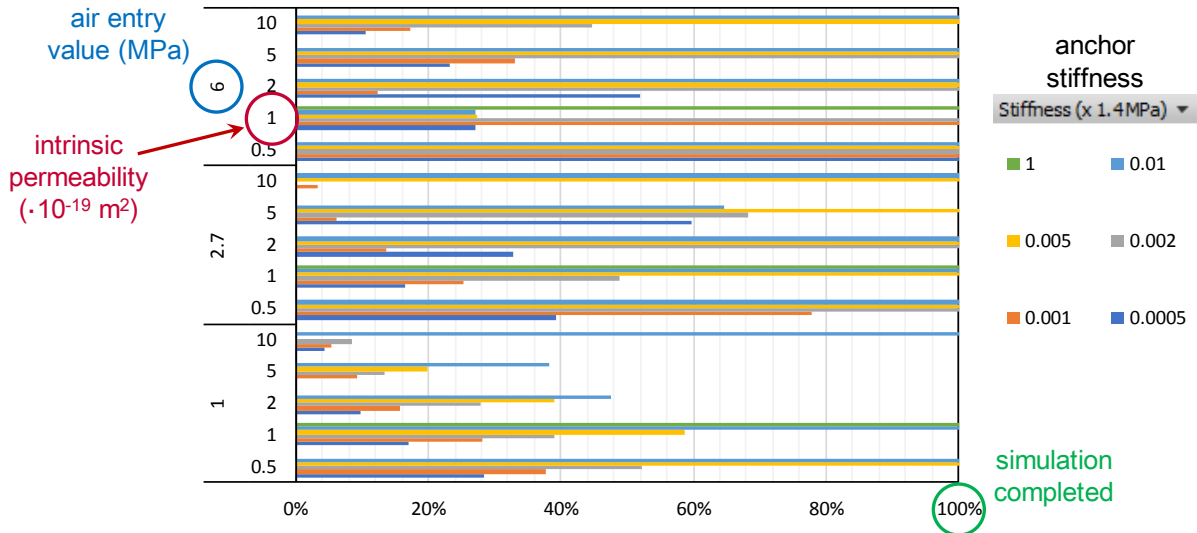


Figure 4-9: Sensitivity analyses – completed and unsuccessful simulations according to the choice of parameters.

For a quantitative comparison of the results of the various simulations, the normalised mean error (NME) and the normalised root mean square error (NRMSE) were used as the error metrics because of their simplicity:

$$NME = \frac{\frac{1}{n} \sum_i^n (S_i - E_i)}{\frac{1}{n} \sum_i^n E_i}; \quad NRMSE = \frac{\sqrt{\frac{1}{n} \sum_i^n (S_i - E_i)^2}}{\frac{1}{n} \sum_i^n E_i}$$

where S_i and E_i represent simulated and experimental values at corresponding times (i), respectively, and n is the number of experimental observations that were considered.

These error metrics were computed in relation to data series of 9 sensors: 4 swelling pressure sensors (P110, P111, U106, P119) and 5 suction sensors (W122, W123, W124, W140, W154). To obtain comprehensive metrics, the data series were combined assigning weights corresponding to their degree of completeness. For instance, if a sensor was functional during 75% of the experiment, a weight of 0.75 was assigned to the data series.

In Figure 4-10, groups of vertical bars indicate successful simulations performed with the same set of parameters except for the stiffness of the anchors, which is confirmed to not play a significant role in the investigated range. On the other hand, the figure shows that the trends of NRMSE are not monotonic with respect the intrinsic permeability, while they are less affected by the choice of air-entry value. By looking at the results in terms of NRMSE and NME comprehensively, it is possible to identify some sets of parameters that provide the best performance (smaller square error, smaller over/underestimation). It is clear, however, that there is not a unique set of parameters that optimises the simulation results both in terms of suctions and swelling pressures, and a trade-off is therefore necessary. This is the reason

why, earlier in this section, the simulation with air-entry value of 2.7 MPa and intrinsic permeability of $2 \cdot 10^{-19} \text{ m}^2$ was chosen as the representative one, even though it provides some overestimation of suctions and, in smaller proportion, also of swelling pressures. By choosing a smaller value of permeability, for instance, the error in terms of swelling pressures would have been minimised, but at the expenses of a much larger overestimation of suctions.

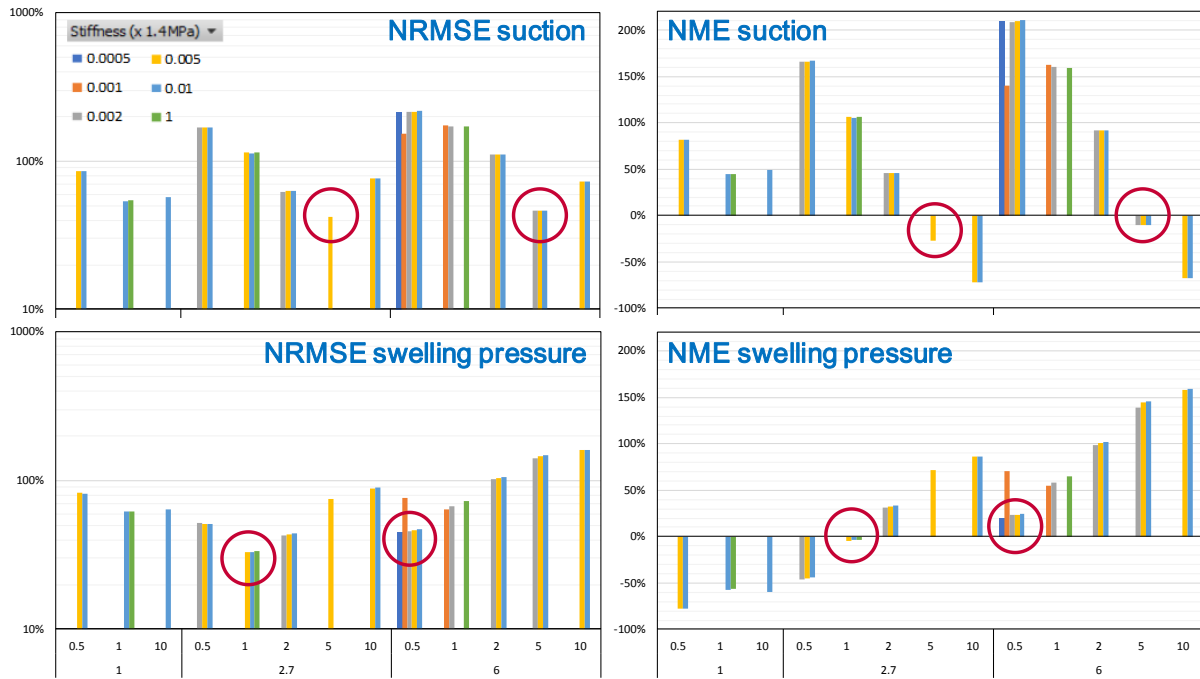


Figure 4-10: Normalised root mean square error (NRMSE) and normalised mean error (NME) relative to experimental data from suction and swelling pressure sensors for all successful simulations (100% completed, cf. Figure 4-9) as a function of the chosen air-entry value of suction (1, 2.7, 6 MPa), intrinsic permeability ($0.5-10 \cdot 10^{-19} \text{ m}^2$), and anchor stiffness (0.0005–1.4 MPa). Red circles indicate the simulation or group of simulations with the lowest NRMSE or NME values.

4.3 ClayTechnology – Code_Bright

The canister retrieval test (CRT) is simulated using the finite-element software Code_Bright, v. 5_2 (see e.g., Alcoverro and Alonso 2001). Since the same model was used within SKB's EBS Task Force only a short description of the model is included here; a more detailed description is given by Kristensson (2019a).

4.3.1 Geometry and discretization

The CRT geometry is assumed to be axisymmetric (see Figure 4-11 for dimensions and discretization). This means that the impact of the adjacent Temperature Buffer Test (TBT) is not accounted for in the simulations. Furthermore, the geometrical representation of the retaining system (R1, R2, and R3) has been simplified.

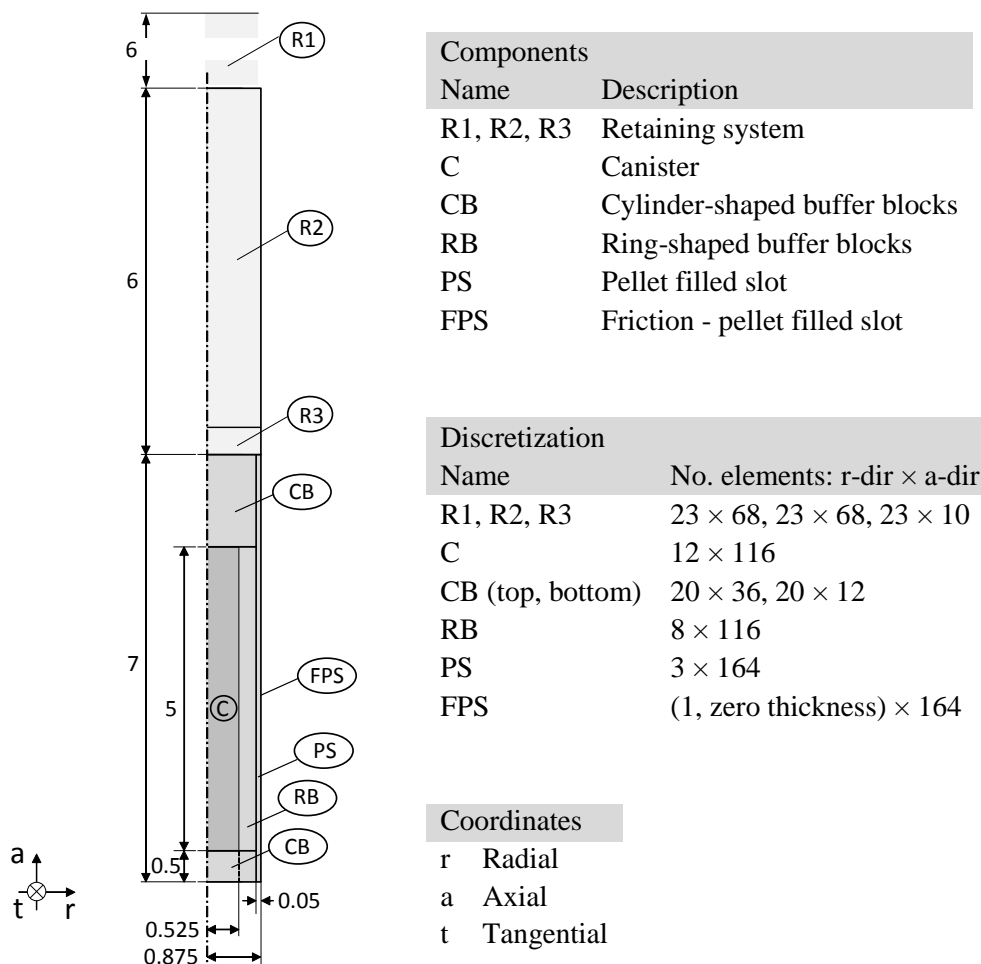


Figure 4-11. Illustration of the numerical model (dimensions in metres).

4.3.2 Input parameters

Porous media

The water retention is given by van Genuchten's law

$$S_l = \left(1 + \left(\frac{p_g - p_l}{P_0} \right)^{\frac{1}{1-\lambda}} \right)^{-\lambda}$$

where S_l is the degree of liquid saturation, p_g is the gas pore pressure, p_l is the liquid pore pressure, and p_0 and λ are either constants (p_0^* and λ^*) or porosity-dependent expressions ($p_0(\phi)$ and $\lambda(\phi)$). In the latter case, the expressions for p_0 and λ are given by

$$P_0(\phi) = P_0^* \exp(a(\phi_0 - \phi)),$$

$$\lambda(\phi) = \lambda^* \exp(b(\phi_0 - \phi)).$$

p_0^* , λ^* , a , b and ϕ_0 are parameters. The parameter values for each component are given in Table 4-5.

Table 4-5. Retention related variables.

Component	p_0^* [MPa]	λ^* [MPa]	a [-]	b [-]	ϕ_0 [-]
R1, R2, R3	0.518	0.26	-	-	-
C	37.27	0.2	-	-	-
CB	17.665	0.2	25.579	2.187	0.389
RB	37.475	0.2	25.579	1.419	0.359
PS	0.518	0.26	15.326	1.011	0.64
FPS	0.518	0.26	-	-	-

The advective mass flow is governed by Darcy's law. Input to Code_Bright is given by the intrinsic permeability (k), which is assumed to be isotropic and either constant or dependent on the porosity (ϕ), and the relative permeability (k_{rl}), which depends on the on the degree of liquid saturation according to S_l^n . Parameter values for each component are presented in Table 4-6.

Table 4-6. Darcy's law, intrinsic permeability and exponent in the law for the relative permeability

Component	k [m ²]	n [-]
R1, R2, R3	$2.18 \cdot 10^{-23}$	3
C	$2.18 \cdot 10^{-21}$	
CB	$1.8 \cdot 10^{-20} \exp(21.764(\phi - 0.5))$	4
RB		
PS	$0.72 \cdot 10^{-20} \exp(21.764(\phi - 0.5))$	-2
FPS		

The diffusive mass flow is governed by Fick's law. Input to Code_Bright is given by the tortuosity (τ_0), which is assumed to be constant. A parameter value of $\tau_0 = 0.5$ has been used for the block materials (CB, RB) and $\tau_0 = 1$ elsewhere.

The conductive heat flux is governed by Fourier's law. Input to Code_Bright is given by the thermal conductivity (λ), which, for the purpose of this study, is assumed to be constant (see Kristensson 2019a). Parameter values for each component are given Table 4-7.

Table 4-7. Fourier's law, thermal conductivity.

Component	λ [W/m·K]
R1, R2	1000
R3	3
C	390
CB	1
RB	1
PS	1
FPS	1000

Solid phase relations

Input parameters for the solid phase are the density (ρ_{s0}) and the specific heat capacity (c_s), which both are assumed to be constant. Parameter values for each component are given in Table 4-8.

Table 4-8. Solid phase parameters, mass density and specific heat capacity.

Component	ρ_{s0} [kg/m ³]	c_s [J/kg·K]
R1, R2	10	10
R3	2400	770
C	8000	450
CB	2780	800
RB		
PS		
FPS	1000	1000

In total, four different mechanical material models have been used in the simulation:

- The retaining system (R1, R2 and R3) is assumed to respond according to a bilinear elastic model. The parameter values are presented in Table 4-9.
- The canister (C) is assumed to respond as linear elastic materials. The parameter values are given in Table 4-10.
- The blocks and pellet-filled slot (CB, RB and PS) are assumed to respond according to a modified version of the Barcelona Basic Model (BBM).

- The parameter values are presented in Table 4-11.
- The simulated interface between the pellet filled slot and the deposition hole walls (FPS) is assumed to respond as an elastic-viscoplastic material. The parameter values are presented in Table 4-12.

Table 4-9. Parameter values for the bilinear model.

Parameter	Component: R1	Component: R2, R3
E_0 [MPa]	$380.5 \cdot 10^{-3}$	380.5
E_C [MPa]	$1141.6 \cdot 10^3$	1141.6
ε_v^{limit}	0.002167	0.001503
ν	0.001	0.001

Table 4-10. Parameter values for the linear elastic model.

Component	E [GPa]	ν [-]
C	100	0.2

Table 4-11. Parameter values for the modified BBM model.

Parameter	Components		
	CB	RB	PS
e_0	0.636	0.56	1.78
K_{ij}		0.13	0.15
α_{ij}		-0.021	0
ν		0.2	0.2
K_{min} [MPa]		20	2
α		0.5	0.5
ρ_0^* [MPa]		16.9	0.242
ρ_c [MPa]		1	1
λ_0		0.184	0.243
ρ_s [MPa]		2.5	0.05
K_{s0}		0.34	0.2
ρ_{ref} [MPa]		1	0.1
α_{ss} [MPa ⁻¹]		-0.007	0

Table 4-12. Parameter values for the elastic-viscoplastic interface model.

Parameter	Component: FPS
m [MPa]	100
α_{min} [MPa]	10^{-4}
K_s [MPa/m]	100
Γ [m/(MPa·s)]	10^{-3}
N [-]	1
ϕ_0 [°]	10
c_0 [MPa]	10^{-6}
u_c^* [m]	10^3

Liquid phase relations

The liquid phase is equal to liquid water. The relations and parameter values

for the mass density, viscosity and specific heat capacity as specified by default in Code_Bright are used in the present modelling work.

Gas phase relations

The gas phase is considered an ideal gas mixture with a constant gas pore pressure (p_g) of 0.1 MPa. The relations and parameters for the vapour pressure, air density, specific latent heat and specific heat capacity as specified by default in Code_Bright are used in the present modelling work.

4.3.3 Initial and boundary conditions

Initial conditions

Initial parameter values are required for porosity, temperature, liquid pore pressure, and state of stress:

- The porosity of the retaining system (R1, R2, R3) is set at 10%.
- The porosity of the canister (C) is set at 0.01%.
- The porosity of the cylinder-shaped buffer blocks (CB) is set at 38.9%.
- The porosity of the ring-shaped buffer blocks (RB) is set at 35.9%.
- The porosity of the pellet filled gap and interface (PS, FPS) is set at 64%.
- The liquid pore pressure is set at -47.174 in all components.
- The initial temperature is set at 15°C in all components.
- An isotropic total stress of -0.11 MPa is assigned to all components.

Boundary conditions

The boundary conditions can be summarized as follows:

- The temperature (T) is 15°C with a heat transfer coefficient (γ) of 1 W/°C along the entire boundary.
- The flow of liquid water (j_l^w) is 0 kg/(m²·s) along the entire boundary except parts that belong to the interface (FPS).

The liquid pore pressure (p_l)/liquid flux (j_l^w) is prescribed according to

- Table 4-13 along the boundary belonging to the interface (FPS).
- Roller conditions are assigned along the entire boundary except parts that belong to the interface (FPS).
- Zero displacements are assigned to the boundary belonging to the interface (FPS).

Table 4-13. Hydraulic boundary conditions assigned to the interface (FPS).

Time interval [days]	Condition	Comment
[0-1]	$p_l = -47.174 + t(46.949)$ MPa	Mimicking a rapid initial water filling of the pellet filled slot.
(1-5]	$p_l = 0.1$ MPa	According to filter pressure protocol.
(5- t^*]	$p_l = 0.1$ MPa	According to filter pressure protocol. t^* is the time at which 260 l of water have been added through the filters.
(t^* -680]	$j_l^w = 0$	Trying to incorporate the effect of filter clogging.
(680-1825]	$p_l = 0.9$ MPa	According to filter pressure protocol.

Body conditions

The thermal load (a constant power of 2 kW) is distributed over the nodes on the canister axis. This is a simplification compared with the actual power evolution (Goudarzi et al. 2006) and used here to obtain a temperature field of “proper magnitude giving rise to reasonable effects” (see Kristensson 2019a).

The retaining system (R1, R2, R3) is prescribed a constant temperature of 15°C.

Liquid pore pressure is prescribed according to

Table 4-13 in the pellet slot (PS) and in the interface (FPS) during the time interval 0-1 days.

4.3.4 Results/discussion

Requested output include the temporal evolution of the temperature, total pressure, suction, dry density and degree of saturation (cf.

Table 4-14) as well as the distribution of the water content and dry density in Ring 5, Ring 10 and Cylinder 3 after 670 days, 1400 days, 1800 days and 1910 days. Comparisons between model results and available measurements are presented in the sections below.

Table 4-14. Request output, locations in the model and available sensors used for comparison with modelling results

Section	Type	Location in model* (r [m], z [m])	Sensor IDs
Ring 5	Temperature	0.635, 2.84 0.685, 2.84 0.735, 2.84	T111 (Ring5\A\635) T121 (Ring5\D\685) T112 (Ring5\A\735)
	Total pressure	0.585, 2.84 0.685, 2.84 0.785, 2.84	P110 (Ring5\A\585) P111 (Ring5\A\685) U106 (Ring5\A\785)
	Suction	0.585, 2.84 0.685, 2.84 0.785, 2.84	W122 (Ring5\A\585) W123 (Ring5\A\685) W124 (Ring5\A\785)
	Dry density	0.540, 2.84 0.685, 2.84 0.785, 2.84 0.8475, 2.84	No sensor data available
	Degree of saturation	0.540, 2.84 0.685, 2.84 0.785, 2.84 0.8475, 2.84	No sensor data available
Ring 10	Temperature	0.685, 5.5	T127 (Ring10\D\685)
	Total pressure	0.685, 5.5	P119 (Ring10\A\685)
	Suction	0.685, 5.5	W140 (Ring10\A\685)
	Dry density	0.540, 5.5 0.685, 5.5 0.785, 5.5 0.8475, 5.5	No sensor data available
	Degree of saturation	0.540, 5.5 0.685, 5.5 0.785, 5.5 0.8475, 5.5	No sensor data available
Cylinder 3	Temperature	0.785, 6.3	T129 (Cyl.3\A\785)
	Total pressure	0.50, 6.3	P125 (Cyl.3\center\50)
	Suction	0.585, 6.3	W154 (Cyl.3\C\585)
	Dry density	0.50, 6.3 0.685, 6.3 0.785, 6.3 0.8475, 6.3	No sensor data available
	Degree of saturation	0.50, 6.3 0.685, 6.3 0.785, 6.3 0.8475, 6.3	No sensor data available

* Location is given in terms of the radial distance from the symmetry axis, r , and the vertical distance, z , measured from the hole bottom (cf. Figure 4-11). The z -values for Ring 5 and Cylinder 3 are in accordance with those given by Talandier (2018) and the z -value for Ring 10 corresponds to the top of the canister in the model.

Temperature evolution

The temperature evolutions at the selected points are presented in Figure 4-12. As expected, given the simplified canister power evolution and

assumption of constant thermal conductivity, neither the quantitative nor the qualitative agreement between modelled and measured temperatures is very good. However, the simulated temperature are of “proper magnitude” as was the intention (cf. Kristensson 2019a).

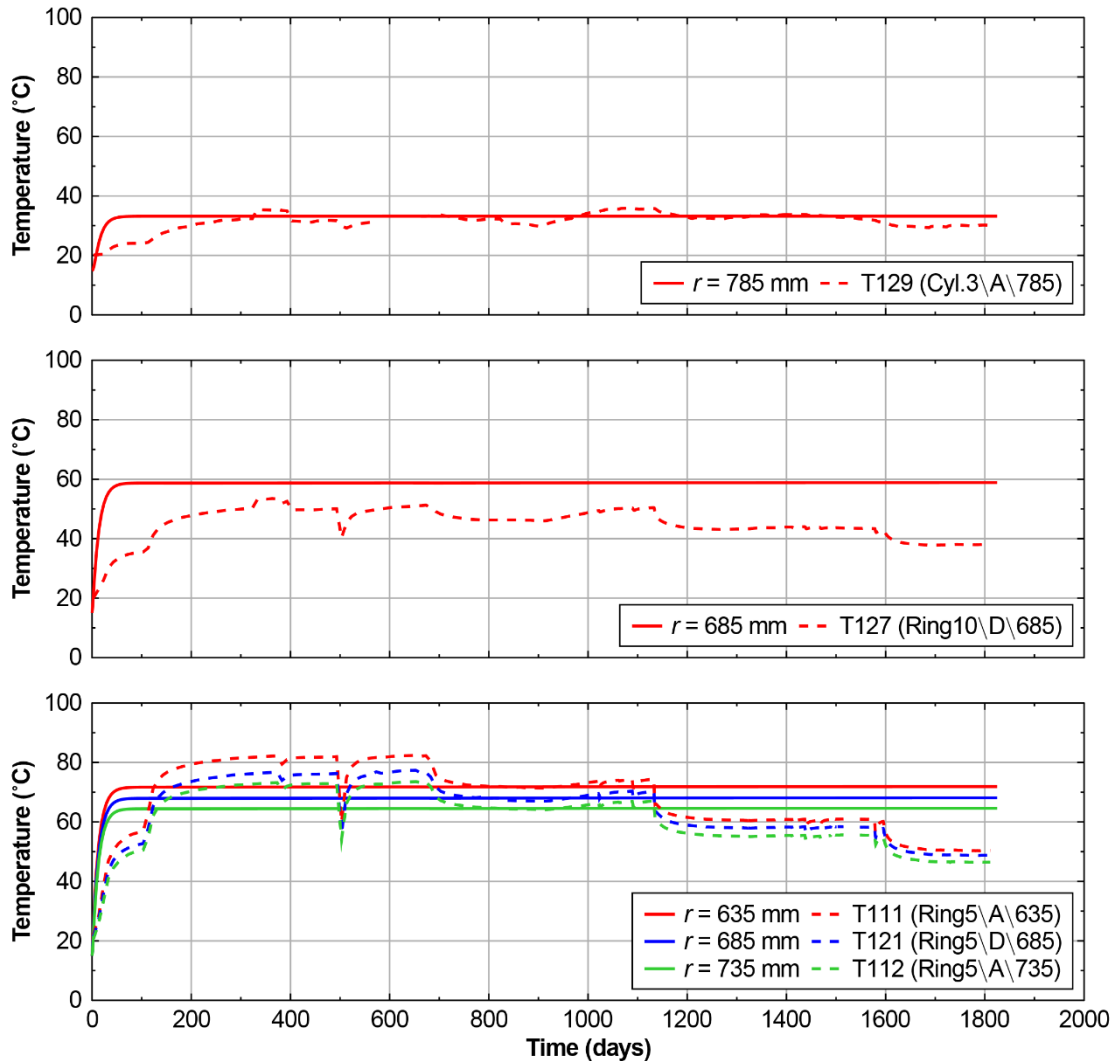


Figure 4-12. Comparison between simulated (solid lines) and measured (dashed lines) temperatures in Cylinder 3 (top), Ring 10 (middle) and Ring 5 (bottom).

Total pressure evolution

The total stress (here axial stress) evolutions at the selected points are presented in Figure 4-13. Similar to the temperatures (see above), the agreement between modelled and measured stress is not very good; the model overestimates the stress at all studied positions. However, the overestimate is only a few MPa and can be considered reasonable given the simplifications in the model.

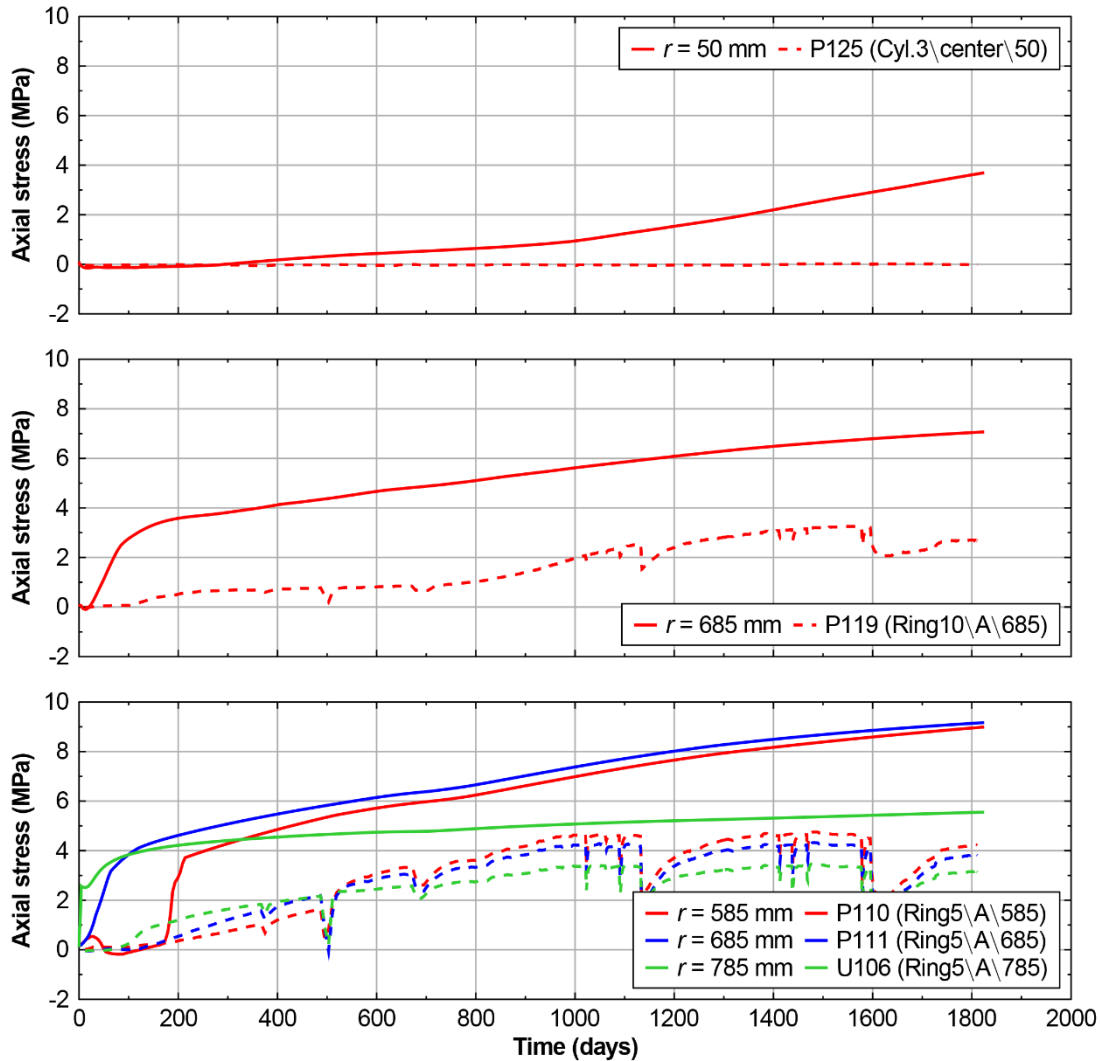


Figure 4-13. Comparison between simulated (solid lines) and measured (dashed lines) axial stress in Cylinder 3 (top), Ring 10 (middle) and Ring 5 (bottom).

Suction evolution

Figure 4-14 shows a comparison between the measured and simulated suction evolutions at the selected points. Here, the suction is computed from model results using

$$s = 0.1 - p_l$$

where p_l is the liquid pore pressure. The agreement between the measurements and model results is generally poor. It should, however, be noted that the sensors can only record suctions that are less than 5 MPa (cf. Talandier 2018) whereas the simulated suctions are significantly larger at the majority of the studied locations.

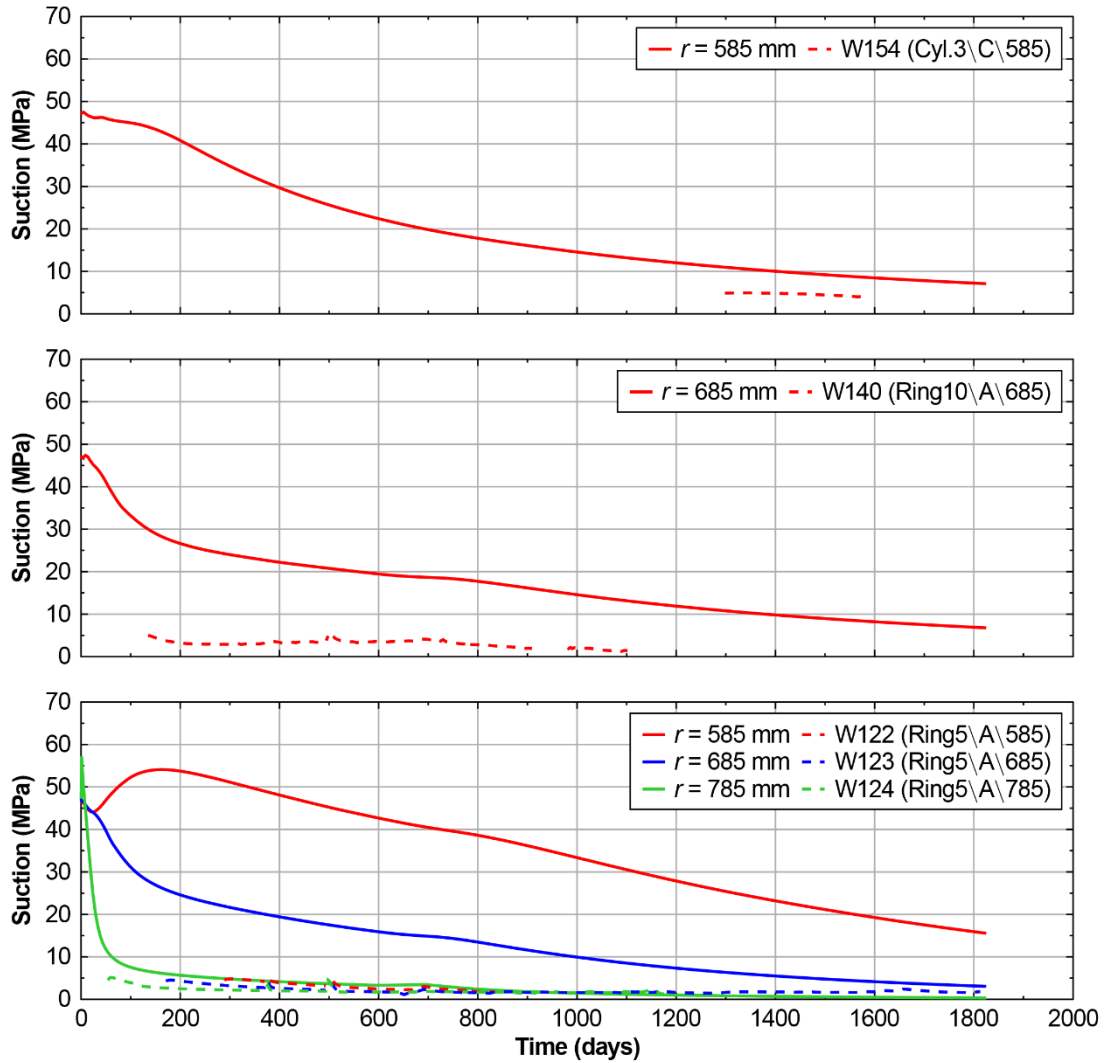


Figure 4-14. Comparison between simulated (solid lines) and measured (dashed lines) suction in Cylinder 3 (top), Ring 10 (middle) and Ring 5 (bottom).

Dry density evolution

Figure 4-15 shows the simulated evolution of the dry density at the selected points. Here, the dry density is computed from model results using

$$\rho_d = \rho_s(1 - \phi) \quad (4-1)$$

where ϕ is the porosity and ρ_s is the particle density (see Table 4-8).

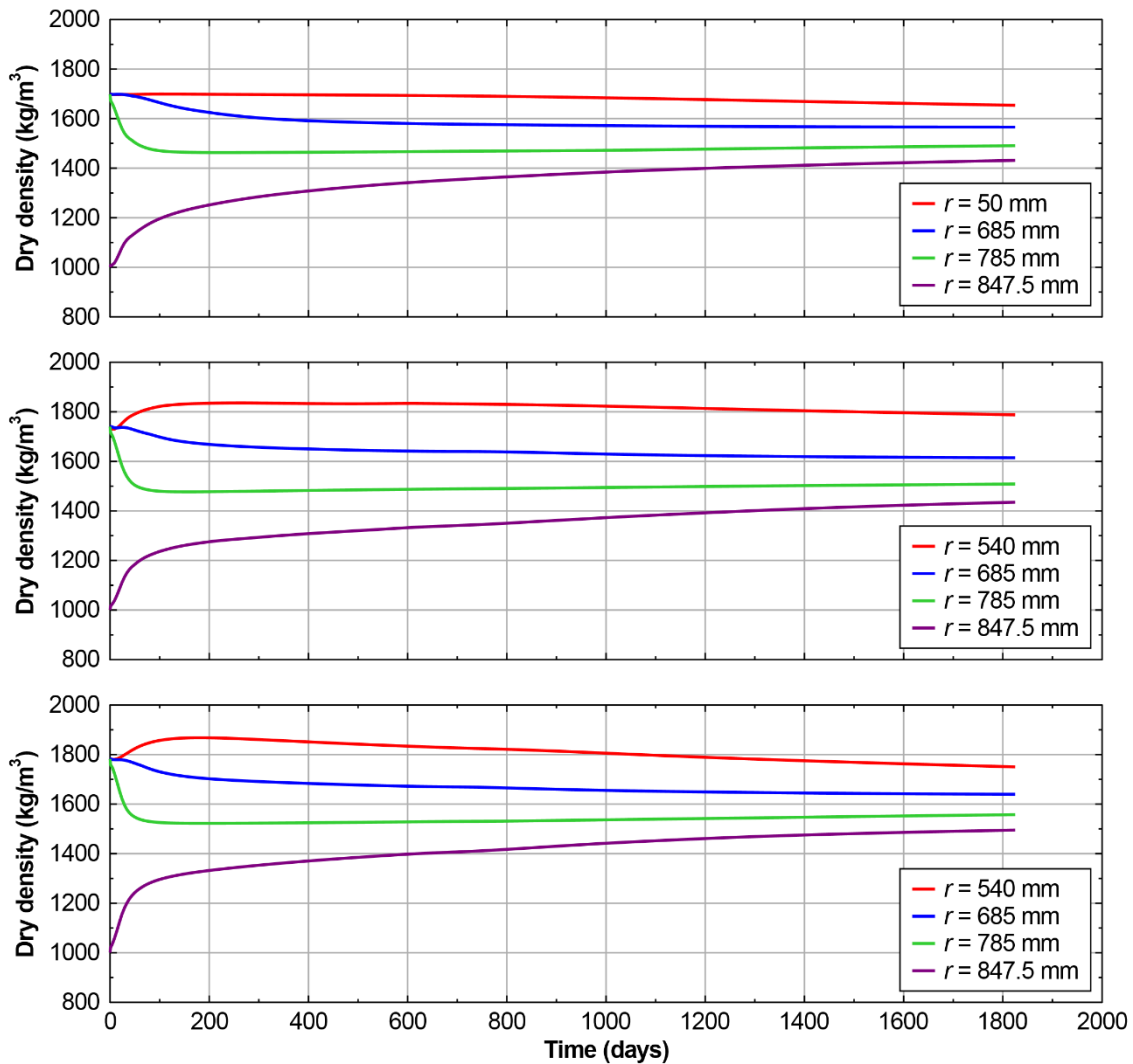


Figure 4-15. Simulated temporal development of the dry density in Cylinder 3 (top), Ring 10 (middle) and Ring 5 (bottom).

Degree of saturation evolution

Figure 4-16 shows the simulated evolution of the degree of saturation at the selected points.

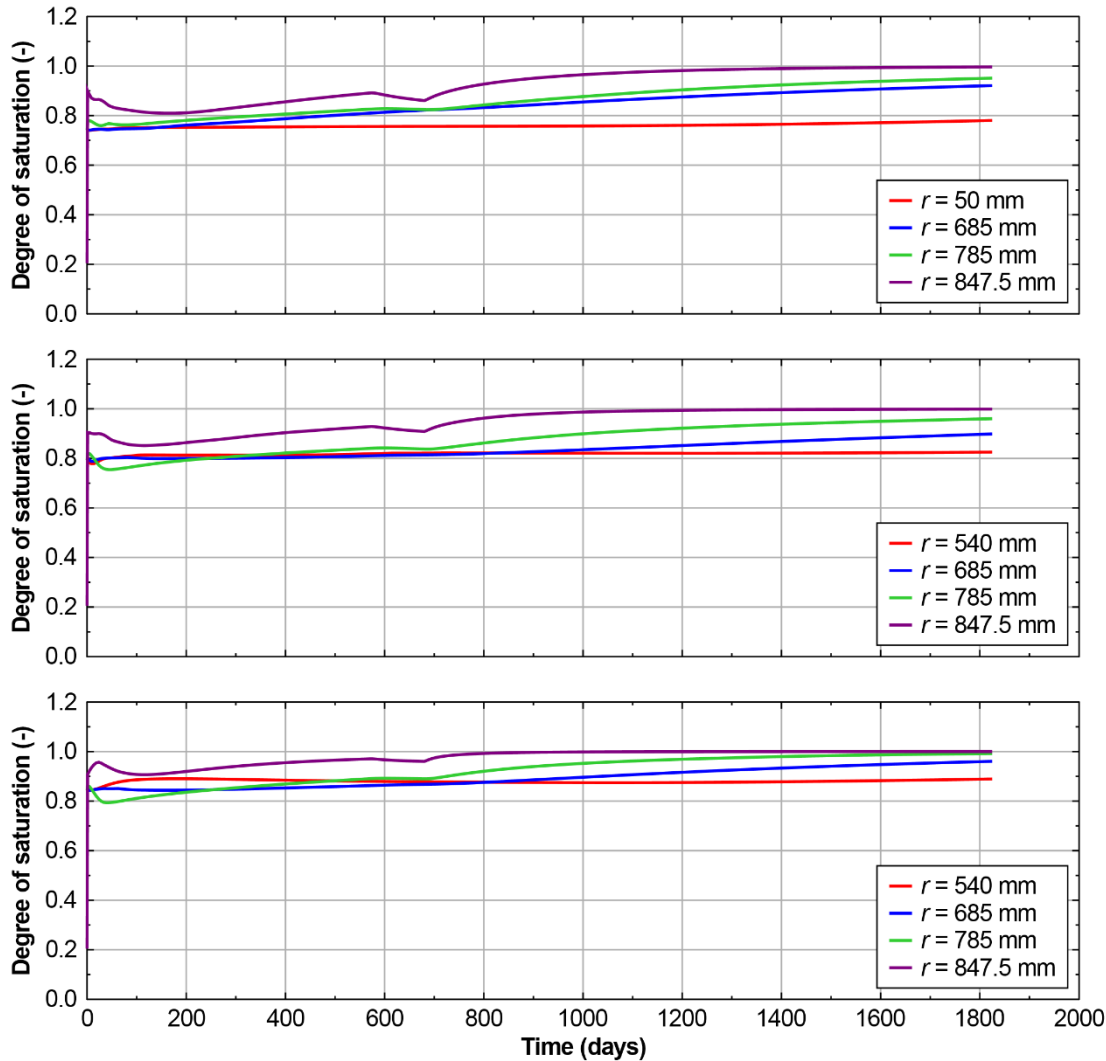


Figure 4-16. Simulated temporal development of the degree of saturation in Cylinder 3 (top), Ring 10 (middle) and Ring 5 (bottom).

Profiles of water content and dry density

Profiles of the water content and dry density at different times are presented in Figure 4-17 and Figure 4-18, respectively. Here, “water content” refers to the gravimetric water content, w , which can be computed from model results using

$$w = S_i \rho_w \left(\frac{1}{\rho_d} - \frac{1}{\rho_s} \right)$$

where S_i is the degree of saturation, ρ_w is the density of water, ρ_d is the dry density (Eq. 4-1) and ρ_s is the particle density (see Table 4-8). Note that the model does not include the cooling phase after the heater was switched off. Therefore, results are only presented for until day ~1800.

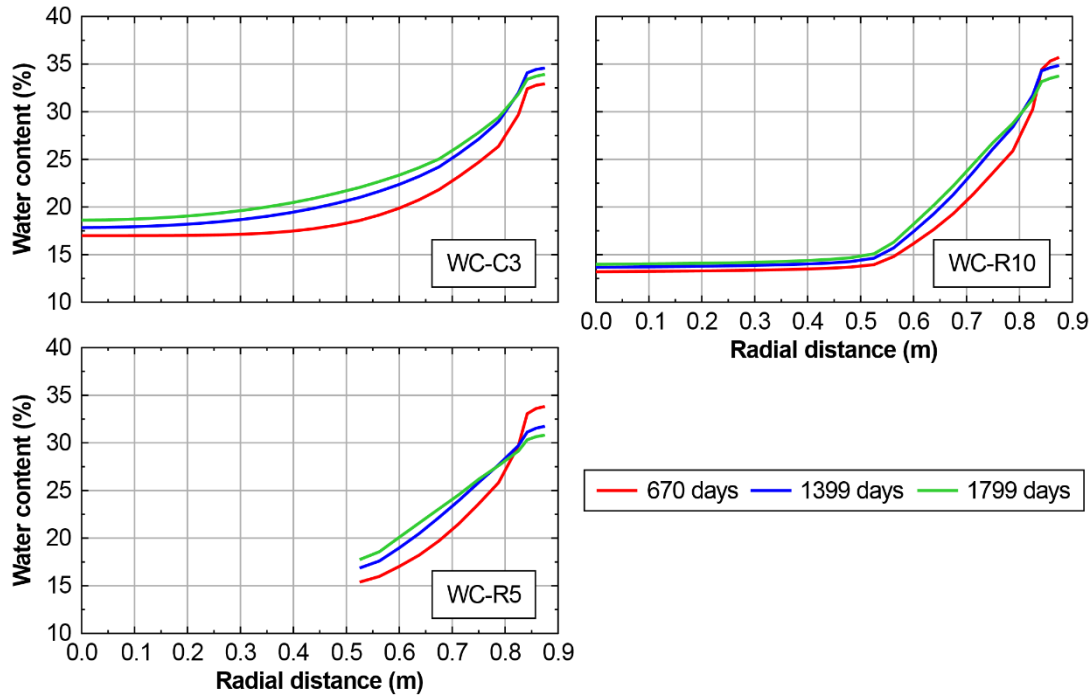


Figure 4-17. Profiles of the simulated water content after 670 days, 1399 days and 1799 days in Cylinder 3 (top left), Ring 10 (top right) and Ring 5 (bottom left).

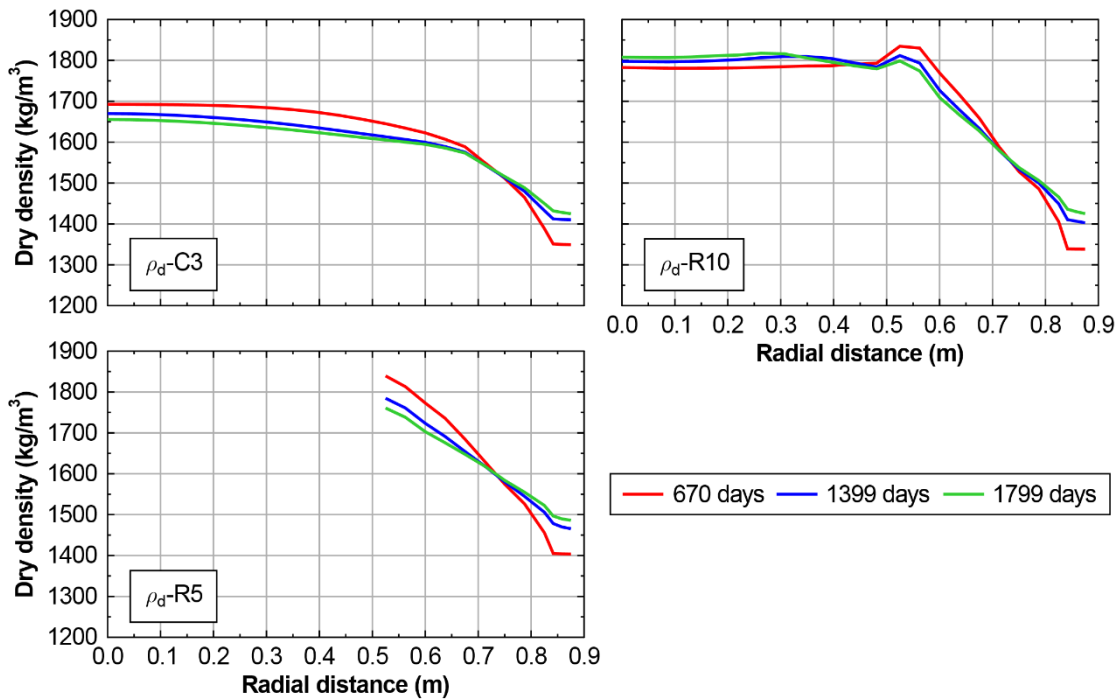


Figure 4-18. Profiles of the simulated dry density after 670 days, 1399 days and 1799 days in Cylinder 3 (top left), Ring 10 (top right) and Ring 5 (bottom left).

4.4 ICL

4.4.1 Geometry and discretization

An axis-symmetric analysis was performed to simulate the Canister Retrieval Test (CRT) experiment, which consisted of a heater placed in a vertical deposition hole and surrounded by compacted MX-80 bentonite. A detail of the finite element mesh, representing the 8.61m depth and 0.875m diameter of the deposition hole, is shown in Figure 4-19. The full mesh extends 11.4m below the base concrete plate and 10m above the 'void' in the z-coordinate direction, and 30m in the x-direction. It consists of 10980 8-noded quadrilateral elements and the z-direction is the axis of symmetry. As the analysis is thermo-hydro-mechanically coupled, pore pressure degrees of freedom are adopted at the corner nodes, while displacement and temperature degrees of freedom are adopted at all nodes of each element.

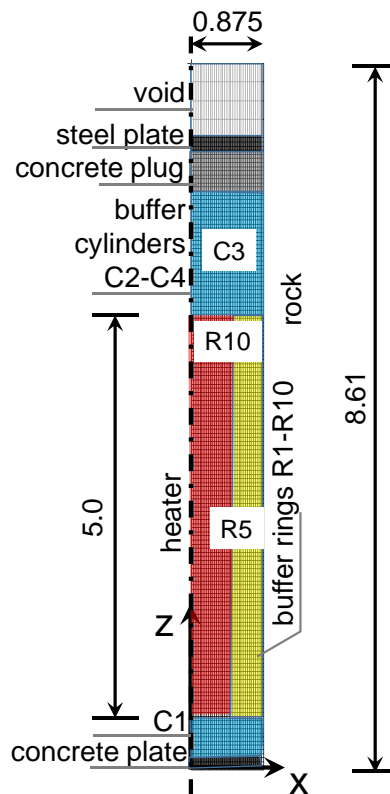


Figure 4-19 Detail of the finite element mesh for CRT experiment

The x-direction of the mesh is discretised with 35 elements from the axis of symmetry to the deposition hole radius at 0.875 m, which results in the smallest element dimension of 0.025m in the buffer, in particular at the locality between the heater and the rock. The radius of the heater is 0.525 m. The compacted bentonite of the buffer was placed in rings R1 to R10 and cylinders C1 to C4, as shown in Figure 4.1. A 0.061m vertical slot between the buffer and the rock was filled with the MX-80 pellet bentonite.

4.4.2 Input parameters

MX-80 bentonite buffer

The hydro-mechanical behaviour of the MX-80 bentonite was represented with the ICDSM constitutive models introduced in Section 2.5. The model parameters for the mechanical ICDSM model were derived from the experimental data sourced in SKB reports TR-10-55 (Dueck & Nilsson, 2010) and TR-14-19 (Kristensson & Borgesson, 2015), Marcial et al. (2008), Seiphoori et al. (2014).

The input parameters for the mechanical ICDSM model are summarised in Table 4-15.

Table 4-15 *Input parameters for the ICDSM for MX-80 bentonite*

Parameter	Value
Parameters controlling the shape of the yield surface, α_f, μ_f	0.4 , 0.9
Parameters controlling the shape of the plastic potential surface, α_g, μ_g	0.4 , 0.9
Strength parameters, M_f, M_g	0.5
Characteristic pressure, p_c (kPa)	1000
Fully saturated compressibility coefficient, $\lambda(0)$	0.25
Elastic compressibility coefficient, κ	0.08
Maximum soil stiffness parameter, r	0.61
Soil stiffness increase parameter, β (1/kPa)	0.00007
Elastic compressibility coefficient for changes in suction, κ_s (kPa)	0.06
Poisson ratio, ν	0.4
Plastic compressibility coefficient for changes in suction, λ_s	0.5
Air-entry value of suction, s_{air} (kPa)	1400
Yield value of equivalent suction, s_0 (kPa)	10^6
Cohesion increase parameter, k Constant or S_r	S_r
Microstructural compressibility parameter, κ_m	0.18
Void factor, VF	0.4
Coefficients for the micro swelling function, c_{s1}, c_{s2}, c_{s3}	0.0001, 1.1, 2.0
Coefficients for the micro compression function, c_{c1}, c_{c2}, c_{c3}	0.0001, 1.1, 2.0

The input parameters for the soil water retention (SWR) model are summarised in Table 4-16 and calibrated SWR curve is shown in Figure 4-20.

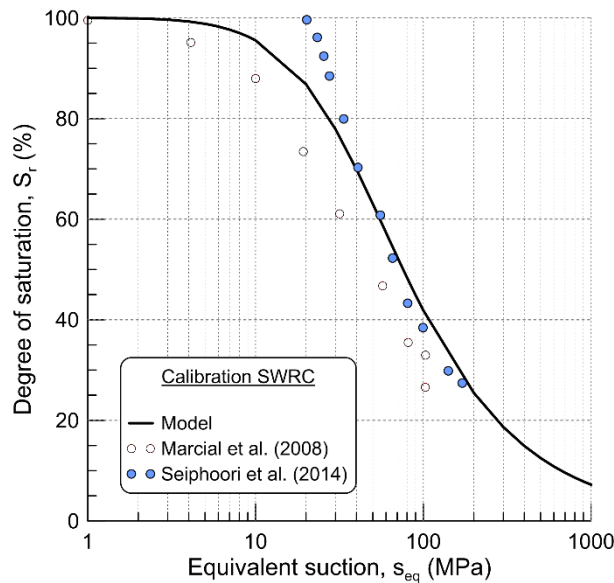


Figure 4-20 Calibrated SWR curve for compacted MX-80 bentonite

Table 4-16 Input parameters for the SWR model for MX-80 bentonite

Parameter	Value
Air entry suction, s_{air} [kPa]	1400
Fitting parameter, α	0.000095
Fitting parameter, n	1.6
Fitting parameter, m	0.5
Effect of specific volume, ψ	2
Residual degree of saturation, S_{r0}	0

The variable permeability (hydraulic conductivity) model, depicted in Figure 2-2, adopts parameters summarised in Table 4-17.

Table 4-17 Input parameters for the variable permeability model for MX-80 bentonite

Parameter	Value
Saturated permeability, k_{sat} [m/s]	$1 \cdot 10^{-13}$
Minimum permeability, k_{min} [m/s]	$0.8 \cdot 10^{-14}$
Suction, p_1 [kPa]	1400
Suction, p_2 [kPa]	20000

The thermal characteristics of the compacted MX-80 bentonite are prescribed as thermal conductivity of $0.9 \cdot 10^{-3}$ kW/mK, a specific heat capacity of the solid phase of 870 J/kgK and a thermal expansion coefficient of $6.5 \cdot 10^{-6}$ K⁻¹.

Host rock

The host rock was simulated with a similar set of parameters as derived for the host rock in the Febex experiment (Section 5.2), as more information was available for the latter. Its mechanical behaviour is simulated with an unsaturated Mohr-Coulomb model. A purely cohesive behaviour was assumed, hence the angle of shearing resistance, $\phi = 0$, while the cohesion is set at $c = 10$ MPa.

The hydraulic conductivity is taken as constant and equal to 10^{-12} m/s. It has been further assumed that the source of water for the buffer hydration was unlimited, hence the rock is modelled as saturated at all times, by prescribing a high $s_{air} = 150$ MPa in the SWR model (Table 4-18), adopted from the simulation of the Febex experiment.

Table 4-18 Input parameters for the SWR model for rock

Parameter	Value
Air entry suction, s_{air} [MPa]	150
Fitting parameter, α	0.4
Fitting parameter, n	0.9
Fitting parameter, m	0.2
Residual degree of saturation, S_{r0}	0.2

The thermal properties of the rock are a value of $3.2 \cdot 10^{-3}$ kW/mK for the thermal conductivity, 920 J/kgK for the specific heat capacity and $8 \cdot 10^{-6}$ K⁻¹ for the coefficient of thermal expansion.

4.4.3 Initial and boundary conditions

The finite element analysis of the CRT experiment is initialised with the host rock being the only material in the entire finite element mesh. The initial state of the rock is assumed saturated, with isotropic initial total stresses of 30 MPa, pore water pressure of 4.2 MPa, void ratio of 0.6, density of 2.6 g/cm³ and temperature of 20° C.

The subsequent steps of the analysis simulate excavation of the deposition hole, placement of the buffer, heater, concrete plug and steel plate at the top of the buffer arrangement. Anchoring of the steel plate into the rock was

not explicitly modelled, instead the appropriate force was applied at the top of the steel plate. The key stages are summarised in Table 4-19.

Upon construction, the state of the buffer is initialised with a suction $s = 40$ MPa, temperature $T = 20^\circ\text{C}$, water content $w = 17\%$, dry density $\rho_d = 1.75\text{ g/cm}^3$, degree of saturation, $S_r = 70\%$ and void ratio $e = 0.66$, as an average input for all compacted blocks.

Table 4-19 Key stages of the CRT analysis

Stage number	Brief description	Start time (day)	Duration (days)
1	Deposition hole excavation	-60	30
2	Buffer and heater construction	-32	30
3	Temperature increase in the heater from $T_{init} = 20^\circ\text{C}$ to $T_{final} = 100^\circ\text{C}$	0	110
4	Operation of the test at $T = 100^\circ\text{C}$ with two short cycles of $\Delta T = \mp 40^\circ\text{C}$	111	683
5	$\Delta T = -15^\circ\text{C}$, followed by operation of the test at $T = 85^\circ\text{C}$	684	1133
6	$\Delta T = -15^\circ\text{C}$, followed by operation of the test at $T = 70^\circ\text{C}$	1134	1595
7	$\Delta T = -10^\circ\text{C}$, followed by operation of the test at $T = 60^\circ\text{C}$	1596	1810

4.4.4 Results/discussion

A selection of the results is presented in this report to compare the calculated evolution of the buffer's thermo-hydro-mechanical evolution over the 5 years of the experiment, against the available field measurements. With reference to Figure 4.1, the measurement locations are in the buffer rings R5 and R10, located in the middle and at the top of the column of compacted MX-80 bentonite rings placed around the heater, and in the buffer cylinder C3, being in the middle of the stack of compacted MX-80 cylinders placed above the heater.

Figure 4-21 depicts the temperature evolution in the buffer. Three measurement points are shown for the buffer ring R5, which are located at the same elevation in the z-direction and at radial distances of 0.635, 0.685 and 0.735 m from the axis of symmetry (see Figure 4-19). The measurements indicate a temperature gradient across the thickness of the ring, with higher temperature recorded in the sensor closer to the heater (0.635 m) and around 10°C lower temperature in the sensor furthest from the heater (0.735 m). It is reminded that the heater/buffer interface and the buffer/rock interface are

at 0.525 m and 0.875 m at this locality, respectively, from the axis of symmetry. The numerical model (curves marked with 'res' in Figure 4-21) captures very well both the temperature evolution in R5, as well as the temperature gradient across the buffer thickness at this locality.

Temperature measurements in ring R10 and cylinder C3 provide further evidence of the temperature field evolution in the buffer, showing large temperature reduction with increased distance from the heater. The sensor C3-785 is located 0.75 m above the heater. The numerical model captures very well both the temperature evolution at sensors R10-685 and C3-785 and the development of the overall temperature field in the buffer.

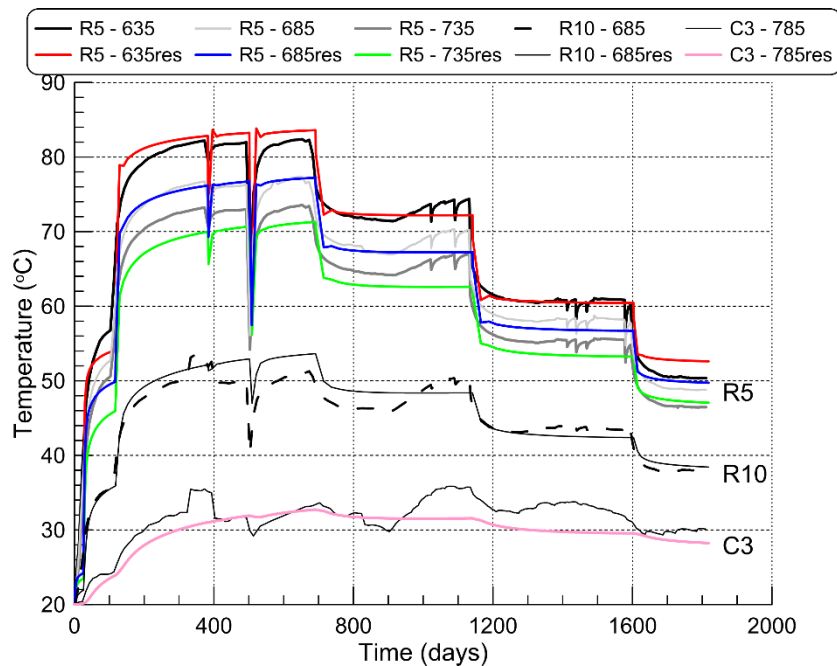


Figure 4-21 Measured and calculated temperature evolution in the buffer during CRT experiment ('res' stands for numerical results)

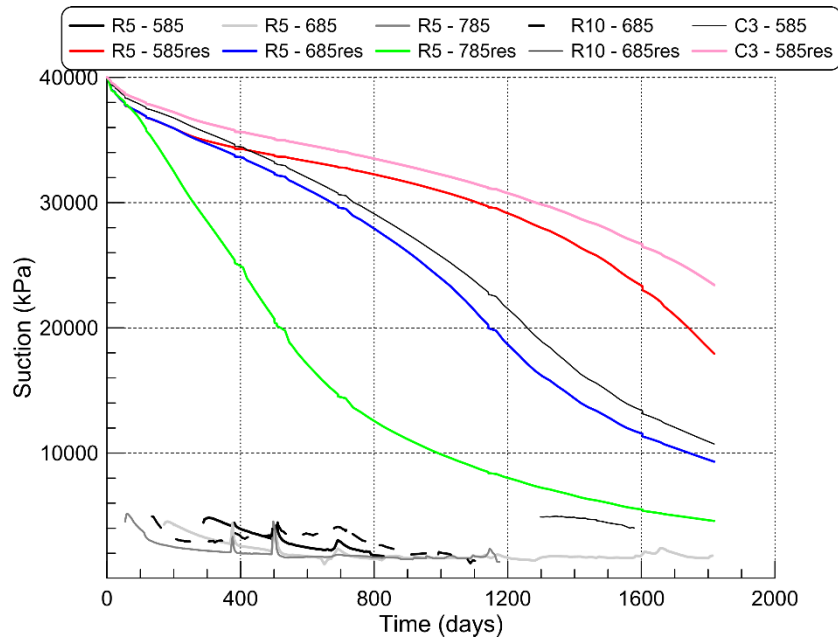


Figure 4-22 Measured and calculated suction evolution in the buffer during CRT experiment ('res' stands for numerical results)

Figure 4-22 shows the evolution of suction in the same parts of the buffer as introduced previously (R5, R10, C3). The measurements appear to be partial and with no clear indication of the initial values of suction at each sensor. It could be also interpreted that the wetting has happened very quickly during the experiment, as all measurements have stabilised. The numerical results indicate much more gradual reduction of suction and are consistent with respect to the position of the measurement point in relation to the source of water, which is at the buffer/rock interface (see Figure 4-19). They also indicate that the buffer is not saturated after 5 years.

Finally, Figure 4-23 shows the evolution of the radial total stress in the same parts of the buffer (R5, R10 and C3). The three measurement points in the ring R5 indicate some difference in the stress across the buffer thickness, while the numerical results show no difference in stress at the same points. Numerical result further indicate lower radial total stresses in R10 and C3, which agrees with the measured trend. However, the measurement C3-585 seems anomalous, being at zero value, while in general the measured radial total stresses are smaller than calculated.

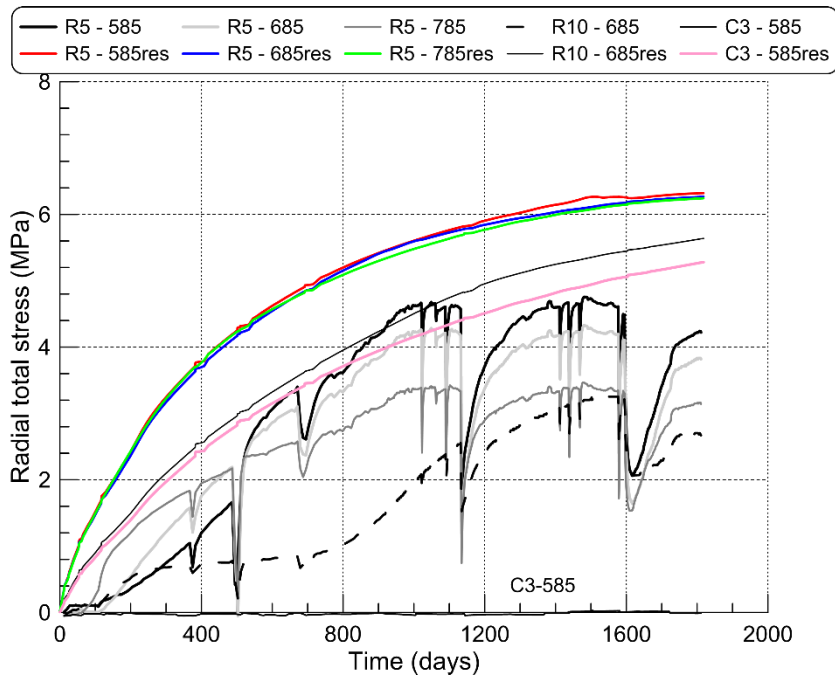


Figure 4-23 Measured and calculated radial total stress evolution in the buffer during CRT experiment ('res' stands for numerical results)

4.4.5 Lessons learnt

The overall numerical model developed for the simulation of the CRT experiment has broadly captured well the trends observed in the measured evolution of the MX-80 bentonite behaviour. The temperature field within the buffer is accurately reproduced (Figure 4-21), indicating a rapid response to applied temperature changes during the experiment.

The measurements of suction in the buffer are less certain (Figure 4-22). There is no indication of the initial value of suction and it would appear that the buffer saturates reasonably fast, within the first year of the experiment, which is not captured by the model. From the interpretation of the initial state of the buffer, the initial suction of 45 MPa was prescribed in the numerical model and the calculated suction changes are consistent in a sense that suction reduces faster in the part of the buffer near the rock interface and slower in elements near the heater, however no part of the buffer is saturated after the full five years of the experiment. The reason for this discrepancy is not thought to be in the formulation of the hydro-mechanical models, but in the selection of model parameters, in particular for the variable permeability (hydraulic conductivity) model. It would appear that the prescribed permeability change from its unsaturated to its saturated value is slower than implied by the field measurements of suction. This could be rectified by adjusting the input parameters of the permeability model.

The calculated total radial stresses in different parts of the buffer are higher

than measured. However, the veracity of total stress measurements is perhaps questionable as magnitudes of the swelling pressure are smaller than those measured on the same material in the swelling pressure tests performed in laboratory (deliverable D5.1), which reach values of 6 to 9 MPa. Consequently, it is believed that the discrepancy between the measurements and the model are not resulting from the model formulation.

4.5 VTT/UCLM

In a first approach, a slice in the buffer (ring block 5) at canister mid-height has been modelled (Section 4.5.1), similar to Subtask 2 carried out in the CRT modelling task of the EBS Task Force. For this purpose, an axisymmetric slice is modelled. After the choice of boundary conditions, the orientation represented is towards the TBT test ("A" in (Kristensson & Börgesson, 2015)). In the second simulation (Section 4.5.2), the entire buffer has been taken into account as for Subtask 3 of the CRT modelling task of the EBS Task Force.

4.5.1 Modelling a slice at canister mid-height

4.5.1.1. Geometry and discretization

The geometry and the used mesh are presented in Figure 4-24.

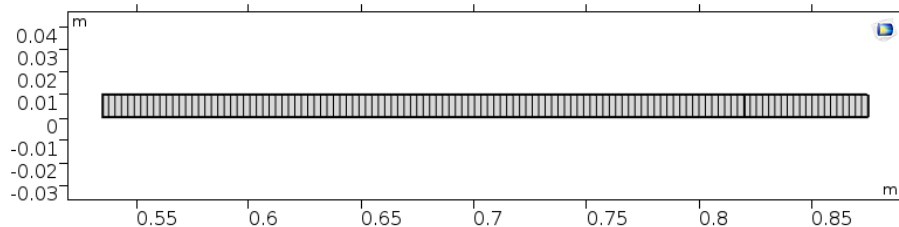


Figure 4-24. Geometry and mesh for the CRT simulation considering a slice at canister mid-height.

The information concerning the spatial and temporal discretization is given in

Table 4-20.

Table 4-20. Spatial and temporal discretization of the CRT simulation considering a slice at canister mid-height.

Spatial discretization of equations solved for following state variables	Liquid pressure (P_L)	Linear elements	Lagrange
	Displacement field (\mathbf{u})	Quadratic elements	Lagrange
	Net/effective stress (σ)	Quadratic elements	Lagrange
	Pre-consolidation pressure for zero suction (p_0^*)	Quadratic elements	Lagrange
	Micro void ratio ($e_{m,inst}^* e_m$)	Linear elements	Lagrange
	Macro2 void ratio (e_{M2})	Quadratic elements	Lagrange
Time dependent solver	Variable step size and variable order of BDF (Backward Differentiation formula) with automatic control of step size and order		
Non-linear solver	Fully coupled damped Newton's method with automatic control of damping factor (initial damping factor of 1)		
Linear solver	Direct solver for sparse matrices (PARDISO)		

4.5.1.2. Input parameters

The input parameters are listed in

Table 4-21.

Table 4-21. Input parameters used for the CRT simulation.

Parameter	Symbol	Value, units	Reference
Hydraulic model			
Molar mass of water	$M_{\text{mol,w}}$	$18.02 \frac{\text{g}}{\text{mol}}$	--
Density of liquid water	ρ_w	$10^3 \frac{\text{kg}}{\text{m}^3}$	--
Constitutive parameter for van Genuchten model	α_{VG}	$1.149 \cdot 10^{-7} \text{ Pa}^{-1}$	(Navarro et al., 2015)
Constitutive parameter for van Genuchten model	m_{VG}	0.733	(Navarro et al., 2015)
Reference intrinsic permeability for liquid water	$K_{\text{int,L,ref}}$	$2.34 \cdot 10^{-21} \text{ m}^2$	Adapted from (Gens et al., 2011)
Parameter of exponential law of intrinsic permeability for liquid water	$b_{\text{int,L}}$	9.91	(Navarro et al., 2017), adapted from (Gens et al., 2011)
Reference macrostructural porosity for intrinsic permeability for liquid water (exponential law)	$\phi_{\text{M,ref}}$	0.0465	(Navarro et al., 2017), adapted from (Gens et al., 2011)
Temperature	T	293.15 K	
Dynamic viscosity of liquid water	μ_L	$661.2 \cdot 10^{-3} \cdot (T - 229)^{-1.562} \text{ Pa} \cdot \text{s}$ Temperature T in K	(Ewen & Thomas, 1989)
Reference density of water vapour	ρ_{V0}	$\frac{e^{0.06374 \cdot (T - 273.15 \text{ K}) - 19}}{\text{Temperature } T \text{ in K}}$	(Ewen & Thomas, 1989)
Molar mass of air (21 vol% oxygen and 78 vol% nitrogen)	$M_{\text{mol,A}}$	$28.97 \frac{\text{g}}{\text{mol}}$	--
Binary diffusion coefficient of water vapour	D_V	$5.9 \cdot 10^{-6} \cdot T^{2.3} \cdot P_G^{-1} \frac{\text{m}^2}{\text{s}}$ Temperature T in K Gas pressure P_G in Pa	(Pollock, 1986)
Tortuosity factor for water vapour	τ_V	1	(Olivella & Gens, 2000)

Mechanical model			
Minimum bulk modulus	$K_{\text{bulk,m}}$	$5 \cdot 10^6 \text{ Pa}$	
Poisson's ratio	ν	0.33	(Toprak et al., 2013)
Reference stress (LC curve)	p^c	10^4 Pa	(Toprak et al., 2013)
Slope of critical state line	M	1.07	(Toprak et al., 2013)
Increase in cohesion with suction	k	0.1	(Kristensson & Åkesson, 2008)
Elastic stiffness parameter for changes in mean net stress at zero macrostructural matric suction	κ_0	0.1	Adapted from (Toprak et al., 2013)
Elastic stiffness parameter for changes in macrostructural matric suction at constant mean stress	$\kappa_{\text{SM},0}$	0.05	(Toprak et al., 2013)
Plastic stiffness parameter for changes in mean net stress at zero macrostructural matric suction	λ_0	0.3	(Toprak et al., 2013)
Parameter for changes of plastic stiffness with varying macrostructural matric suction	r_{SM}	0.8	(Toprak et al., 2013)
Parameter for changes of plastic stiffness with varying macrostructural matric suction	β	$2 \cdot 10^{-8} \text{ Pa}^{-1}$	(Toprak et al., 2013)
Elastic M2 stiffness parameter for changes in mean net stress	κ_{M2}	0.7	--
Water exchange coefficient between M1 and M2	g_{MM2}	$4 \cdot 10^{-7} \frac{\text{kg}}{\text{s} \cdot \text{m}^3 \cdot \text{MPa}}$	Adapted from (Sánchez et al., 2016)

4.5.1.3. Initial and boundary conditions

The initial and boundary conditions are presented in Table 4-22 and

Table 4-23, respectively.

Table 4-22. Initial conditions of the simulation of the CRT considering a slice at canister mid-height.

Ring blocks	<p>Hydraulic:</p> <ul style="list-style-type: none"> • $P_{L,init} = -4.59 \cdot 10^7$ Pa <p>Mechanical:</p> <ul style="list-style-type: none"> • $\sigma_{r,init} = \sigma_{\phi,init} = \sigma_{z,init} = 10^3$ Pa • $\tau_{rz,init} = 0$ Pa • $p_{0,init}^* = 1 \cdot 10^6$ Pa <p>Thermal:</p> <ul style="list-style-type: none"> • $T_{init} = 17$ °C <p>Microstructural:</p> <ul style="list-style-type: none"> • $e_{m,init} = 0.47$ • $e_{TOT,init} = 0.56$
Pellet fill	<p>Hydraulic:</p> <ul style="list-style-type: none"> • $P_{L,init} = -7.20 \cdot 10^7$ Pa <p>Mechanical:</p> <ul style="list-style-type: none"> • $\sigma_{r,init} = \sigma_{\phi,init} = \sigma_{z,init} = 10^3$ Pa • $\tau_{rz,init} = 0$ Pa • $p_{0,init}^* = 8 \cdot 10^6$ Pa <p>Thermal:</p> <ul style="list-style-type: none"> • $T_{init} = 17$ °C <p>Void ratios:</p> <ul style="list-style-type: none"> • $e_{m,init} = 0.28$ • $e_{M2,init} = 1.32$ • $e_{TOT,init} = 1.78$

Table 4-23. Boundary conditions of the simulation of the CRT considering a slice at canister mid-height.

Hydraulic	<ul style="list-style-type: none"> • $P_{L,rock} = -1.4 \cdot 10^6$ Pa (Dirichlet BC) on rock boundary • $-\hat{I}_{MW} \cdot n = 0 \frac{kg}{m^2s}$ No water flow on horizontal boundaries • Water inflow $q(t)$ for the canister gap boundary • Contact water flow for block-pellet interaction q_{cont}
Mechanical	<ul style="list-style-type: none"> • $u \cdot n = 0$ m (roller) on horizontal and rock boundaries • Spring force function of radial displacement $\sigma(u)$ on canister gap, to simulate no confinement while the gap is open and full confinement when the block reaches contact with the canister • Contact force for block-pellet interaction σ_{cont}
Thermal	<ul style="list-style-type: none"> • T_{rock} (Dirichlet BC) from 3D simulation by (Börgesson et al., 2016) of sensor TR125 (towards TBT experiment) on rock boundary (see figure below) • $T_{canister}$ (Dirichlet BC) from 3D simulation by (Börgesson et al., 2016) at canister mid-height in canister boundary (see figure below) • Contact heat flow for block-pellet interaction $I_{h,cont}$ • No heat flow on horizontal boundaries <div data-bbox="399 1052 1197 1478" style="text-align: center;"> </div>
<div style="text-align: center;"> </div>	

4.5.1.4. Results/discussion

Figure 4-25 shows the temperature evolution measured by Vaisala sensors

W119T, W120T and W121T, located at a radial distance of 585, 685 and 785 mm from the canister centre, respectively, together with the corresponding numerical results. The orientation of the measurements is towards the TBT experiment corresponding to orientation “A” in (Kristensson & Börgesson, 2015). The fit between readings and modelled results is very satisfactory. Note that the reading of the sensors was lost at around 600 days.

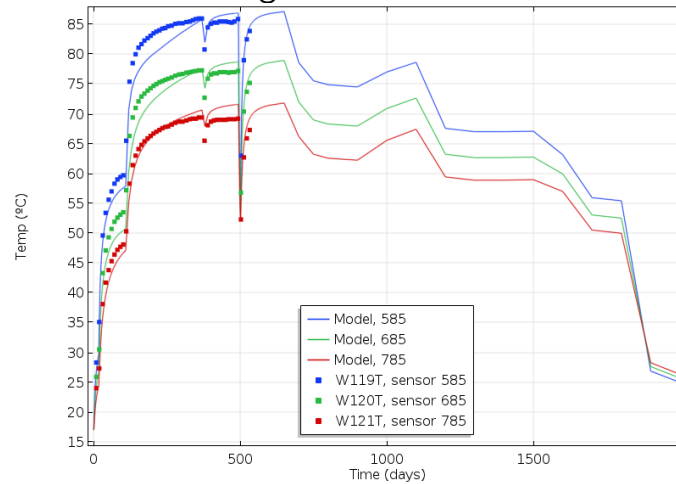


Figure 4-25. Simulation of the CRT considering a slice at canister mid-height. Temperature evolution at Vaisala sensors W119T, W120T and W121T. Experimental: markers, model: lines.

In Figure 4-26, the suction measured with Wescor psychrometers W122, W123 and W124, located at a radial distance of 585, 685 and 785 mm from the canister centre, respectively, and the corresponding numerical results are plotted. These three sensors are also located towards the TBT experiment. Note that Wescor sensors can only record suctions less than approx. 5 MPa, and therefore, the readings for the initial hydration phase are missing. The fit between the sensor data and the modelling results is acceptable.

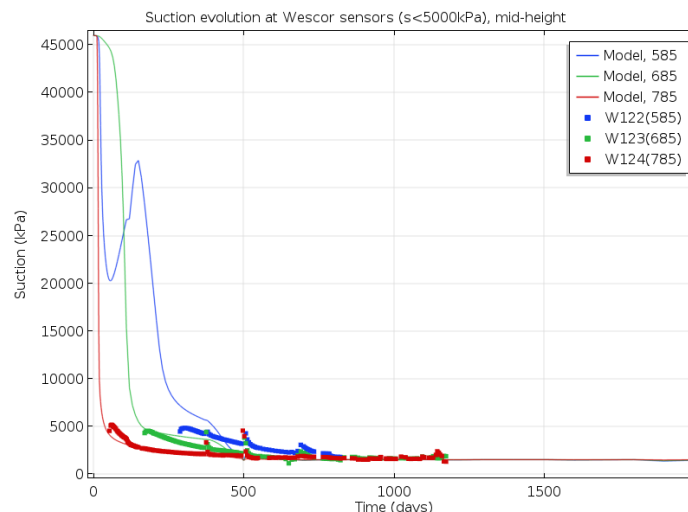


Figure 4-26 Simulation of the CRT considering a slice at canister mid-height. Suction evolution at Wescor psychrometers W122, W123 and W124. Experimental: markers, model: lines.

The results of the post-mortem analysis for water content and dry density are shown in Figure 4-27 and Figure 4-28, respectively. Note that the presented measurements were taken at ring block 6, immediately above the simulated ring block 5, for which unfortunately no post-mortem data exist. The radial distributions of water content and dry density have been captured well and the numerical values are in the range of the measured ones. The significant homogenisation that occurred in CRT regarding the initially high difference in density between the compacted blocks and the pellet fill is also seen in the simulation.

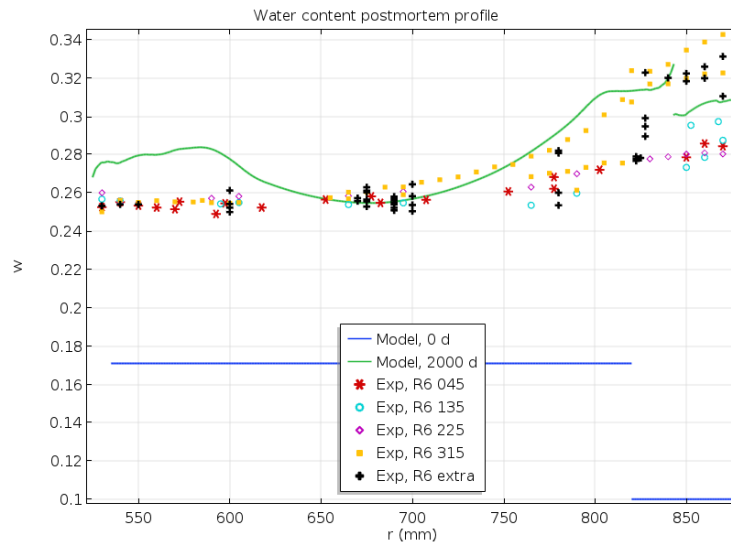


Figure 4-27 Simulation of the CRT considering a slice at canister mid-height. Post-mortem water content profile as a function of the radial distance to the canister centre. Experimental: markers, model: lines. Note that the model represents the canister mid-height (Ring 5) while the closest available experimental data corresponds to Ring 6 (block immediately above Ring 5, each ring 0.5 m high)

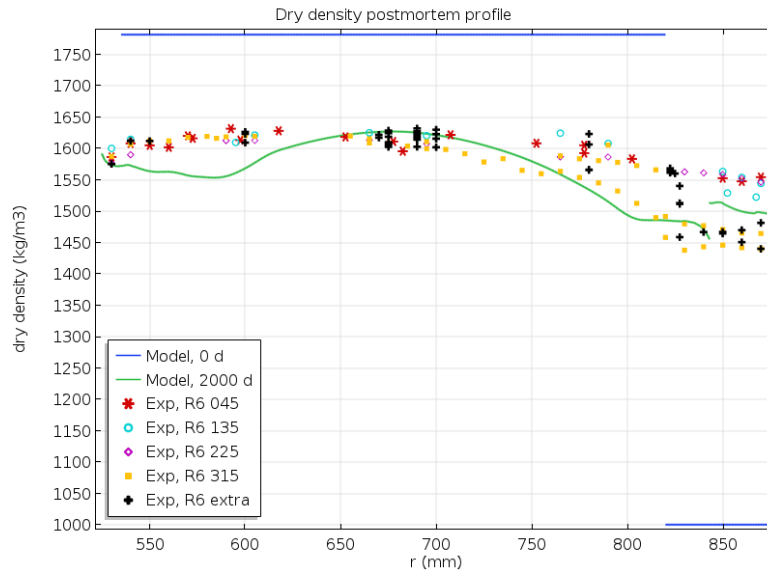


Figure 4-28. Simulation of the CRT considering a slice at canister mid-height. Post-mortem dry density profile as a function of the radial distance to the canister centre. Experimental: markers, model: lines. Note that the model represents the canister mid-height (Ring 5) while the closest available experimental data corresponds to Ring 6 (block immediately above Ring 5, each ring 0.5 m high).

4.5.2 Modelling the entire CRT

4.5.2.1. Geometry and discretization

The axisymmetric geometry and the used mesh are presented in Figure 4-29.

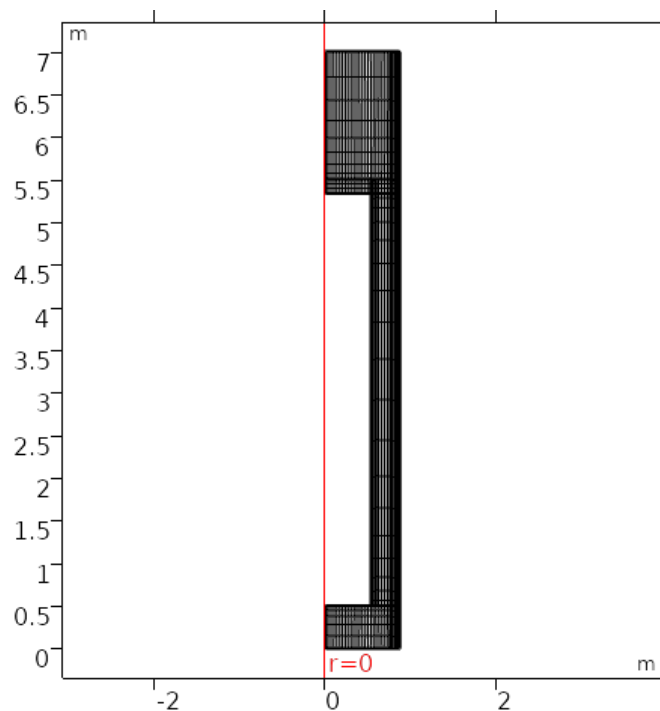


Figure 4-29. Geometry and mesh for the CRT simulation considering the entire buffer.

The information concerning the spatial and temporal discretization is given in Table 4-24.

Table 4-24. Spatial and temporal discretization of the CRT simulation considering the entire buffer.

Spatial discretization of equations solved for following state variables	Liquid pressure (P_L)	Linear elements	Lagrange
	Displacement field (\mathbf{u})	Quadratic elements	Lagrange
	Net/effective stress ($\boldsymbol{\sigma}$)	Quadratic elements	Lagrange
	Pre-consolidation pressure for zero suction (p_0^*)	Quadratic elements	Lagrange
	Micro void ratio ($e_{m,inst}^*$, e_m)	Linear elements	Lagrange
	Macro2 void ratio (e_{M2})	Quadratic elements	Lagrange
Time dependent solver	Variable step size and variable order of BDF (Backward Differentiation formula) with automatic control of step size and order		
Non-linear solver	Fully coupled damped Newton's method with automatic control of damping factor (initial damping factor of 1)		
Linear solver	Direct solver for sparse matrices (PARDISO)		

4.5.2.2. Input parameters

See Section 4.5.1.2.

4.5.2.3. Initial and boundary conditions

The initial and boundary conditions are given in Table 4-25 and Table 4-26, respectively.

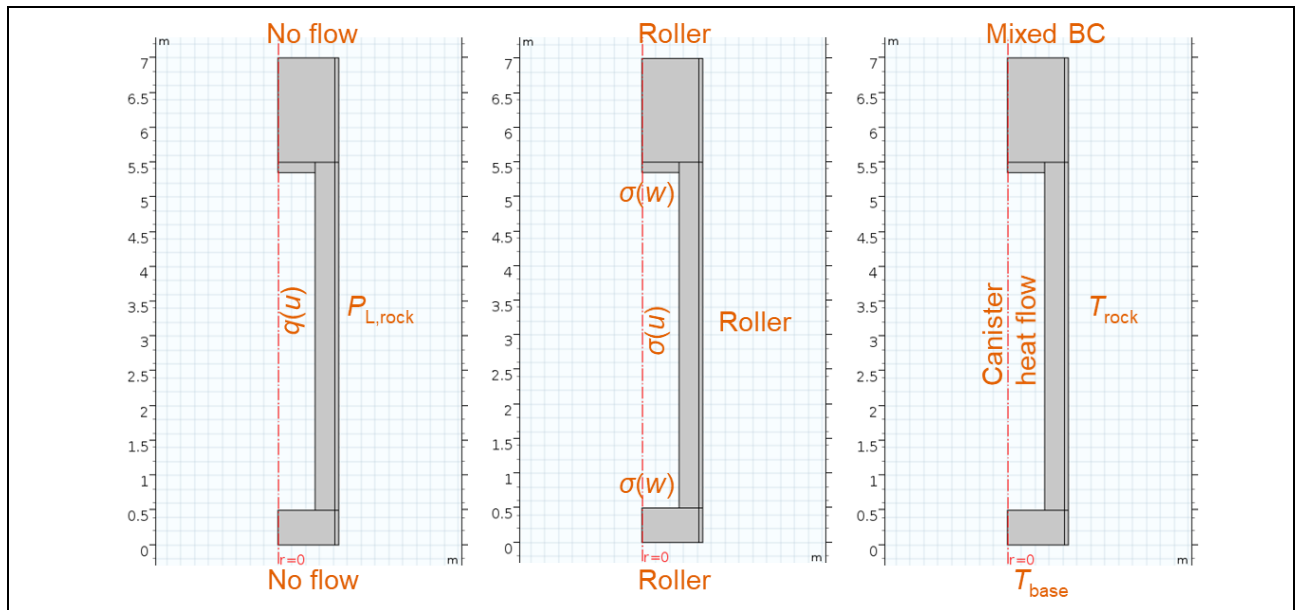
Table 4-25. Initial conditions of the simulation of the entire CRT.

Ring blocks	<p>Hydraulic:</p> <ul style="list-style-type: none"> • $P_{L,init} = -4.59 \cdot 10^7$ Pa <p>Mechanical:</p> <ul style="list-style-type: none"> • $\sigma_{r,init} = \sigma_{\phi,init} = \sigma_{z,init} = 10^3$ Pa • $\tau_{rz,init} = 0$ Pa • $p_{0,init}^* = 1 \cdot 10^6$ Pa <p>Thermal:</p> <ul style="list-style-type: none"> • $T_{init} = 17$ °C <p>Microstructural:</p> <ul style="list-style-type: none"> • $e_{m,init} = 0.47$ • $e_{TOT,init} = 0.56$
Cylinder blocks	<p>Hydraulic:</p> <ul style="list-style-type: none"> • $P_{L,init} = -4.54 \cdot 10^7$ Pa <p>Mechanical:</p> <ul style="list-style-type: none"> • $\sigma_{r,init} = \sigma_{\phi,init} = \sigma_{z,init} = 10^3$ Pa • $\tau_{rz,init} = 0$ Pa • $p_{0,init}^* = 1 \cdot 10^6$ Pa <p>Thermal:</p> <ul style="list-style-type: none"> • $T_{init} = 17$°C <p>Microstructural:</p> <ul style="list-style-type: none"> • $e_{m,init} = 0.48$ • $e_{TOT,init} = 0.64$
Bricks	<p>Hydraulic:</p> <ul style="list-style-type: none"> • $P_{L,init} = -5.02 \cdot 10^7$ Pa <p>Mechanical:</p> <ul style="list-style-type: none"> • $\sigma_{r,init} = \sigma_{\phi,init} = \sigma_{z,init} = 10^3$ Pa • $\tau_{rz,init} = 0$ Pa • $p_{0,init}^* = 1 \cdot 10^6$ Pa <p>Thermal:</p> <ul style="list-style-type: none"> • $T_{init} = 17$ °C <p>Microstructural:</p> <ul style="list-style-type: none"> • $e_{m,init} = 0.46$ • $e_{TOT,init} = 0.72$

Pellet fill	<p>Hydraulic:</p> <ul style="list-style-type: none"> • $P_{L,init} = -7.20 \cdot 10^7$ Pa <p>Mechanical:</p> <ul style="list-style-type: none"> • $\sigma_{r,init} = \sigma_{\phi,init} = \sigma_{z,init} = 10^3$ Pa • $\tau_{rz,init} = 0$ Pa • $p_{0,init}^* = 8 \cdot 10^6$ Pa <p>Thermal:</p> <ul style="list-style-type: none"> • $T_{init} = 17^\circ\text{C}$ <p>Void ratios:</p> <ul style="list-style-type: none"> • $e_{m,init} = 0.28$ • $e_{M2,init} = 1.32$ • $e_{TOT,init} = 1.78$
-------------	--

Table 4-26. Boundary conditions of the simulation of the entire CRT.

Hydraulic	<ul style="list-style-type: none"> • $P_{L,rock}$ (Dirichlet BC) on rock boundary. • $-\hat{I}_{MW} \cdot \mathbf{n} = 0 \frac{\text{kg}}{\text{m}^2\text{s}}$ No water flow on horizontal boundaries. • Water inflow $q(t)$ for the canister gap top boundary. • Water inflow function of horizontal displacement $q(u)$ for the canister gap side boundary.
Mechanical	<ul style="list-style-type: none"> • $\mathbf{u} \cdot \mathbf{n} = 0$ m (roller) on bottom, rock side and plug boundaries. • Spring force function of horizontal displacement $\sigma(u)$ on canister gap, to simulate no confinement while the gap is open and full confinement when the block contacts the canister. <p>Spring force function of vertical displacement $\sigma(w)$ on the top and bottom of the canister, to simulate no penetration into canister (although it can be displaced upwards or downwards).</p>
Thermal	<ul style="list-style-type: none"> • T_{rock} (Dirichlet BC) at the rock boundary from averaging and interpolating the data from sensors TR101, TR105, TR113, TR109, TR117, TR125, TR121, TR129, TR137 and TR133, thermocouples in the rock at the rock surface and at different levels and orientations. • T_{base} (Dirichlet BC) at the bottom from sensor TR101, thermocouple in the rock located at elevation of 0 and at the rock surface. • Heat flux at the canister side boundary proportional to the canister heater power • Heat loss at top to an external temperature of 17°C, $\mathbf{n} \cdot \Gamma = \alpha(T - 17^\circ\text{C})$, where $\alpha = 0.01 \frac{\text{W}}{\text{m}^2 \cdot ^\circ\text{C}}$.



4.5.2.4. Results/discussion

In Figure 4-30, the temperatures recorded at thermocouples T111, T112, T127 and T129, located in ring blocks R5, R5 and R10 and cylinder block C3, respectively), at radial distances of 635, 735, 685 and 785 mm from the canister centre, respectively, are compared against the respective numerical results. Note that sensors T111, T112 and T129 are oriented towards “A” while sensor T127 has the opposite orientation (towards “D”). The modelled results follow the same trends as the experimental results and the fits for all sensors are very satisfactory.

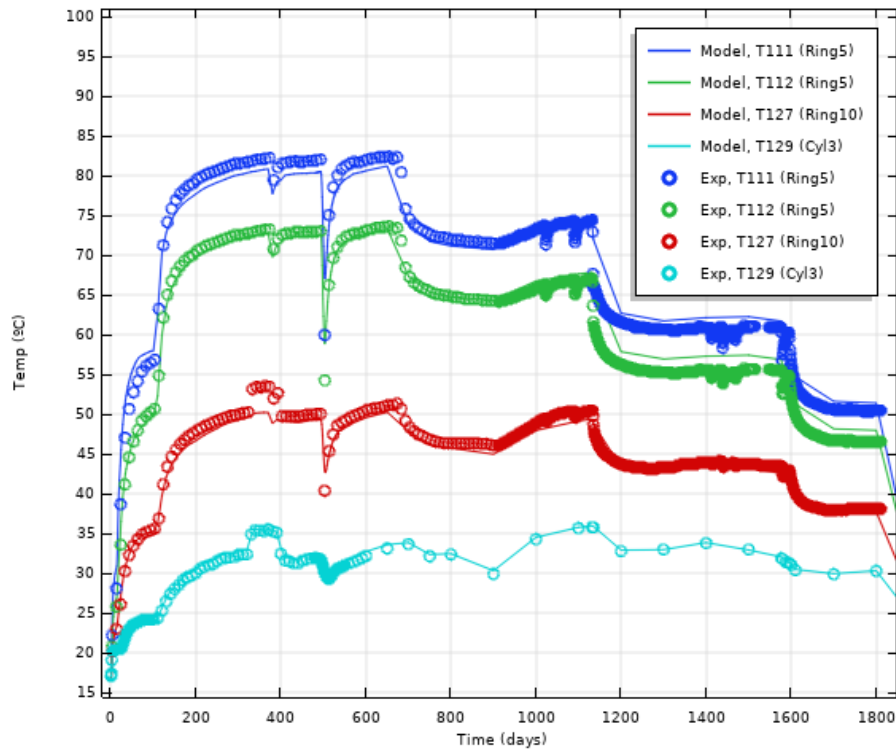


Figure 4-30. Simulation of the entire CRT. Temperature evolution at thermocouple sensors T111, T112, T127 and T129. Experimental: markers, model: lines.

In Figure 4-31, the suction measurements obtained with Wescor psychrometers in ring block 5 (W122, W123 and W124 located at a radial distance of 585, 685 and 785 mm from the canister centre, respectively, and oriented towards “A”), in ring block 10 (W140 at a radial distance of 685 mm from the canister centre, oriented towards “A”) and cylinder block 3 (W154 at a radial distance of 585 mm from the canister centre, oriented 90° from “A”, orientations “B” and “C”) are shown together with the numerical results. Note that the used Wescor sensors can only record suctions approximately 5 MPa and less. Therefore, the readings are missing for the initial hydration phase, which was subject to uncertainties related to the artificial wetting (Section 2.6). The fit between sensor data and modelled results is satisfactory.

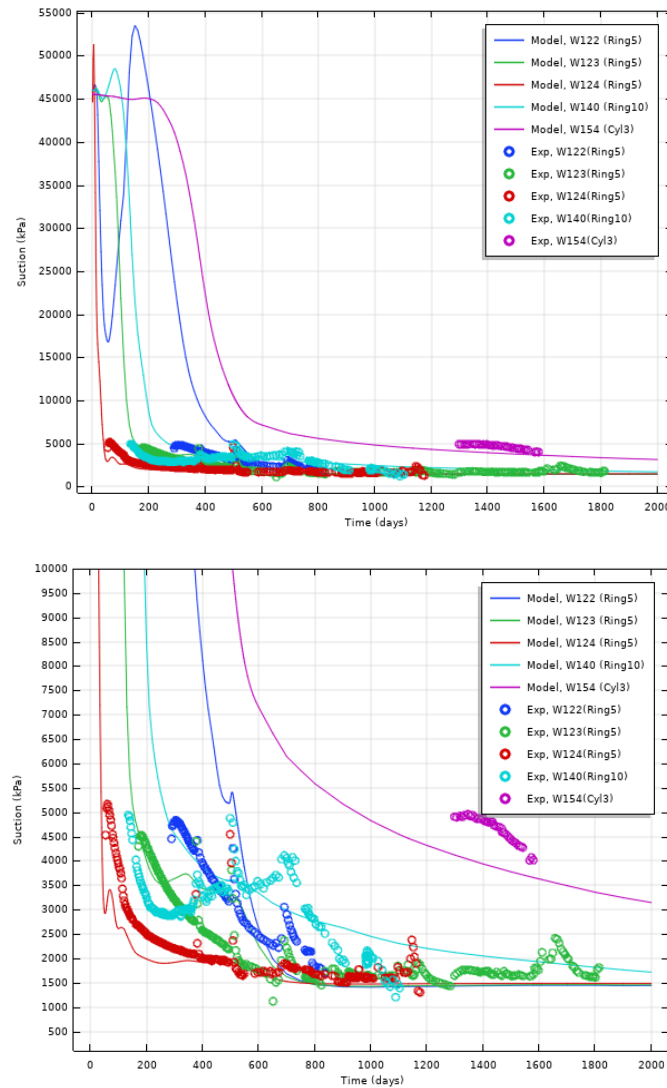


Figure 4-31. Simulation of the entire CRT. Suction evolution at Wescor sensors W122, W123, W124, W140 and W154. Experimental: markers, model: lines. Full suction range (top) and detailed view for suction range 100-10 000 kPa (bottom).

Figure 4-32 represents the results of pressure sensors P110, P111 and U106 located in ring block 5 at radial distances of 585, 685 and 785 mm from the canister centre, respectively, as well as of pressure sensor P119 in ring block 10 at a radial distance of 685 mm from the canister centre. The orientation of the measurements is towards the TBT experiment corresponding to orientation “A” in (Kristensson & Börgesson, 2015). The model results represented are the total mean stress values. While the general trends are captured, the numerical simulation overestimates the measured pressures, except for sensor U106. However, when analysing the results, one should bear in mind the measurement variability and errors reported in (Kristensson & Börgesson, 2015).

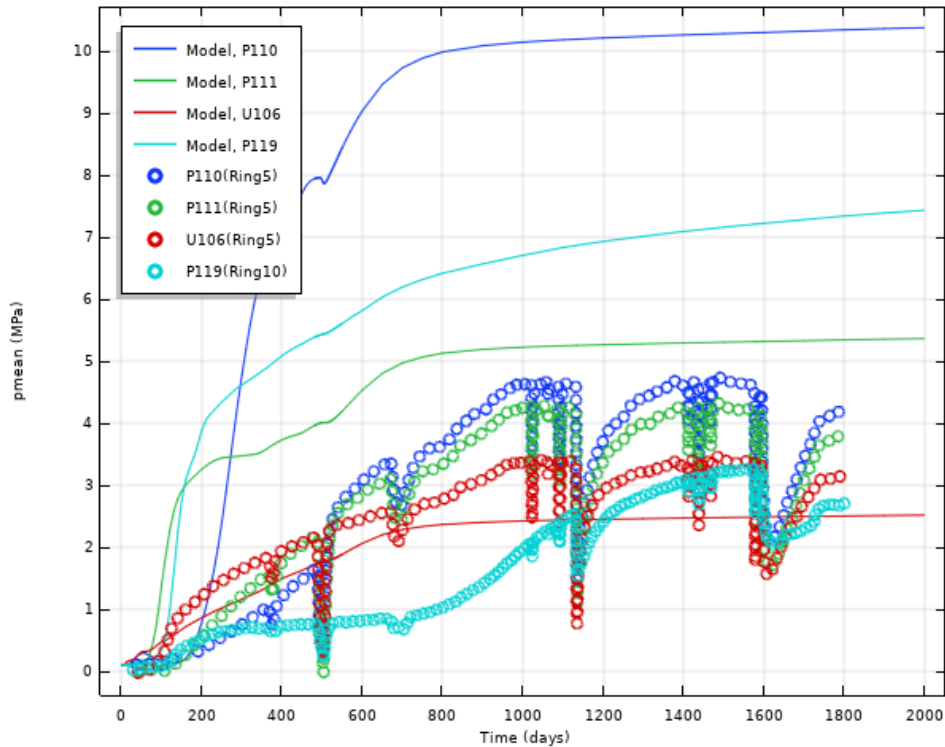


Figure 4-32. Simulation of the entire CRT. Total stress evolution at pressure sensors P110, P111, U106 and P119 (“A” orientation, towards TBT). Experimental: markers, model: lines.

The results of the post-mortem analysis for water content and dry density are shown in Figure 4-33 and Figure 4-34, respectively. Note that the presented measurements were taken at ring block 6. There is some deviation in the fit, but the range of final values and the homogenisation have been captured to a reasonable extent. An exception is the outer part of the pellet domain, which seems to be too compressed in the model.

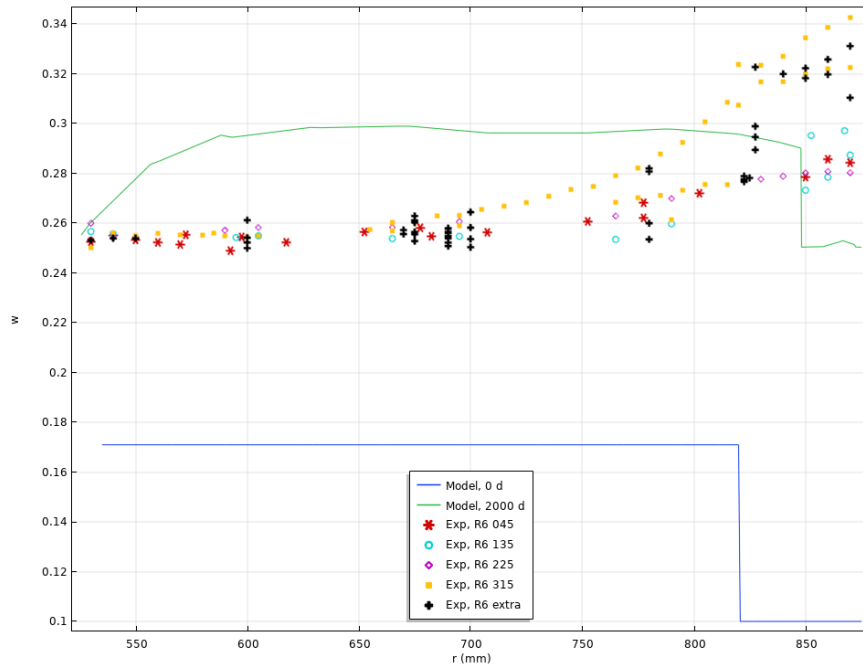


Figure 4-33. Simulation of the entire CRT. Post-mortem water content profile (ring block 6) as a function of the radial distance to the canister centre. Experimental: markers, model: lines.

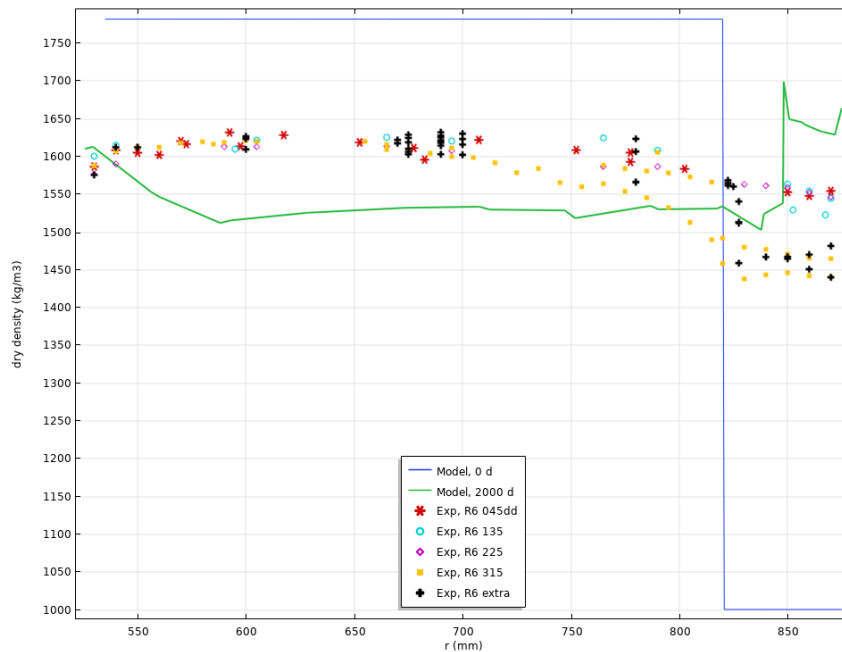


Figure 4-34. Simulation of the entire CRT. Post-mortem dry density profile (ring block 6) as a function of the radial distance to the canister centre. Experimental: markers, model: lines.

4.5.3 Lessons learnt

Based on the opinion of the VTT-UCLM modelling group, the following section discusses, which specific aspects or features taken into consideration in the

CRT simulation allowed to capture the main trends in the evolution of the test and led to the satisfactory agreement between experimental and numerical results.

First, it is important to acknowledge that the CRT was an in-situ full-scale experiment and thus, the initial and boundary conditions could not be defined as accurately as for small-scale lab experiments. In particular, it was beneficial to consider the thermal effect of the near-by experiment TBT on the CRT. Taking this into account in the boundary conditions, the evolution of temperature is reproduced very satisfactorily.

In addition, as discussed, water leakage into the inner gap was detected at the start of the test. Therefore, by choosing the hydraulic boundary conditions accordingly, a water supply at the inner gap is modelled for the initial phase, when the inner gap has not been closed yet by the swelling bentonite blocks. Consequently, the hydration of the buffer started from two ends, i.e., from the artificially wetted outer pellet fill resulting in a wetting front moving radially inwards, and from the inner gap with a wetting front moving radially outwards. Regarding the latter, due to the vicinity of the heater, it is very important that the model is able to take into account water vapour. However, it need to be born in mind that the leakage to the inner gap is afflicted with uncertainties and expert judgment is required for an appropriate estimation. These uncertainties lead to a less adjusted reproduction of relative humidity in the shorter term, but suctions in the longer term are satisfactorily captured.

In order to reduce the number of elements and to ease the numerical simulation, the canister and the inner gap are modelled implicitly using appropriate boundary conditions. This concerns the possible vertical movement of the canister due to the swelling of bentonite and the closing of the inner gap, which has been modelled as a contact problem. This could affect the reproduction of stresses in the test. However, as Kristensson and Börgesson (2015) point out, the stress sensors show "lower magnitudes of stress than what is expected" which "probably comes from an installation effect". The stresses obtained with the model lie within what can be expected for the obtained dry densities, and the general trends are captured.

By using a triple porosity approach for the pellet fill, the inter-pellet porosity is taken into account explicitly/separately. By contrast to a double porosity approach, the processes occurring on the different structural and functional levels can be modelled without the need of averaging parameters or state functions over the different levels, or modifying them to be able to achieve reasonable matches with experimental data, which may lead to a loss of the physical meaning of the respective parameters. Instead, the evolution of the system can be tracked in more detail, in particular with regard to changes in the different porosity levels and the corresponding mechanical and hydraulic response. This helps to depict the transient behaviour of the buffer, e.g., regarding the compression of the pellet fill and reduction in inter-pellet porosity due to the swelling blocks, which is directly associated with the

homogenisation of density differences.

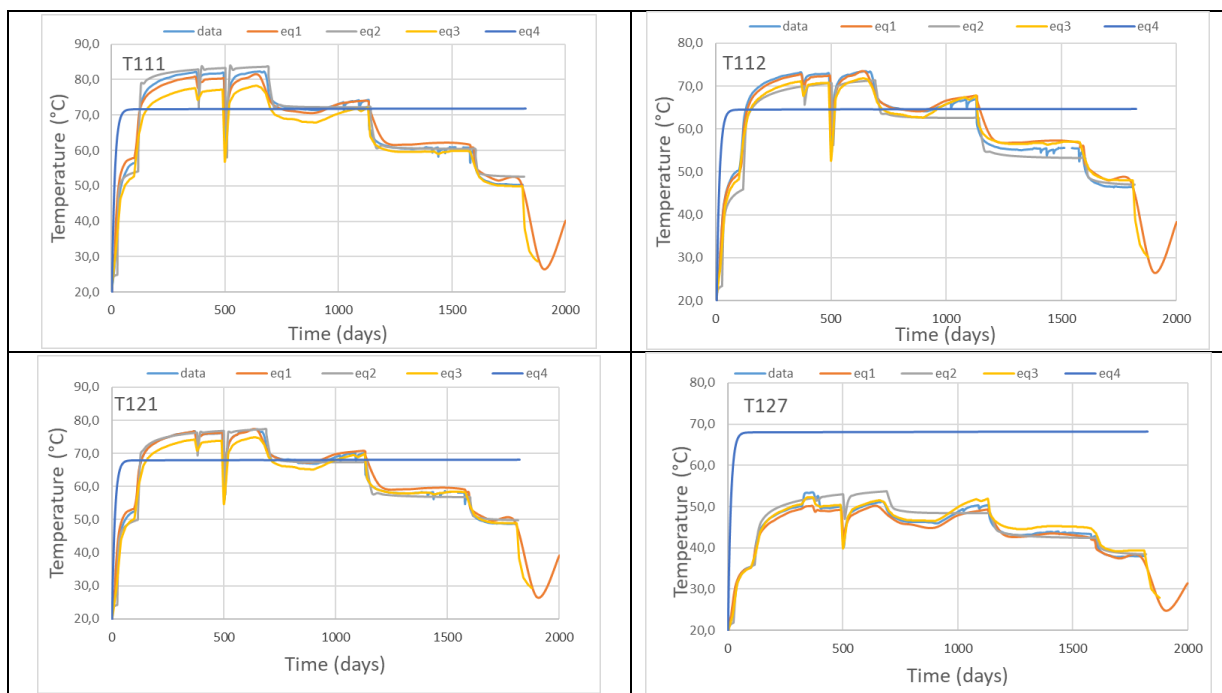
Despite the substantial homogenisation successfully captured with the current model, it is advisable to improve the model behaviour at the interface between compacted blocks and pellets in the future.

4.6 Synthesis of results for CRT – key lessons (Andra + All)

A selection of results are presented in this paragraph showing the differences between the models used for this exercise and try to investigate where are the main difficulties in terms of reproduction of the data.

This experiment, in contrast to the other tests modelled in the Beacon project, requires temperature to be taken into account. This introduces a new complexity in the physical processes and new coupling terms in the models.

Figure 4-35 presents the evolution of temperature at several locations in the buffer: at half-height of the canister (T111, T112 and T121), on the top of the canister (T127) and above it (T129). It can be observed that temperature gradient in the buffer around the canister is very well approached by the models. This observation should be related to the way the boundary condition is applied (imposed temperature in most cases). But it is important to see that the gradients are well reproduced by the models. Above the canister the differences between the numerical results and the measurements could be certainly attributed to the boundary condition on the top of the set-up.



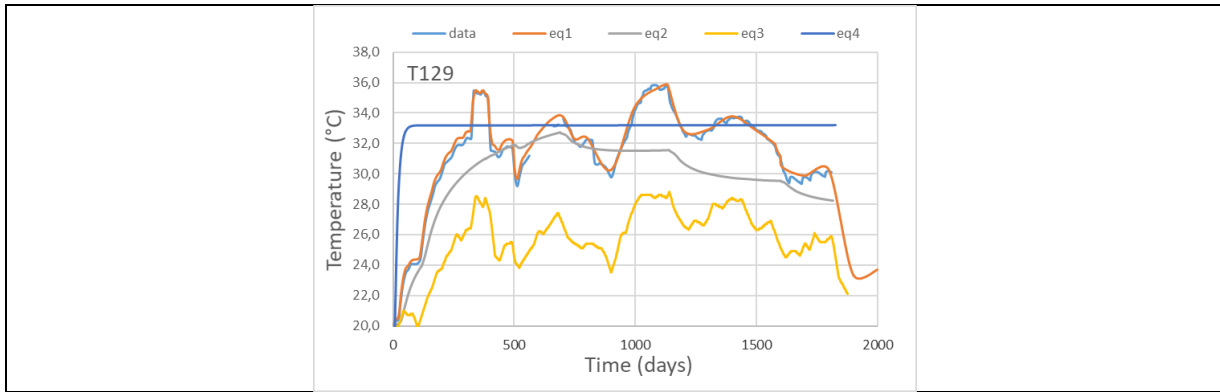
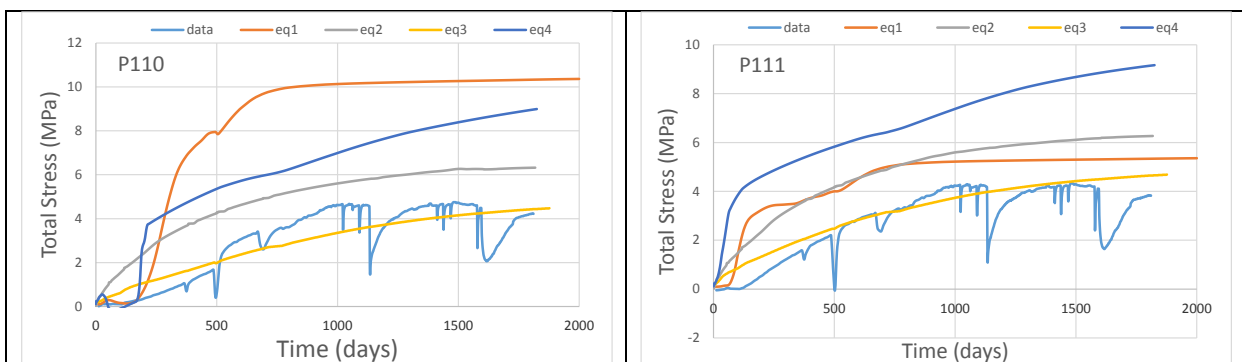


Figure 4-35 Temperature evolution at several locations/ Comparison between the numerical results obtained and the measurements

Development of total pressure at different locations in the buffer is presented on Figure 4-36. The comparison shows a good agreement between the measurements and the models especially in the mid part of the canister in ring 5 (P110, P111 and U106 locations).

The trend of swelling pressure development is well captured suggesting that the swelling parameters of the bentonite, as well as the hydraulic conductivity were calibrated reasonably well. As indicated in (Kristensson & Börgesson, 2015), deviation in sensors could lead to an underestimate in the total pressure measurement and should certainly explain a part of the differences observed between numerical results and measured quantities. The fluctuations in temperature seem to have a significant influence on the sensor responses due certainly to the coupling with the pore pressure but this point is not well reproduced by the models which propose much smoother curves for total pressure evolution. The sensor P125 located in cylinder 3 above the canister gave very low values which seems not representative of what was expected in terms of THM behaviour of the bentonite. Estimations made by (Kristensson & Börgesson, 2015) based on the averaged dry density obtained after dismantling indicate swelling pressure between 5 and 7MPa much more consistent with the numerical predictions.



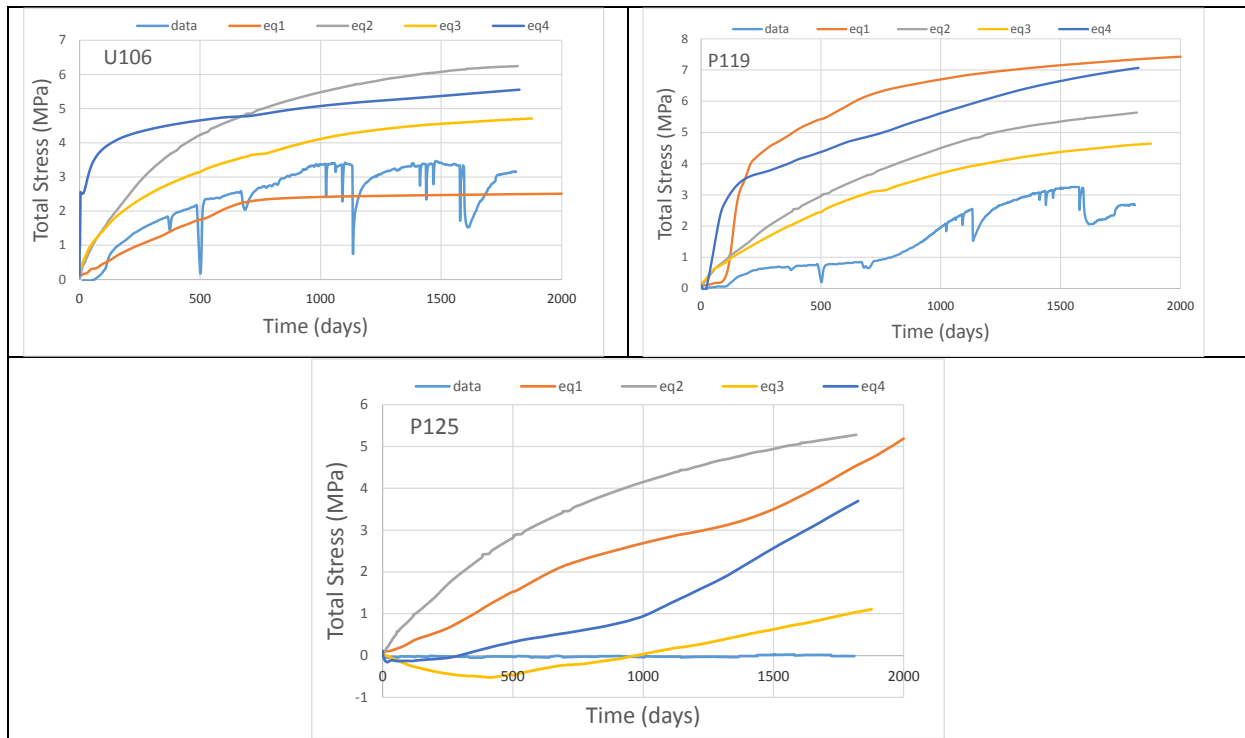
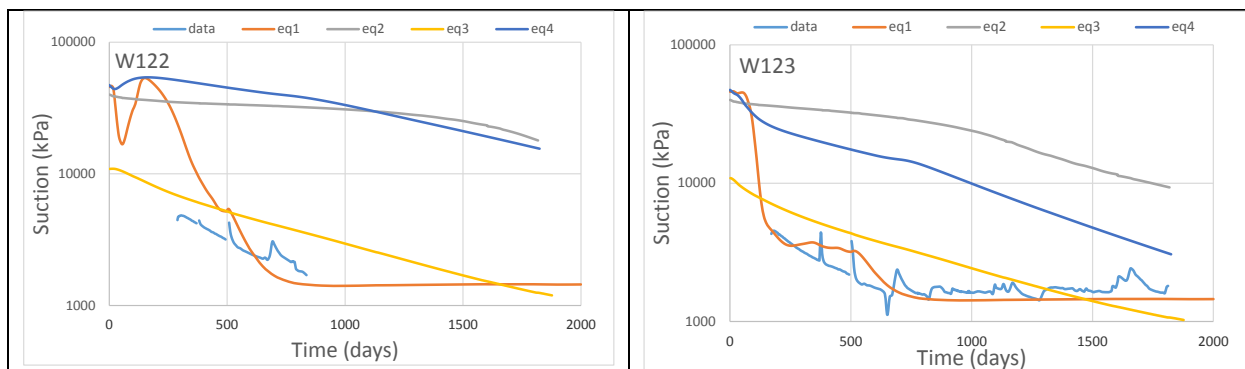


Figure 4-36 Total pressure evolution at several locations/ Comparison between the numerical results obtained and the measurements

On Figure 4-37 the suction evolutions measured and the numerical results are presented. The quantities are measured in ring block 5 (W122, W123, W124), in ring block 10 (W140) and above the canister in cylinder block 3 (W154) by Wescor psychrometers. These sensors work well for $RH > 95\%$ (or below 5 MPa in suction). Consequently, a part of the transient phase couldn't be caught at the beginning of the water saturation. All the numerical results reproduced the trend even if some of them seem to minor the resaturation time. It is also interesting to see that a very good agreement has been obtained by some teams for both trend and measured quantities in the range of available data. As for other quantities, the fluctuations in temperature evolution has a low influence on suction predicted by the models which provided very smooth evolution curves. As for the total pressure, it reveals certainly the limit in the model to consider coupling between hydraulic and thermal processes.



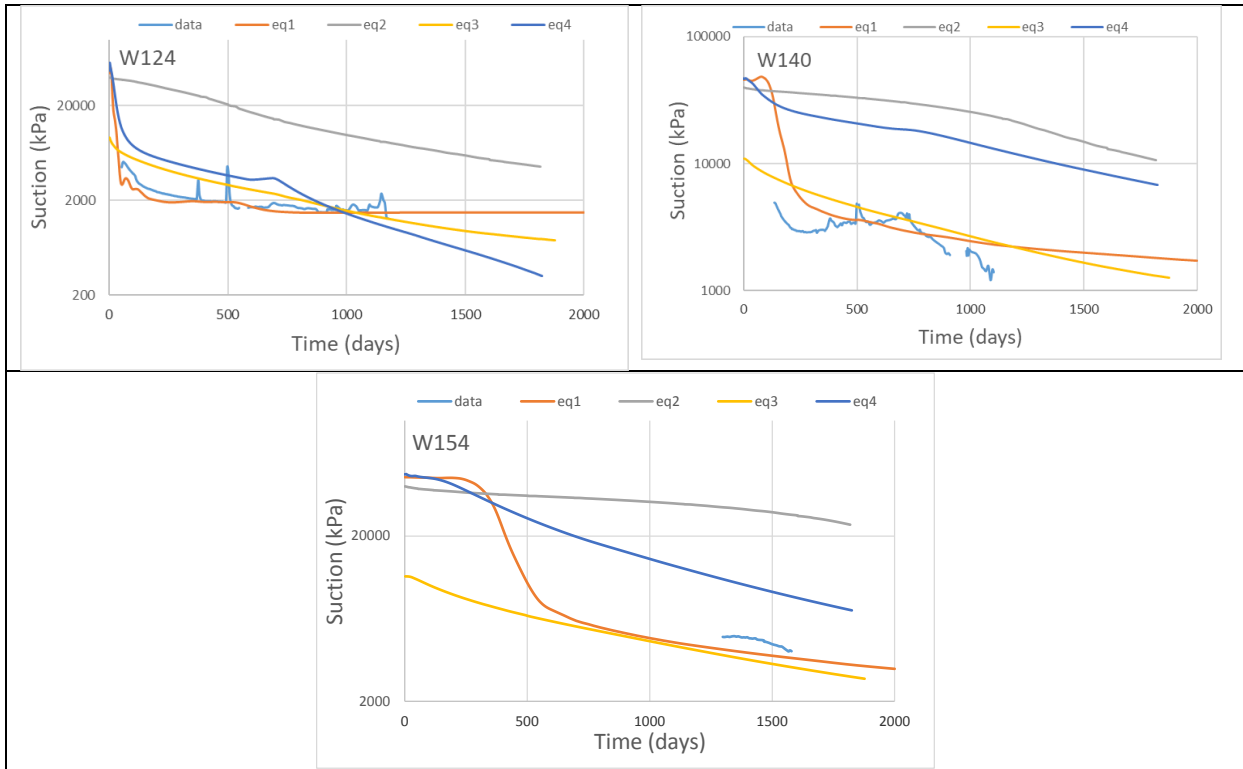
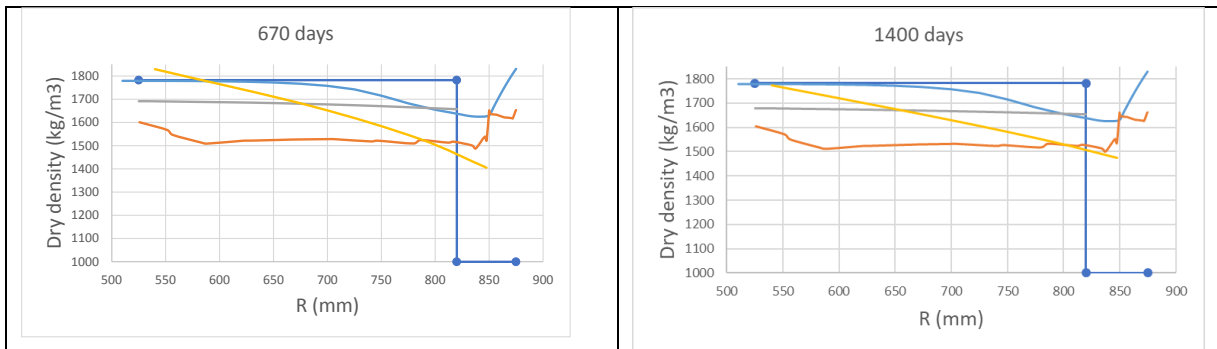


Figure 4-37 Suction evolution at several locations/ Comparison between the numerical results obtained and the measurements

Interesting part, directly in link with the aim of the Beacon project is the ability of the model to predict how the bentonite will be able to homogenize during hydration. At the beginning, large difference of dry density is introduced in the CRT experiment due to the presence of compacted blocks around the canister and pellets used to fill the gap between the bentonite blocks and the host rock.

As it can be seen on Figure 4-38, the initial dry density for the bentonite blocks is about 1780 kg/m³ compared to dry density of the pellets zone estimated around 1000kg/m³.



Beacon

D5.2.2 – Synthesis of the results obtained of test cases from task 5.2

Dissemination level: PU

Date of issue: 15/07/2020

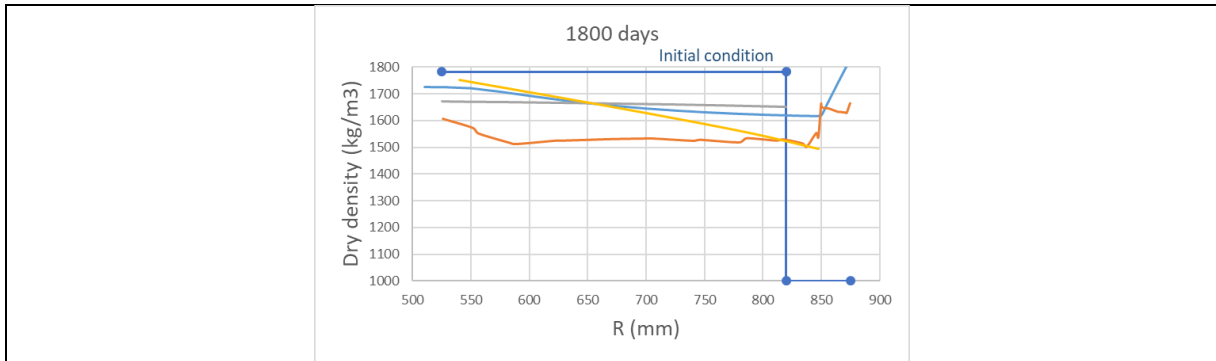


Figure 4-38 Dry density radial profile in ring block R5 at $t=670$ days, $t=1400$ days, $t=1800$ days and the initial condition; Relative humidity evolution measured in ring block R5 (relative humidity sensors Vaisala)

In Ring block R5, the sensors indicates that the relative humidity reached 100% after some hundred days (Figure 4-39a) explaining why the profiles are very similar between 670 days and 1800 days (Figure 4-38).

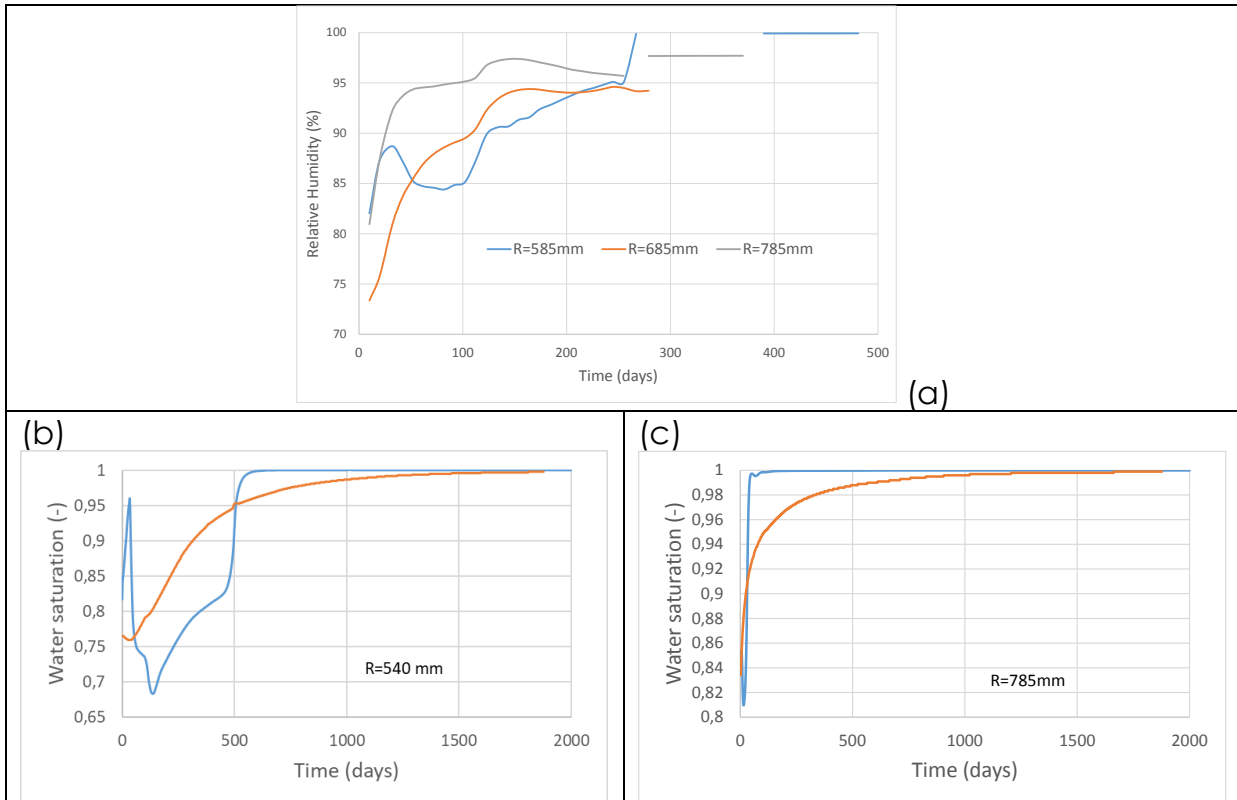


Figure 4-39 (a) Relative humidity evolution measured in ring block R5 (relative humidity sensors Vaisala); Numerical results for water saturation evolution in ring block R5 at $R=540$ mm (b) and $R=785$ mm (c)

This is confirmed in Figure 4-39 (b) and (c) where the evolution of water saturation estimated by the models in R5 is presented. The figure shows clearly the rapid saturation of ring block 5 and with shorter time of saturation at the interface with the host rock.

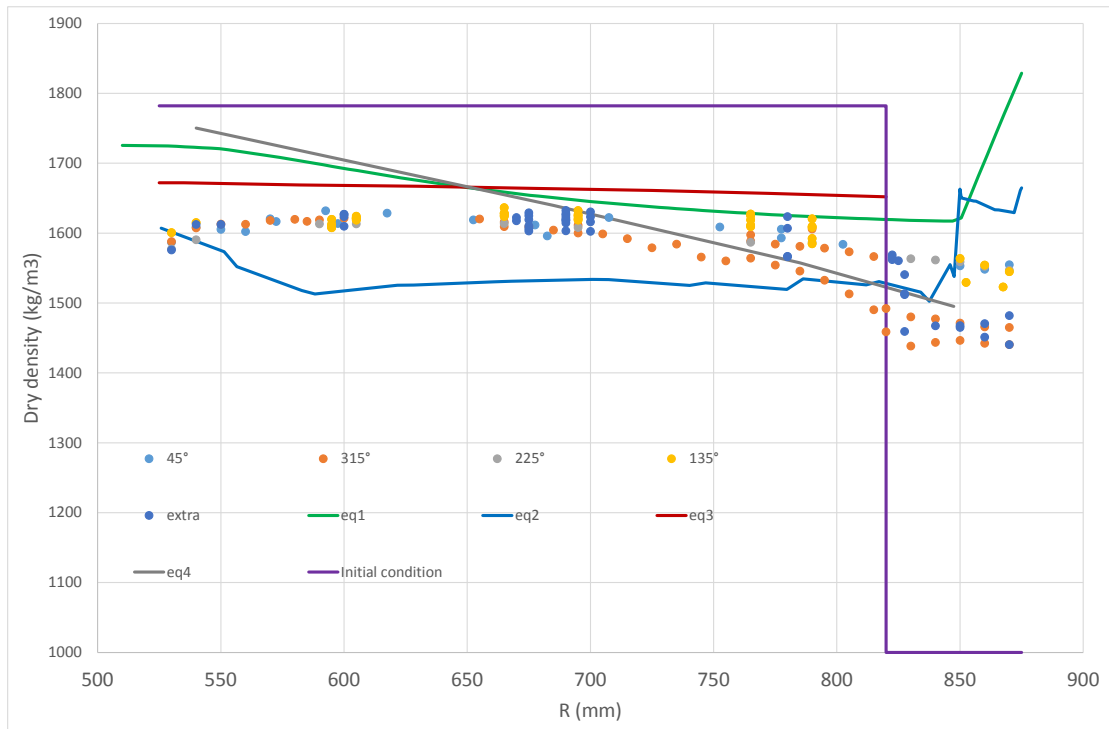


Figure 4-40 Horizontal profile of dry density after dismantling in ring R5, comparison with numerical results

Figure 4-40 presents a horizontal profile in ring R5 of dry density measured after dismantling. It can be observed remaining differences of dry density between the initial pellets zone and the block. Globally the dry density in the block decreased from 1780 kg/m³ to about 1600 kg/m³. It increased in the pellets zone from 1000 kg/m³ to about 1500 kg/m³. On the same graph, the numerical results are presented showing that the order of magnitude is well obtained by the models with slight differences concerning the distribution of density on the horizontal profile.

This results and those presented before tend to confirm that the models used in the framework of Beacon project to simulate CRT experiment give a well estimation of the final state of the bentonite component.

5 Febex

5.1 Main feature of the test – why it is relevant for Beacon

Full-scale Engineered Barrier Experiment in Crystalline Host Rock, is a research and demonstration project that was initiated by ENRESA (Spain). The aim of the project is to study the behaviour of near-field components in a repository for high-level radioactive waste in granite formations. The main objectives of the project can be grouped in two areas:

- Demonstration of the feasibility of constructing the engineered barrier system in a horizontal configuration according to the Spanish concept for deep geological storage, and analysis of the technical problems to be solved for this type of disposal method,
- Better understanding of the thermo-hydro-mechanical (THM) and thermo-hydrogeochemical (processes in the near field, and development and validation of the modelling tools required for interpretation and prediction of the evolution of such processes.

Last section of FEBEX was dismantled after 18 years of heating and natural hydration.

The gaps between the bentonite blocks and at the bentonite-granite interface play certainly an important role in saturation process and stress development. This leads to local variations in porosity with an impact on hydraulic properties. Gaps can be considered as initial heterogeneities in the system and this test is effectively relevant for Beacon project. Thermal stress and the natural hydration pathway also play an important role in the evolution of bentonite influencing the final state. How the model will be able to predict first the evolution of the bentonite blocks and then the final distribution of main properties such as dry density, total pressure or water content is in perfect line with the objectives of this project.

5.2 ICL

5.2.1 Geometry and discretization

An axi-symmetric finite element analysis was performed to simulate the Febex experiment. A detail of the finite element mesh is shown in Figure 5-1, representing the 17.4 m length and 1.14 m radius of the Febex tunnel. The full mesh extends to 50 m in both the x and z coordinate directions and consists of 5742 8-noded quadrilateral elements. As the analysis is thermo-hydro-mechanically coupled, pore pressure degrees of freedom are adopted at the corner nodes, while displacement and temperature degrees of freedom are adopted at all nodes of each element. The z-direction is the axis of symmetry.

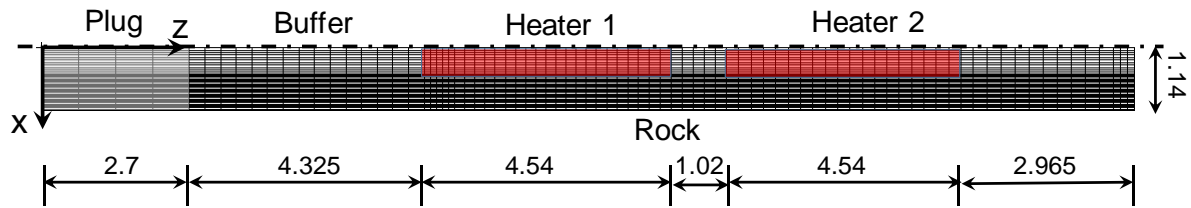


Figure 5-1 Finite element mesh for Febex experiment

The bentonite buffer is discretised with 40 elements in the radial, x-direction, of which 30 elements are placed between the heaters and the rock, giving the smallest element size of 0.023m across the 0.69m thickness of the buffer at that locality.

5.2.2 Input parameters

Febex bentonite buffer

The constitutive models for the simulation of the mechanical and hydraulic behaviour of the compacted Febex bentonite, introduced in section 2.7, were calibrated on the experimental data sourced principally from ENRESA (2000), FEBEX (2017), Villar (2005).

The input parameters for the mechanical model ICDSM are summarised in

Table 5-1.

Table 5-1 Input parameters for the ICDSM for Febex bentonite

Parameter	Value
Parameters controlling the shape of the yield surface, α_f, μ_f	0.4 , 0.9
Parameters controlling the shape of the plastic potential surface, α_g, μ_g	0.4 , 0.9
Strength parameters, M_f, M_g	0.5
Characteristic pressure, p_c (kPa)	500
Fully saturated compressibility coefficient, $\lambda(0)$	0.2
Elastic compressibility coefficient, κ	0.06
Maximum soil stiffness parameter, r	0.61
Soil stiffness increase parameter, β (1/kPa)	0.00007
Elastic compressibility coefficient for changes in suction, κ_s (kPa)	0.02
Poisson ratio, ν	0.4
Plastic compressibility coefficient for changes in suction, λ_s	0.5
Air-entry value of suction, s_{air} (kPa)	1000
Yield value of equivalent suction, s_0 (kPa)	10^6
Cohesion increase parameter, k Constant or S_r	S_r
Microstructural compressibility parameter, κ_m	0.1
Void factor, VF	0.3
Coefficients for the micro swelling function, c_{s1}, c_{s2}, c_{s3}	-0.1, 1.1, 2.0
Coefficients for the micro compression function, c_{c1}, c_{c2}, c_{c3}	-0.1, 1.1, 2.0

The input parameters for the soil water retention (SWR) model are summarised in Table 5-2, while the calibrated SWR curve is shown in Figure 5-2.

Table 5-2 Input parameters for the SWR model for Febex bentonite

Parameter	Value
Air entry suction, s_{air} [kPa]	1000
Fitting parameter, α	0.00002
Fitting parameter, n	1.7
Fitting parameter, m	0.4
Effect of specific volume, ψ	0
Residual degree of saturation, S_{r0}	0

The parameters for the hydraulic permeability model, as depicted in Figure 2-2, are summarised in Table 5-3.

Table 5-3 *Input parameters for the variable permeability model for Febex bentonite*

Parameter	Value
Saturated permeability, k_{sat} [m/s]	$1 \cdot 10^{-13}$
Minimum permeability, k_{min} [m/s]	$0.8 \cdot 10^{-14}$
Suction, p_1 [kPa]	1000
Suction, p_2 [kPa]	20000

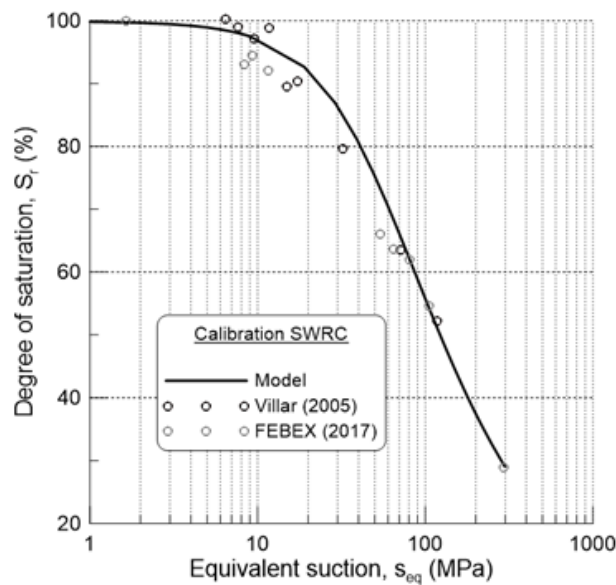


Figure 5-2 *Calibrated SWR curve for compacted Febex bentonite*

In terms of its thermal characteristics, the Febex bentonite is characterised with a thermal conductivity of $0.55 \cdot 10^{-3}$ kW/mK, a specific heat capacity of the solid phase of 870 J/kgK and a thermal expansion coefficient of $6.5 \cdot 10^{-6}$ K⁻¹.

Host rock

The mechanical behaviour of the host rock is simulated with an unsaturated Mohr-Coulomb model, but with the assumption of having a purely cohesive behaviour. Consequently, the angle of shearing resistance, $\phi = 0$, while the cohesion is set at $c = 10$ MPa.

The hydraulic conductivity is taken as constant and equal to 10^{-12} m/s (FEBEX, 2017). The data for the rock’s retention behaviour were sourced from Pintado & Lloret (1997) and Finsterle & Pruess (1995) and shown in Figure 5-3. They

demonstrate a significant scatter, but are also concentrated over a limited suction interval (up to ~2 MPa), indicating that the rock would saturate and de-saturate almost instantaneously. As it has been assumed that the source of water for the buffer hydration was unlimited, the rock is modelled as saturated at all times, by prescribing a high $s_{air} = 150$ MPa in the SWR model (Table 5-4).

Table 5-4 *Input parameters for the SWR model for rock*

Parameter	Value
Air entry suction, s_{air} [MPa]	150
Fitting parameter, α	0.4
Fitting parameter, n	0.9
Fitting parameter, m	0.2
Residual degree of saturation, S_{r0}	0.2

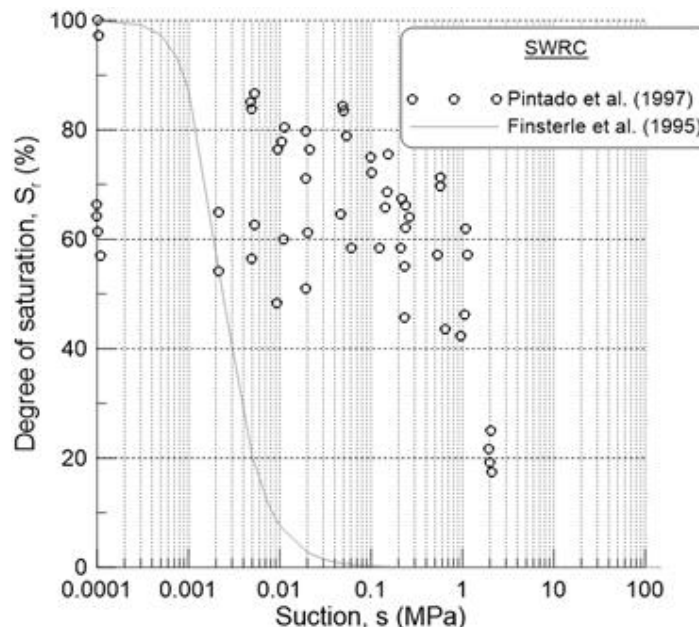


Figure 5-3 *Data for the retention characteristics of the host rock*

The thermal properties of the rock are a value of $3.2 \cdot 10^{-3}$ kW/mK for the thermal conductivity, 920 J/kgK for the specific heat capacity and $8 \cdot 10^{-6}$ K⁻¹ for the coefficient of thermal expansion.

5.2.3 Initial and boundary conditions

The finite element analysis of the Febex experiment is initialised with only the host rock occupying the complete finite element mesh. The initial state of the rock is assumed saturated, with isotropic initial total stresses of 28 MPa, pore water pressure of 4.5 MPa, void ratio of 0.6, density of 2.64 g/cm³ and

temperature of 10° C.

The subsequent steps of the analysis simulate the two phases of the experiment, Phase 1 over the first ~5 years and Phase 2 over the subsequent ~13 years. The key stages are summarised in Table 5-5, indicating the applied boundary conditions and the duration of each stage. Overall, the analysis simulates tunnel excavation in the host rock (removal of the relevant elements), emplacement of the buffer, heaters and concrete plug, 5 years of heating and hydration in Phase 1, excavation for the dismantling of Heater 1 after 5 years, construction of the new plug and the remaining heating and hydration processes for the next 13 years (Phase 2). Figure 5-4 shows a schematic view of the emplaced parts of the buffer and heaters in the Febex tunnel, for both phases of the experiment.

Upon construction, the state of the buffer is initialised with a suction, $s = 120$ MPa, void ratio, $e = 0.66$, temperature, $T = 12^\circ$ C, dry density, $\rho_d = 1.65$ g/cm³, water content $w = 12.2\%$ and degree of saturation, $S_r = 50\%$.

The elements of the heater are prescribed an initial temperature of $T = 12^\circ$ upon construction.

Table 5-5 Key stages of the Febex analysis

Stage number	Phase	Brief description	Start time (day)	Duration (days)
1	Phase 1	Tunnel excavation	-66	24
2		Buffer and heater construction	-42	42
3		Temperature increase in both heaters from $T_{init} = 12^\circ\text{C}$ to $T_{final} = 100^\circ\text{C}$	0	60
4		Phase 1 operation of the test at $T = 100^\circ\text{C}$	61	1725
5		Heater #1 switched off; $\Delta T = -2.5^\circ\text{C}$	1726	1755
6		Excavation for first dismantling of plug, part of buffer and heater #1	1756	1836
7		Construction of dummy canister and new plug	1837	1852
8	Phase 2	Phase 2 operation – only heater #2	1853	6152

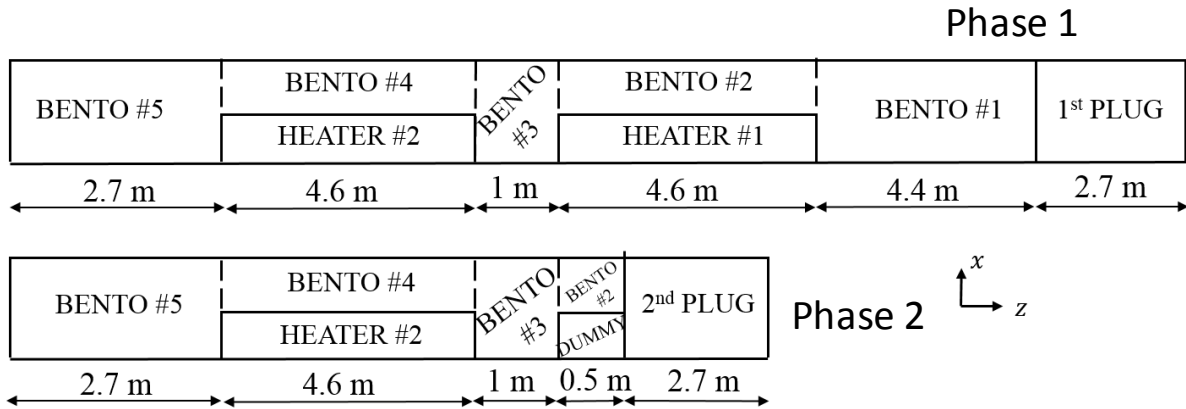


Figure 5-4 Details of the materials in the Febex tunnel in Phase 1 and Phase 2 of the simulated experiment

5.2.4 Results/discussion

A selection of the results is presented in this report, principally comparing the calculated evolution of the buffer’s thermo-hydro-mechanical behaviour over the 18 years of the experiment, against the available field measurements. Additionally, some of the available post-mortem analyses of the field data are compared against numerical predictions.

Thermo-hydro-mechanical evolution of the buffer

Figure 5-5 shows a schematic view of the Febex tunnel at Phase 2 of the experiment, with cross-sections interrogated for the Beacon project marked on the figure. The output was required for the evolution of temperature, total stress, pore pressure and relative humidity at selected measurement points in each cross-section.

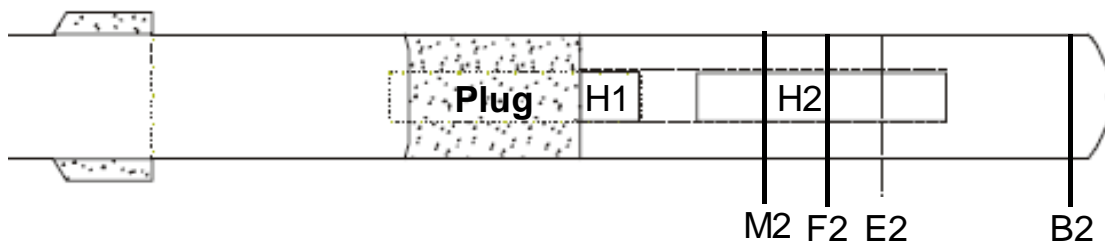


Figure 5-5 Schematic view of the Febex tunnel and cross-sections investigation for Beacon

Figure 5-6 compares the evolution of the measured and calculated temperature in the buffer section F2. The measurement points are shown in the inset on the right, which depicts their position in the F2 section. The sensors at the interface with the heater H2 (01, 02, 03, 04) indicate a measured temperature range of around 90° to 100° C while the numerical prediction (F2-03res) is at 100° C, as this was the applied boundary condition in the analysis. It would be expected that all four temperature sensors at the

buffer/heater interface measure similar temperatures and the reason for the observed discrepancy is not clear. The calculated temperature distribution across the thickness of the buffer is in good agreement with measurements at sensors 06 (~90° C) and 05 (~70° C). It is also observed that the temperature field in the buffer was established very early in the experiment and the numerical model follows this very closely. In general, the evolution of the temperature fields in other sections of the buffer was well captured by the numerical model.

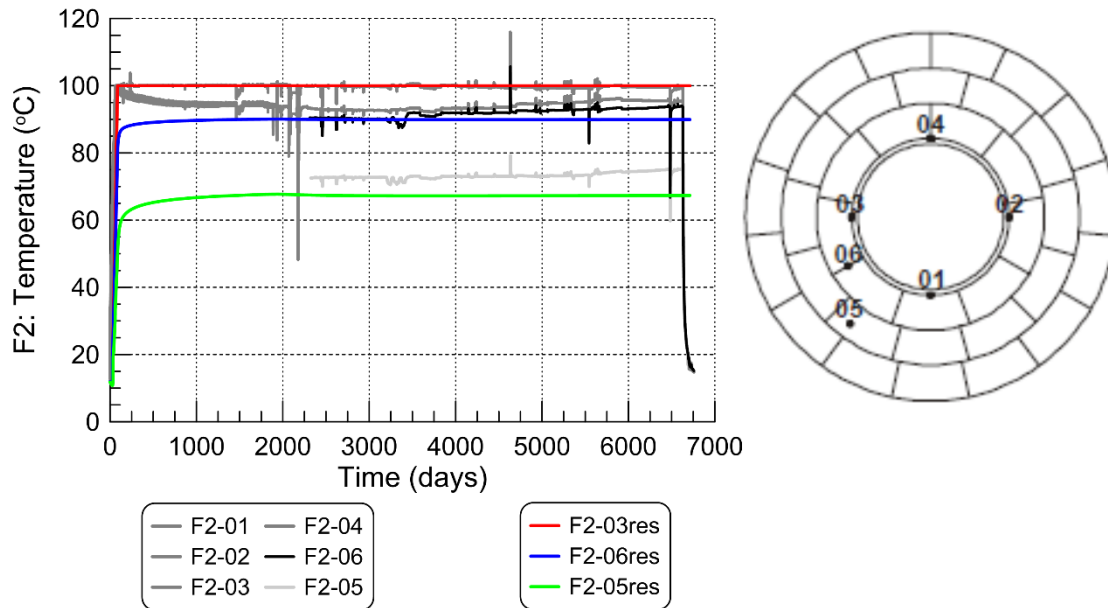


Figure 5-6 Measured and calculated temperature evolution in section F2

Figure 5-7 compares the evolution of the measured and predicted radial total stress in the buffer in section F2. Sensors 01, 02, 03 and 04, all located at the buffer/rock interface, show some discrepancy in the measurements over the duration of Phase 1 (first 5 years) of the Febex experiment, with sensor 01 indicating much higher stress values compared to the other three, which show similar measurements. The numerical prediction of the interface radial total stress (F2-01res) agrees well with the magnitude of the total stress measured in sensors 02, 03 and 04 at the end of Phase 1, after which they ceased to work, and indicates a steady gradient of stress increase until the end of the experiment. This gradient is in good agreement with that derived from sensors 05 and 06, which became operational after Phase 1, as well as with the gradient of the total radial stress evolution in sensor 01 during Phase 2. Both the measurements and numerical results indicate marginal difference in the radial total stress values across the buffer thickness.

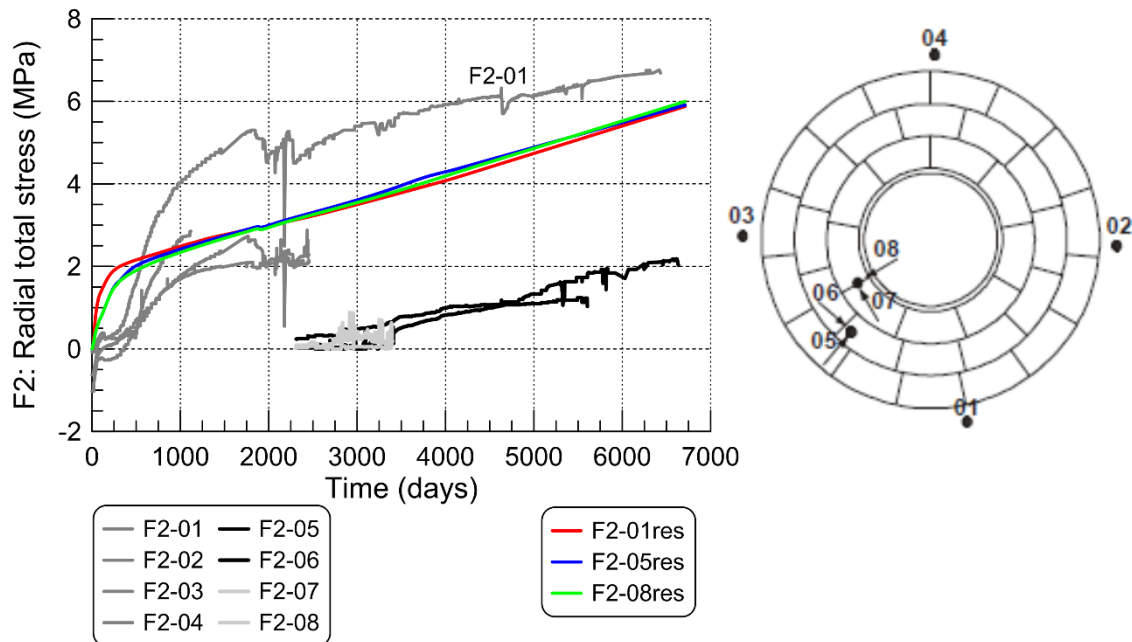


Figure 5-7 Measured and calculated evolution of the radial total stress in Section F2

Further examination of the calculated evolution of the radial total stress is offered in Figure 5-8, showing section B2 (see Figure 5-5) which contains only the buffer. The measurements further indicate little difference in stress values across the buffer (as seen in section F2) and the numerical results agree very well with the measurements in section B2 and with the calculated radial total stress evolutions in section F2 (Figure 5-7). Based on the measurements and modelling results in Figure 5-7 and Figure 5-8, it may be concluded that the measurement in sensor F2-01 is not representative of the actual stress state in the buffer and that the numerical results provide a realistic evolution of the total stress field in the buffer.

The evolution of the relative humidity (RH) is shown in Figure 5-9 for section F2. The sensors in the outer ring of the buffer (close to the rock) indicate a rapid RH increase to around 90-100 %, facilitated by the vicinity of the wetting boundary at the rock interface. The numerical result (F2-05res) shows an initially rapid RH increase, then reaching 100% more gradually. The calculated RH evolution in the middle ring (F2-03res) agrees well with the range of measurements taken in that ring. The RH measurements in the inner ring (closest to the heater) are only partial and differ significantly. The numerical result (F2-14res) in this ring agrees well with the depicted measurement in sensor 14.

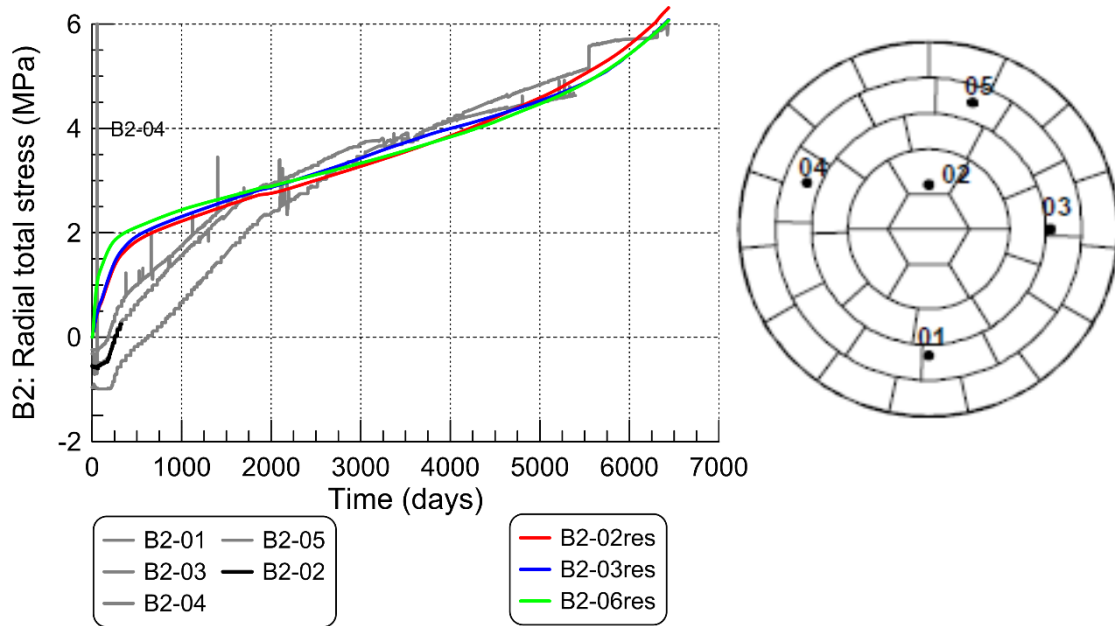


Figure 5-8 Measured and calculated evolution of the radial total stress in Section B2

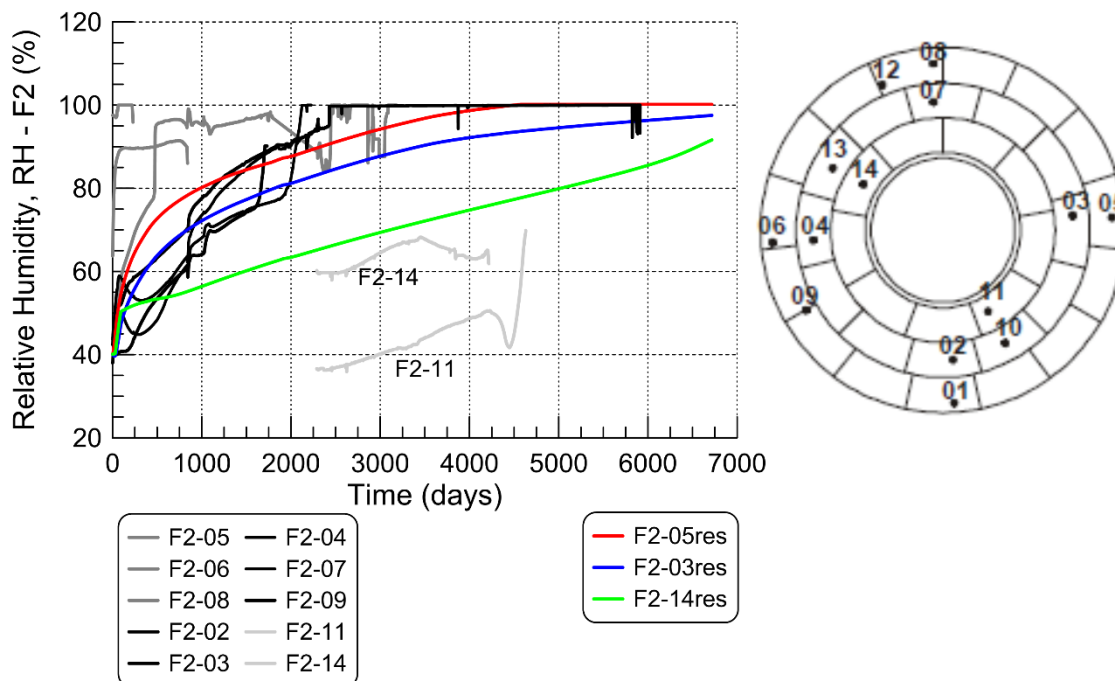


Figure 5-9 Measured and calculated evolution of the relative humidity in Section F2

Post-mortem analysis

Following the completion of the Febex experiment, a number of buffer samples were taken for analysis during the dismantling process. Four sections, 49, 52, 56 and 61, as depicted in Figure 5-10, have been explored for the Beacon project, interpreting degree of saturation, S_r , water content, dry density, ρ_d , and relative humidity, RH.

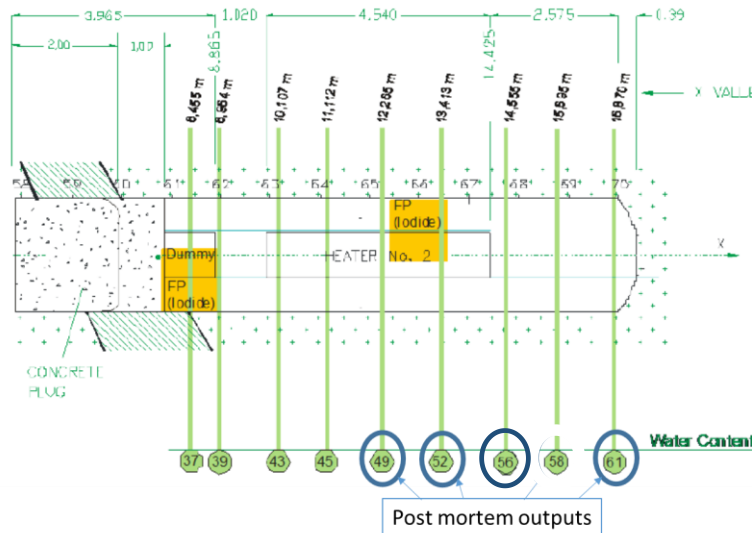
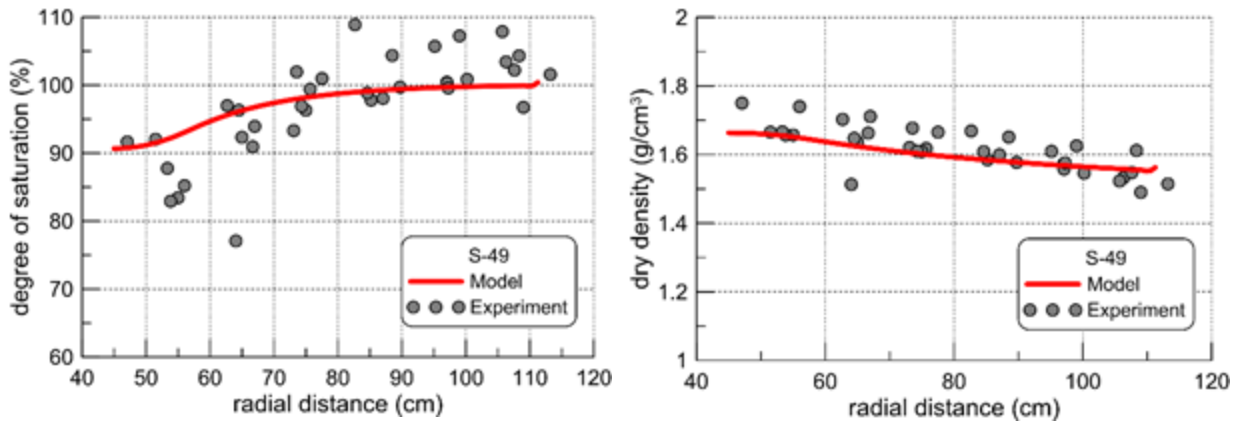


Figure 5-10 Febex buffer sections for post-mortem analyses

Again, only a selection of results is shown in this report, including section 49 in the middle of the Heater 2. The degree of saturation is a direct output from the analysis. To calculate the relative humidity, the temperature and the suction in each section are retrieved as direct outputs of the analysis, while the universal gas constant $R = 8.31432 \text{ J/molK}$, the molecular mass of water vapour, $M_w = 18.016 \text{ kg/kmol}$ and the density of water $\rho_w = 998 \text{ kg/m}^3$. To calculate the water content the specific gravity of the bentonite is taken as 2.72 g/cm^3 , while for the interpretation of dry density, the bulk density of the bentonite is taken as 2.05 g/cm^3 .



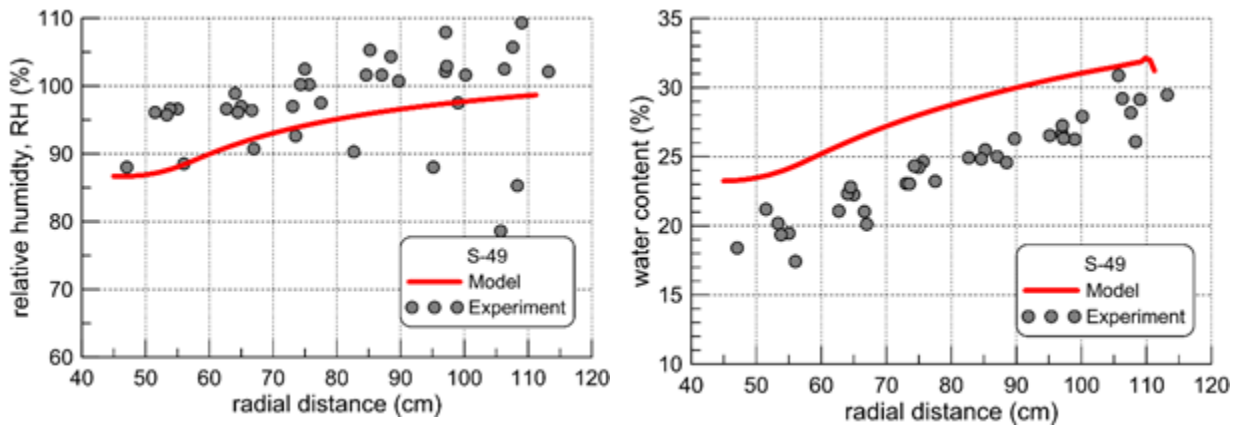


Figure 5-11 Post-mortem analysis of section 49

The results in Figure 5-11, and in the remaining sections (52, 56 and 61) not shown here for brevity, indicate good agreement between the field measurements and numerical results derived from the analysis of the Febex experiment.

In general, the in-situ measurements have been shown to be reasonably consistent, despite the inevitable experimental scatter. In particular, the measurements at the start of the Febex experiment show different starting points, some lag in the response, even negative initial values or $S_r > 100\%$. The results from the numerical modelling of the Febex experiment presented in this section show good agreement and consistency with the experimental data, verifying the accuracy and robustness of the adopted numerical model.

5.2.5 Lessons learnt

The numerical model developed for the simulation of the Febex experiment is thought to have reproduced very well the measured thermo-hydro-mechanical evolution of the Febex buffer. Both the rate of temperature change and the temperature field across the buffer thickness are reproduced well.

Most of the measurements of the total radial stress and relative humidity (RH) evolutions indicate uncertain starting points (Figure 5-7, 5-8, 5-9). Equally, some of the sensors at the same radial distance from the heater, but at different locations around the perimeter, show significantly different magnitudes of the measured quantities. However, if carefully interpreted, the measurements seem consistent and the model predicts well the evolution of both the total radial stress and relative humidity. Some discrepancy is, nonetheless, observed in the rate of the relative humidity evolution, in particular at locations near the rock interface where measurements indicate a rapid increase of RH to around 100%. The model reproduces the same rate initially, but then slows down and reaches the 100% value later in the experiments. The reason for this is not believed to be in the formulation of the

hydro-mechanical models, but in the selection of model input parameters. In particular, the prescribed rate, in the variable permeability model, of the hydraulic conductivity change during buffer saturation is likely to be lower. Also, the parameters of the ICDSM model that define the interaction function that controls the evolution of the micro-structure may need be adjusted to achieve a better prediction.

The post-mortem analysis of the measurements of dry density, relative humidity, degree of saturation and water content in transverse sections of the buffer indicate scatter and also some unrealistic values (e.g. degree of saturation and relative humidity measurements of over 100%). However, numerical calculations average well the measured scatter and, more importantly, do not predict unrealistic values.

5.3 LEI

5.3.1 Geometry and discretization

The CODE_BRIGHT model for FEBEX experiment has been done under 2-D axis-symmetric geometry (gravity is not considered) along the longitudinal axis of the tunnel. Only part of the tunnel was analysed - the length of the model is 9.13 m and the outer boundary is at a distance of 50 m as it could be seen in Figure 5-12. The bentonite barrier and granite are modelled materials while heaters are not modelled itself but considered as temperature boundary conditions. The presence of the access drift and the concrete plug is not taken into account as well as the steel liner. The analysed domain was discretized into 2637 quadrilateral mesh elements. Model has less mesh elements in the host rocks and is more discretized in bentonite buffer to reduce numerical errors and to have more accurate modelling result for the comparison with measurements.

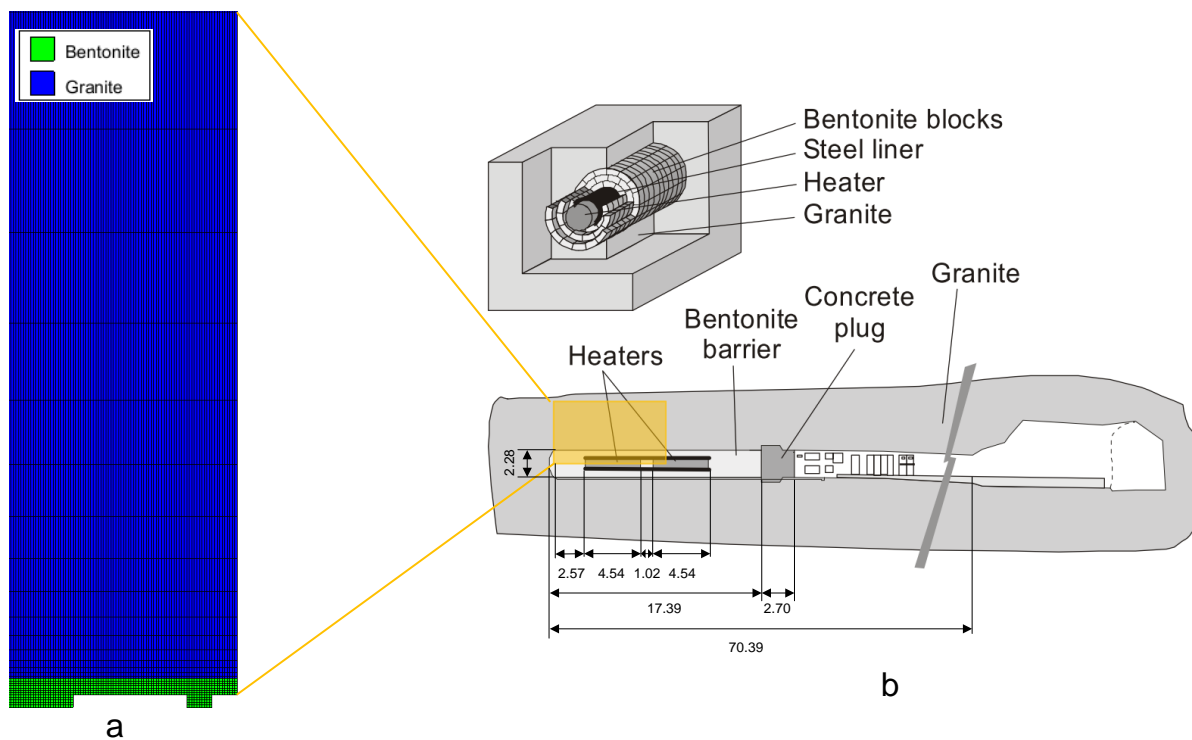


Figure 5-12. Geometry, materials and mesh considered for LEI used CODE_BRIGHT model (a); cross and longitudinal sections of FEBEX tunnel (b) (modified from Martinez et al., 2016)

5.3.2 Input parameters

Before selection of input parameters for LEI model, the analysis of THM parameter values published in scientific papers and reports were performed. The research papers and reports presenting modelling results of FEBEX in-situ or mock-up experiments were analysed in details. The list of analysed references

and LEI modelled cases are summarised in Table 5-6.

Table 5-6. Summary of analysed literature and LEI modelled cases

Authors	FEBEX experiment	Modelling tool	LEI modelled cases
ENRESA, 1999	In-situ	CODE_BRIGHT	<u>Case1a</u> - drying retention curve for bentonite and BBM parameters for bentonite at dry density 1.6 g/cm ³ <u>Case1b</u> - wetting retention curve for bentonite and BBM parameters for bentonite at dry density 1.6 g/cm ³ <u>Case1c</u> - drying retention curve for bentonite and BBM parameters for bentonite at dry density 1.7 g/cm ³
A. Rodriguez-Dono et al., 2018	In-situ	CODE_BRIGHT	Case2
L. Zheng, et al., 2020	In-situ	TOUGHREACT-FLAC3D	Case3 - values of BBM parameters for bentonite considered the same as in Case2, while mechanical model is different as BBM
CODE_BRIGHT tutorial example, 2019	Mock-up	CODE_BRIGHT	Case4
M. Villar et al., 2008	In-situ	CODE_BRIGHT	Case5

Initial values of THM parameters for bentonite and granite in analysed cases are summarized in Table 5-7 and Table 5-8, respectively. As some parameters necessary for LEI modelling were not reported in analysed literature, they were assumed the same as in the other analysed models and marked in red in both tables.

Table 5-7. Initial values of THM parameters for bentonite in analysed cases

Parameter	Case1a	Case1b	Case1c	Case2	Case3	Case4	Case5	LEI Case*	
Thermal	Thermal conductivity for dry conditions, λ_{dry} [W/m·°C]	0.5	0.5	0.5	0.47	0.47	0.47	0.5	
	Thermal conductivity for saturated conditions, λ_{sat} [W/m·°C]	1.28	1.28	1.28	1.15	1.15	1.15	1.28	
	Solid phase specific heat, C_s [J/kg·K]	1091	1091	1091	1000	1091	1000	1000	1091
Hydraulic	Air entry pressure, P_0 [MPa]	62	7	62	20	91	20	28	35
	Shape function of retention curve, λ [-]	0.42	0.35	0.42	0.18	0.45	0.18	0.18	0.3
	Residual saturation, S_{lr} [-]	0.01	0.01	0.01	0.01	0.1	0.01	0.01	0.01
	Maximal saturation, S_{ls} [-]	1	1	1	1	1	1	1	1

Parameter	Case1a	Case1b	Case1c	Case2	Case3	Case4	Case5	LEI Case*
Pressure related to the suction at zero degree of saturation, P_d [MPa]	-	-	-	-	-	-	1100	4000
Model parameter, λ_d [-]	-	-	-	-	-	-	1.1	1.5
Intrinsic permeability, k_0 [m ²]	6·10 ⁻²¹	6·10 ⁻²¹	6·10 ⁻²¹	1.9·10 ⁻²¹	2.15·10 ⁻²¹	5·10 ⁻²¹	1.9·10 ⁻²¹	3.92·10 ⁻²¹
Reference porosity for intrinsic permeability, ϕ_0 [-]	0.407	0.407	0.407	0.4	0.41	0.4	0.4	0.41
Liquid phase relative permeability law	Power	Power	Power	Power	Power	Power	Power	Power
Index of Power law (PL)	3	3	3	3	3	3	3	3
Diffusion coefficient of vapour in air, D_a^g , [m ² /s]	5.9·10 ⁻⁶	5.9·10 ⁻⁶	5.9·10 ⁻⁶	5.9·10 ⁻⁶	7.03·10 ⁻⁵	5.9·10 ⁻⁶	5.9·10 ⁻⁶	1.25·10 ⁻⁵
Coefficient of tortuosity, τ [-]	1	1	1	0.8	0.8	0.8	0.8	0.8
Dry density, ρ_{dry} [g/cm ³]	1.6	1.6	1.7	1.664	1.63	1.662	1.66	1.623
Solid density, ρ_{solid} [g/cm ³]	2.7	2.7	2.7	2.773	2.78	2.77	2.773	2.75
Initial porosity, n [-]	0.407	0.407	0.37	0.4	0.41	0.4	0.4	0.41
Initial (zero suction) elastic slope for specific volume-mean stress, K_{io} [-]	0.05	0.05	0.05	0.05	0.05	0.05	0.04	0.02
Initial (zero suction) elastic slope for specific volume-suction, K_{so} [-]	0.25	0.25	0.3	0.25	0.25	0.3	0.25	0.1
Minimal bulk module, K_{min} [MPa]	0.1	0.1	0.1	0.1	0.1	0.1	0.1	0.1
Poisson's ratio, ν [-]	0.4	0.4	0.4	0.4	0.4	0.4	0.4	0.4
Parameter for K_s , a_{ss} [-]	-0.03	-0.03	-0.03	-	-	-	-	-0.02
Parameter for K_i , a_i [-]	-0.003	-0.003	-0.003	-0.003	-0.003	-0.003	-0.003	-
Parameter for K_s , a_{sp} [-]	-0.1609	-0.1609	-0.147	-0.161	-0.161	-0.147	-0.147	-0.161
Reference mean stress, p_{ref} [MPa]	0.01	0.01	0.01	0.01	0.01	0.01	0.01	0.01
Parameter for thermal expansion due to elastic strain, a_0 [1/°C]	1.5·10 ⁻⁴	1.5·10 ⁻⁴	1.5·10 ⁻⁴	1.5·10 ⁻⁴	1.5·10 ⁻⁴	1.5·10 ⁻⁴	1.5·10 ⁻⁴	1.5·10 ⁻⁴
Slope of void ratio - mean stress curve at zero suction, $\lambda(0)$ [-]	1.5	1.5	1.5	0.15	0.15	0.15	0.15	1.5
Parameter defining the maximal soil stiffness, r [-]	0.75	0.75	0.75	0.925	0.925	0.75	0.75	0.925
Parameter controlling the rate of increase of soil stiffness with suction, β [MPa ⁻¹]	0.05	0.05	0.05	0.05	0.05	0.05	0.05	0.05
Parameter that takes into account decrease of tensile strength due to temperature, ρ [1/°C]	0.2	0.2	0.2	0.2	0.2	0.2	0.2	0.2
Parameter that takes into account increase of tensile strength due to suction, k [-]	0.1	0.1	0.1	0.1	0.1	0.1	0.1	0.1

Mechanical

Beacon

D5.2.2 – Synthesis of the results obtained of test cases from task 5.2

Dissemination level: PU

Date of issue: 15/07/2020

Parameter	Case1a	Case1b	Case1c	Case2	Case3	Case4	Case5	LEI Case*
Tensile strength in saturated conditions, p_{s0} [MPa]	0.1	0.1	0.1	0.1	0.1	0.1	0.1	0.1
Reference pressure, p^c [MPa]	0.1	0.1	0.1	0.5	0.5	0.1	0.1	0.5
Critical state line parameter, M [-]	1.5	1.5	1.5	1	1	1	1.5	1
Non-associativity parameter, a [-]	0.395	0.395	0.395	0.53	0.53	0.3	0.395	0.53
Initial preconsolidation mean stress for saturated soil, p_0^* [MPa]	8	8	14	12	12	14	14	12

* Selected initial values of THM parameters for bentonite in LEI used CODE_BRIGHT model

Table 5-8. Initial values of THM parameters for granite in analysed cases

Parameter	Case1a	Case1b	Case1c	Case2	Case3	Case4	Case5	LEI Case*	
Thermal	Thermal conductivity for dry conditions, λ_{dry} [W/m \cdot °C]	3.6	3.6	3.6	3.6	3.2	3.6	3.6	3.2
	Thermal conductivity for saturated conditions, λ_{sat} [W/m \cdot °C]	3.6	3.6	3.6	3.6	3.3	3.6	3.6	3.3
	Solid phase specific heat, C_s [J/kg \cdot K]	793	793	793	793	793	793	793	793
Hydraulic	Air entry pressure, P_0 [MPa]	2.1	2.1	2.1	0.1	2.1	0.1	0.1	2.1
	Shape function of retention curve, λ [-]	0.7	0.7	0.7	0.33	0.7	0.33	0.33	0.7
	Surface tension at 20°C, σ_0 [N \cdot m $^{-1}$]	0.072	0.072	0.072	-	-	-	-	-
	Residual saturation, S_{lr} [-]	0.01	0.01	0.01	0	0.01	0	0	0
	Maximal saturation, S_{ls} [-]	1	1	1	1	1	1	1	1
	Intrinsic permeability, k_0 [m 2]	8 \cdot 10 $^{-18}$	2 \cdot 10 $^{-18}$	8 \cdot 10 $^{-18}$	8 \cdot 10 $^{-18}$	2 \cdot 10 $^{-18}$			
	Liquid phase relative permeability law	VG	VG	VG	-	Power	-	-	-
	Shape function of Van Genuchten retention curve, λ [-]	0.5	0.5	0.5	-	-	-	-	-
	Index of Power law, n [-]	-	-	-	-	1	-	-	-
	Diffusion coefficient of vapour in air, D_a^v , [m 2 /s]	-	-	-	-	7.03 \cdot 10 $^{-5}$	-	-	-
Coefficient of tortuosity, τ , [-]	-	-	-	-	1	-	-	-	
Mechanica	Solid density, ρ_{solid} [g/cm 3]	2.7	2.7	2.7	2.75	2.7	2.75	2.75	2.7
	Porosity, n [-]	0.01	0.01	0.01	0.01	0.01	0.01	0.01	0.01
	Young modulus, E [GPa]	36.3	36.3	36.3	11.7	11.7	11.7	11.7	11.7
	Poisson's ratio, ν [-]	0.345	0.345	0.345	0.3	0.3	0.3	0.3	0.3

Parameter	Case1a	Case1b	Case1c	Case2	Case3	Case4	Case5	LEI Case*
Thermal expansion coefficient b_s [$1/^\circ\text{C}$]	$7.8 \cdot 10^{-6}$							

* Selected initial values of THM parameters for granite in LEI used CODE_BRIGHT model

Analysis of LEI modelling results using different sets of parameter values from Table 5-7 and Table 5-8 indicated that trend of temperature evolution correlates quite well between analysed cases and measurements. Figure 5-13 presents comparison of temperature evolution in bentonite, 10 cm away from the heater (section F2). Only modelled temperature of Case1b is lower compared to others cases and it is related to selected retention curve of bentonite, which influences on slower resaturation of buffer as it could be seen in Figure 5-14 and influence on the lower coefficient of thermal conductivity.

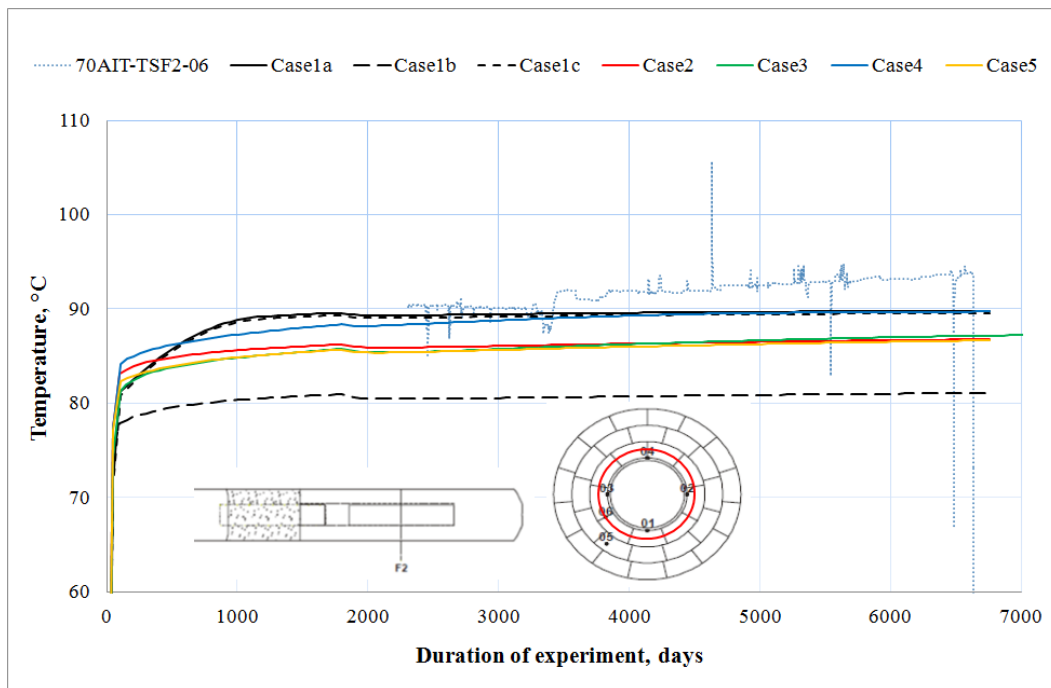


Figure 5-13. Comparison of modelling results (solid and dashed lines) and measurements (dotted lines) of temperature evolution in bentonite, 10 cm away from the heater (section F2)

However, modelling results of hydraulic and mechanical parameters are much more dispersed between analysed cases. For example, Figure 5-14 and Figure 5-15 present the comparison of the evolution of relative humidity and radial stress in section F2, in bentonite 10 cm away from the heater and in bentonite near the host rock, respectively.

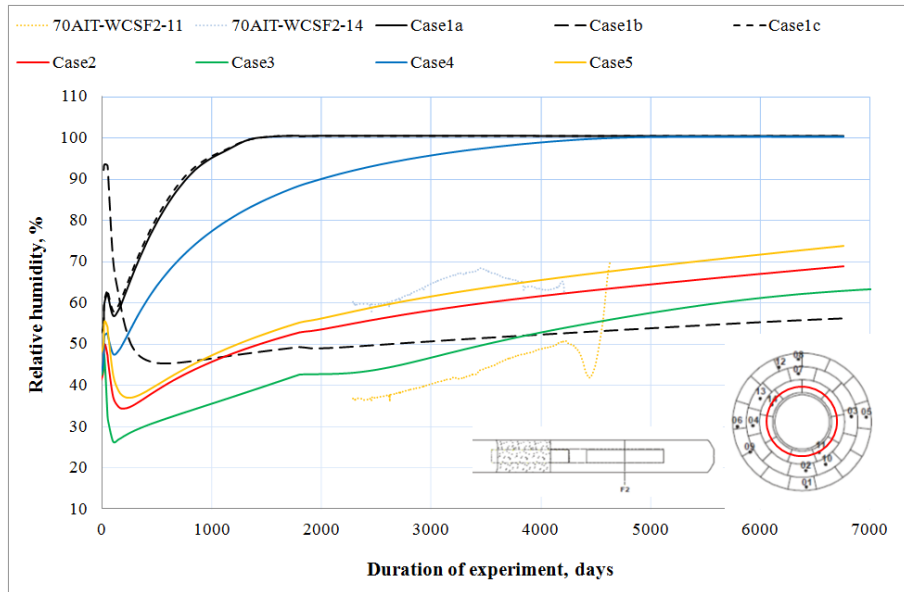


Figure 5-14. Comparison of modelling results (solid and dashed lines) and measurements (dotted lines) of the evolution of relative humidity in bentonite 10 cm away from the heater (section F2)

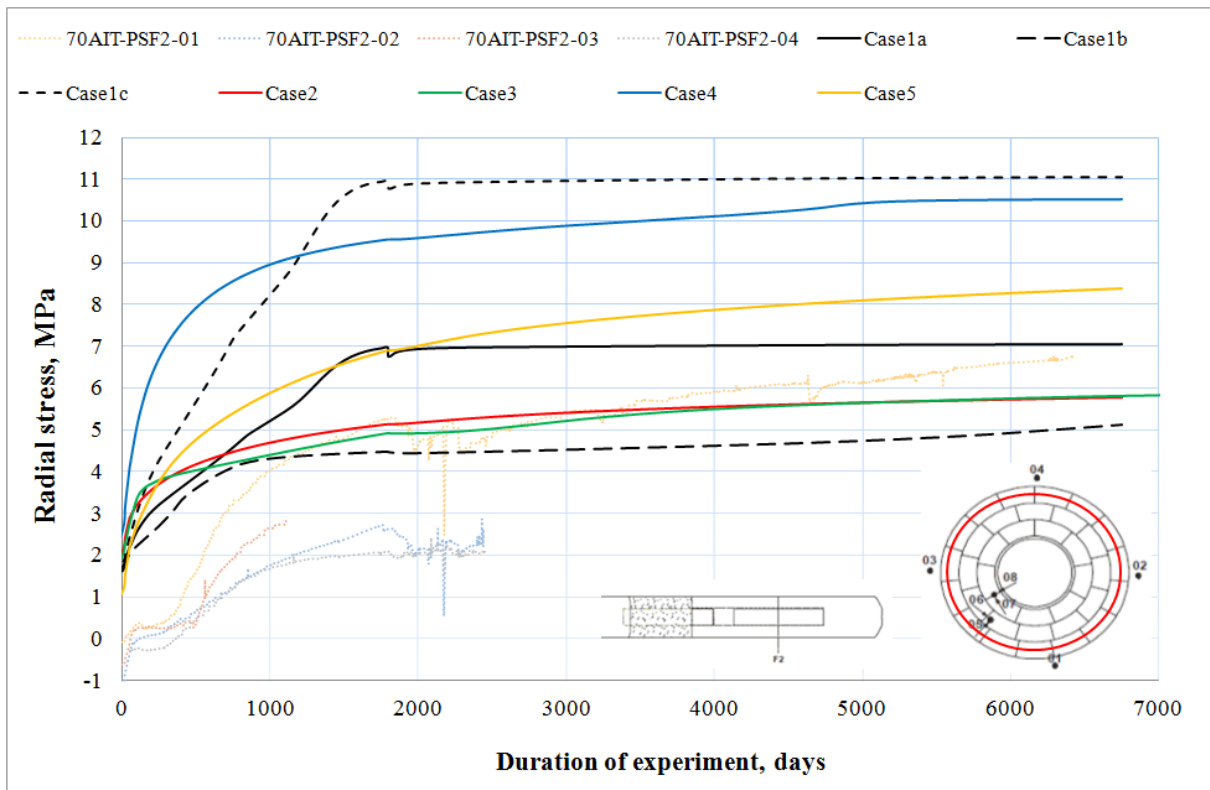


Figure 5-15. Comparison of modelling results (solid and dashed lines) and measurements (dotted lines) of the evolution of radial stress in bentonite near host rock (section F2)

As it could be seen in Figure 5-14, very different trends of the evolution of relative humidity were estimated between modelled cases. The results of Case1b, Case2, Case3 and Case5 were in between measured data, despite

these data are only for short period of time (slightly more than 2 000 days). Modelling results of radial stress were dispersed between analysed cases as well. The peak stress varies between 5 and 11 MPa, as the peak measured stress was more than 6 MPa. The results of Case2 and Case3 were the closest to the measured data.

The final step of LEI modelling work in this task was to compile the dataset of THM parameters (based on available experimental (Talandier, 2018) and modelling (Enresa, 1999) data) and to get the best correlation between model output and measurements (during FEBEX experiment and after dismantling). After precise testing of the model, the optimum as possible datasets for bentonite and granite were selected. They are presented in the last columns of Table 5-7 and Table 5-8, respectively.

5.3.3 Initial and boundary conditions

Boundary conditions

Thermal

Thermal boundary conditions in experiment stages considered in LEI used CODE_BRIGHT model are presented in Table 5-9.

Table 5-9. Experiment stages and thermal boundary conditions considered in LEI used CODE_BRIGHT model

No. of stage	Description of stage	Initial time, days	Final time, days	Duration, days
1	Stress equilibrium (no heating)	-155	-135	20
2	Construction (no heating)	-135	0	135
3	Heating: 1200 W/heater	0	21	21
4	Heating: 2000 W/heater	21	54	33
5	Heating: 100 °C temperature on surfaces of both heaters till switch-off of Heater #1	54	1827	1773
6	Heating: 100 °C temperature on surface of Heater #2	1827	6630	4803
7	Dismantling of experiment (no heating)	6630	6758	128
				Total: 6913

Heaters were not modelled itself but they were considered as thermal boundary conditions on bentonite surface (at $r=0.49$ m) for different modelling stages. At the outer boundary ($r=50$ m) the constant temperature of 12 °C was prescribed for all stages.

Hydraulic

At the outer boundary ($r=50$ m) the constant water pressure of 0.7 MPa was prescribed for all stages. For the other boundaries of model domain no flow

conditions were assumed.

Mechanical

At the outer boundary ($r=50$ m) the constant radial stress of 28 MPa was prescribed for all stages.

For the top, bottom and side boundaries of the model a zero displacement conditions were prescribed.

Initial conditions

Bentonite

The initial temperature assumed uniform and equal to 12 °C.

Based on sensors data in section M2 (Martinez et al., 2016), the initial (at time $t=0$) values of volumetric water content in bentonite are between 20 % and 23 %. It corresponds to degree of saturation of 49 % – 55 %. Taking into account installation time of bentonite (construction stage), the initial degree of saturation of 48 % was assumed to match the sensors data. According to adopted retention curve the initial suction was 160 MPa.

An initial uniform and isotropic stress field of 0.5 MPa (hydrostatic value) was assumed in bentonite.

Initial porosity in bentonite was assumed 0.41 (it corresponds to dry density of 1.623 g/cm³), taking into account potential gaps between blocks and technological voids.

Granite

Initial stages of the model simulate the excavation of the tunnel and subsequent mechanical and hydraulic equilibration. For this reason, initial conditions in granite correspond to situation before tunnel excavation.

The initial temperature in the entire host rock was assumed to be uniform and equal to 12 °C.

Despite the water pressure is not uniform around the drift region, the initial value of 0.7 MPa was considered.

The uniform and isotropic stress field of 28 MPa was assumed as initially and porosity was taken to be 0.01.

5.3.4 Results/discussion

In this section LEI modelling results using CODE_BRIGHT are presented and compared to measured data. Comparison was made in two sub-sections: first evolution in time of THM parameters (temperature, relative humidity, radial stress, dry density and volumetric water content) in various locations is presented; later analysis of post-mortem data (relative humidity, degree of saturation, gravimetric water content and dry density) was done.

Evolution in time of THM parameters

Temperature

The contours of temperature distribution in bentonite buffer around the heaters after each heating phase are shown in Figure 5-16. As it could be seen the temperature around the heaters rises progressively up to 100 °C. The temperature around the 1st heater dropped fast after it was switched-off (day 1827). The lowest temperature in bentonite was increased continuously from 12 °C to around 42 °C during heating phases. However, changing model geometry in axial direction (taking into account cemented plug and rock mass) would decrease this result.

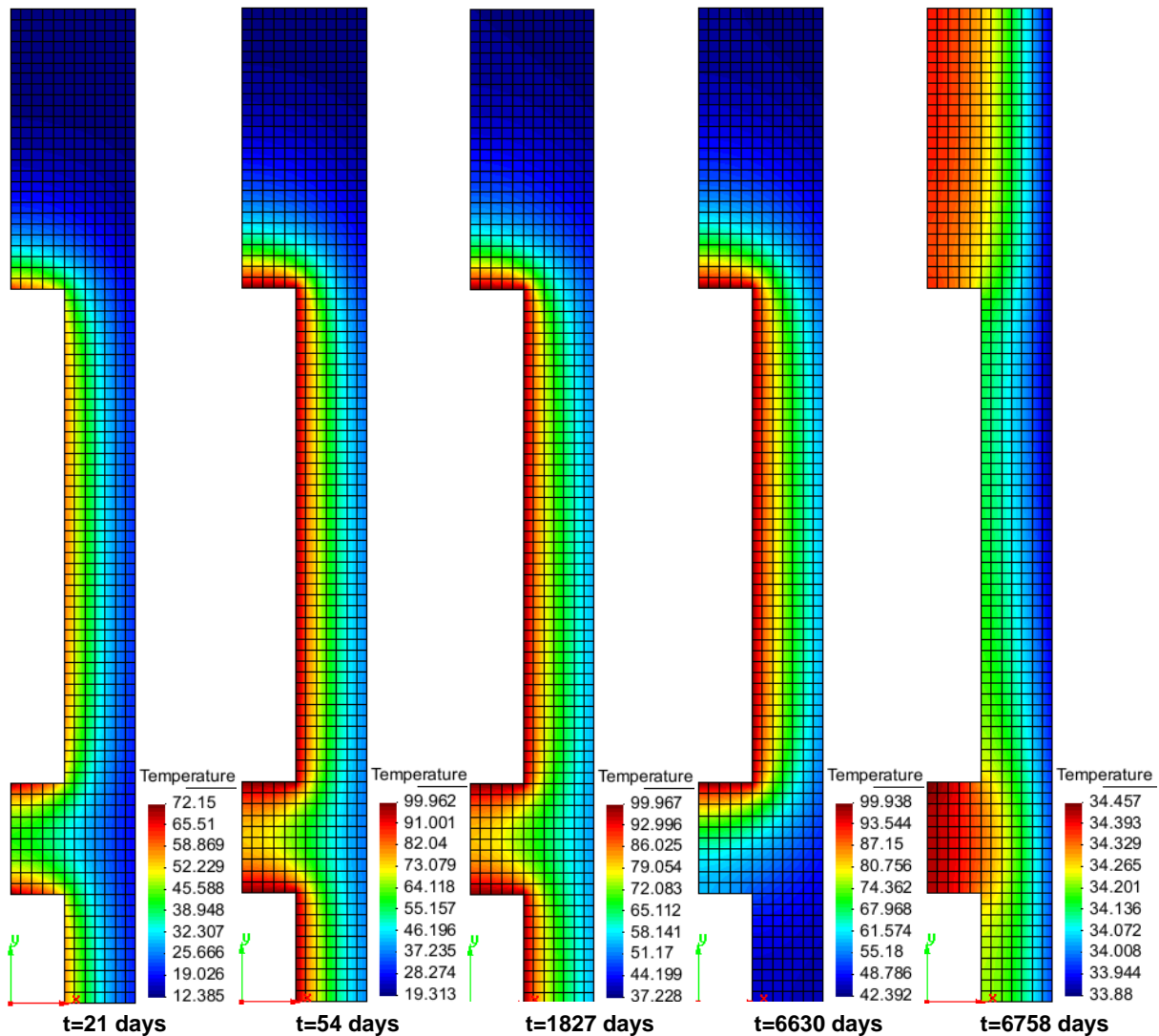


Figure 5-16. Contour of modelled distribution of temperature in bentonite buffer around the heaters after each heating phase

Modelling results and measured data of temperature evolution at particular bentonite points of section F2 are presented in Figure 5-17. As it could be seen modelled temperature at analysed points were in line with measured data without significant differences.

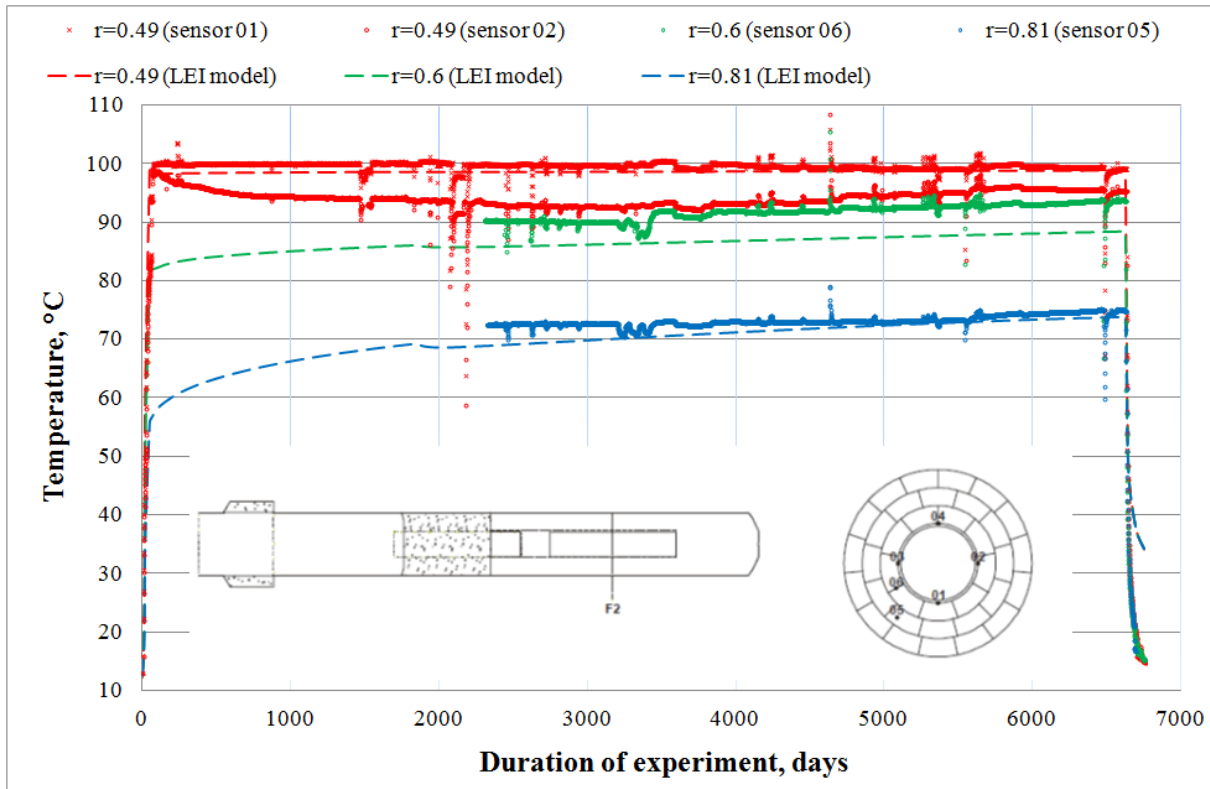


Figure 5-17. Comparison of LEI modelling results (dashed lines) and measurements (dotted lines) of temperature evolution at different radial distances of bentonite (section F2)

Relative humidity

The contours of distribution of relative humidity in bentonite buffer after each experiment stage are shown in Figure 5-18. It was observed that during the first 135 days (EBS construction stage) bentonite was allowed to hydrate. Predicted hydration results also revealed that relative humidity in bentonite near the heaters decreased during the first heating phases (results after 21 and 54 days) but later started to increase due to water flow from the host rock (results after 1827 and 6300 days). It is also could be seen that bentonite was not fully saturated just before or after dismantling phases (results after 6300 and 6758 days).

Modelling results and measured data of the evolution of relative humidity at particular bentonite points of section F2 are presented in Figure 5-19. As more than one sensor of relative humidity was installed at the same radial distance of section F2, the comparison of modelled and measured data were made in separate graphs. As it could be seen modelled result at $r=1.05$ were in line with measured data. However, correlation of the results 10 cm away from the heater ($r=0.6$) was not clear due to lack of measured data. The relative humidity profiles at $r=0.81$ correlate well up to 2 000 days, but full resaturation time in the model were much longer as measured data.

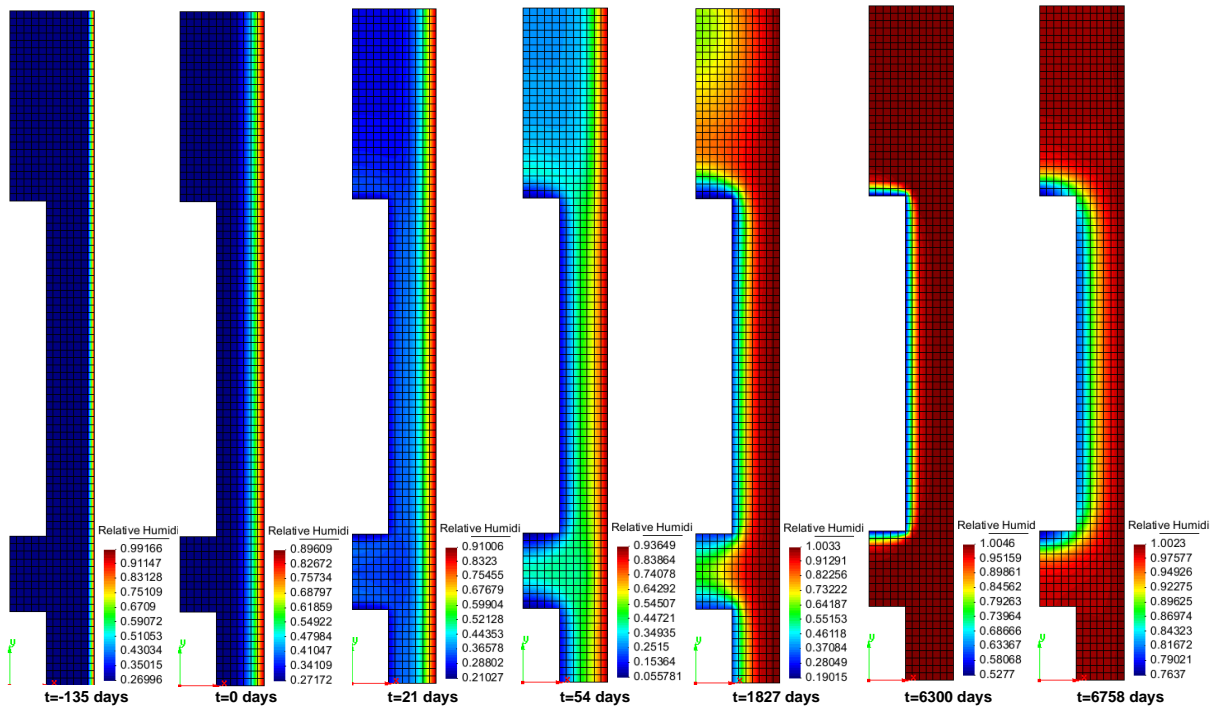


Figure 5-18. Contour of modelled distribution of relative humidity in bentonite buffer after each experiment stage

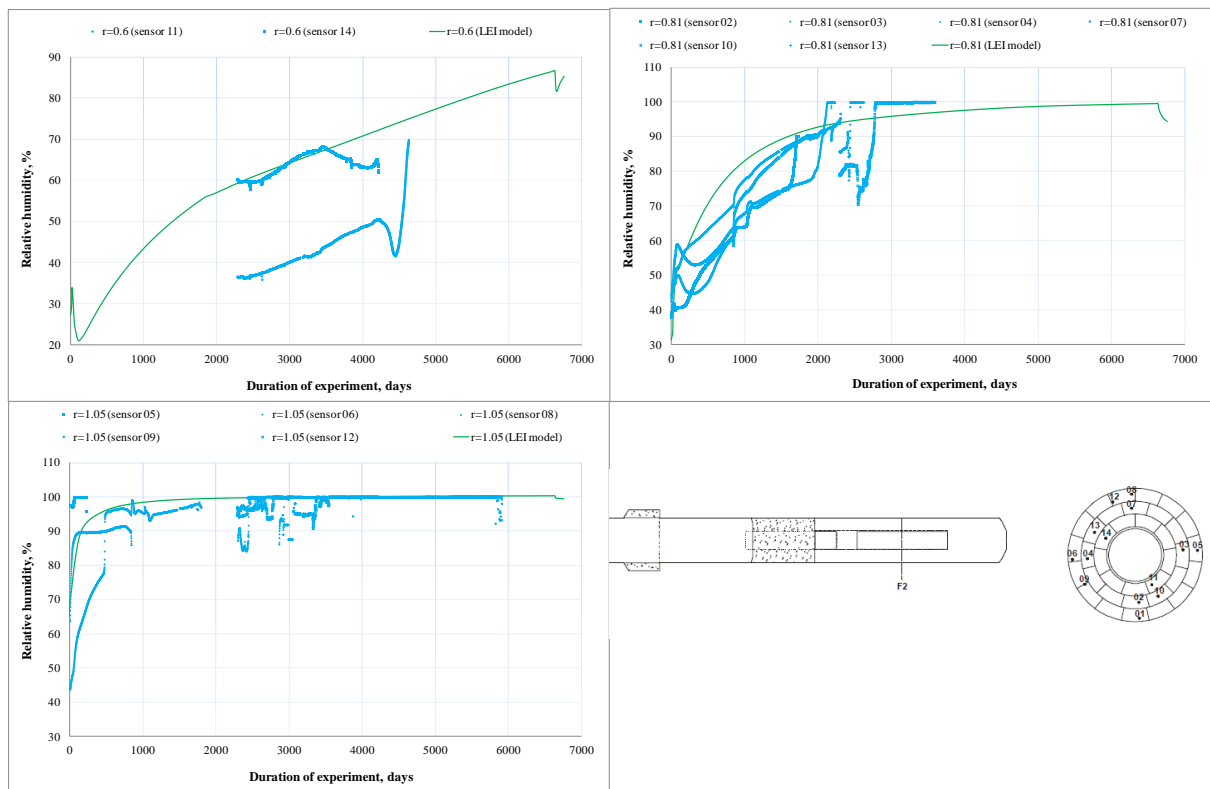


Figure 5-19. Comparison of LEI modelling results (solid green lines) and measurements (dotted blue lines) of the evolution of relative humidity at different radial distances of bentonite (section F2)

Radial stress

Beacon

D5.2.2 – Synthesis of the results obtained of test cases from task 5.2

Dissemination level: PU

Date of issue: 15/07/2020

Modelling results and measured data of the evolution of radial stress at particular bentonite points in three different sections are presented in Figure 5-20. All three sections were in bentonite buffer, just F2 and E2 were hot sections (had direct contact with heater) and B2 was cold section (no direct contact with heater).

Modelling results of radial stress at particular points of hot sections (F2 and E2) revealed that the higher stresses were obtained further away from the heater and this trend correlates well with measured data. However, the value of the peak stresses differs between modelled and measured data in hot sections. Despite lack of measured data in these sections, it could be concluded that model underestimated the peak stress at bentonite and host rock interface ($r=1.135$) and overestimated near the heater (at $r=0.49$ and $r=0.6$) and in the middle of bentonite ($r=0.81$). It was estimated that the highest radial stress in hot sections of the model reached 5.7 MPa.

Modelling results of radial stress at particular points of cold section (B2) showed good agreement with measured data at radial distance $r=0.76$. It was estimated that the highest radial stress in cold section of the model reached 6.5 MPa at radial distance $r=1.13$ (no measured data at this distance).

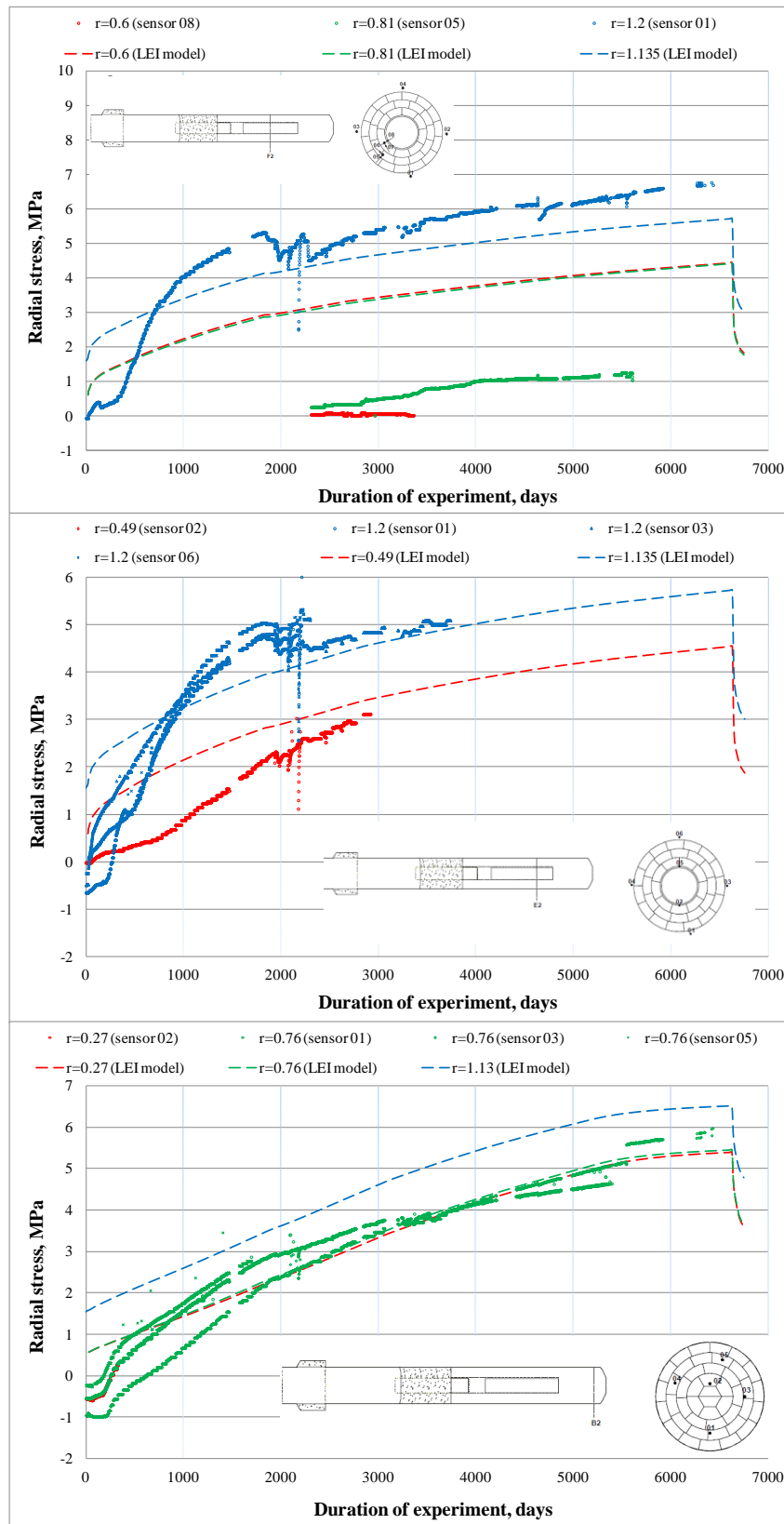


Figure 5-20. Comparison of LEI modelling results (dashed lines) and measurements (dotted lines) of radial stress evolution at different radial distances of bentonite in three different sections

Volumetric water content

Modelling results and measured data of the evolution of volumetric water content at particular bentonite points of section M2 are presented in Figure 5-21. As more than one sensor was installed in the same radial distances of section M2, the comparison of modelled and measured data were made in separate graphs. As it could be seen the modelled results correlate with measured data quit well, especially further away from the heater, at radial distances $r=0.74$, $r=0.85$ and $r=1.02$. Not so good correlation, especially after 4 500 days, were obtained in bentonite 10 cm away from the heater, at radial distances $r=0.59$.

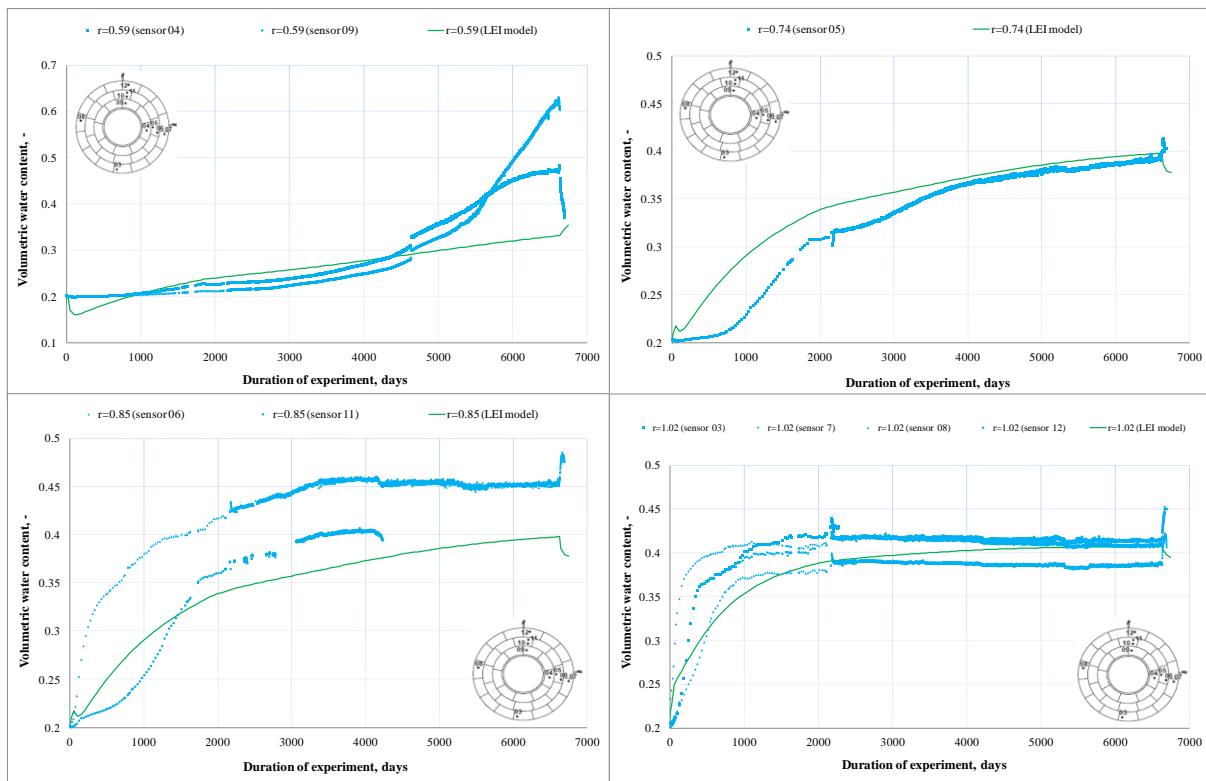


Figure 5-21. Comparison of LEI modelling results (solid green lines) and measurements (dotted blue lines) of the evolution of volumetric water content at different radial distances of bentonite (section M2)

Dry density

Comparison of modelling results of the evolution of dry density at particular bentonite points of hot and cold sections (F2 and B2) are presented in Figure 5-22. As it could be seen obtained values of dry density varied between 1.60 and 1.65 g/cm^3 in both sections. It corresponds to porosity changes between 0.418 and 0.4 , respectively. Initial dry density of bentonite was assumed 1.623 g/cm^3 (it corresponds to porosity 0.41).

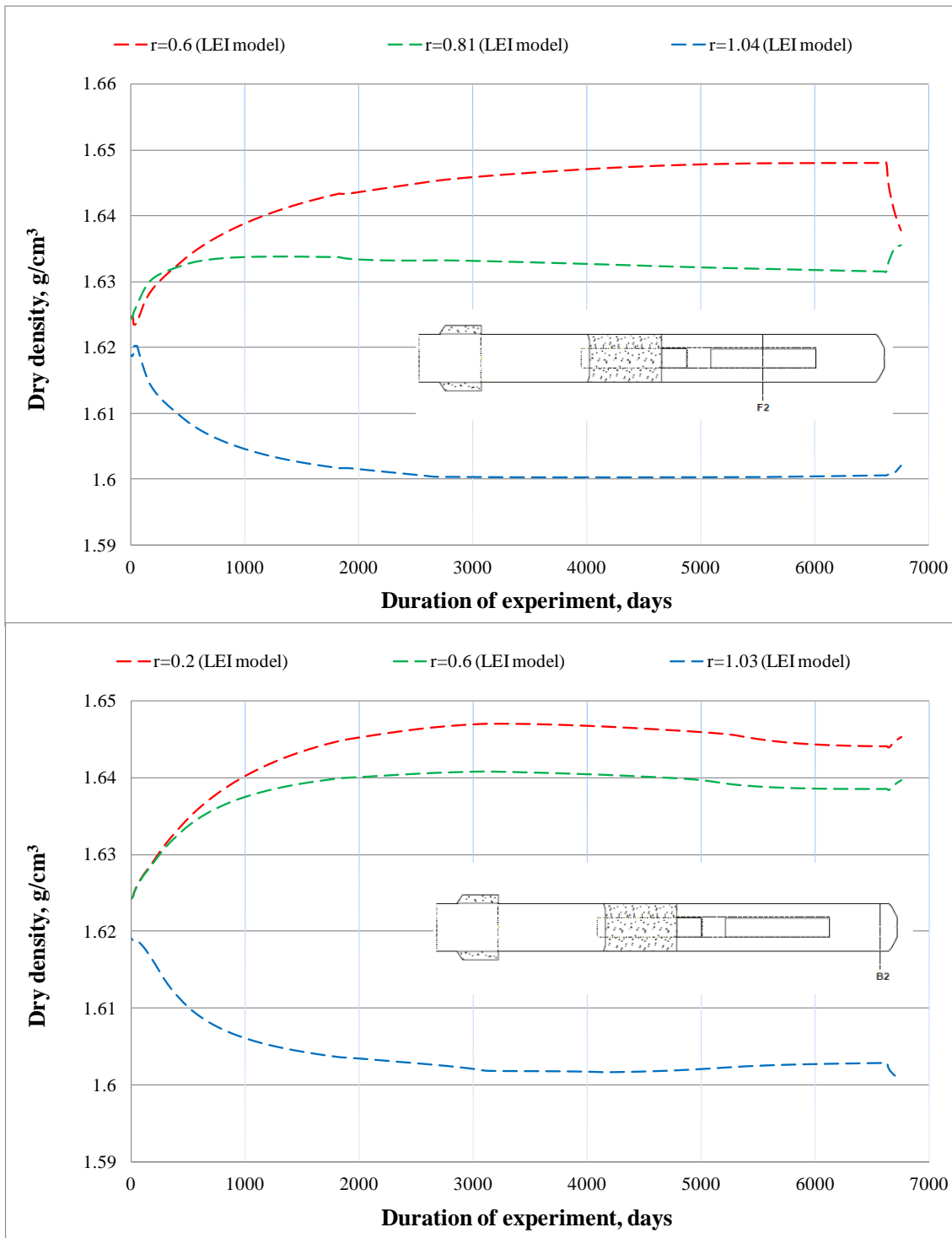


Figure 5-22. Comparison of LEI modelling results of dry density evolution at different radial distances of bentonite in sections F2 and B2

Results of parameters after dismantling of experiment (post-mortem)

Four different sections were selected for the comparison of modelling results and measurements obtained after the final dismantling of experiment. These sections are indicated in Figure 5-23.

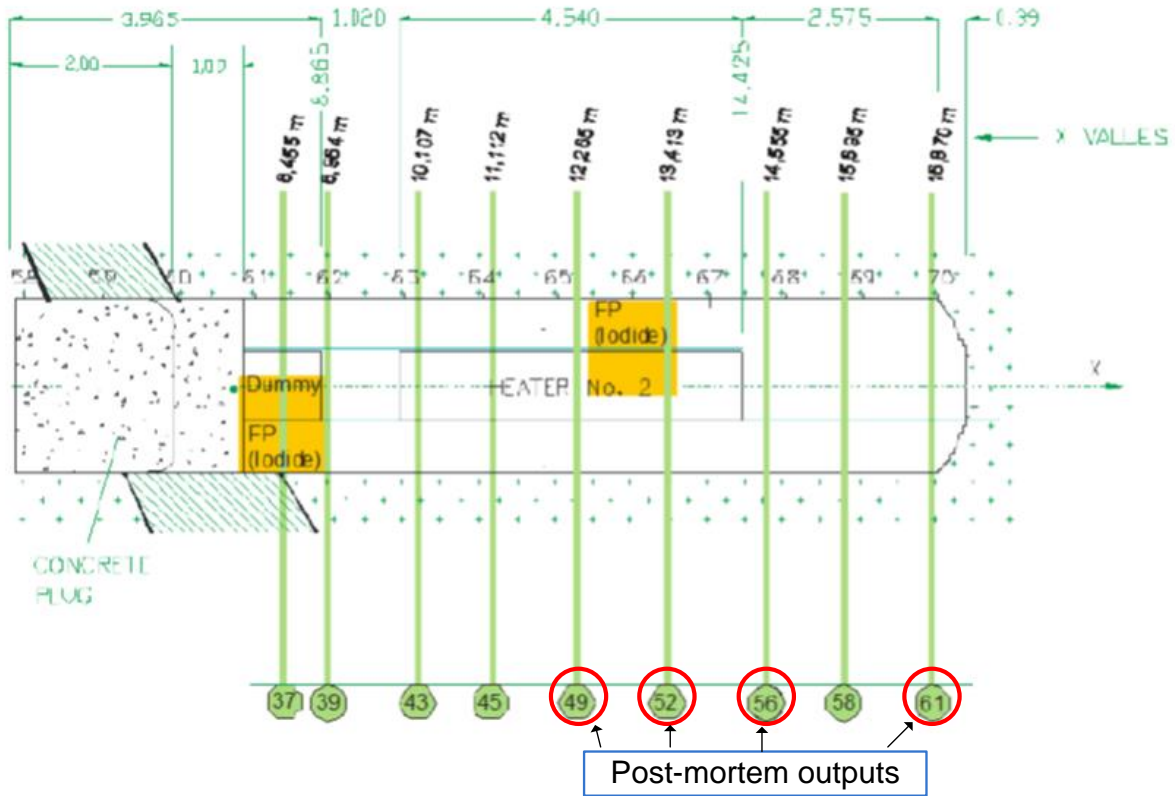


Figure 5-23. Sections for the comparison of modelling results with measurements obtained after the final dismantling of experiment

Relative humidity and degree of saturation

Modelling results and measured data of the evolution of relative humidity and degree of saturation in bentonite at radial distances of all 4 sections are presented in Figure 5-24 and Figure 5-25, respectively. As it could be seen LEI modelling results of both parameters were in between measured data for all sections, except relative humidity near the heater in hot sections S49 and S52.

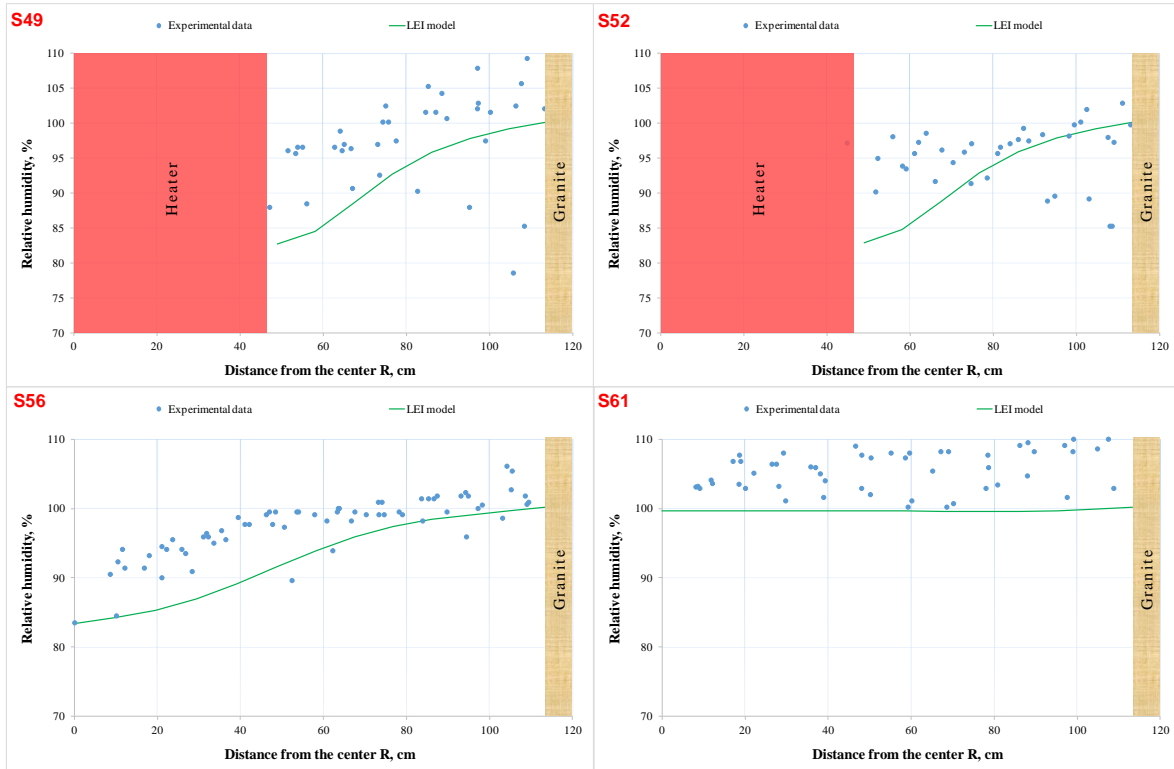


Figure 5-24. Comparison of LEI modelling results of relative humidity and post-mortem outputs at different sections

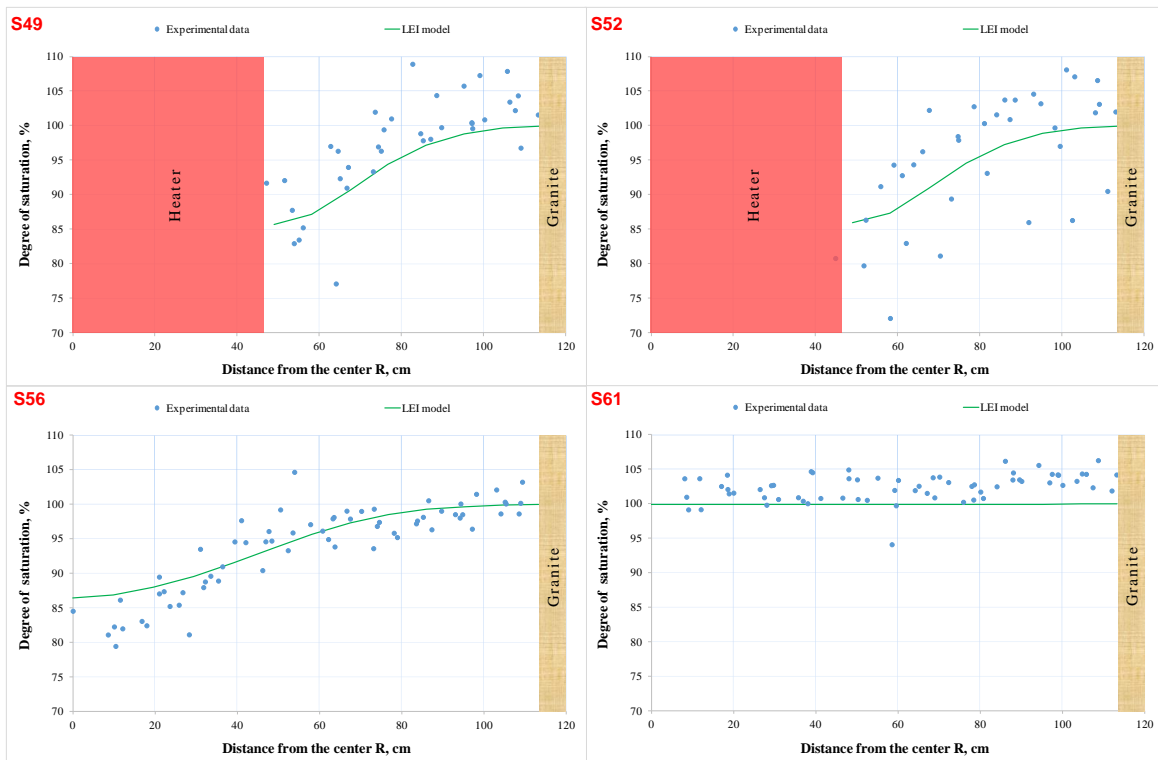


Figure 5-25. Comparison of LEI modelling results of degree of saturation and post-mortem outputs at different sections

Dry density

Modelling results and measured data of the evolution of bentonite dry density at radial distances of all 4 sections are presented in Figure 5-26. As it could be seen LEI modelling results were in between measured data for hot sections (S49 and S52), but correlation was poor near bentonite-granite interface in cold section S56 and no correlation at all in cold section S61. Section S61 was located in the end of the tunnel (see Figure 5-23) and was filled with different shapes of bentonite blocks. It resulted in the lower initial dry density (or higher initial porosity) compared to other sections. LEI model did not take this into account.

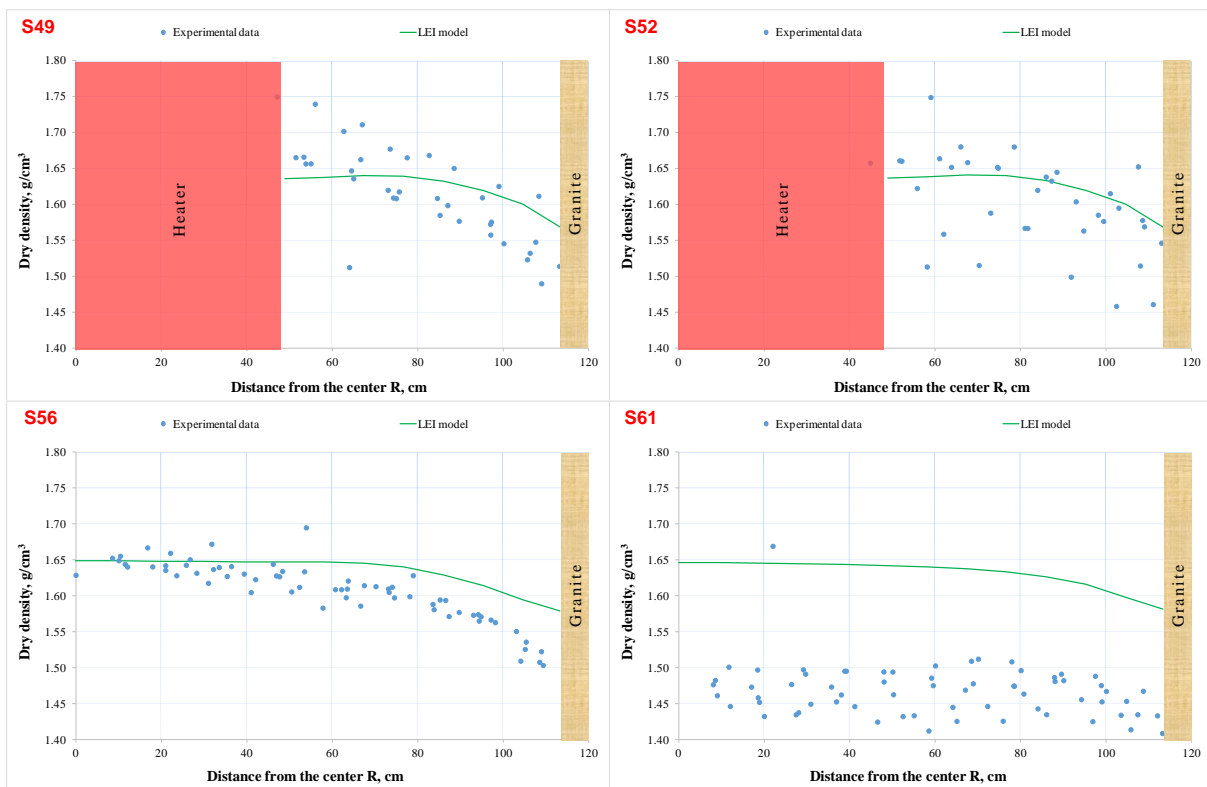


Figure 5-26. Comparison of LEI modelling results of dry density and post-mortem outputs at different sections

Gravimetric water content

Modelling results and measured data of the evolution of gravimetric water content in bentonite at radial distances of all 4 sections are presented in Figure 5-27. As it could be seen LEI modelling results were in between measured data for hot sections (S49 and S52), and for almost all radial distance of cold section S52 (except the last 20 cm near bentonite-rock interface). No correlation was found in section S61 for the same reason as in dry density case.

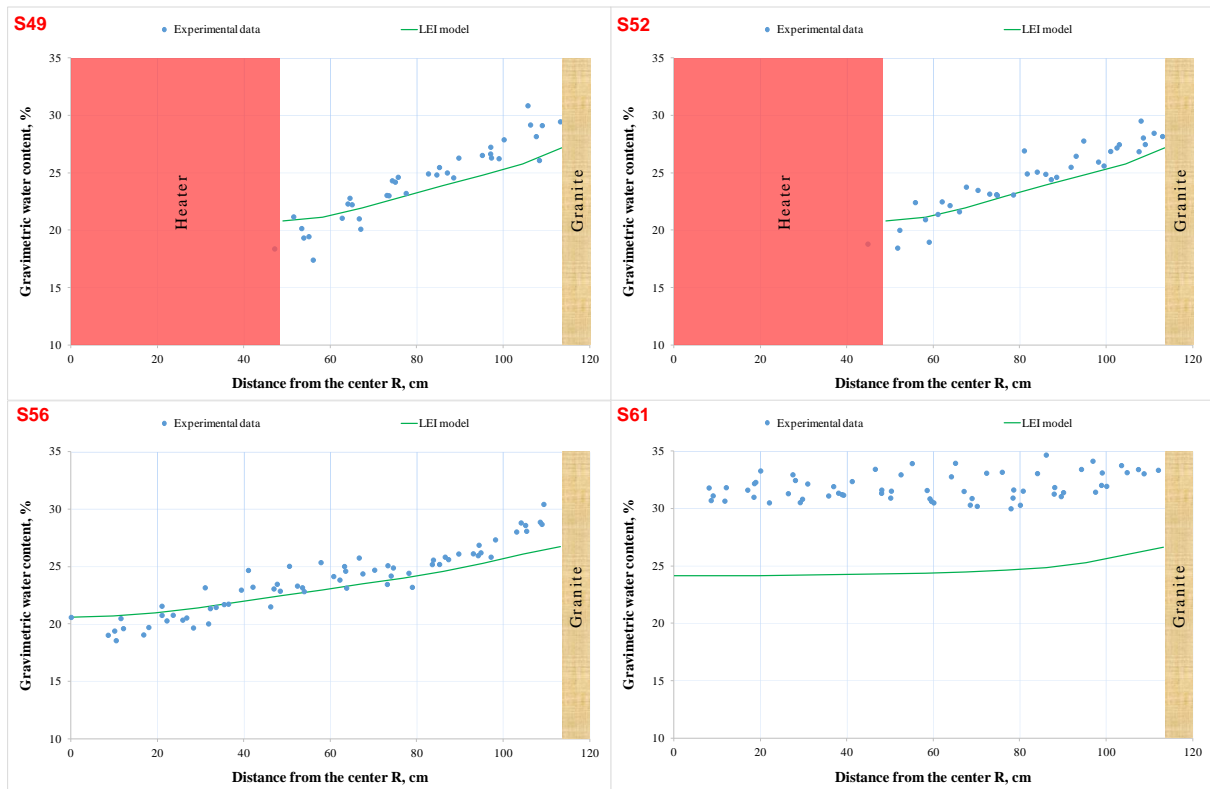


Figure 5-27. Comparison of LEI modelling results of gravimetric water content and post-mortem outputs at different sections

The FEBEX in situ experiment has been successfully modelled applying the finite element code CODE-BRIGHT v9.3. Fully coupled THM model developed by UPC were used to predict the behaviour of bentonite barrier. The LEI modelling involved such experiment stages as construction, heating and dismantling. The selection of the values of THM parameters for bentonite and granite were based on available experimental and modelling data. In general, there is good agreement between LEI modelling results and measured data despite that radial stresses were underestimated at bentonite and host rock interface and overestimated near the heater. As well as dry density values in the end of the tunnel (section S61). However, this model could be used for similar analysis in the future.

5.4 Quintessa

5.4.1 Geometry and discretization

Three simplified models of the FEBEX geometry were tested:

- 1D model with r discretisation centred on Heater 2;
- 2D axisymmetric model with $r - z$ discretisation;
- 2D model with $r - \theta$ discretisation centred on Heater 2.

These enabled the heterogeneities of the experiment to be investigated without having to run a full 3D model, which is computationally expensive. The 1D model enabled quick testing of different model assumptions. The 2D axisymmetric model was used to investigate behaviour along the length of the heater and away from the heater. The 2D model with angular discretisation enabled the effect of asymmetry in the void space to be investigated.

In each model, only the bentonite around Heater 2 was explicitly represented, with the heater and host rock modelled using boundary conditions. The bentonite was modelled as a cylinder of radius 1.135 m with the additional outer void space represented as a boundary condition. The volume corresponding to the heater (with length 4.54 m and radius 0.45 m) was discarded from the model. The region around Heater 1 was not modelled.

The discretisation of the 1D radial model centred on Heater 2 is shown in Figure 5-28. The bentonite is discretised into 20 equal-sized compartments.

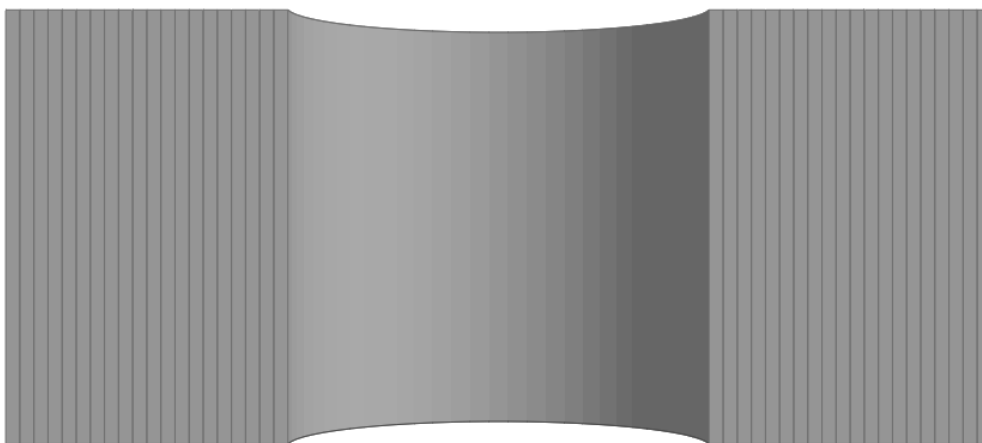


Figure 5-28: Discretisation of 1D radial model centred on Heater 2.

The discretisation of the 2D $r - z$ axisymmetric model is shown in Figure 5-29. The bentonite is discretised into 12 radial compartments (two between the gallery axis and the outside of the heater, and 10 from the outside of the heater to the rock) and 11 axial compartments (6 along the length of the

heater). The radial discretisation is coarser than the 1D model to enable faster runtime.

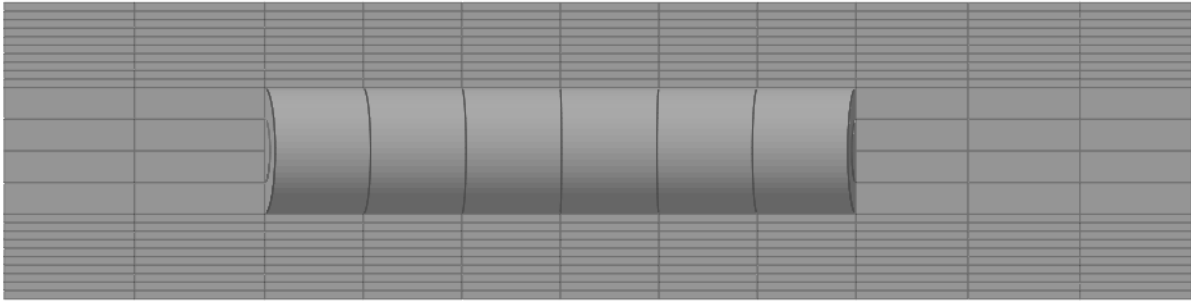


Figure 5-29: Discretisation of the 2D $r-z$ axisymmetric model.

The discretisation of the 2D $r - \theta$ model centred on Heater 2 is shown in Figure 5-30. The bentonite is discretised into 10 radial compartments and 15 angular compartments.

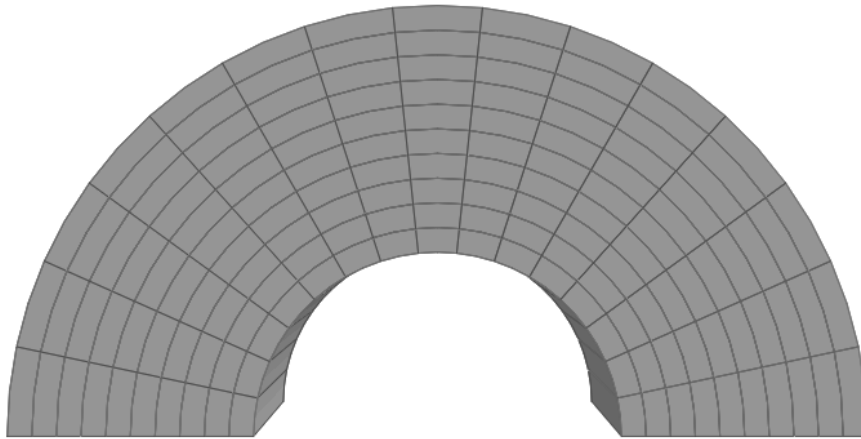


Figure 5-30: Discretisation of the 2D $r-\theta$ model centred on Heater 2.

5.4.2 Input parameters

Input parameters for the QPAC model are given in

Table 5-10. Where available, values have been taken from the FEBEX experiment specification (ENRESA, 2000). Parameters for the ILM (p_0 and λ) were calibrated to water retention, swelling and oedometer data for FEBEX bentonite as shown in Section 2.9 (Thatcher, 2017).

Table 5-10: Input parameters for Quintessa's FEBEX model.

Parameter	Value	Units	Reference
Thermal Parameters			
Specific Heat Capacity, water	4183	J kg ⁻¹ K ⁻¹	Thatcher, 2017
Specific Heat Capacity, bentonite	1100	J kg ⁻¹ K ⁻¹	Thatcher, 2017
Specific Heat Capacity, vapour	1850	J kg ⁻¹ K ⁻¹	Thatcher, 2017
Coefficient of Thermal Expansion	See Equation 1		
Thermal Conductivity	See Equation 2		
Mechanical Parameters			
Grain Density, bentonite	2700	kg m ⁻³	ENRESA, 2000
Poisson's Ratio	0.27	-	Thatcher, 2017
Initial Bulk Modulus	100	MPa	Thatcher, 2017
Bulk Modulus Scaling Factor	30	-	Thatcher, 2017
ILM p_0	See Equation 3		
ILM $1/\lambda$	-7	-	Thatcher, 2017
Hydraulic Parameters			
Reference Vapour Diffusivity	See Equation 4		
Tortuosity	0.8	-	ENRESA, 2000
Intrinsic Permeability	See Equation 5		

As discussed in Section 2.9, thermal expansion was included in this model. The coefficients of linear thermal expansion are assumed to be isotropic and show a temperature dependence (ENRESA, 2000):

$$\alpha = -1.256 \cdot 10^{-4} + 6.5 \cdot 10^{-6}T \quad (1)$$

where α is the coefficient of linear thermal expansion in each direction [°C⁻¹] and T is temperature [°C].

Thermal conductivity of FEBEX bentonite is also taken from the experimental specification (ENRESA, 2000):

$$\lambda_T = \frac{0.57 - 1.28}{1 + \exp\left(\frac{S_w - 0.65}{0.1}\right)} + 1.28 \quad (2)$$

where λ_T is thermal conductivity [W m⁻¹ K⁻¹] and S_w is water saturation [-].

As discussed in Section 2.9, water retention data for FEBEX bentonite at different temperatures suggested a temperature dependence for the internal limit curve. Fitting to this data suggested an equation for p_0 of:

$$p_0 = -7.895[\text{MPa} \cdot \text{C}^{-1}] \cdot T + 1674[\text{MPa}] \quad (3)$$

Finally, this model also used a dry density-dependence for the hydraulic

conductivity of FEBEX bentonite (ENRESA, 2000):

$$K = \begin{cases} 10^{-6} \cdot \rho_d^{-4.09}, & \rho_d \leq 1.47 [g \cdot cm^{-3}] \\ 10^{-2.96} \cdot \rho_d^{-8.57}, & \rho_d > 1.47 [g \cdot cm^{-3}] \end{cases} \quad (4)$$

where K is hydraulic conductivity [$m \cdot s^{-1}$] and ρ_d is dry density. Intrinsic permeability can then be derived from hydraulic conductivity as:

$$k_0 = \frac{K \cdot \nu}{g} \quad (5)$$

where k_0 is intrinsic permeability [m^2], g is acceleration due to gravity ($9.81 [m \cdot s^{-2}]$) and ν is kinetic viscosity [$m^2 \cdot s^{-1}$]. Kinetic viscosity of water at different temperatures can be found in a lookup table (Dean & Lange, 1999).

5.4.3 Initial and boundary conditions

The initial temperature throughout the bentonite is set to 12°C (equal to the measured temperature in the granite host rock and in the gallery). The initial water content of the bentonite is 14.4% and the dry density is 1.69 $g \cdot cm^{-3}$ (ENRESA, 2000). The dry density has not been adjusted to account for void space since the main voids are accounted for in the outer boundary condition.

The heater is represented as a boundary condition on the inner surface of the bentonite. For the first 53 days, a specified heat flux condition is used to represent the initial heating ramp; a constant 1.2 kW for the first 20 days, linearly ramping up to 1.5 kW by 53 days. In the experiment, the maximum power applied was 2 kW, but in the model, this was found to result in the temperature at the heater surface overshooting the 100°C target by 35°C. After this period, the heater boundary is set to a constant temperature of 100°C. The outer boundary has a fixed heat flux calculated assuming ambient temperature at 2 m into the granite, designed to approximate the heat flux out of the bentonite.

The hydraulic boundary conditions are no-flow apart from the bentonite-tunnel wall where water may flow into the bentonite from the rock. This is represented simply as a constant pressure boundary with water at atmospheric pressure.

The mechanical boundary conditions are zero displacement everywhere apart from into the void space at the outside of the bentonite. This void space is represented as a specified stress boundary condition which allows free swelling until a displacement threshold, which corresponds to the width of the gap is reached. After this point, the boundary is very stiff such that further swelling is almost completely inhibited. In the 1D and 2D R-Z models,

the void is assumed to be 3 cm. In the 2D R- θ model, the void is assumed to be 3 cm at the top of the bentonite and 0 cm at the bottom of the bentonite, decreasing sinusoidally between the two.

The model starts at time 0 days, corresponding to the start of heating and water infiltration. In the experiment, there was a short period of infiltration before the heating (operational) stage but no details are given about this period so it has not been included in the model. The entire operational period of the experiment is modelled - 6758 days. The 2D R- θ model was stopped at an earlier stage (after 3.25 years) since the solver struggled to converge in a reasonable time. This issue will hopefully be resolved in a new version of QPAC.

5.4.4 Results/discussion

Temperature

Temperature evolution results from the 1D radial model centred on Heater 2 (at location F2) are compared with data in Figure 5-31. As discussed in the previous section, with the specified heater power applied, temperatures at the heater were significantly higher in the model than reported, so the boundary heat flux during the initial heating phase was calibrated and then a fixed boundary temperature of 100°C was applied for the remainder of the model run.

After the initial 53-day heating phase, both the model and the sensors show very little change in temperature for the rest of the operational period. There is a maximum error of approximately 5°C between modelled and measured temperatures. The temperature discrepancy very close to the heater casing suggests either that the heater boundary condition does not accurately reflect the real behaviour of the heater or that void space between the heater casing and the bentonite had a significant effect on heat conductivity into the bentonite. This void space is not included in the model; the temperature at the inner surface of the bentonite is assumed to be equal to the temperature of the heater casing. The 1D assumption could also affect the temperature results, since heat transfer can only occur radially whereas in the experiment, some heat will be transferred towards the ends of the heater.

Sensor data adjacent to the heater casing (sensors 01, 02, 03 and 04 at position F2) show up to a 6°C difference between angles, with sensor 01 at an almost constant 100°C, consistent with the model, and sensor 03 (plotted in Figure 5-31) showing the lowest equilibrium temperature. This could either be due to heterogeneity of the voids, or uncertainty in the measurements.

In the 2D R- θ model, void space between the heater and the bentonite is not modelled, and the heater casing is at a uniform temperature of 100°C; since there is no angular variation in the initial or inner boundary conditions, the

temperature of the bentonite close to the heater is almost homogenous. At the outside of the bentonite, the model predicts a maximum 2°C difference between the top and bottom of the experiment due to differences in deformation at the outer boundary.

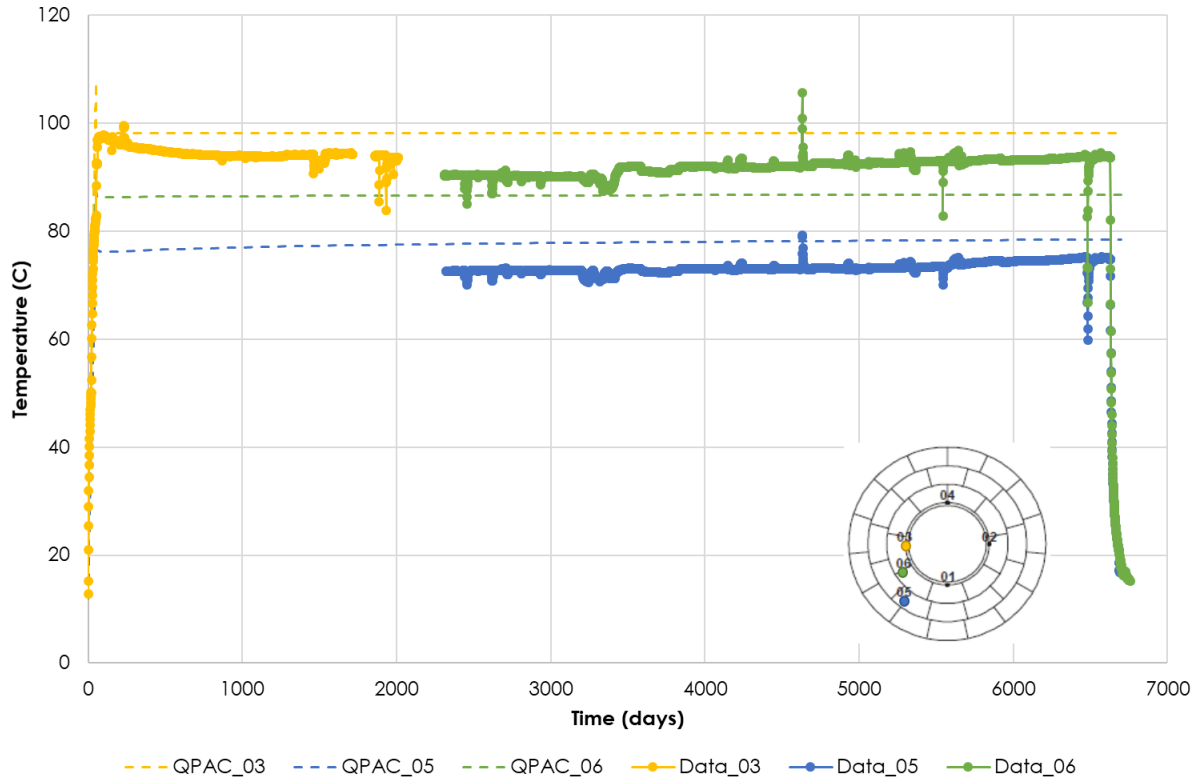


Figure 5-31: Temperature evolution calculated by the 1D model (dashed lines) compared with data (markers) at sensor locations 03 ($r=0.5m$), 05 ($r=0.8m$) and 06 ($r=0.6m$).

In the 2D R-Z model, the boundary condition ensures that the heater casing remains at a temperature of 100°C along the length of the heater. In the adjacent bentonite compartments, there is a temperature gradient of approximately 2°C along the length of the heater. The data also shows little or no temperature gradient along the heater. At location E2, approximately 1 m axially from the centre of the heater, the agreement between the model and data is very good (Figure 5-32).

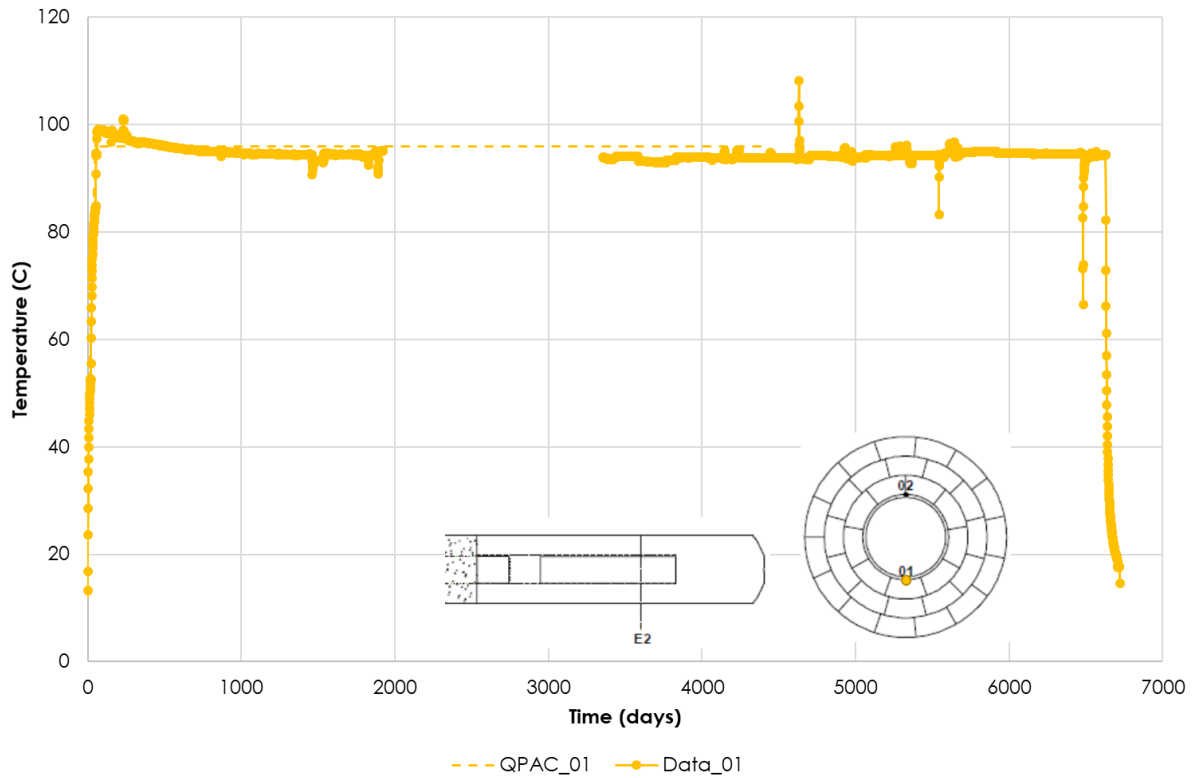


Figure 5-32: Temperature evolution calculated by the 2D R-Z model (dashed line) compared with data (markers) at z-position E2, r-position 0.5 m.

Away from the heater, the temperature drops significantly. At location B2, the furthest end of the bentonite from the heater, measured temperatures are less than 25°C (Figure 5-33). There is a much slower rise in temperature, which is well captured by the model. Again, the model predicts overall higher temperatures in the bentonite, as well as a steeper radial gradient. After 1900 days, there is a drop in measured temperature (corresponding to the time of dismantling Heater 1) which is not reproduced by the model.

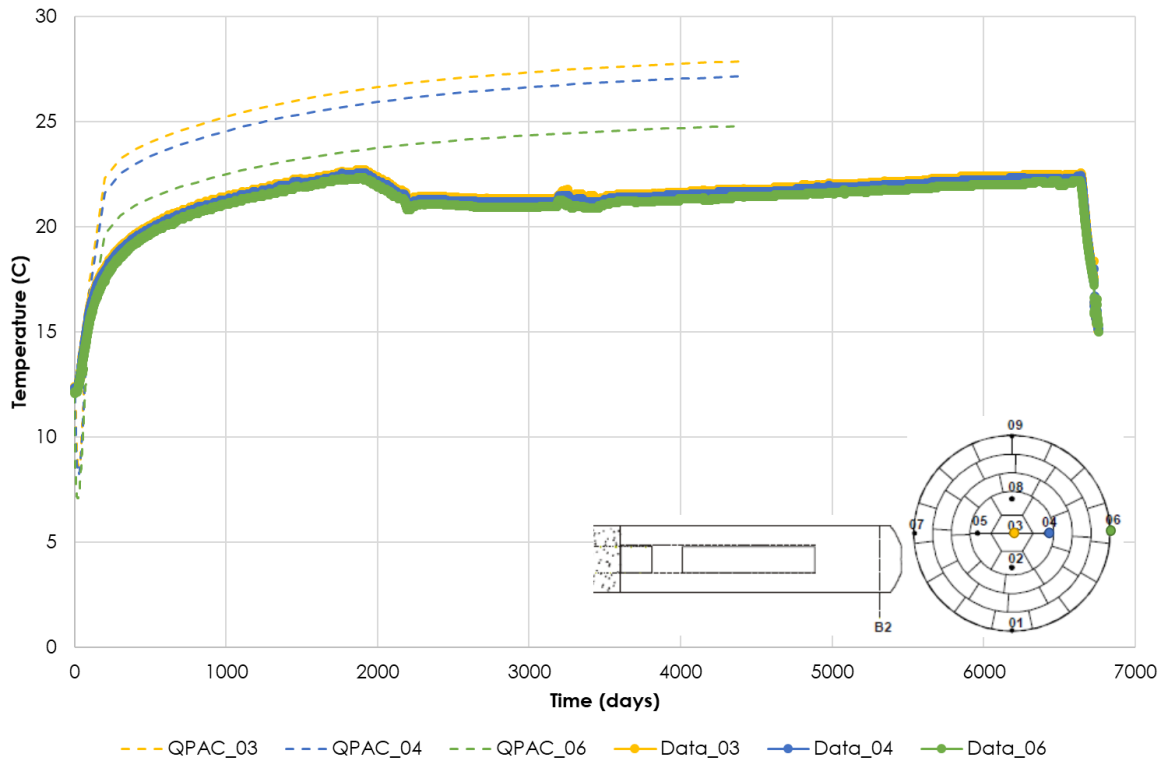


Figure 5-33: Temperature evolution calculated by the 2D R-Z model (dashed lines) compared with data (markers) at z-position B2, sensor locations 03 ($r=0m$), 04 ($r=0.4m$) and 06 ($r=1.1m$).

Relative Humidity

Relative humidity evolution results from the 1D slice centred on Heater 2 (at location F2) are compared with data in Figure 5-34. There are limited sensor data for relative humidity and none that cover the whole period. However, the modelled relative humidity behaviour is generally consistent with the measurements. Both show that a relative humidity of 100% is reached fairly rapidly at the outer bentonite block (location 05 and 06). Relative humidity at the centre of the bentonite (location 03) also tends to 100% over a longer period.

The model initially saturates more rapidly than the experiment but then slows down. The experimental data show a large variation in saturation time between sensors at the same radial distance. For example, in the outer bentonite block (at a radius of approximately 1.05 m from the gallery axis), the model predicts an initial relative humidity of 45%, taking 70 days to reach a relative humidity of 90% and 1500 days to reach a relative humidity of 99%. This is slightly faster than the measured behaviour at Sensor 06, which shows a very similar initial relative humidity of 44%, taking 475 days to reach 90% and 2450 days to reach 99%. However, Sensor 05 at an equivalent radial distance (180° apart from Sensor 06) measures a very high initial relative humidity of 97%, reaching 99% within the first 60 days of operation. Again, this angular heterogeneity is not predicted by the 2D $r-\theta$ model, which calculates almost

no difference in relative humidity with angle. This suggests that there are further heterogeneities within the bentonite which have not been included in the model (such as voids between bentonite blocks or wet spots on the tunnel walls).

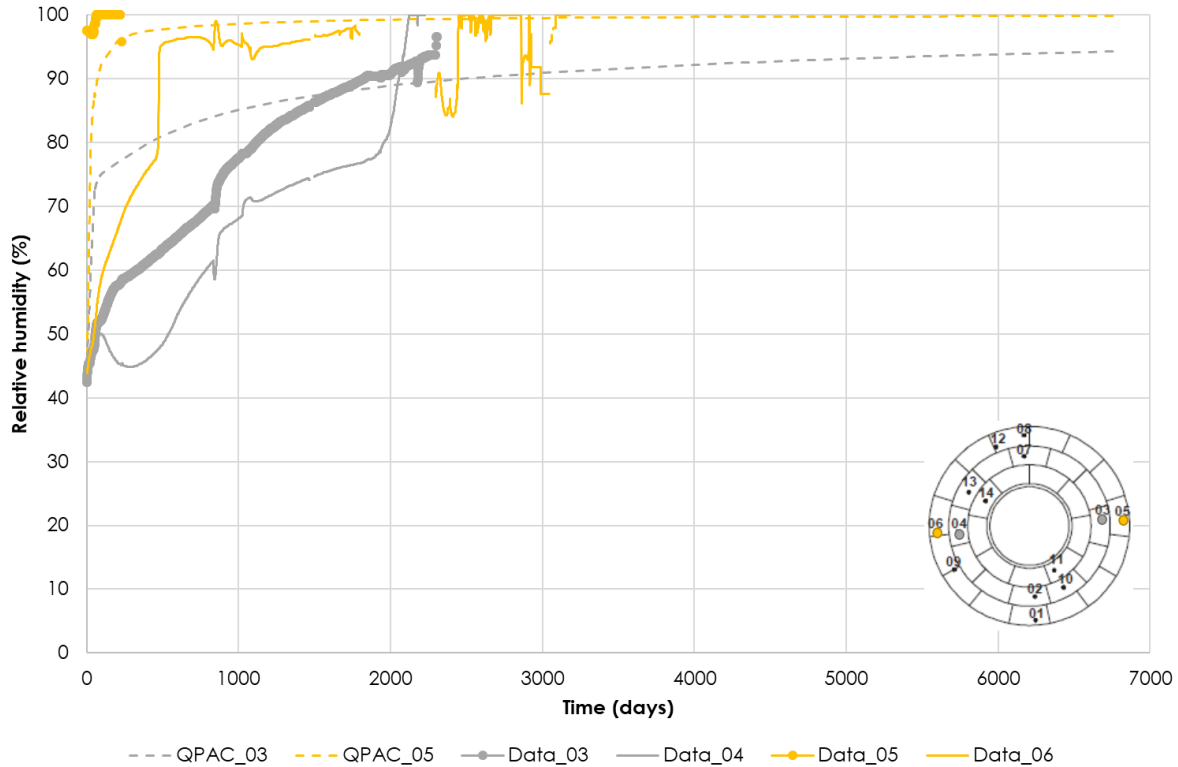


Figure 5-34: Relative humidity evolution calculated by the 1D model (dashed lines) compared with data (markers, solid lines) at sensor locations 03, 04 ($r=0.8m$) and 05, 06 ($r=1.05m$).

Results from the 2D R-Z model predict similar relative humidity profiles along the length of the heater, with generally higher relative humidity away from the centre of the heater (where there are lower temperatures and hence less vapour flux). Again, data for comparison is limited due to early sensor failures (Figure 5-35). In the bentonite closest to the heater, both the model and sensors show an initial decrease in relative humidity as the bentonite dries.

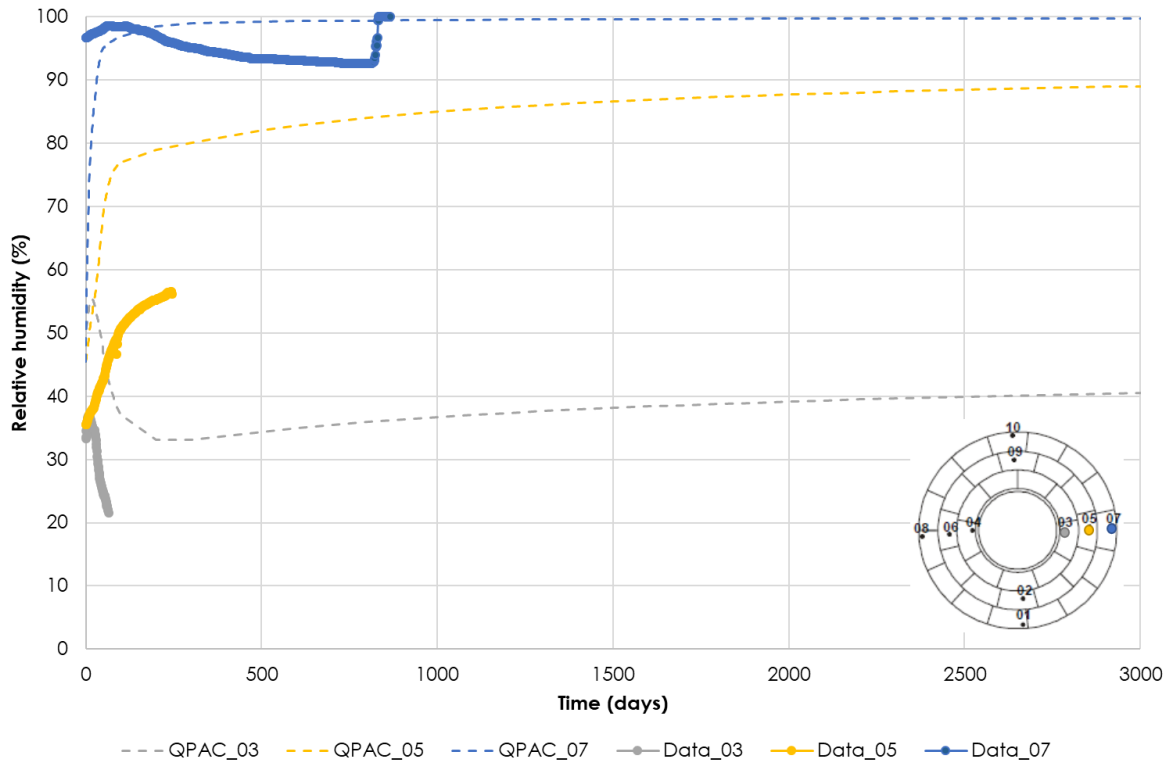


Figure 5-35: Relative humidity evolution calculated by the 2D R-Z model (dashed lines) compared with data (markers) at sensor locations 03 ($r=0.5m$), 05 ($r=0.8m$) and 07 ($r=1.1m$).

Stress

Radial stress evolution results from the 1D slice centred on Heater 2 (at location F2) are compared with data in Figure 5-36. In general, stresses are overpredicted by the model – particularly closer to the heater, where measured stresses are very low. This large difference in measured radial stress between the middle and outside of the bentonite could suggest that friction is important, or hoop stresses are preventing radial collapse of the bentonite. The final radial stress at the outside of the bentonite (location 01, for which there is complete sensor data) is well-predicted by the model. However, the evolution of stress is less well predicted.

The initial spike and collapse in radial stress at the outside of the bentonite during the initial heating period appears to be overpredicted by the model. It is not possible to compare the predicted and measured behaviour from other locations within the bentonite during this initial period, since measurements at sensors 05-08 did not begin until 2310 days.

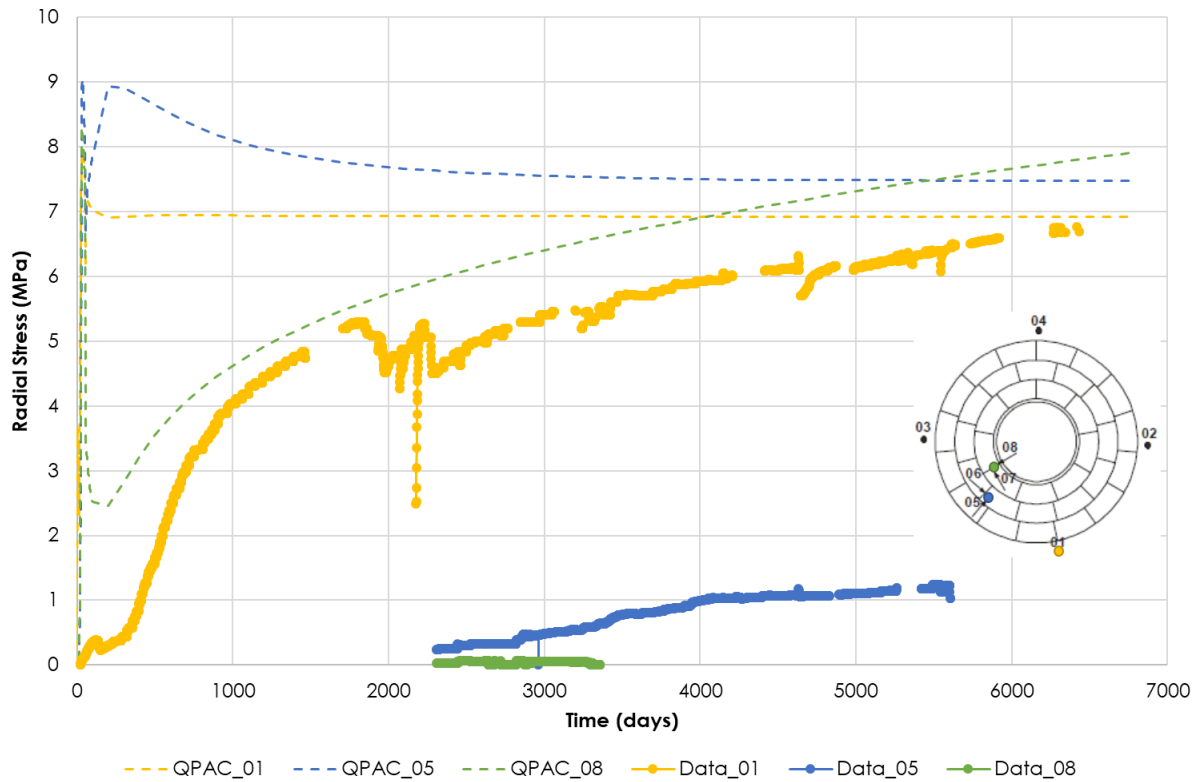


Figure 5-36: Radial stress evolution calculated by the 1D model (dashed lines) compared with data (markers) at sensor locations 01 ($r=1.1m$), 05 ($r=0.8m$) and 08 ($r=0.6m$).

The low measured stresses close to the heater could be an indication of the importance of vapour transport in the system. Figure 5-37 compares the modelled final total stresses in the 1D radial model with and without vapour transport. With no vapour transport, there is a very shallow stress gradient across the bentonite, with the highest stresses at the heater and lowest at the outer boundary. This corresponds to the profile of dry density, which is also lowest at the outside of the bentonite due to water-induced swelling into the outer voids. With vapour transport included in the model, there is now an area of low stress close to the heaters. This is due to the temperature-driven transport of vapour away from the heater which dries the bentonite closest to the heater, causing it to contract and reduce in stress.

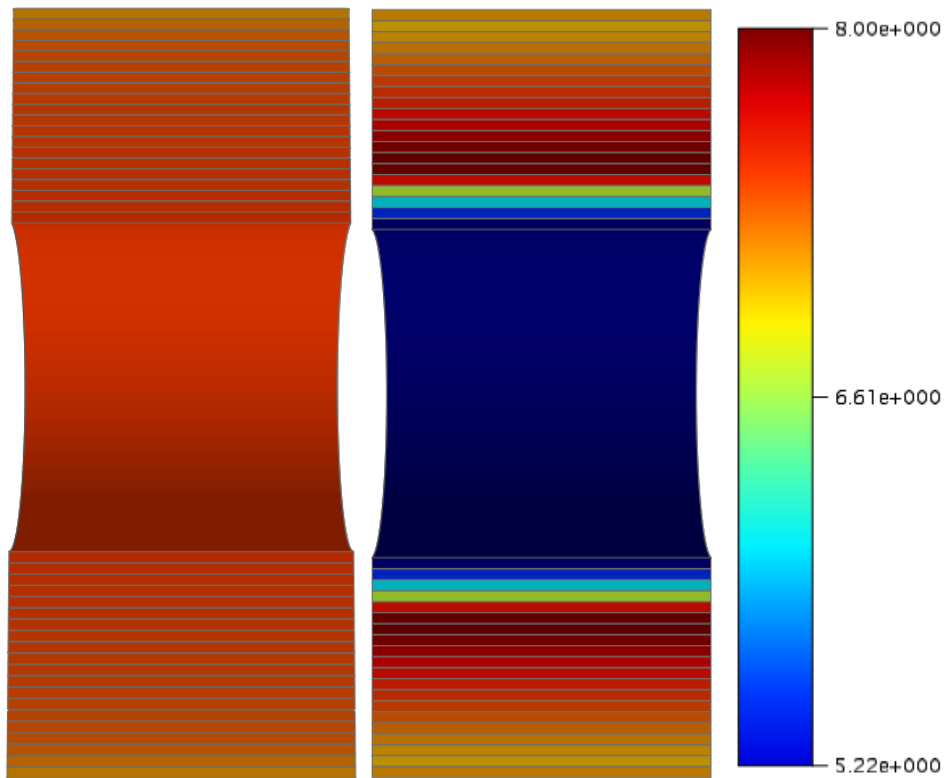


Figure 5-37: Comparison of modelled total effective stresses in 1D model without vapour transport (left) with model with vapour transport (right), in [MPa].

The 2D R- θ model predicts a large difference in stresses between the top and bottom of the bentonite due to the void space at the top of the bentonite (Figure 5-38). At the outside of the bentonite, this difference is of the order of 8 MPa. This is larger than the measured difference of approximately 3 MPa – consequently, the predicted stress at the bottom of the bentonite is much too high. This suggests that a lower effective dry density should be used to account for other void space within the bentonite (e.g. between the blocks). Towards the heater, the model predicts an angular difference in radial stress of the order of 4 MPa but there is only one sensor point to compare with.

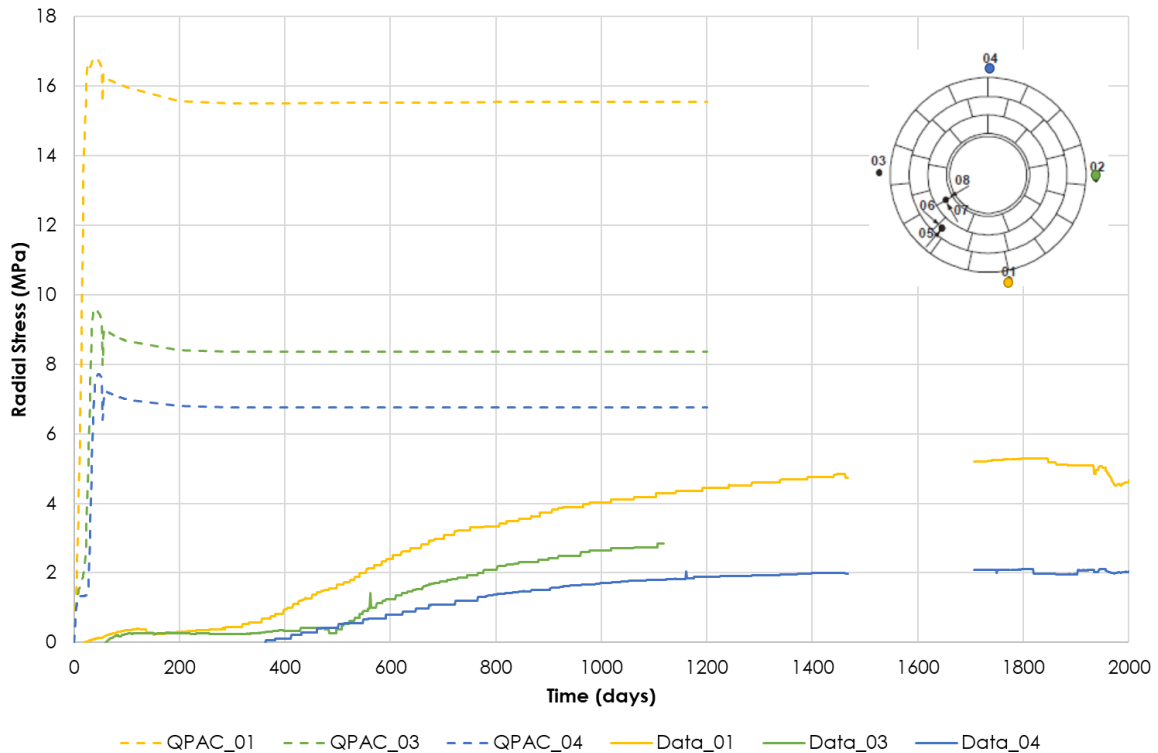


Figure 5-38: Radial stress evolution calculated by the 2D R- θ model (dashed lines) compared with data (markers) at sensor locations 01, 02 and 04 ($r=1.1m$).

Results from the R-Z model at location E2 (1m axially from the centre the Heater 2) show a similar trend to those in Figure 5-36. At the outside of the bentonite, swelling pressures are generally well predicted. Towards the heater, radial stresses appear to be overpredicted although there is almost no sensor data to compare with. Stresses are also overpredicted far from the heater, at location B2.

Dry Density

Final radial dry density profiles from the 1D slice centred on Heater 2 (at location F2) are compared with data in Figure 5-39. The model predictions lie within the scatter of the measured results from dismantling. Both the model and data show a dry density gradient from the drier and more compact bentonite near the heater, to the wetter bentonite close to the rock. This suggests that water-driven swelling of the bentonite dominates over thermal expansion processes. Towards the heater, the model and data show very similar dry density gradients, whereas the model predicts a flatter gradient in the outer half of the bentonite. This could be because the effect of the void space between the bentonite and the rock is not being fully captured in the model, so the dry density at the edge of the bentonite is overestimated.

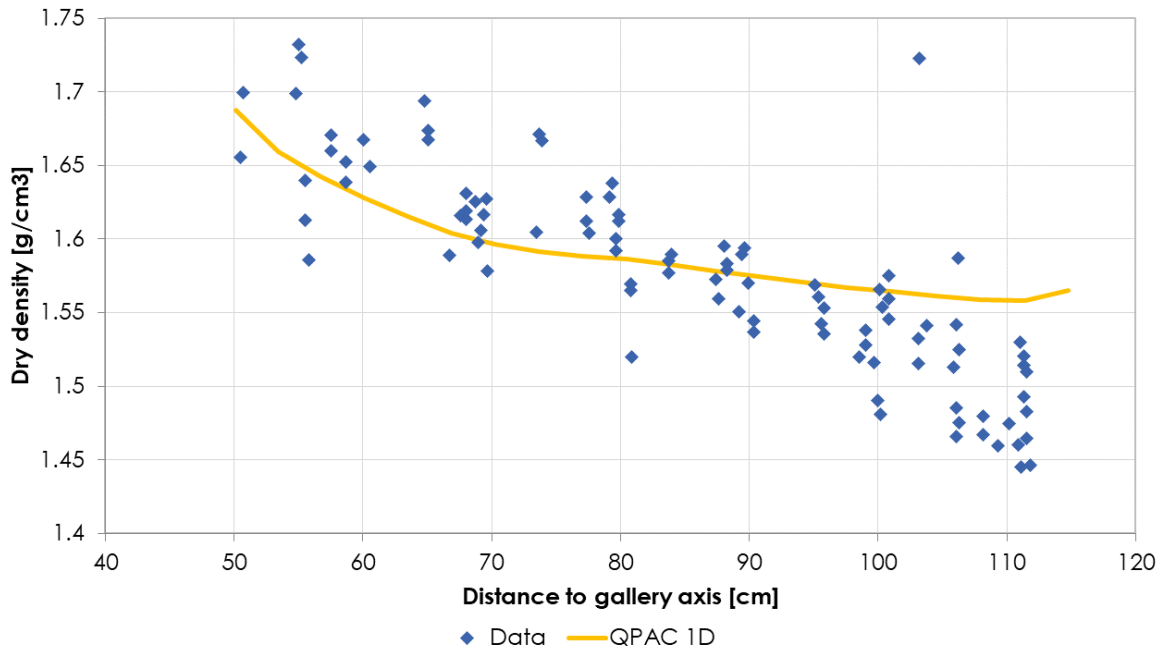


Figure 5-39: Radial dry density profile calculated by the 1D model compared with data.

Radial dry density profiles from the 2D R- θ slice centred on Heater 2 (at location F2) are compared with the same data in Figure 5-40. The 2D R- θ model did not run to completion, so results are taken from 1200 days. The results show a difference of 0.1 g/cm³ between the top and bottom of the bentonite. These predictions lie within the scatter of the data, but towards the higher range, which could explain the overprediction of swelling pressure.

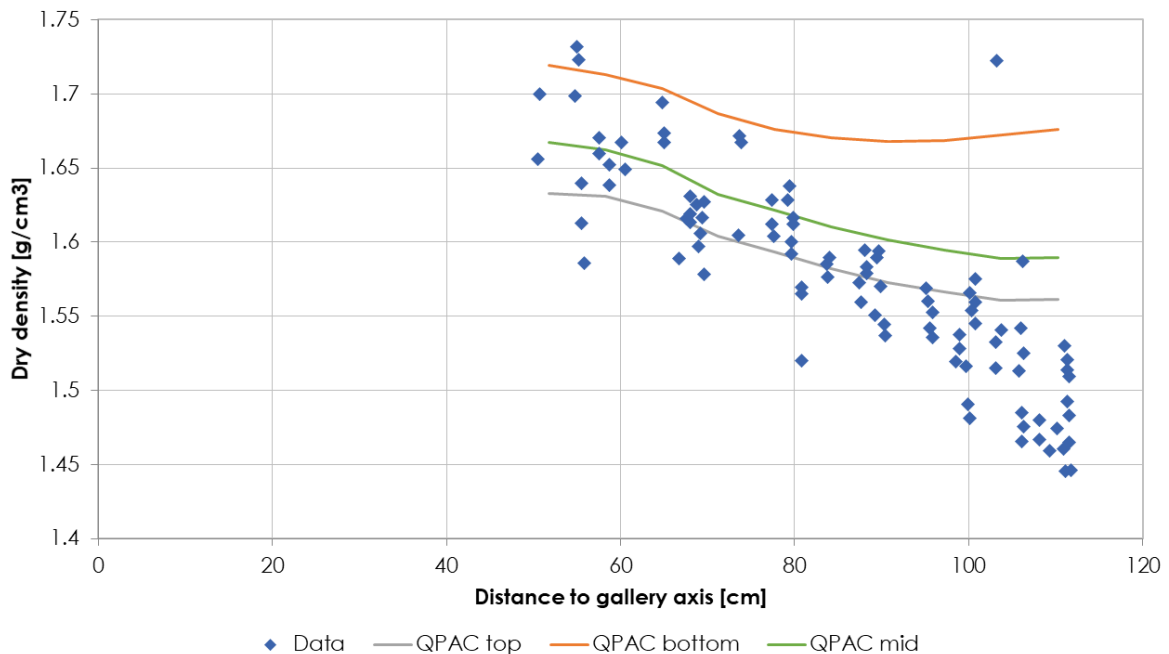


Figure 5-40: Radial dry density profile calculated by the 2D R- θ model compared with data.

5.5 Clay Technology - Comsol

When performing the presented work, large characteristic discrepancies between experimental data and the solution were taken as indications of inadequacies in the formulation which were to be addressed. The presently analysed type of large and complex experimental setups will, however, inherently have a large portion of fuzziness/ambiguity. That is why attempts to chase perfect fit to experimental data have not been pursued.

In line with the objectives of Beacon the main focus has here been to evaluate if the HBM formulation is capable of producing a representative homogenization process. For the Febex test this necessitate incorporation of vapor transport and thereby thermal physics as well. The thermal problem has been dealt with in a rather pragmatic way just to get a relevant driving force for the vapor.

The main idea behind the model is to let buffer blocks, with the correct initial dry density (1700 kg/m^3), take up water and swell into initially open gaps, with correct total volume, as to obtain the average dry density measured at dismantling (1600 kg/m^3). Thus, we start with the reported state at installation and study how well the homogenization process is represented by comparing stress levels and the final dry densities. The model has been simplified by gathering all gaps into one and locate this between the block material and tunnel wall.

5.5.1 Geometry and discretization

A vertical section of buffer at H2 mid has been modelled. This was represented using an axisymmetric plane geometry with an inner radius of 0.485 m and an outer radius of 1.112 m at the initial state, see Figure 5-1. The outer boundary was enabled to move 28 mm outwards in the radial direction in order to allow for swelling/homogenization of the dense (dry density 1700 kg/m^3) buffer blocks to an average dry density of 1600 kg/m^3 . This is the same setup as used by Clay Technology (Mattias Åkesson) described in Papafotiou et al. (2017). The geometry was discretized into 20 elements with higher mesh density towards the inner and outer boundaries, see Figure 5-1. No significant changes were obtained when increasing the mesh density. Information about the shape functions/elements are given in Table 5-11.

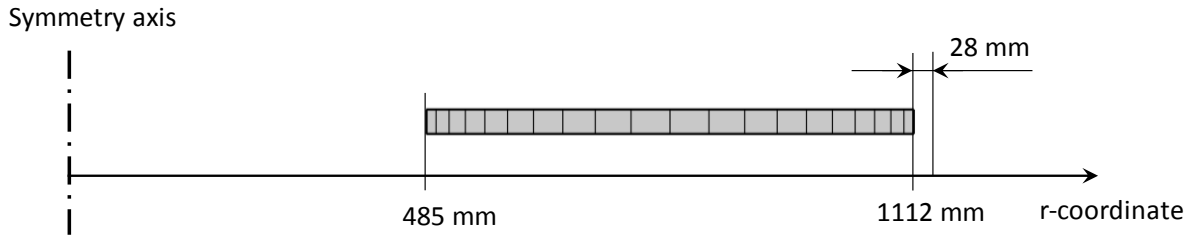


Figure 5-1. Geometry and discretization

Table 5-11 Numerical discretization description

Variable	Shape function type	Element order
Stress	Discontinuous Lagrange	Quadratic
Path variable	Discontinuous Lagrange	Quadratic
Micro void ratio	Discontinuous Lagrange	Quadratic
Liquid pore pressure	Lagrange	Linear
Displacement	Serendipity (i.e. "Reduced Lagrange")	Quadratic or Cubic
Temperature	Lagrange	Linear

5.5.2 Input parameters

Input parameters are given in Table 5-12, Table 5-13 and Table 5-14. Hydraulic and thermal parameter values without a specified source are standard handbook values or used by other codes (here Code_Bright has been an inspiration). The values of the HBM parameters R and e_{step} were obtained after studying small example problems and confirming that a sought behavior was achieved.

Table 5-12 HBM parameters

Parameter	Value
c_0^{low} (1)	7.2322
c_1^{low} (1)	-8.5239
c_2^{low} (1)	2.0694
c_3^{low} (1)	-0.1912
c_0^{high} (1)	7.5771
c_1^{high} (1)	-8.3087
c_2^{high} (1)	2.3612
c_3^{high} (1)	-0.2425
$(p_{sw}^{low \& high})_0$ (1)	10^6 Pa
γ (2)	7
K_{aa} (2)	40
K_{ab} (2)	40
R	0.9
e_{step}	0.05

Table 5-13 Hydraulic parameters

Parameter	Value
e_{perm} (3)	0.7
β_{perm} (3)	6
k_{ref} (3)	$0.45 \cdot 10^{-20}$ m ²
μ	$1 \cdot 10^{-3}$ Pa s
τ (4)	0.8
D_0	$5.9 \cdot 10^{-6}$ m ² ·Pa/s
n	2.3

Table 5-14 Thermal parameters

Parameter	Value
λ_{dry} (5)	0.5 W/m/K
λ_{sat} (5)	1.3 W/m/K
C_p^s (6)	1091 J/kg/K
C_p^l	4180 J/kg/K
λ_l	0.65 W/m/K

(1) Calibrated using data (Tab. A-18) in Villar et al. (2018). (2) Value for K_{aa} reported in D5.1.2 and here $K_{ab} = K_{aa}$ for simplicity. (3) Calibrated using data (Tab. A-19) in Villar et al. (2018). (4) From task specifications. (5) Linear fit to data (Figure 1-18 in Appendix) in task specifications. (6) Papafotiou et al. (2017).

In Figure 5-2, the clay potential functions are shown together with the corresponding experimental data to which the functions were fitted. The fitting was performed in lin-log space and the lin-lin graph reveals that for low micro void ratios ($e_\mu < 0.6$) the functions underestimate the measured data.

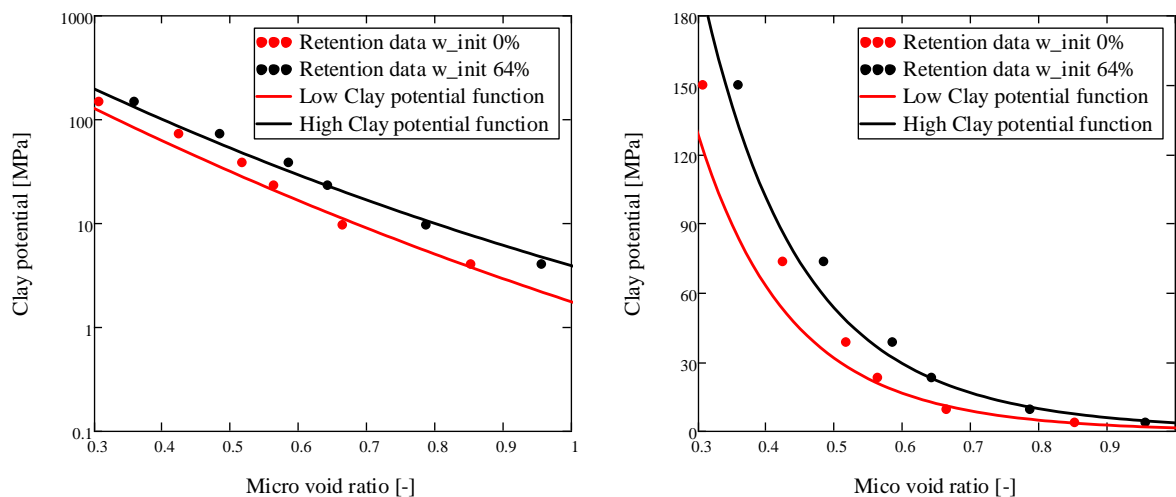


Figure 5-2. High and Low clay potential functions together with the corresponding experimental data in lin-log and lin-lin graphs, left and right, respectively.

The left graph of Figure 5-3 shows the clay potential functions (equal to swelling pressures at zero suction) given as functions of dry density. In the range 1500 – 1700 kg/m³, relevant for the present study, the functions agree well with the experimental data (indicated by the red and black dots). If compared to swelling pressure data given in the task description, reproduced to the right in Figure 5-3, the adopted functions in the left graph overestimate the measured swelling pressures.

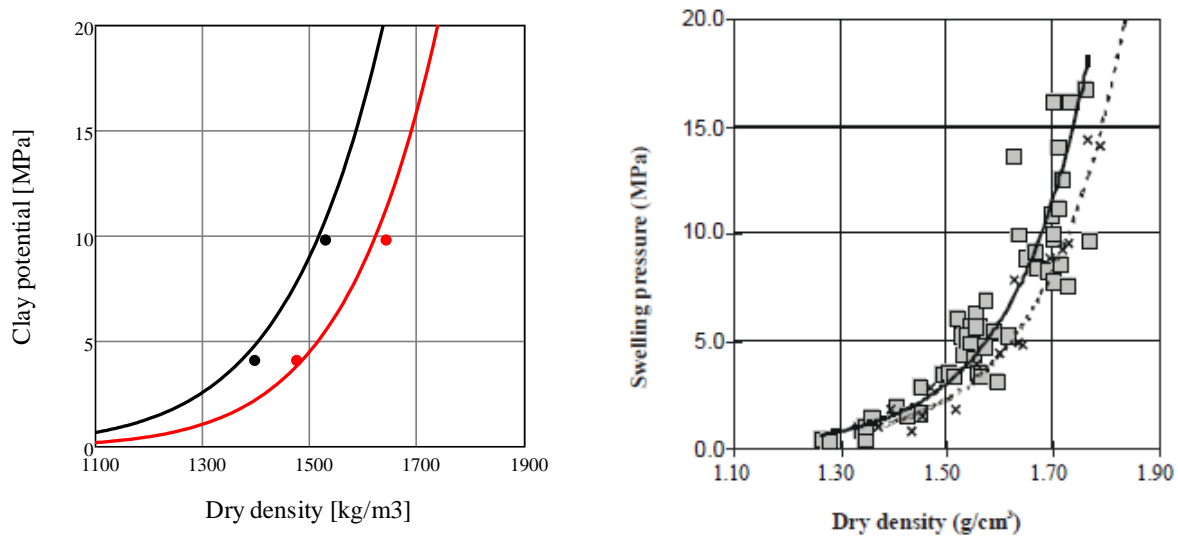


Figure 5-3. (Left) High and Low clay potential functions together with the corresponding experimental data. (Right) Swelling pressure data from the task description.

5.5.3 Initial and boundary conditions

Table 5-15 Initial condition

Variable	Value	Comment
ρ_s	2735 kg/m ³	Svensson et al. (2011)
ρ_d	1700 kg/m ³	Average for blocks at installation
RH	40%	According to sensor data
w	0.125	Within the given range (0.125-0.155). Choice based on the used retention properties (see Table 5-12) and initial RH. In hindsight, the model performance could probably benefit from using a higher value.
$\sigma: \sigma = \sigma_1$	-0.01 MPa	
T	12 °C	According to sensor data

Derived variable	Value	
$e = \rho_s / \rho_d - 1$	0.609	
$s: RH = \exp\left(\frac{-sM_w}{RT \mu \tilde{\rho}_l(s)}\right)$	114.4 MPa	
$e_\mu = \rho_s / \rho_l(s) w$	0.361	
$f: \mathbf{f} = f \mathbf{1}, \tilde{\alpha}(e, e_\mu)(\tilde{\psi}(e_\mu, \mathbf{f}) - s \mathbf{1}) + \boldsymbol{\sigma} = \mathbf{0}$	0.307	

The simulated timeline:

The simulation incorporates three phases:

- Installation, pre-heating: $t_{\text{sim}} < 135$ days
- Operation, H2 switched on: $135 \text{ days} < t_{\text{sim}} < 6630$ days
- Dismantling II, H2 switched off: $6630 \text{ days} < t_{\text{sim}} < 6710$ days

In the simulated timeline the pre-heating period was not compensated for and therefore the operational phase ended up 135 days too short. This does not have any significant effect on the results.

Thermal boundary conditions:

- No flow conditions at the horizontal boundaries.
- $t_{\text{sim}} < 135$ days: 12 °C at inner and outer boundary.
- $135 \text{ days} < t_{\text{sim}} < 189$ days: Increasing temperatures linearly to 94 °C at the inner boundary and 44 °C at the outer boundary.
- $189 \text{ days} < t_{\text{sim}} < 6630$ days: keep 94 °C at the inner boundary and 44 °C at the outer boundary.
- $6630 \text{ days} < t_{\text{sim}} < 6710$ days: no flow at the inner boundary, prescribing flux with 2.5 W/(m² K) and $T_{\text{ref}} = 20^\circ\text{C}$ at the outer surface.

Hydraulic boundary conditions:

- No-flow conditions at all boundaries except the outer.
- At the outer boundary the flux is specified as varying linearly with suction. The value $p_l = 0.5$ MPa was obtained by studying measurements of hydraulic pressure in boreholes.
 - $t_{\text{sim}} < 20$ days: $p_l = 0.1$ MPa gives zero flux.
 - $t_{\text{sim}} > 20$ days: $p_l = 0.5$ MPa gives zero flux

Mechanical boundary conditions:

- Roller boundary conditions at all boundaries aside from the outer.
- The outer boundary could move 28 mm radially outwards under "stress-free conditions" to mimic an initially open gap of 28 mm.

5.5.4 Results/discussion

Below, model results are plotted together with experimental data at H2 mid. The plotted sensor data (temperature, RH and radial compressive stress)

belong to section F2 and the post-mortem analysis results (water content, dry density, degree of water saturation, RH) belong to sample section 49. Sensors are identified by their individual number solely, e.g. 70AIT-TSF2-01 is identified by 01. In the graphs showing sensor data evolution day 0 is the day when the heaters were switched on, i.e. equal to $t_{sim} = 135$ days.

In Figure 5-4 the T-3 response can be compared with temperature sensor data {01, 02, 03, 04} all being measured at the inner surface of the bentonite buffer. Since the thermal BC was designed using these data good agreement is expected. The agreement between the T-5 and T-6 response and corresponding measurements, 05 and 06, respectively, is not very good. The measurement 06, however, seems not to be consistent with {01, 02, 03, 04} either.

The mistake regarding the length of the simulation is here evident, the time of the operational phase should stretch 135 days further.

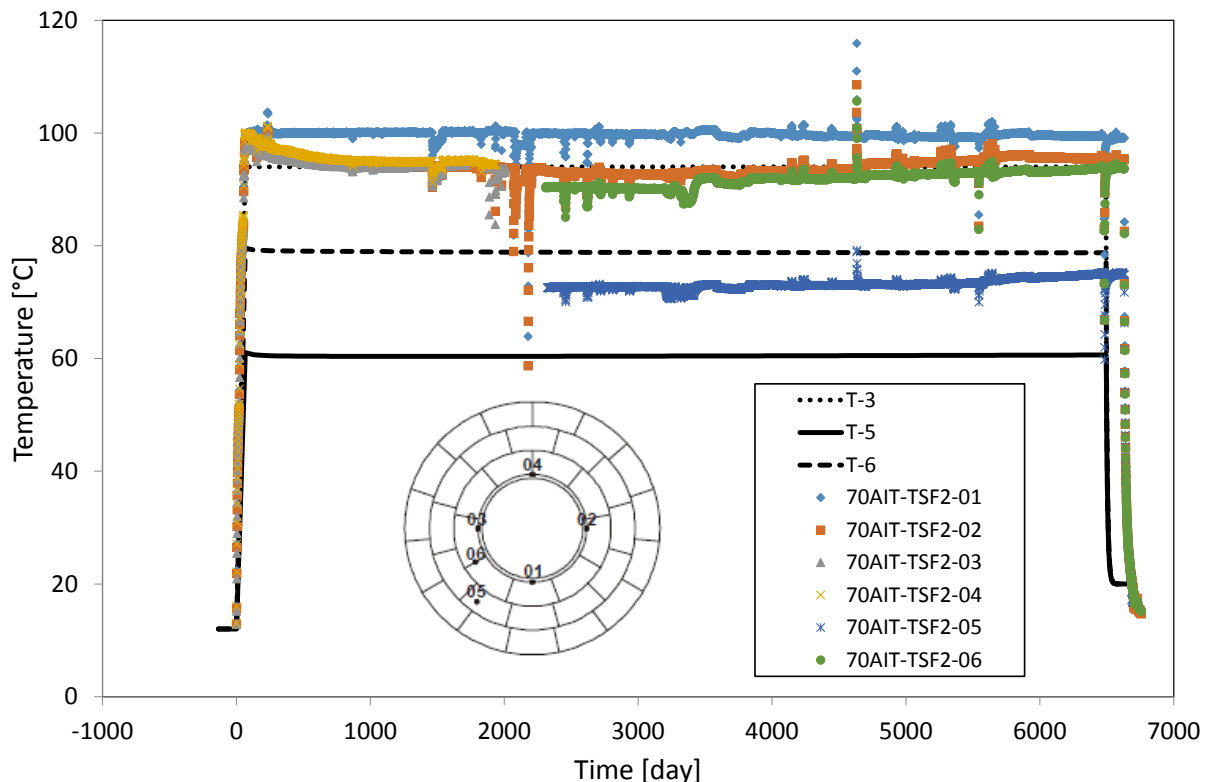


Figure 5-4. Temperature, (symbols) sensor data at section F2 and (lines) model results.

In Figure 5-6, RH-3 can be compared with {02, 03, 04, 07, 10*, 13*}, RH-5 with {05, 06, 08, 09*, 12*} and RH-11 with {11*, 14*}. The sensors marked with * were activated about the first dismantling. The experimental data is scattered but individual general trends can be seen for all three groups defined above. The model results agree reasonably with the corresponding general trend of the experimental data.

If going more into detail, RH-3 and RH-5 increases faster than sensor data. For RH-5, recorded at a point close to the rock wall, RH increases immediately from start which is not seen in the sensor data. RH-3, recorded at a point in the middle of the buffer, start to increase after about 40 days and then increases rapidly until about day 70 where the curve gradually starts to level out. When the sensor data starts about 40%, at day zero in the graph, RH-3 already show 54%. At the time when both sensor data and RH-3 starts to level out the difference between model and experiment is 15-35% depending on which sensor data is selected.

Possible reasons for the discrepancy could be: using 0.5 MPa from start in the pore pressure boundary condition might be too high, the clay potential function fitment might be improper, representation of water transport in the clay might be improper, the disregarded axial processes might be influential and the disregarded “gap-network” within the buffer could have a significant influence on water transport in the initial phase.

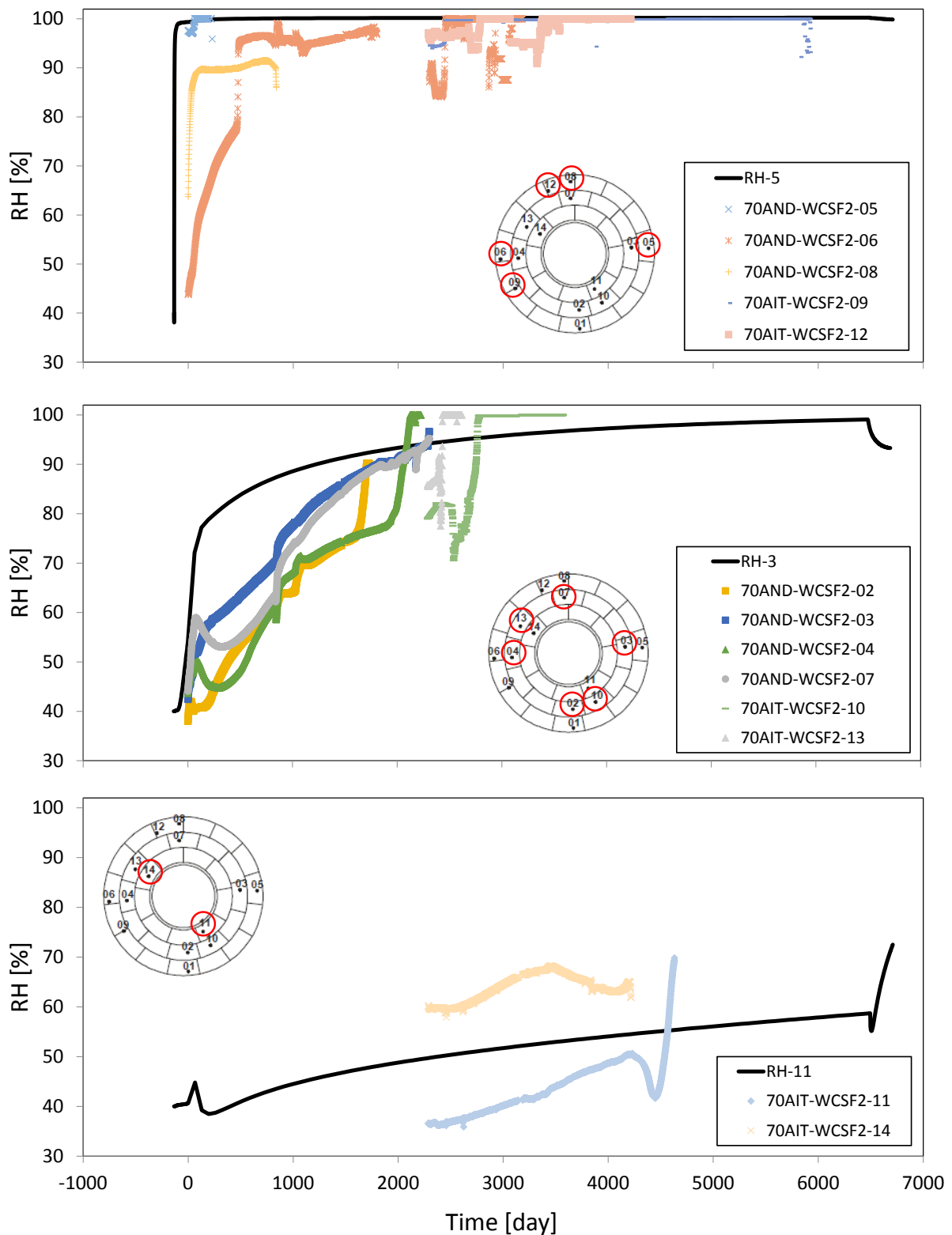


Figure 5-5. RH, (symbols) sensor data at section F2 and (lines) model results.

When studying 05 and 08 sensor data in Figure 5-6 it is evident that these

stress measuring sensors were initialized at a value close to zero at the time when recording begun, 2311 days after switching on the heaters. If this also was the case for sensors 01-04 is, however, not as clear. Were they calibrated as to give zero stress when activated, at the time when the heaters were switched on? In the present model significant stresses are present at the time when the heaters were switched on, due to water uptake during the pre-heated phase, so this has a significant effect when performing the analysis. In order to deal with the ambiguity, both unaltered and adjusted model data are considered.

In the upper graph of Figure 5-6, unaltered model result, STS-1, and adjusted result, 'STS-1 Adj.', shifted to start from zero at the day when the heaters were switched on, can be compared with sensor data {01, 02, 03, 04}. In the lower graph of Figure 5-6, unaltered model results, STS-5 and STS-8, and adjusted results, 'STS-5 Adj.' and 'STS-8 Adj.', shifted as to start from zero when sensors 05 and 08 were activated 2311 days after switching on the heaters can be compared with sensor data {05, 08}.

When, in the upper graph of Figure 5-6, comparing unaltered, STS-1, and adjusted, 'STS-1 Adj.', responses with the relevant sensor data, the most significant difference in appearance is in the initial phase up to about 500 days. The model responses lack the plateau which the sensor data have. This is most probably an effect of the fast wetting (or lack of initial drying) in the model as compared to the experiment, also mentioned in the comparison of RH evolutions. The experimental and simulated stress rates agree well. The magnitude of stress is overestimated, something which was anticipated when investigating the clay potential parametrisation, see 5.5.2.

Sensor 08 does not indicate any increase in stress and breaks down after a short time. Thus, model results 'STS-5 Adj.' and 'STS-8 Adj.' are compared to data recorded by sensor 05. The agreement between model and data is very good.

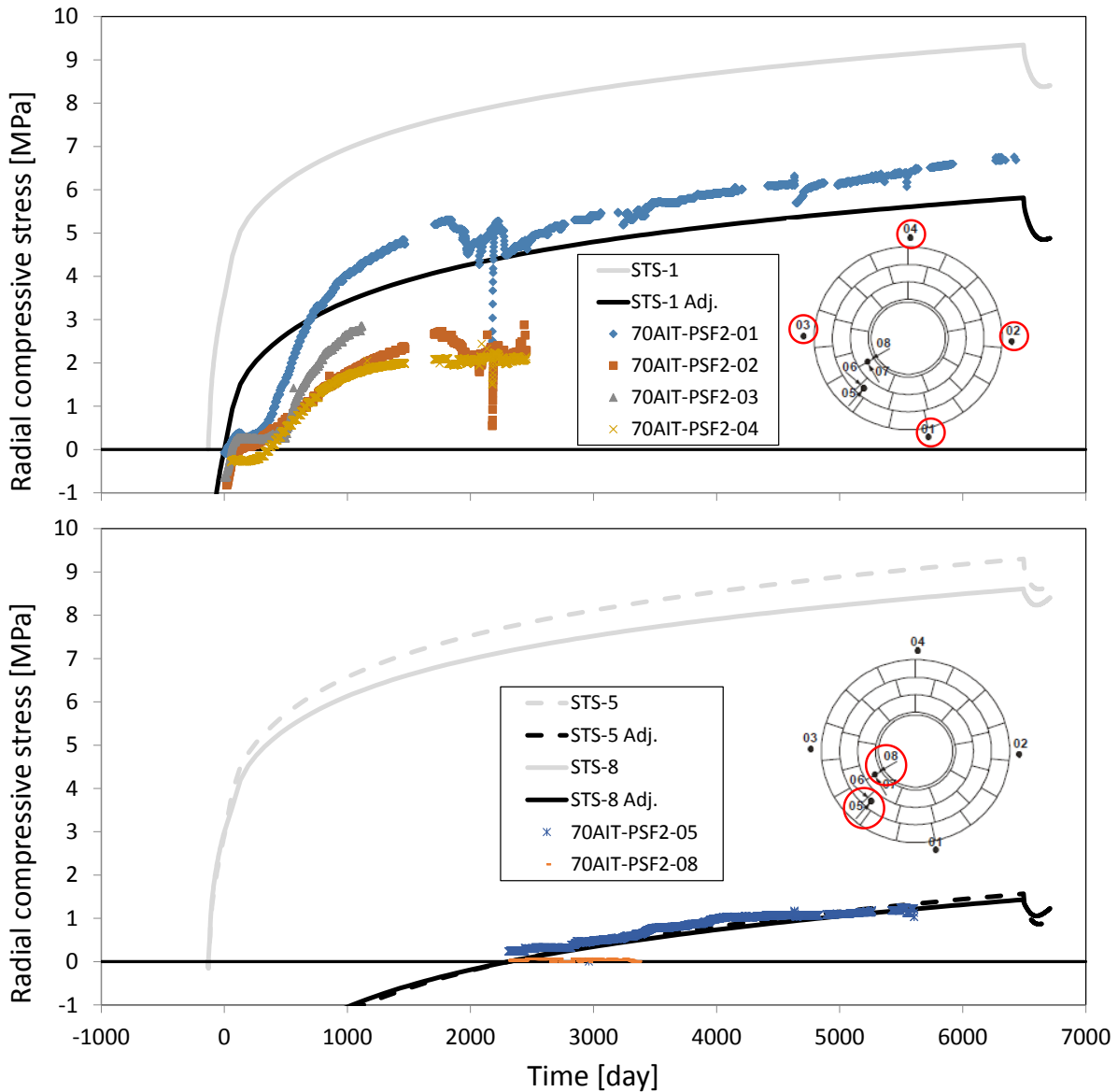


Figure 5-6. Radial compressive stress, (symbols) sensor data at section F2 and (lines) model results.

In Figure 5-7 the calculated profile of water content (water mass / solid mass) is plotted together with experimental data. The model agrees reasonably well with the experiment. At the inner positions the model has lower values which could come from using a low initial value (12.5%), an overestimation of radially outward vapor transport, an underestimation of radially inward liquid water transport and the axial symmetry assumption disabling axial inflow.

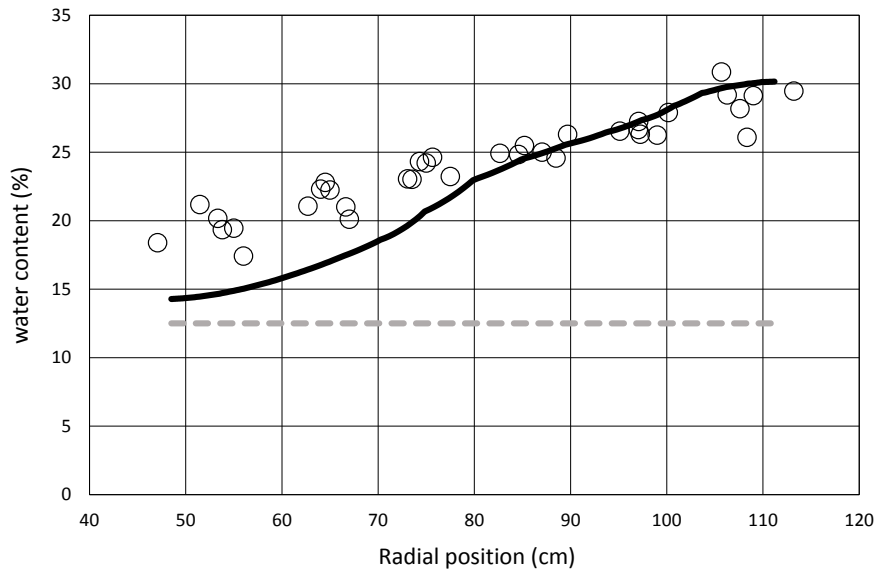


Figure 5-7. Water content profiles, (symbols) analysed from samples taken in section 49, (solid line) calculated and (hatched line) initial.

In Figure 5-8 the calculated profile of dry density (solid mass / total volume) is plotted together with experimental data. The model agrees well with the experiment.

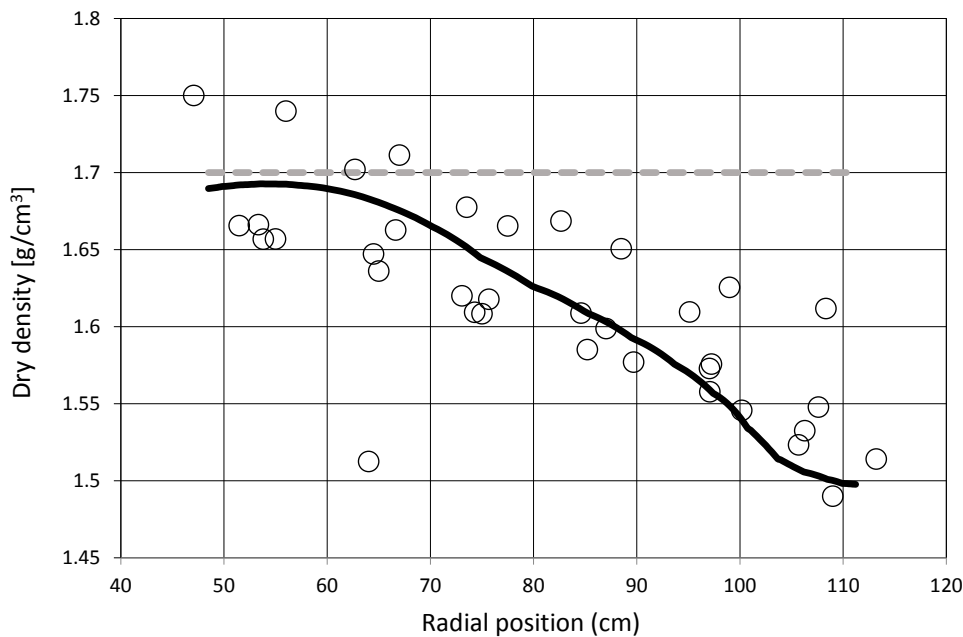


Figure 5-8. Dry density profiles, (symbols) analysed from samples taken in section 49, (solid line) calculated and (hatched line) initial.

In Figure 5-9 the calculated profile of degree of saturation (liquid water volume/pore volume) is plotted together with experimental data. The model agrees reasonably well with the experiment. As with the water content, however, at the inner positions the model has lower values. The possible

reasons for this are the same as mentioned for the water content.

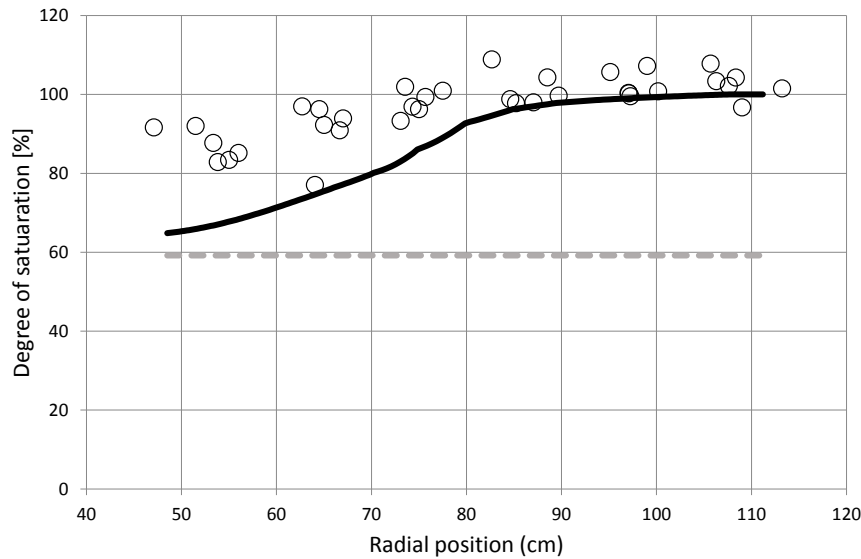


Figure 5-9. Degree of water saturation profiles, (symbols) analysed from samples taken in section 49, (solid line) calculated and (hatched line) initial.

In Figure 5-10 the calculated profile of RH (calculated from suction) is plotted together with experimental data. Again, the agreement is fair but at the inner positions the suction potential is higher (RH is lower) in the model than what was found in the samples. See the discussion of the water content for possible reasons.

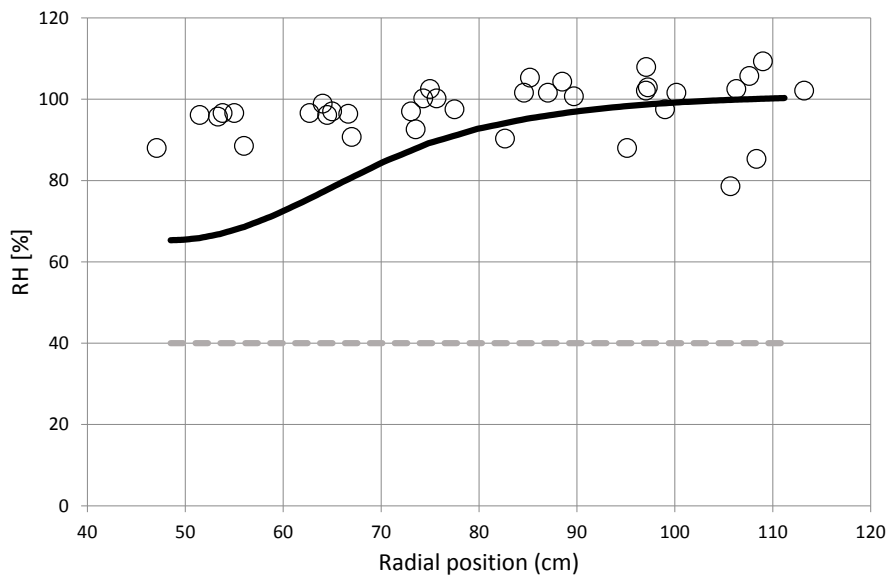


Figure 5-10. RH profiles, (symbols) analysed from samples taken in section 49, (solid line) calculated and (hatched line) initial.

5.6 Clay Technology – Code_Bright

The Febex experiment is simulated using the finite-element code Code_Bright, v. 9 (see e.g., Alcoverro and Alonso 2001). Since the same model was used within SKB's EBS Task Force only a short description of the model is included here; a more detailed description is given by Kristensson (2019b). For the purpose of this study, three phases of the experiment are considered; the dismantling phase is ignored:

- Phase 0 ($t = -135$ to 0 days). Water uptake and water redistribution during 135 days prior to the start of the heating (heating starts at $t = 0$ days).
- Phase 1 ($t = 0$ to 1855 days). Heating from both canisters, water uptake and water redistribution.
- Phase 2 ($t = 1855$ to 6758 days). Heating from the innermost canister only, water uptake and water redistribution.

5.6.1 Geometry and discretization

The experimental geometry is approximated to be axisymmetric, see Figure 5-41. It includes the host rock (R, marked in grey), the plug (P, turquoise), the heaters (H, pink), the bentonite blocks (B, blue) and a gap (G, dark red) between the blocks and the rock. In order to allow for radial expansion of the bentonite without having to include friction elements in the model, two artificial openings were introduced between the buffer and the rock in the innermost part of the drift and between the buffer and the plug, see Kristensson (2019b) for details.

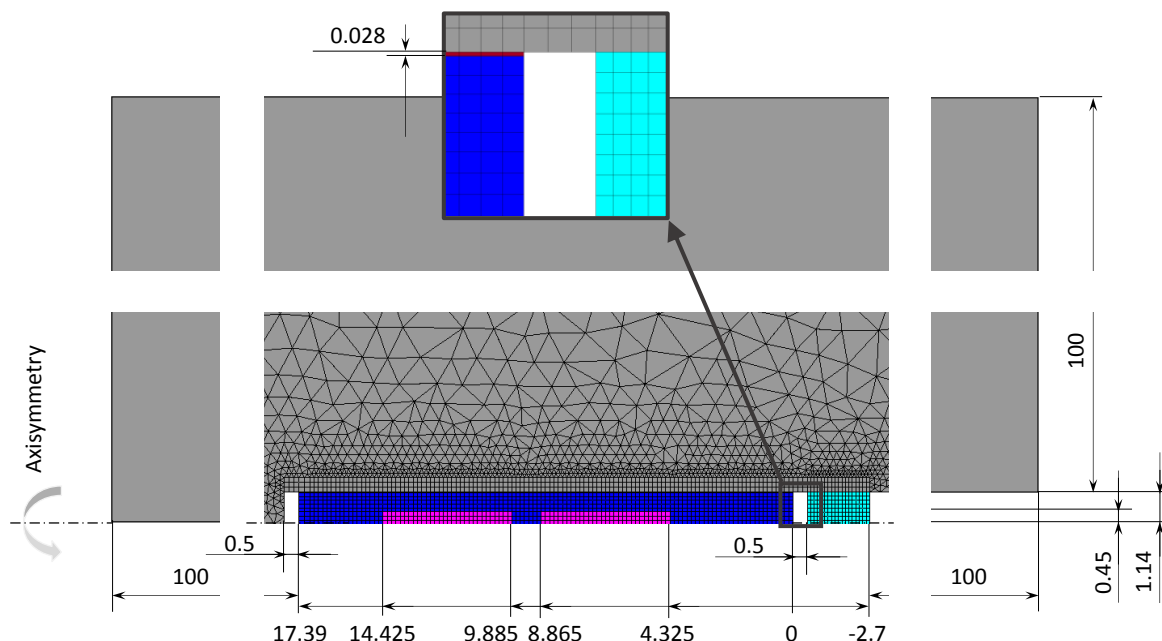


Figure 5-41. Illustration of the model (dimensions in m). Note that the actual mesh used in the calculations is finer than the one shown here, see main text for details. From Kristensson (2019b).

The model is discretized with two types of elements:

- Linear quadrilateral elements with four integration points and selective integration by means of the “B-matrix” (used in the innermost part of the model). The model has 18 elements radially across the cylinder-shaped blocks and 2 elements radially across the gap.
- Linear triangular elements (used in the outer parts of the model representing the host rock)

The total number of elements in the model is 8064 and the total number of nodes is 7244.

5.6.2 Input parameters

Porous media relations

The water retention is given by van Genuchten's law

$$S_l = f_d \left(1 + \left(\frac{p_g - p_l}{p_0} \right)^{\frac{1}{1-\lambda}} \right)^{-\lambda}$$

where S_l is the degree of liquid saturation, f_d is a function that extends the ordinary version of the law (see Table 5-16), p_g is the gas pore pressure, p_l is the liquid pore pressure, and p_0 and λ are constants. Parameter values are given in Table 5-16.

Table 5-16. Retention related variables.

Component	p_0 [MPa]	λ [-]	p_d [MPa]	λ_d [-]	f_d [-]	Comment
R	1.74	0.6	-	-	1	The impact of the retention properties of these components are not considered significant for the model. The rock properties are, however, similar to those given in section 3.2.2 in the task specification (Talandier 2018).
P	0.6	0.24	-	-	1	
H	1	0.6	-	-	1	
B	22.5	0.09	1100	2.1	$\left(1 - \frac{p_g - p_l}{p_d} \right)^{\lambda_d}$	In agreement with Papafotiou et al. (2017, Chapter 4)
G	1.74	0.6	-	-	1	Same as for the rock

The advective mass flow is governed by Darcy's law. Input to Code_Bright is given by the intrinsic permeability (k), which is assumed to be isotropic and either constant or dependent on the porosity (ϕ), and the relative permeability (k_{rl}), which is either constant or dependent on the degree of liquid saturation. Parameter values for each component are presented in Table 5-17

Table 5-17. Darcy's law, intrinsic and relative permeability.

Component	k [m ²]	k_{rl} [-]	Comment
R	10 ⁻¹⁰	$\sqrt{s_l} \left(1 - \left(1 - s_l^{\frac{1}{0.6}} \right)^{0.6} \right)^2$	The value of k is generic and chosen to be significantly higher than that of the blocks. The expression for k_{rl} is similar to that given in section 3.2.2 in the task specification (Talandier 2018).
P	10 ⁻¹⁷	$\sqrt{s_l} \left(1 - \left(1 - s_l^{\frac{1}{0.24}} \right)^{0.24} \right)^2$	The value of k is chosen from a range that was used in SKB's safety assessment SR-Site (Åkesson et al. 2010)
H	10 ⁻²⁹	1	Assumed to be impermeable
B	$1.1 \cdot 10^{-21} \frac{\phi^3 (0.378 - 1)^2}{(\phi - 1)^2 \cdot 0.378^3}$	S_l^3	In agreement with Papafotiou et al. (2017, Chapter 4)
G	10 ⁻¹⁰	$\sqrt{s_l} \left(1 - \left(1 - s_l^{\frac{1}{0.6}} \right)^{0.6} \right)^2$	The value of k is generic and chosen to be significantly higher than that of the blocks.

The diffusive mass flow is governed by Fick's law. Input to Code_Bright is given by the tortuosity (τ_0), which is assumed to be constant. Parameter values for each component are given in Table 5-18.

Table 5-18. Fick's law, tortuosity.

Component	τ_0 [-]	Comment
R	1	Permeable to vapour
P	1	Permeable to vapour
H	0.00 1	Impermeable to vapour
B	0.5	Based on results for MX-80 bentonite reported in Pintado et al. (2002), but is here assumed to be relevant also for Febex bentonite. The parameter choice also agrees well with what is given in Figure 1-22 in Appendix 1 of the task specification.
G	1	Permeable to vapour

The conductive heat flux is governed by Fourier's law. Input to Code_Bright is given by the thermal conductivity (λ), which is either assumed to be constant or dependent on the degree of saturation. Parameter values for each component are given in Table 5-19.

Table 5-19. Fourier's law, thermal conductivity.

Component	λ [W/m·K]	Comment
R	3.8	(Kristensson 2019b, Appendix 1); also within range given in the task specification (Talandier 2018, Table 3-2).
P	1.7	Handbook value for concrete
H	45	Handbook value for steel
B	$0.57 + \frac{1.28 - 0.57}{1 + \exp\left(\frac{S_t - 0.65}{-0.1}\right)}$	Fitted to experimental data from Papafotiou et al. (2017, Fig. 4-8), see Kristensson (2019b).
G	1.3	In agreement with the fully saturated block material

Solid phase relations

Input parameters for the solid phase are the density (ρ_{s0}) and the specific heat capacity (c_s), which both are assumed to be constant. Parameter values for each component are given in Table 5-20.

Table 5-20. Solid phase parameters, mass density and specific heat capacity.

Component	ρ_{s0} [kg/m ³]	c_s [J/kg·K]	Comment
R	2660	920	In agreement with values given in the task specification (Talandier 2018, Table 3-2)
P	2000	900	Handbook value for concrete
H	7800	460	Handbook value for steel
B	2735	1091	In agreement with Papafotiou et al. (2017, Chapter 4)
G	2660	920	Equal to rock properties

In total, three different mechanical material models have been used in the simulation:

- The rock, plug and heaters are assumed to respond as linear elastic materials. The parameter values are given in Table 5-21.
- The blocks are assumed to respond according to a modified version of the Barcelona Basic Model (BBM). The parameter values are presented in Table 5-22.
- The gap is assumed to respond according to a bilinear elastic model. The parameter values are presented in Table 5-23.

Table 5-21. Parameter values for the linear elastic model.

Component	E [GPa]	ν [-]	Comment
R	100	0.2	Generic values chosen such that the materials are stiff in comparison with the blocks. The parameter values are also in reasonable agreement with values given in the task specification (Talandier 2018, Table 3-2)
P			
H			

Table 5-22. Parameter values for the modified BBM model (cf. Papafotiou et al. 2017, Chapter 4).

Parameter	Component : B	Comment
e_0	0.609	The value of the void ratio is based on the initial value of the porosity (cf. section 0)
K_{i0}	0.12	
α_{ij}	-0.12	
ν	0.2	
K_{min} [MPa]	200	The value has been increased compared with that used by Papafotiou et al. (2017, Chapter 4) in order to avoid a significant initial compression close to the canister at small stresses. More details are given by Kristensson (2019b).
α	0.5	
p_0^* [MPa]	19	
p_c [MPa]	1	
λ_0	0.2	
p_s [MPa]	2.6	
M	0.234	
K_{s0}	0.3	
p_{ref} [MPa]	0.5	The value has been reduced compared with that used by Papafotiou et al. (2017, Chapter 4) in order to reduce the swelling/shrinking of the material. More details are given by Kristensson (2019b).
α_{ss} [MPa ⁻¹]	-0.02	

Table 5-23. Parameter values for the bilinear model.

Parameter	Component : G	Comment
E_0 [MPa]	0.1	The parameters are set as to obtain a soft material (as compared to the blocks) when the gap is open and stiff when the gap is closed, defined as when the volumetric strain $> \epsilon_{v,limit}$.
E_C [MPa]	$1 \cdot 10^3$	
$\epsilon_{v,limit}$	100	
ν	0.2	

Liquid phase relations

The liquid phase is equal to liquid water. The relations and parameter values for the mass density, viscosity and specific heat capacity as specified by default in Code_Bright are used in the present modelling work.

Gas phase relations

The gas phase is considered an ideal gas mixture with a constant gas pore pressure (p_g) of 0.1 MPa. The relations and parameters for the vapour pressure, air density, specific latent heat and specific heat capacity as specified by default in Code_Bright are used in the present modelling work.

5.6.3 Initial and boundary conditions

Initial conditions

Initial parameter values are required for porosity, temperature, liquid pore pressure, and state of stress:

- The porosity of the rock is set at 1% in agreement with the range given in the task specification (Talandier 2018, Table 3-2). The same value is assigned to the plug and heaters (this value is too low for the plug but is judged not to have a significant impact on the solution).
- The porosity of the blocks is set at 37.8% based on an average initial dry density of 1700 kg/m³ (Lanyon and Gaus 2013) and a particle density of 2735 kg/m³ (Svensson et al. 2011).
- The porosity of the gap is set at 90%.
- The liquid pore pressure in the rock and plug is set at 0.1 MPa (cf. hydraulic boundary conditions, below).
- The liquid pore pressure in the blocks is set at -124.9 MPa (Papafotiou et al. 2017, Chapter 4). The same value is assumed for the heaters and gap.
- The initial temperature is based on sensor data and set at 12°C in all components.
- An isotropic total stress of -0.11 MPa is assigned to all components.

Boundary conditions

Thermal boundary conditions:

- The temperature (T) is 12°C on the outer rock boundary,
- $T = 12^\circ\text{C}$ and heat transfer coefficient (γ) is 10 W/°C on the tunnel boundary, and
- $T = 12^\circ\text{C}$ (phase 0) and $T = 16^\circ\text{C}$ (phases 1 and 2) on the plug boundary.

Hydraulic boundary conditions:

- The flow of liquid water (j_i^w) is 0 kg/(m²·s) on the outer rock boundary
- The liquid pore pressure (p_i) on the outer plug boundary and on the tunnel boundary is 0.1 MPa and outflow is allowed.

Mechanical boundary conditions:

- Roller boundaries on all outer boundaries

Body conditions

The thermal load is applied along the centre of the heater representations (see Figure 5-42, top). The power evolution used as input to the Code_Bright model was obtained by fitting a piecewise linear function to the measured heater powers (see Figure 5-42, bottom). A more detailed description is given by Kristensson (2019b).

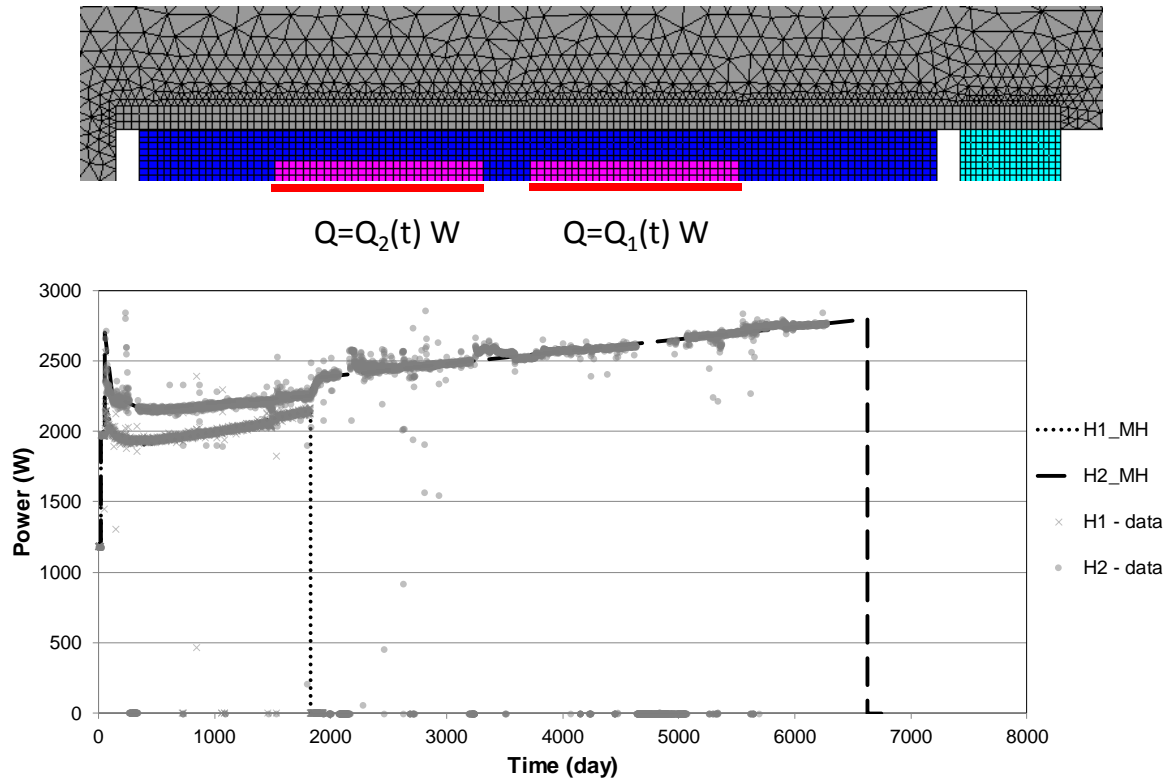


Figure 5-42. Top: Thermal load application. Bottom: Measured (plot symbols) and simulated heater power (lines). From Kristensson (2019b).

A liquid source was introduced by prescribing the liquid pore pressure to 0.1 MPa at a line positioned 0.5 m outside of the outer boundary of the bentonite buffer, as shown in Figure 5-43. This allowed the buffer to have full access to water and was motivated from considering the reports of a highly permeable and water bearing host rock in the experiment (cf. Papafotiou et al. 2017, Chapter 4).

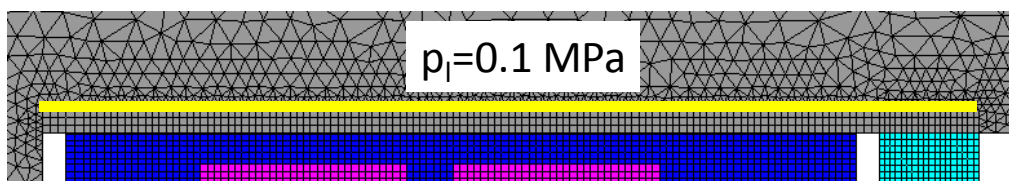


Figure 5-43. Hydraulic load (source) prescription. From (Kristensson 2019b).

5.6.4 Results/discussion

Requested output include the temporal evolution of the temperature, relative humidity, total pressure, water content, and pore pressure (cf. Table 5-24) as well as the final distribution of the water content, dry density, degree of saturation and relative humidity in sections S49, S52, S56 and S61. Comparisons between model results and available measurements are presented in the

sections below. Note that in the current formulation of Code_Bright, the pore pressure gives a measure of the suction and not the actual water pressure in the bentonite. Comparisons between simulated and measured pore pressures are, therefore, not included here.

Table 5-24. Sensors used for comparison with modelling results. In the following, the sensors and corresponding modelling results are identified by section label and number, e.g., F2-03.

Section	Type	Sensor IDs
F2	Temperature	70AIT-TSF2-03 70AIT-TSF2-05 70AIT-TSF2-06
	Relative humidity	70AND-WCSF2-03 70AND-WCSF2-05
	Total pressure	70AIT-PSF2-01 70AIT-PSF2-05 70AIT-PSF2-08
E2	Temperature	70AIT-TSE2-01
	Relative humidity	70AND-WCSE2-03 70AND-WCSE2-05 70AND-WCSE2-07
	Total pressure	70AIT-PSE2-05 70AIT-PSE2-06
B2	Temperature	70AIT-TSB2-03 70AIT-TSB2-04 70AIT-TSB2-06
	Total pressure	70AIT-PSB2-02 70AIT-PSB2-03
M2	Water content	70AIT-WT-M2-04 70AIT-WT-M2-05 70AIT-WT-M2-06 70AIT-WT-M2-07

Temperature evolution

The temperature evolutions at the selected points are presented in Figure 5-44. The agreement between modelled and measured temperatures is good or reasonable in all investigated sections.

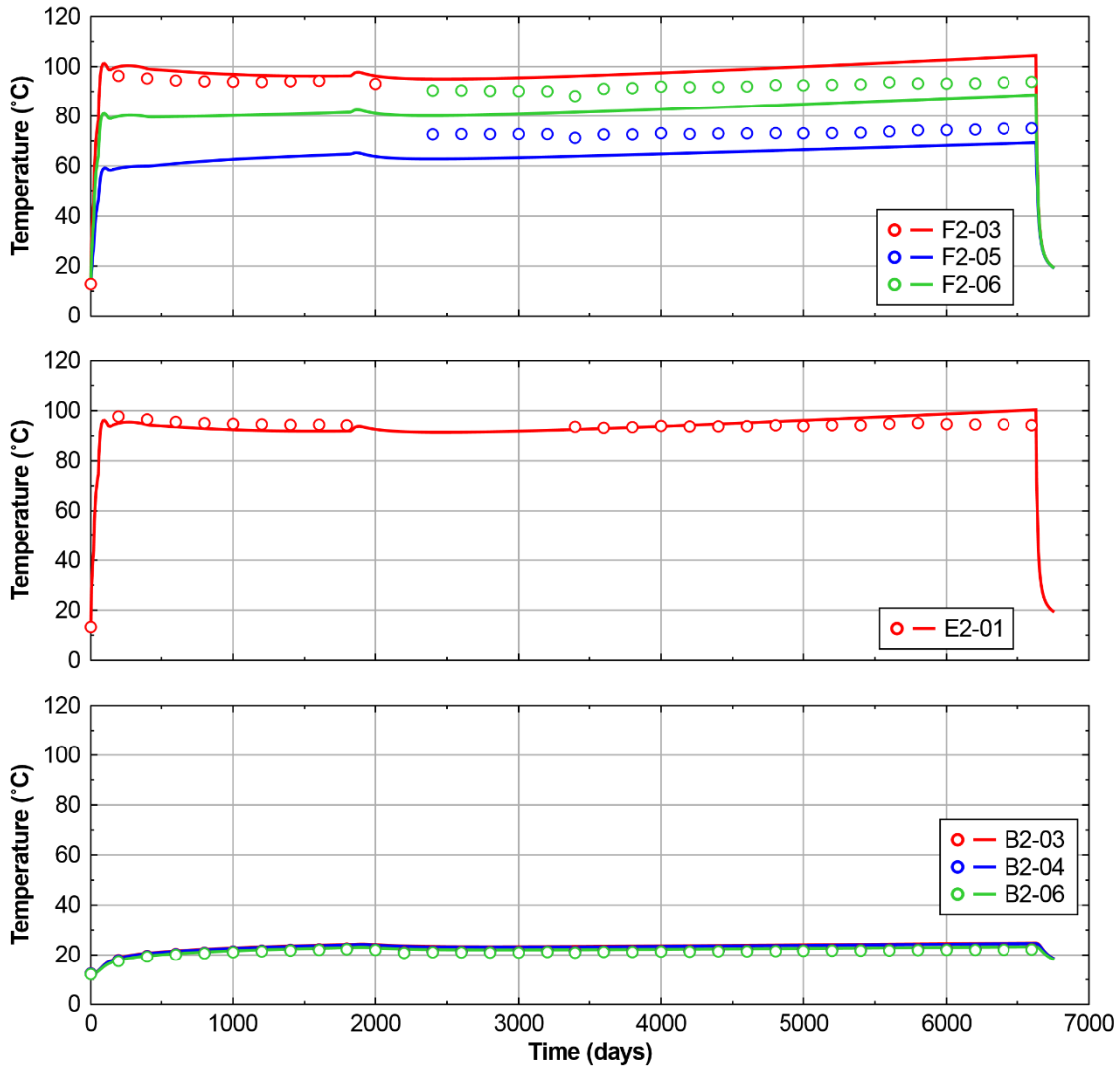


Figure 5-44. Comparison between simulated (lines) and measured (plot symbols) temperatures in section F2 (top), section E2 (middle) and section B2 (bottom). Note that for clarity, the measurement data are shown with approximately 200 day-intervals.

Relative humidity evolution

The relative humidity evolutions at the selected points are presented in Figure 5-45. Note that only one instrument (F2-03) worked for any length of time. At this location, however, the agreement between modelled and measured relative humidity is very good.

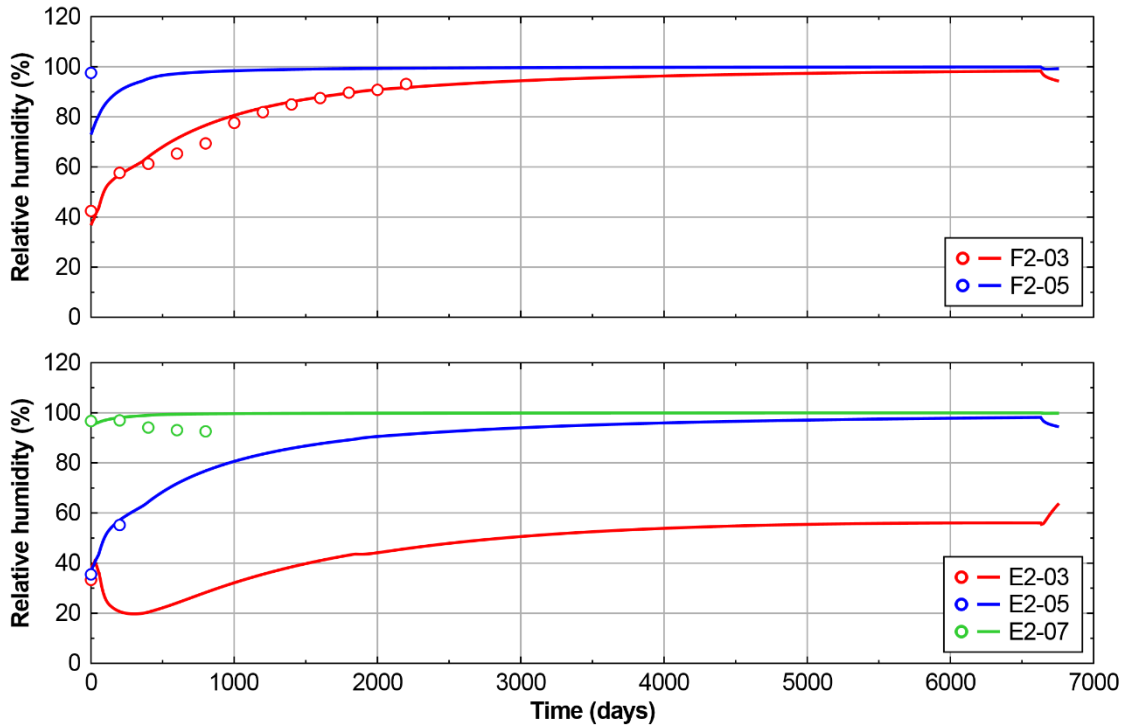


Figure 5-45. Comparison between simulated (lines) and measured (plot symbols) relative humidity in section F2 (top), section E2 (bottom). Note that for clarity, the measurement data are shown with approximately 200 day-intervals.

Total pressure evolution

The total pressure evolutions (radial stress in sections F2 and E2, and axial stress in section B2) at the selected points are presented in Figure 5-46. The agreement between modelled and measured radial stress at positions corresponding to sensors F2-01 and E2-06 (sensor E2-05 stopped working on day 28 (Martínez et al. 2016)) is very good. Note that sensors F2-05 and F2-08 started recording on day 2311 (e.g., Martínez et al. 2016) and measure the change in stress from that day. By shifting the simulated radial stress (blue and green curves in Figure 5-46, top) downwards in the graph such that they start from zero on day 2311 a very good agreement is obtained between model and measurements also at these locations.

The agreement between the modelled and measured axial stress in section B2 is poor (see Figure 5-46, bottom). A possible explanation for the discrepancy may be associated with the lower density in this section (resulting from difficulties during installation of the buffer blocks) that has not been accounted for in the model (cf. Kristensson 2019b).

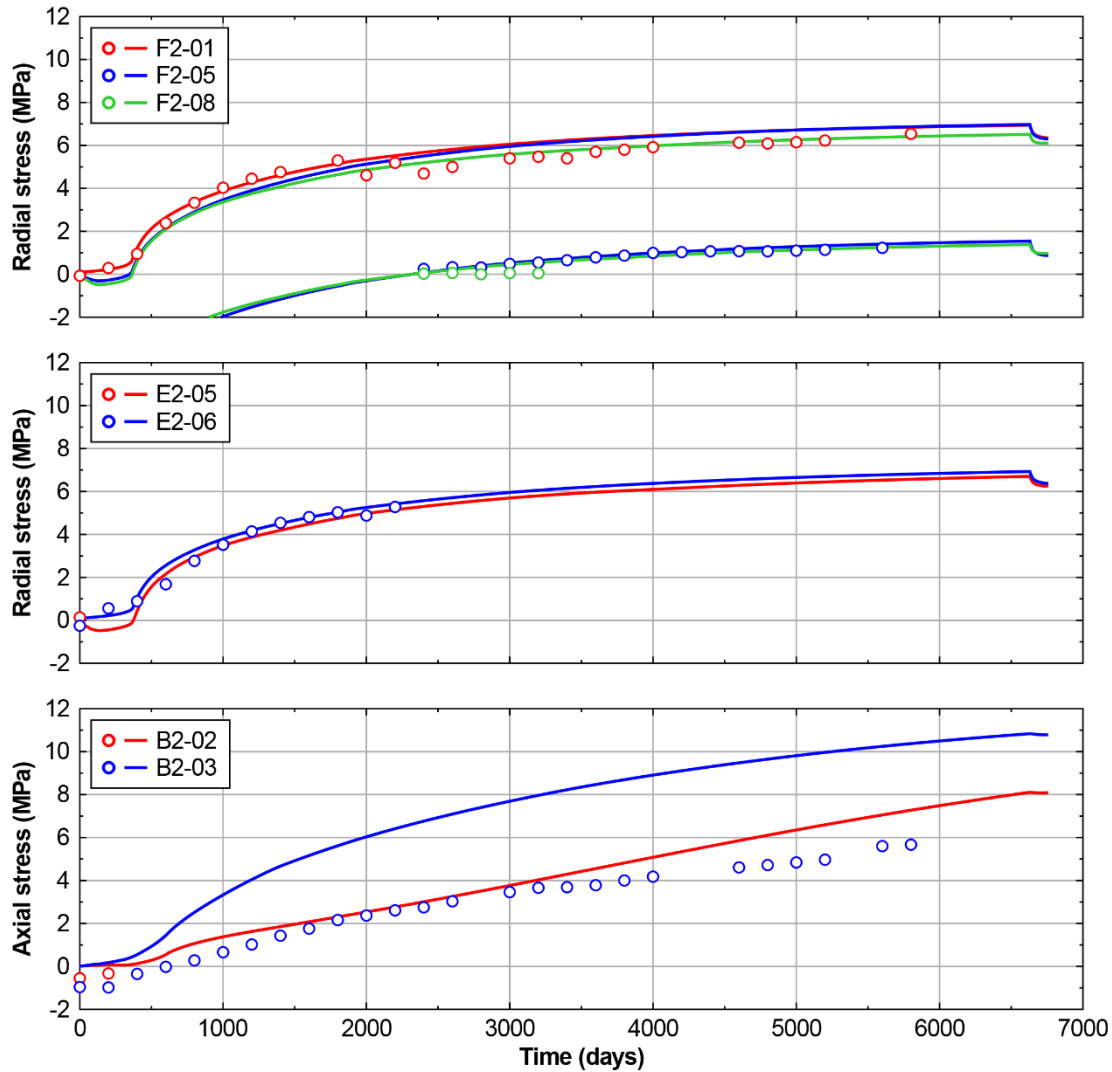


Figure 5-46. Comparison between simulated (lines) and measured (plot symbols) stress in section F2 (top; the simulated radial stress at positions F2-05 and F2-08 (blue and green curves) have been shifted downwards to match the starting points of instruments (cf. Martínez et al. 2016)), section E2 (middle) and section B2 (bottom). Note that for clarity, the measurement data are shown with approximately 200 day-intervals.

Volumetric water content evolution

The instruments in section M2 measure the volumetric water content (θ), which is defined as (Fredlund and Rahardjo 1993)

$$\theta = S_l \phi$$

where S_l and ϕ are the degree of saturation and the porosity, respectively. Figure 5-47 shows a comparison between the modelled (calculated from simulated S_l and ϕ) and the measured volumetric water content. The agreement is reasonable (with the exception at the location corresponding to sensor M2-04 during the later stages of the experiment).

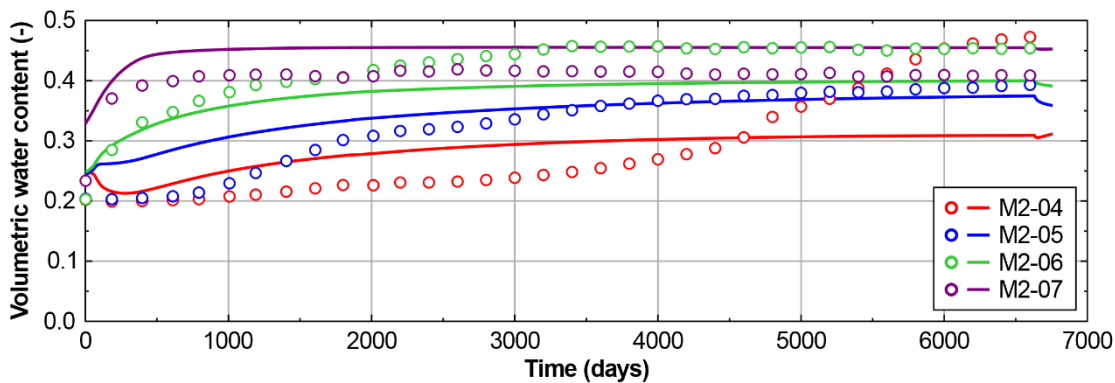


Figure 5-47. Comparison between simulated (lines) and measured (plot symbols) volumetric water content in section M2. Note that for clarity, the measurement data are shown with approximately 200 day-intervals.

Final distributions of water content, dry density, degree of saturation and relative humidity

Profiles of the water content, dry density, degree of saturation and relative humidity in sections S49, S52, S56 and S61 are presented in Figure 5-48 to Figure 5-51. Here, “water content” refers to the gravimetric water content, w , which can be computed from model results using

$$w = S_l \rho_w \left(\frac{1}{\rho_d} - \frac{1}{\rho_s} \right)$$

where S_l is the degree of saturation, ρ_w is the density of water, ρ_d is the dry density (see below) and ρ_s is the particle density (see subsection 0). The dry density is computed from model results using

$$\rho_d = \rho_a (1 - \phi)$$

where ϕ is the porosity. The degree of saturation and the relative humidity are obtained directly from the Code_Bright model.

The results can be summarized as follows:

- In sections S49, S52 and S56, the agreement between modelled and measured water content, dry density and degree of saturation is good or reasonably good. The model underestimates the relative humidity at the inner positions.
- In section S61 (innermost part of the tunnel), the agreement between all modelled and measured quantities is poor. The model significantly underestimates the water uptake. This may be associated with the lower density in this section (resulting from difficulties during installation of the buffer blocks) that has not been accounted for in the model (cf.

Kristensson 2019b).

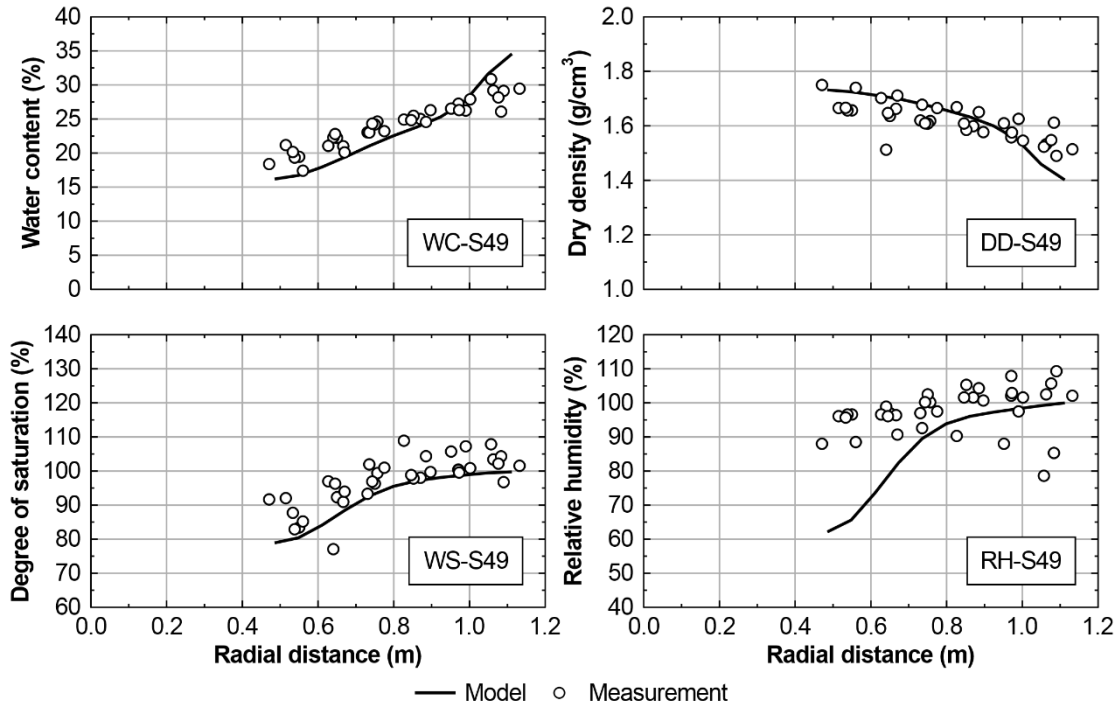


Figure 5-48. Comparison between simulated (lines) and measured (plot symbols) profiles of water content (top left), dry density (top right), degree of saturation (bottom left) and relative humidity (bottom right) in section S49.

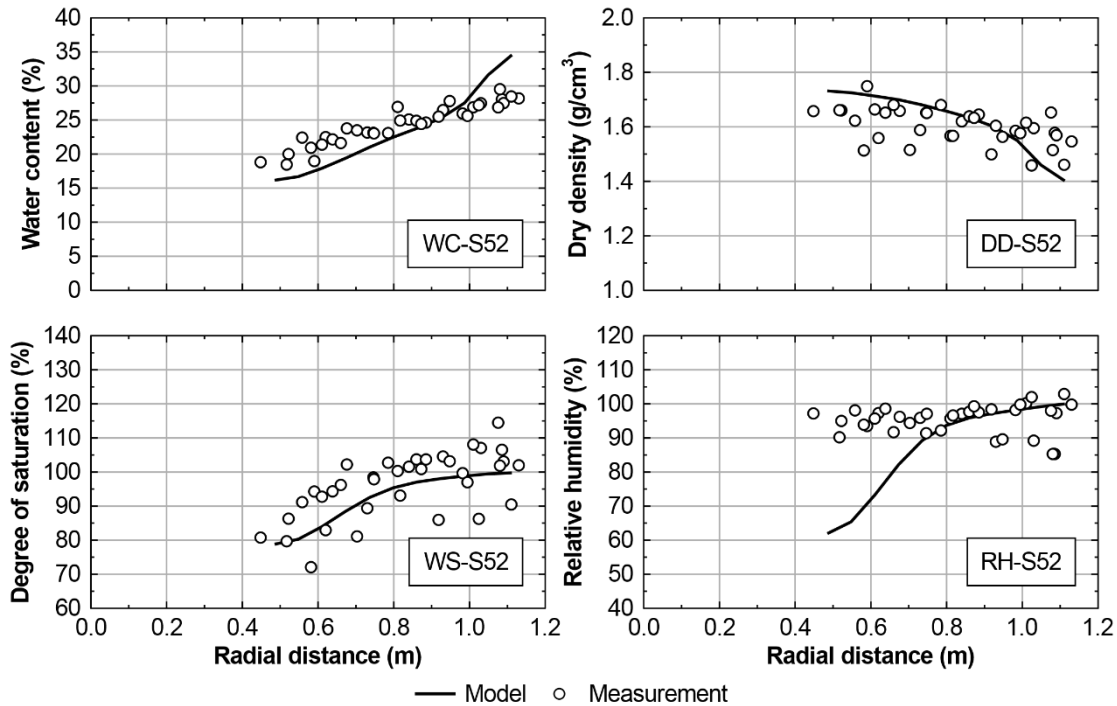


Figure 5-49. Comparison between simulated (lines) and measured (plot symbols) profiles of water content (top left), dry density (top right), degree of saturation (bottom left) and relative humidity (bottom right) in section S52.

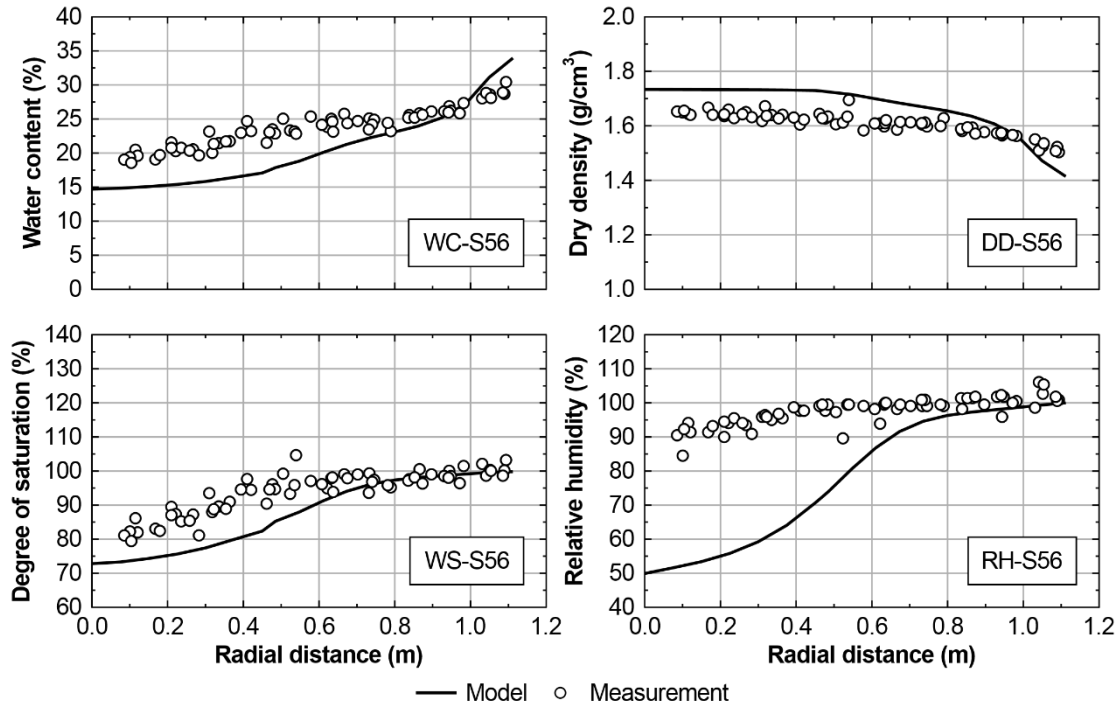


Figure 5-50. Comparison between simulated (lines) and measured (plot symbols) profiles of water content (top left), dry density (top right), degree of saturation (bottom left) and relative humidity (bottom right) in section S56.

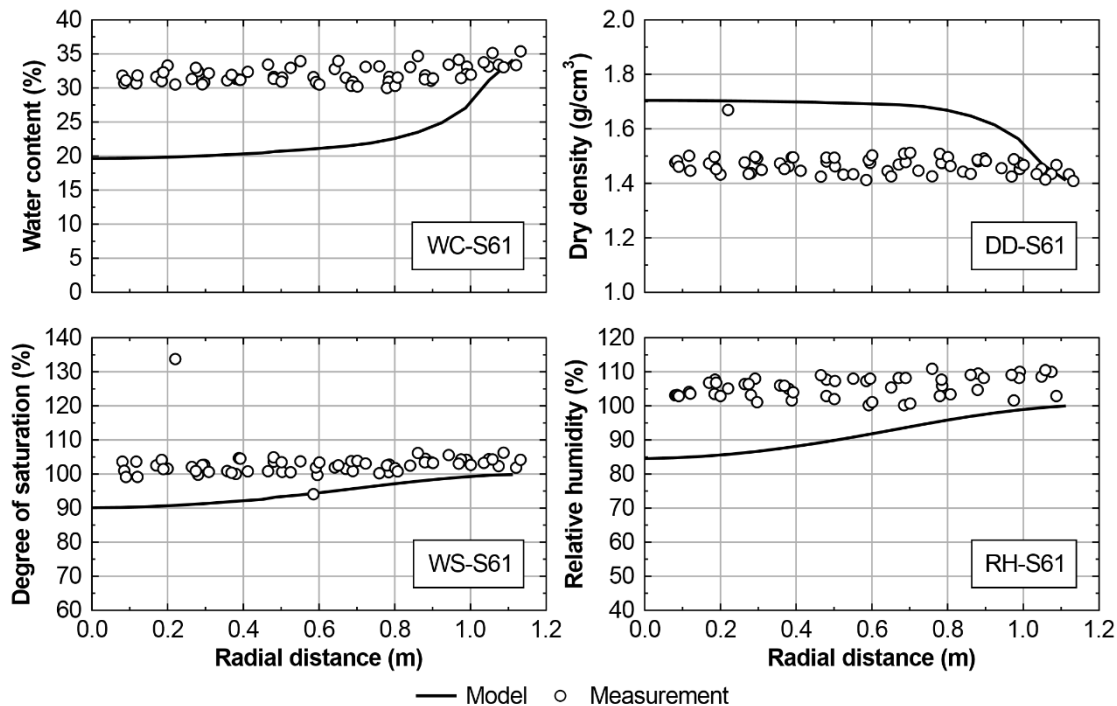


Figure 5-51. Comparison between simulated (lines) and measured (plot symbols) profiles of water content (top left), dry density (top right), degree of saturation (bottom left) and relative humidity (bottom right) in section S61.

5.7 EPFL

5.7.1 Geometry and discretization

Figure 5-52 shows the geometry, discretisation and boundary conditions used in the finite element model. In order to avoid the influence of the imposed boundary conditions, the distance of the external boundary to the engineered barrier is located at 60 m in both the axial and radial directions. The perpendicular displacements of all boundaries are prevented, except for the gallery surface boundary of the service tunnel which is assumed to be deformable during the whole simulation. The temperature and water pressures at the boundaries are fixed to the in situ measured values. The air pressure is fixed to the atmospheric pressure over the entire domain.

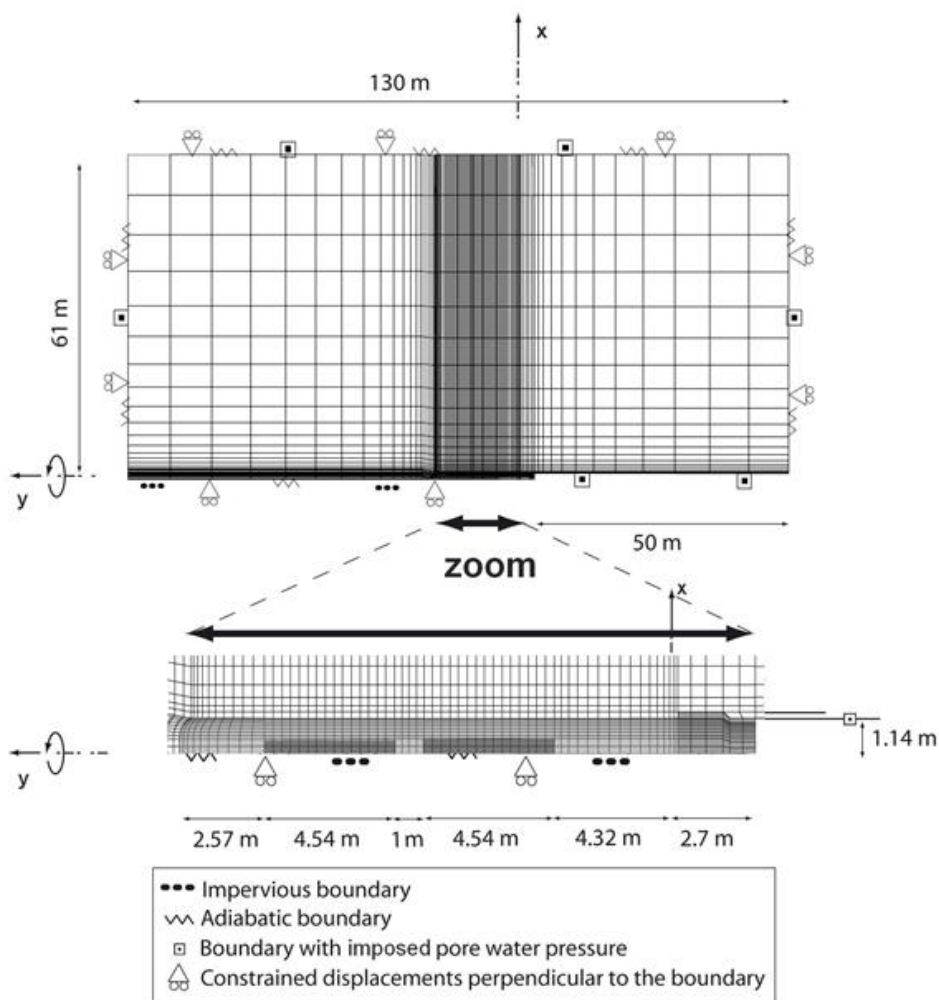


Figure 5-52 Finite element mesh used in the simulation of the in-situ FEBEX experiment. The y axis is the axis of symmetry of revolution.

5.7.2 Input parameters

Febex bentonite

The constitutive model developed in the context of the Beacon WP3, summarised in section 2 of the present report, is used to model the stress-strain behaviour of the bentonite blocks simultaneously subjected to stress, relative humidity and temperature.

The degree of saturation is one of the main state variables used in the model to interpret the mechanical response. Thus, the water retention curve must be accurately described prior to calibrate the mechanical parameters. At the same time, a water retention model allows less uncertainty in the description of the water and heat flow processes, as they depend directly on the evolution of the degree of saturation.

The water retention curve is calibrated with the data presented by Lloret et al. (2003) which is shown in Figure 5-53. The tests consisted in wetting paths, performed under constant volume conditions and at dry densities that are representative of that in the Febex test. The water retention is seen to be rather independent on dry density for suctions above 10 MPa, which suggests that water at high suction is held by means of surface adsorption. It is noted that the adsorbed water density has been adjusted to 1.2 Mg/m³ in order to be able to match the water contents at low values of suction. This has implications when comparing the values of degree of saturation that were obtained from the post-mortem analysis, which were obtained using water density of 1 Mg/m³. More details will be given in the section of results.

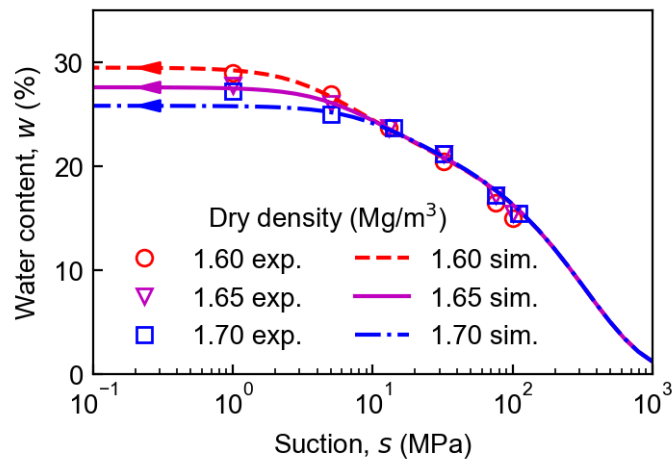


Figure 5-53 Calibration of the water retention curve of FEBEX bentonite for wetting under constant volume conditions at three different dry densities. Experimental data from Lloret et al. (2003).

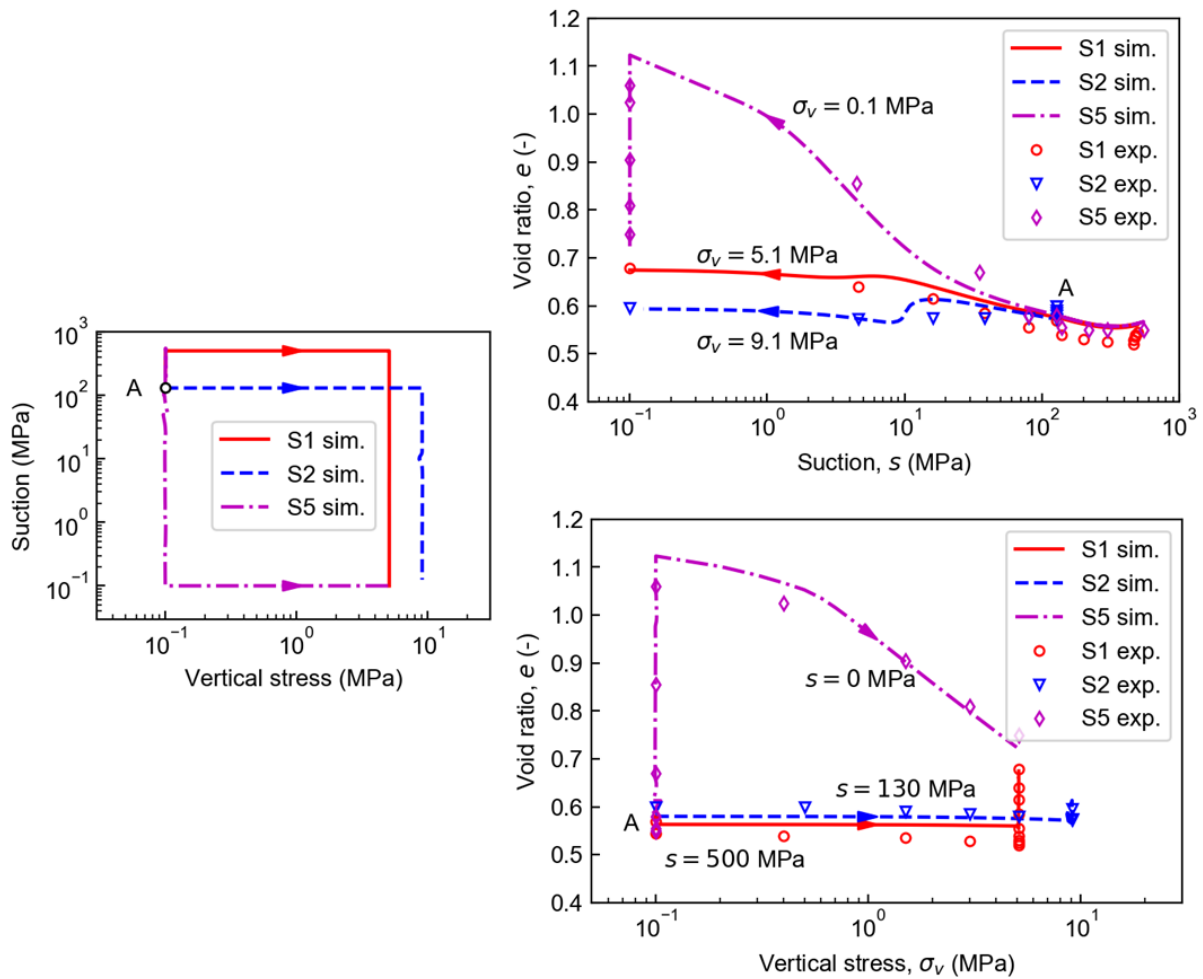


Figure 5-54 Calibration of the mechanical parameters against suction controlled oedometer tests performed by Lloret et al. (2003).

The material parameters have been calibrated based on suction-controlled oedometric tests reported by Lloret et al. (2003). Figure 5-54 shows the model calibration. These results span several ranges of suction-stress values, following different stress paths that are relevant of the Febex test. For instance, test S1 involved a first drying to high suction, prior to be compressed and then saturated. Thus, the test S1 is representative of a bentonite element close to the canister in the sense that the initial heating will entail high suction, then it will be compressed by the outer bentonite swelling due to the hydration from the host rock. Finally, it will be progressively saturated as the wetting front evolves. The other two stress paths would be representative of the outer ring (test S5) and the middle ring (test S2).

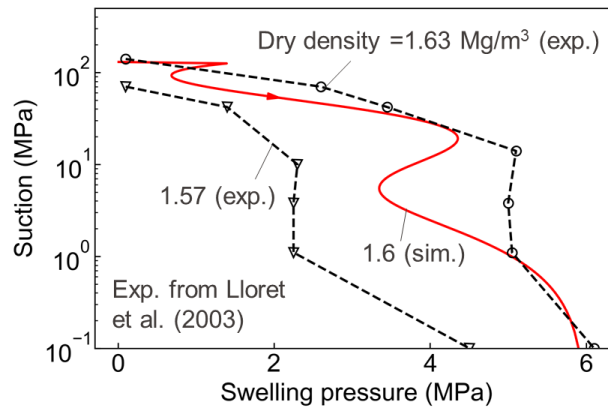


Figure 5-55 Model calibration of the swelling pressure developed at a dry density representative of the overall buffer. Experimental data obtained by Lloret et al. (2003).

However, these stress paths do not allow to assess the response of bentonite wetted under constant volume conditions, which is representative of the overall buffer. A complementary test that allows these interactions to be studied is the swelling pressure test, ideally performed under controlled suction. It is noted that while the bentonite blocks that constitute the buffer have a dry density of 1.7 Mg/m³, the overall dry density of the buffer is of 1.6 Mg/m³. This difference arises due to the gaps existing between the blocks and between the tunnel. These gaps are not explicitly considered and accordingly, the dry density of the bentonite has been taken as 1.6 Mg/m³. This density is assumed to be initially homogeneous throughout the buffer, corresponding to an initial porosity of 0.412.

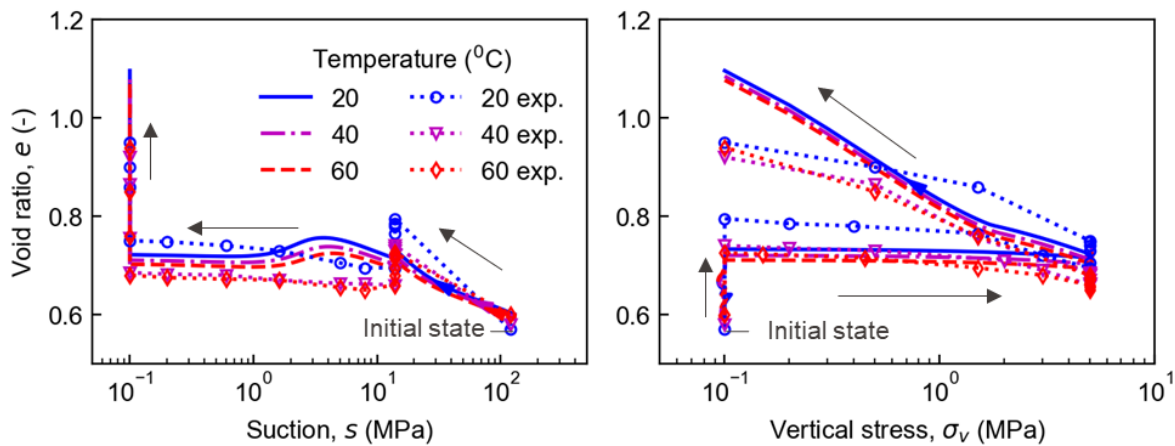


Figure 5-56 Calibration (continuous lines) of the thermo-plastic parameter against suction and temperature controlled oedometric tests reported by Romero et al. (2005) (marked-dotted lines).

According to the aforementioned aspects, parameters ζ and ξ are calibrated using the swelling pressure tests reported by Lloret et al. (2003), with a dry density close to 1.6 Mg/m³, which represents the overall buffer. This is because this stress path is more sensitive to these parameters than those of wetting under constant load. The calibration with these swelling pressure tests is shown in Figure 5-56.

Thermal plasticity might play a role as observed in the tests reported by Romero et al. (2005). Therefore, the thermo-plastic parameter has been adjusted to reproduce the behaviour of bentonite as reported by Romero et al. (2005) as shown in Figure 5-55.

Regarding water and heat flow parameters, these have not been substantially modified with respect to a previous analysis performed by EFPL (Dupray et al. 2013). Figure 5-57 shows the adjustment of the hydraulic conductivity and thermal conductivity functions. The constitutive parameters for the water flow are defined on the basis of experimental data on saturated hydraulic conductivity at different dry densities. Thermal conductivity is established as a function of degree of saturation. The remaining parameters are taken as usual values for air and water, such as free water density, viscosity, specific heat and compressibility. The values of all water, air and heat flow parameters, are reported in Table 5-26.

Table 5-25 summarises the parameters calibrated for the bentonite buffer

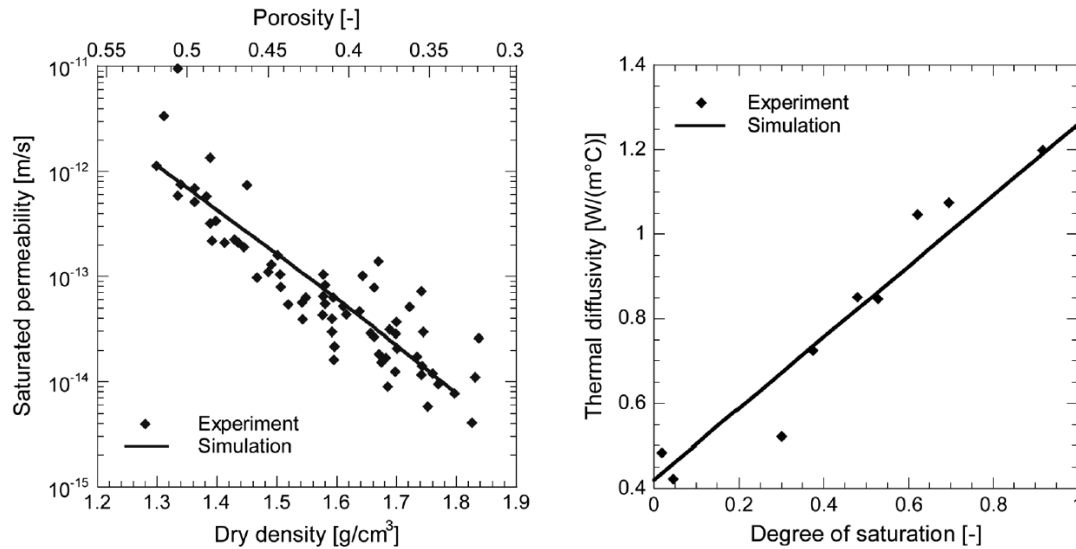


Figure 5-57 Calibration of the permeability dependency with density (left) and of the thermal conductivity dependency with the degree of saturation (right) (From Dupray et al. 2013).

Table 5-25 THM material parameters for FEBEX bentonite

Mechanical model		Water retention model		Heat and water flow	
Parameter	Value	Parameter	Value	Parameter	Value
κ	0.065	a	2 MPa^{-1}	Γ_s	$0.7 \text{ W}/(\text{m}^\circ\text{C})$
ν	0.35	b	1.5	Γ_w	$2.6 \text{ W}/(\text{m}^\circ\text{C})$
λ_{sat}	0.085	n	1.8	Γ_a	0
$\phi'_c = \phi'_e$	16°	m	2.5	$c_{p,s}$	$1091 \text{ J}/(\text{kg}^\circ\text{C})$
α	0.4	$e_{w,a}^c$	0.48	$c_{p,w}$	$4183 \text{ J}/(\text{kg}^\circ\text{C})$
p'_r	10^{-7} MPa	$\rho_{w,a}$	$1.2 \text{ Mg}/\text{m}^3$	$c_{p,a}$	$1000 \text{ J}/(\text{kg}^\circ\text{C})$
r	0.40			$k_{f,0}$	$3 \times 10^{-21} \text{ m}^2$
ζ	6.7			M	6
ξ	1.0			N	4
β_{T0}	$1.8 \times 10^{-4}/^\circ\text{C}$			α_k	2.9
γ_T	0.25				
e_0	0.70				
ρ_s	$2720 \text{ g}/\text{m}^3$				

Host rock

The granite is assumed to be fully saturated in the whole analysis. Because the permeability of the Grimsel granite is about two orders of magnitude higher than that of the FEBEX bentonite, it is expected that this assumption does not impact significantly the EBS evolution, which is the focus of the present model. For this reason, a high air-entry value has been chosen for the granite. The stress-strain behaviour of granite is modelled with an elastic model, defined by the Young modulus E and Poisson ratio ν , on the basis of laboratory results from early studies in the Grimsel laboratory (ENRESA 1998). The mechanical, thermal and hydraulic parameters of the granite are reported in Table 5-26.

Steel and granite

The parameters of the steel of the heaters, as well as the concrete of the plug, have been set in the range of usual parameters for these materials. Their mechanical behaviour has been assumed to be linear elastic. The steel is considered as impervious and the concrete plug as fully saturated. All these

parameters are included in Table 5-26.

Table 5-26 THM material parameters of the granite, concrete and steel

Parameter	Granite	Concrete	Steel
Γ [W/(m°C)]	3.34	1.7	-
c_p [J/(kg°C)]	1000	750	-
$k_{f,0}$ [m ²]	4.5×10^{-19}	4×10^{-19}	-
τ [-]	0.6	0.6	-
n_0 [-]	0.01	0.15	-
ρ_s [kg/m ³]	2660	2500	7800
E [GPa]	50	30	200
ν [-]	0.35	0.2	0.3

5.7.3 Initial and boundary conditions

The phases considered in the simulation are excavation of the gallery, gallery ventilation, EBS construction, initial heating phase, constant temperature of the heaters, the cooling processes and the dismantling phases. In total, the simulation spans 7133 days. The corresponding time scale for each phase is summarized in Table 3.

Since the simulations include also the excavation and ventilation phases, the initial conditions refer to the original domain before the experiment initiated. The test is modelled as an axisymmetric problem (gravity is not considered). An initial isotropic total stress of 28 MPa was assumed for granite domain, based on in situ measurements. The initial water pressure is also assumed to be uniform with a value of 0.7 MPa. The initial temperature is 12°C in the whole domain.

The excavation process is simulated by releasing the radial stress along the drift from the initial value of 28 MPa to 0 MPa during the first 35 days. The ventilation process is simulated by setting the water pressure of the drift surface from the initial value of 0.7 MPa to atmospheric pressure for 385 days. During these phases, the bentonite, canisters and plug elements are not included in the mesh, instead, virtual elastic material elements, with a small Young's modulus are used. The bentonite buffer construction, canister installation and plug construction are modelled by activating the bentonite, canister and plug elements at day -242, replacing the virtual material elements.

Given the relative humidity measured at the beginning of the test, an initial suction of 130 MPa is considered for the bentonite buffer. The external total stress on the bentonite is initially zero. Given that there are 135 days between the end of the EBS construction and the beginning of heating process, the bentonite located at the outer ring was allowed to hydrate from the granite during this period.

The temperature ramp in the experiment was imposed with a controlled power. The sequence involved a first stage of 1200 W per heater for 20 days and subsequently 2000 W per heater over the following 33 days until reaching the desired temperature of 100 °C. The same scheme is reproduced in the simulation. The thermal losses due to the presence of air in the construction gaps, mainly due to the existence of the liner containing the heaters and at the frontier between bentonite and granite, could be estimated at 15 %. Accordingly, the power applied in the simulation is 85 % of the real power, with the same ramp and the centre of the heaters reaches 100 °C at the same time of the experiment. After the temperature of the heater centre reached 100 °C, the temperature on all heater nodes (both heater #1 and #2) is kept constant; this allows maintaining the small variations in heater temperature between the corners and centre. After 1826 days of heating, the power of heater #1 was switched off. This is simulated by releasing the temperature control in all nodes of heater #1. The dismantling process is simulated by switching off the plug elements, bentonite elements and canister elements from the model domain, following the same sequence of the dismantling plan. These elements were replaced by virtual material elements with a very small Young's modulus to replace them. The initial external stress of the virtual material elements is zero, which leads to an axial unloading of the EBS elements. The second plug construction is simulated by replacing the virtual material elements with concrete plug elements. The initial water pressure in the second plug is assumed to be at the atmospheric pressure. After 6607 days of heating, heater #2 is switched off in the simulation. At this point, the temperature on the entire heater #2 is set free without input heating power. The sequence used in the final dismantling is analogous to the one used in the first dismantling phase. The simulation stops after day 7133.

Table 3: Processes considered in the FEBEX simulation

Start time	Activities	Starting day (ref.)	Duration (Days)	Problem analysis
25/09/1995	TBM excavation of FEBEX tunnel <ul style="list-style-type: none"> ▪ Excavation last 35days 	-520	278	HM
01/07/1996	Engineered barrier system construction	-242	107	HM
15/10/1996	End of EBS construction	-135	135	HM
28/02/1997	Heating <ul style="list-style-type: none"> ▪ 1200W for 20 days ▪ 2000W for 33 days ▪ Constant T from 21/04/1997, taking 8 days in three steps: 95-99-100°C 	0	1826	THM
28/02/2002	Switch off Heater #1	1826	33	THM
02/04/2002	Partial dismantling <ul style="list-style-type: none"> ▪ Concrete plug part, finished on 28/05/2002 ▪ Extraction of heater #1 on 19/06/2002 ▪ Shotcrete plug on 23-24/07/2002 ▪ Second part on 23-27/06/2003 	1859	116	THM
26/07/2002	End of partial dismantling	1975	4632	THM
01/04/2015	Switch off Heater #2	6607	6	THM
07/04/2015	Dismantling	6613	102	THM

5.7.4 Results/discussion

In the following the requested results are presented. Because the model is axisymmetric with respect to the x axis of the test, all variables evolve symmetrically and therefore no distinction is made between the three radial directions. Comparison of the monitored results with the model simulations will only be done in those cases in which the requested results correspond to locations where monitored data is available. Post-mortem results (dry density, water content and apparent degree of saturation) will be compared to the model predictions.

Evolution and distribution of temperature

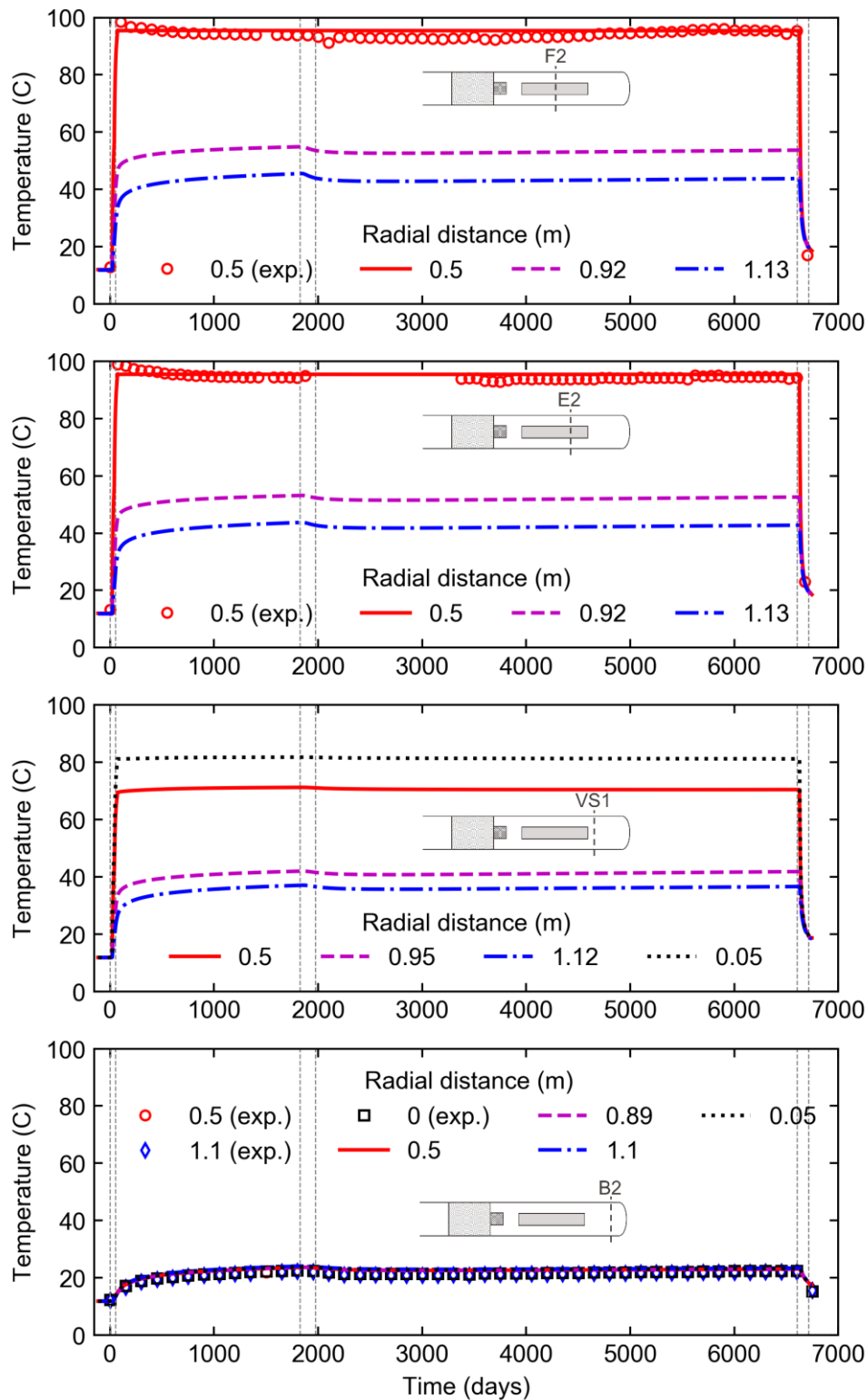


Figure 5-58 Model results of temperature evolution at the requested locations corresponding to 4 sections. Closest monitored values (exp.) are shown for comparison. Grey-dashed vertical lines indicate transition between phases.

The results of the model in terms of temperature evolution are represented in

Figure 5-58. The four sections include two hot sections (F2 and E2), one section not directly in contact with the heater (VS1) and a cold section (B2). The temperature in the two hot sections (F2 and E2) is seen to evolve without significant differences. Likewise, the temperature field is quite homogeneous throughout the cold section (B2). The impact that switching off the first heater had on the EBS (day 1826) is appreciated in all sections by a small decrease in temperature, with the exception of the points that are located close to the heater (radial distance of 0.5 m) where the temperature was rather dominated by the constant temperature imposed in the heater. After switching off the heater (day 6607) the temperature field tended to a uniform value regardless of the distance to the heater. Except for the dependence of thermal conductivity on the degree of saturation, thermal flow is not strongly influenced by the fluid flow and mechanical actions. Therefore, temperature evolution is dependent only on the heating sequence of the heaters.

Figure 5-59 shows the spatial distribution of temperature in the four sections studied. Again, the evolution in the two hot sections, F2 and E2, is visibly the same, which suggests that these sections can be approximated to one-dimensional behaviour. The temperature distribution remains fairly constant for a given section, until the dismantling. In this representation is seen that the temperature distribution after the heater is switch off tends to homogenise through the entire domain to a value around 20°C.

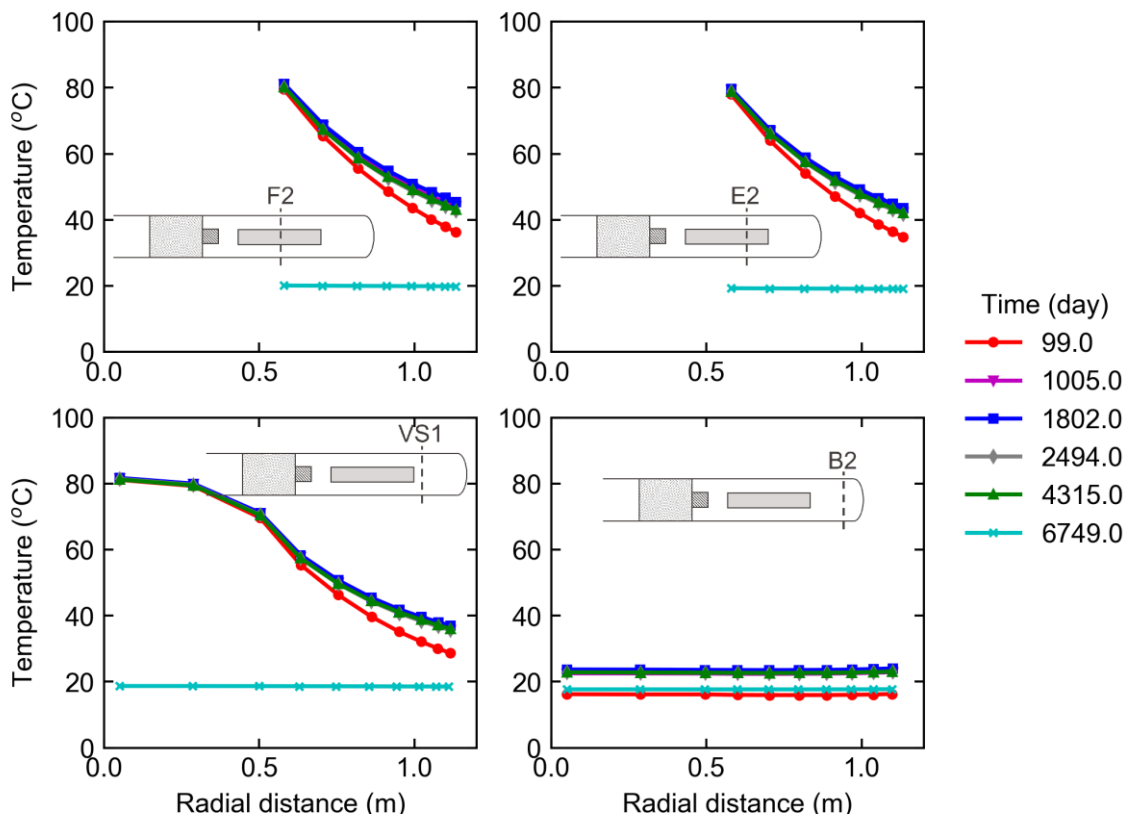


Figure 5-59 Model results of the evolution of temperature distribution in the four sections of interest.

Evolution and distribution of relative humidity

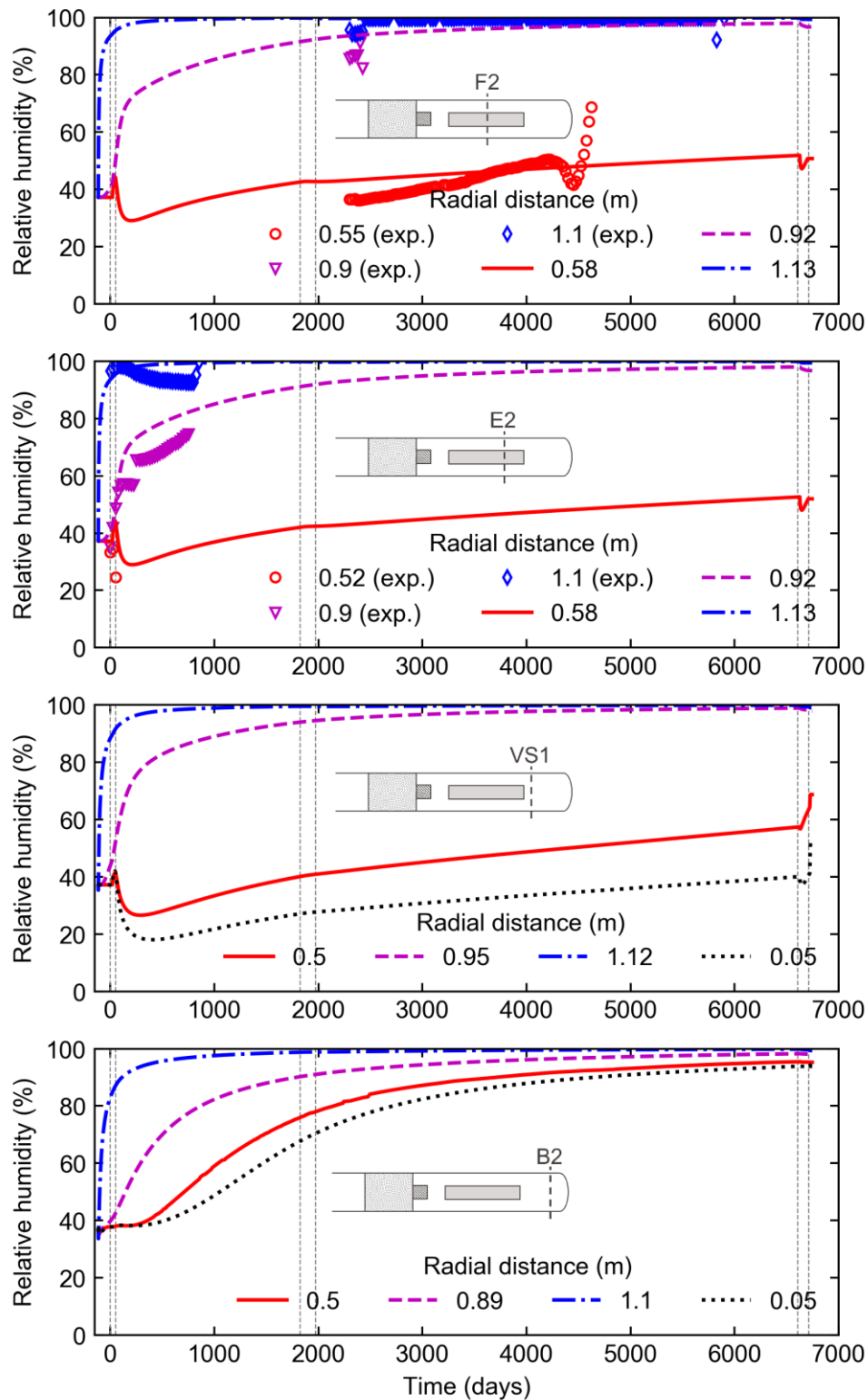


Figure 5-60 Model results of relative humidity evolution at the requested locations corresponding to 4 sections. Closest monitored values (exp.) are shown for comparison. Grey-dashed vertical lines indicate transition between phases.

Figure 5-60 shows the evolution of relative humidity (RH) in the four sections of

interest. It is observed that in the points closer to the host rock, the RH increases rapidly before the heating stage starts (day 0). This is due to the gap in time between the EBS construction and the beginning of heating. Therefore, the bentonite was allowed to hydrate during this period of time. Once the heating starts it is well appreciated the decrease of RH (drying) in the elements close to the heaters. The drying of the inner elements resulted in a subsequent hydration, due to vapour flow, of the elements located in the middle ring ($r=0.92$ m). This is why such an important difference is observed between the hydration rate of the inner ring of hot sections (F2 and E2) and that of the cold section (B29). For the same reason, once the heater is switch off (day 6607), a sudden decrease in relative humidity is observed in the points at $r=0.58$, which is due to the fast decrease of vapour flow. Because water permeability is lower than air, this decrease is not compensated immediately. This competition effect, between vapour decrease and water increase flows, is better observed comparing the points $r=0.5$ m and $r=0.05$ m in section VS1. Thus, the closer to the heater, the more important is the contribution of vapour condensation in RH. Indeed, it appears that RH in section B2 is not affected by temperature oscillations, evolving in a consistent trend for all the four points monitored.

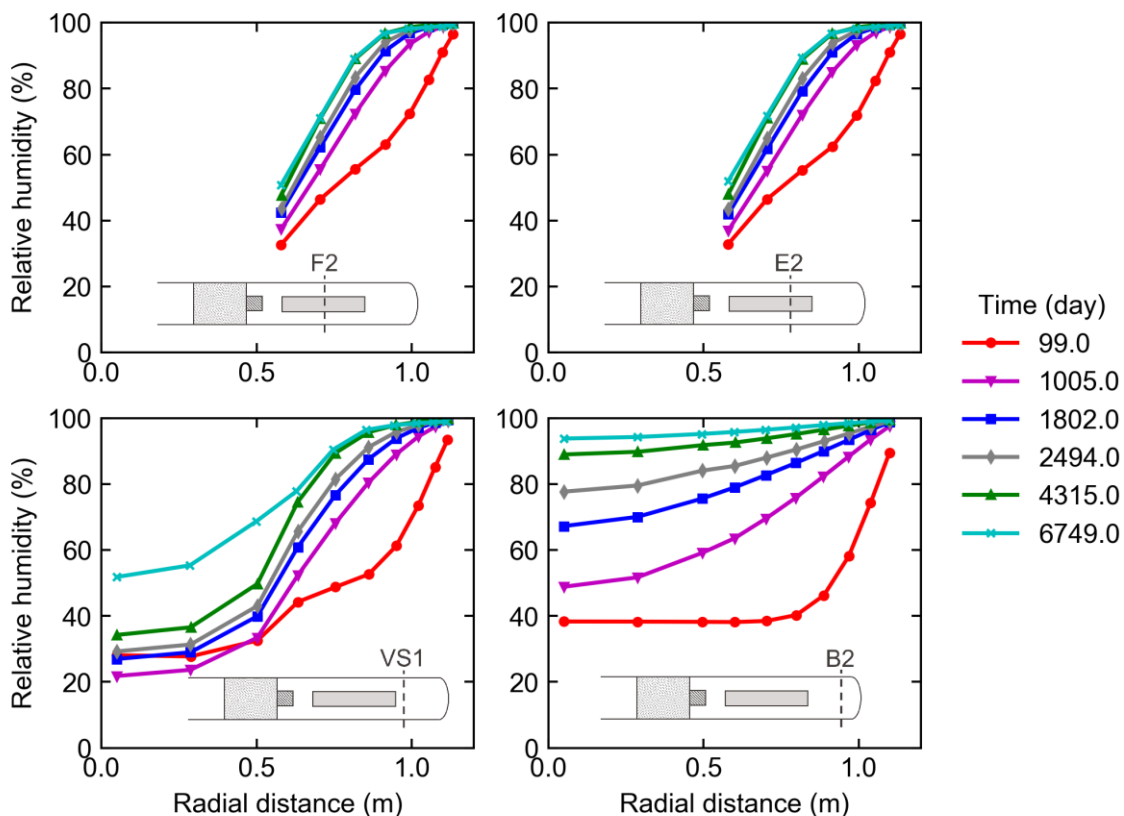


Figure 5-61 Model results of the evolution of relative humidity distribution in the four sections of interest.

Similar observations regarding the influence of heating in the RH can be made observing its evolution in space. Figure 5-61 shows the results of the four sections as a function of radial distance at different times. The influence of the heater is clearly seen comparing the hot sections F2 and E2 and the cold section B2. Section VS1, presents a response that is very similar to those observed in the hot sections. Of particular interest is the gradient observed at $t=100$ days at a radial distance corresponding to the location of the heater in the neighbouring section. This initial gradient decreases as time advances, ending with a distribution more similar to that of the cold section B2. Nevertheless, it is interesting to observe that the saturation of the outer elements is achieved faster than in the cold section. This difference is most likely due to the contribution of vapour flow, which does not affect the cold section. In contrast, for the same reason, the relative humidity in the central part of the section VS1 is significantly lower than in section B2.

Evolution and distribution of total stress

Figure 5-62 shows the evolution of radial stress in the hot section E2, and the evolution of axial stress in the cold section B2. As in previous figures, the days at which phase changes took place are denoted by the dashed vertical lines.

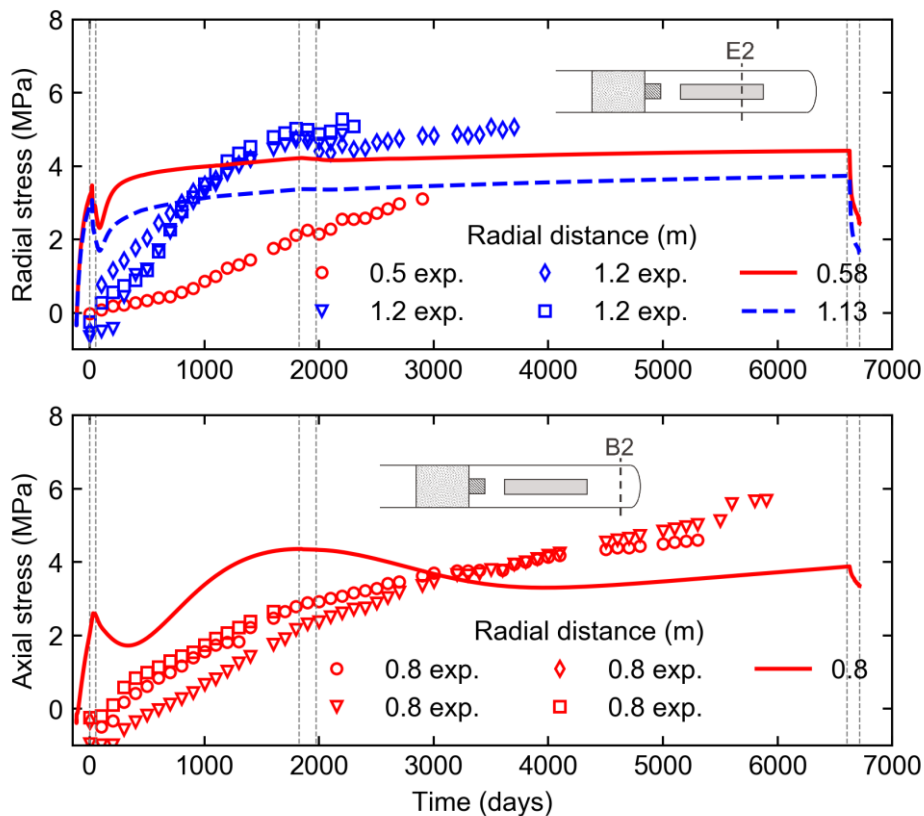


Figure 5-62 Model results of total stress evolution at the requested locations corresponding to 2 sections. Closest monitored values (exp.) are shown for comparison. Grey-dashed vertical lines indicate transition between phases.

A significant increase in both radial and axial pressure is observed before the activation of the heating power. This increase is related to the hydration of the bentonite before the heating started (day 0). Once the heaters are activated a decrease in pressure is observed that in section F2 stops once the temperature of the heater is kept constant. This result is related to the thermo-plastic formulation of the model. When temperature increased continuously, the stress state reached the yield surface and less pressure was required to maintain constant overall volume of the EBS. Once temperature was stabilised, the hydration front dominated again the increase in pressure until it stabilised to a given value, which was higher closer to the heater. The impact of switching off the first heater is appreciated but without significant stress changes. In contrast, once the second heater is switched off, a drastic decrease of stress is observed, particularly in the hot section.

The decrease in pressure observed in the axial stress of section B2 is more related to the hydration front rather than the temperature field. While this is not clear with respect to the activation of the heaters, it is clearer when the effects of switching off the heaters (days 1826 and 6607) are compared to the results in section F2. Indeed, the decrease in stress observed when the first heater is switched off is too progressive to be related to the instant change in temperature, and minor changes (compared to the hot section F2) are observed when the second heater is switched off. Because the compressibility of the model is formulated in terms of the degree of saturation, as the hydration proceeds, the stress state moves closer to the yield surface (in a similar way as with the temperature) and once the yield stress is reached, the material might reduce its stress in order to maintain constant volume conditions. Once saturation is reached, the collapse potential reduces, and the pressure develops again.

Evolution and distribution of dry density, water content and degree of saturation

Figure 5-63 shows the evolution of the dry density of the four sections studied at different radial distance. In sections F2 and E2 (hot sections), it is straightforward to see the influence of the early hydration of the part in contact with the host rock. A significant decrease in dry density, induced by swelling, is obtained before the heating phase starts. Once heating starts, the increase of temperature induces shrinkage of the inner ring and this leads to an even further, although smaller, decrease of density of the outer ring. This decrease of density is partially compensated as hydration proceeds in time towards the middle ring of the EBS. A notable effect is observed induced by switching off the first heater and its subsequent dismantling. As it is expected intuitively, the second dismantling has a non-negligible effect on the final dry density, particularly in the outer ring. The evolution of dry density in the cold section B2, is more homogeneous, probably due to the constant temperature (see Figure 5-58) and a strictly increasing relative humidity (Figure 5-60). Nevertheless, since the outer elements show a non-recoverable decrease of

density, it is still relevant the hydration sequence.

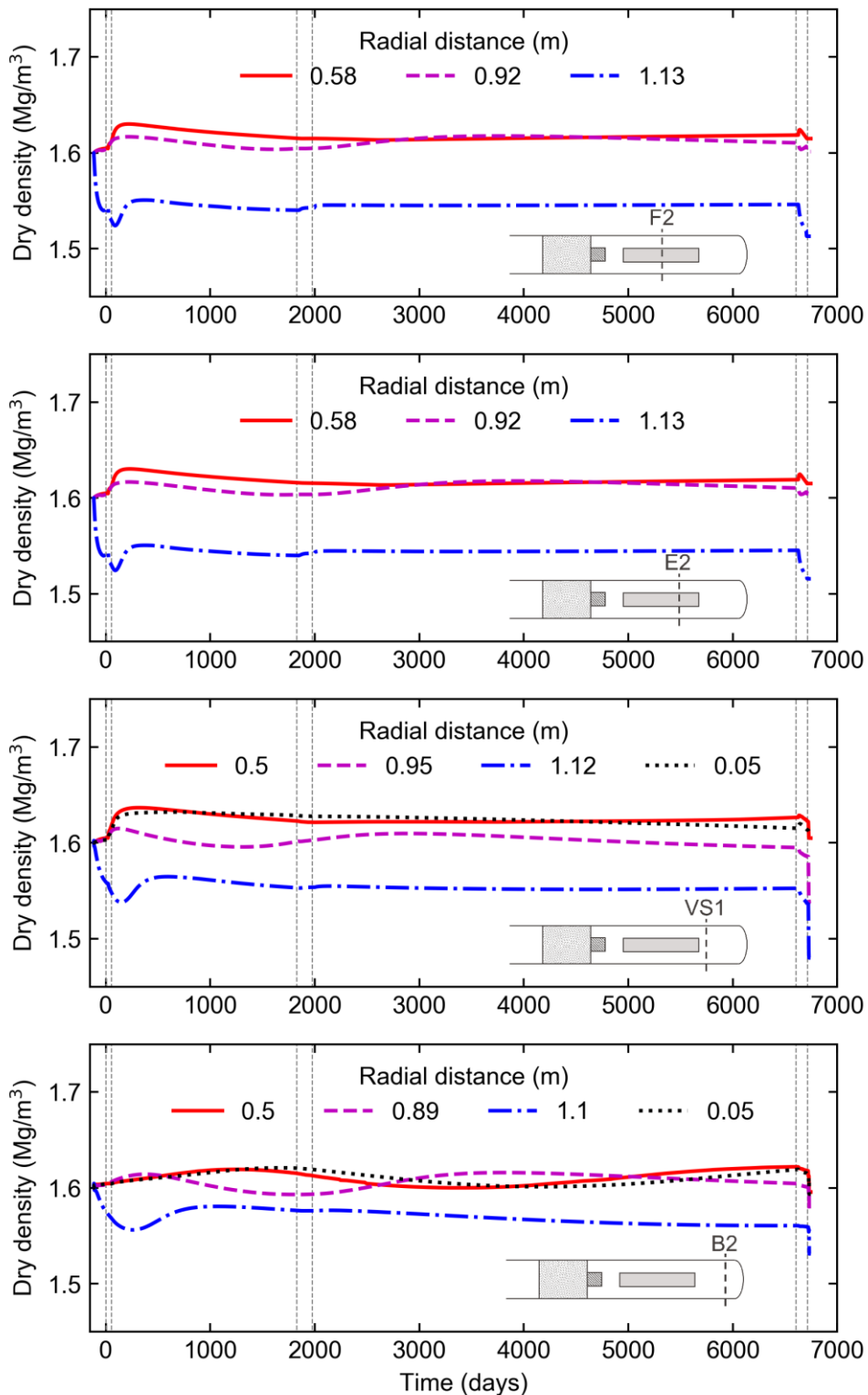


Figure 5-63 Model results of dry density evolution at the requested locations corresponding to 4 sections. Grey-dashed vertical lines indicate transition between phases.

As it can be seen, the outer ring does not recover the initial dry density once the central part becomes hydrated.

Figure 5-64 shows the evolution of the spatial distribution of the four sections studied. The influence of the heaters is clearly observed comparing the results in sections F2 and E2 with those of section B2. Section VS1, presents a distribution that remains strongly influenced by the temperature. In all sections, especially sections VS1 and B2, a strong decrease of dry density is observed due to the dismantling phase, which suggests that this effect should not be neglected. The increases in dry density due to dismantling are probably due to a redistribution of stresses and degree of saturation, which led to local collapse.

Figure 5-65 shows the distribution of dry density in the axial direction of the central axis. The influence that switching off and dismantling the first heater had on dry density is clearly seen comparing the results before and after day 1800.

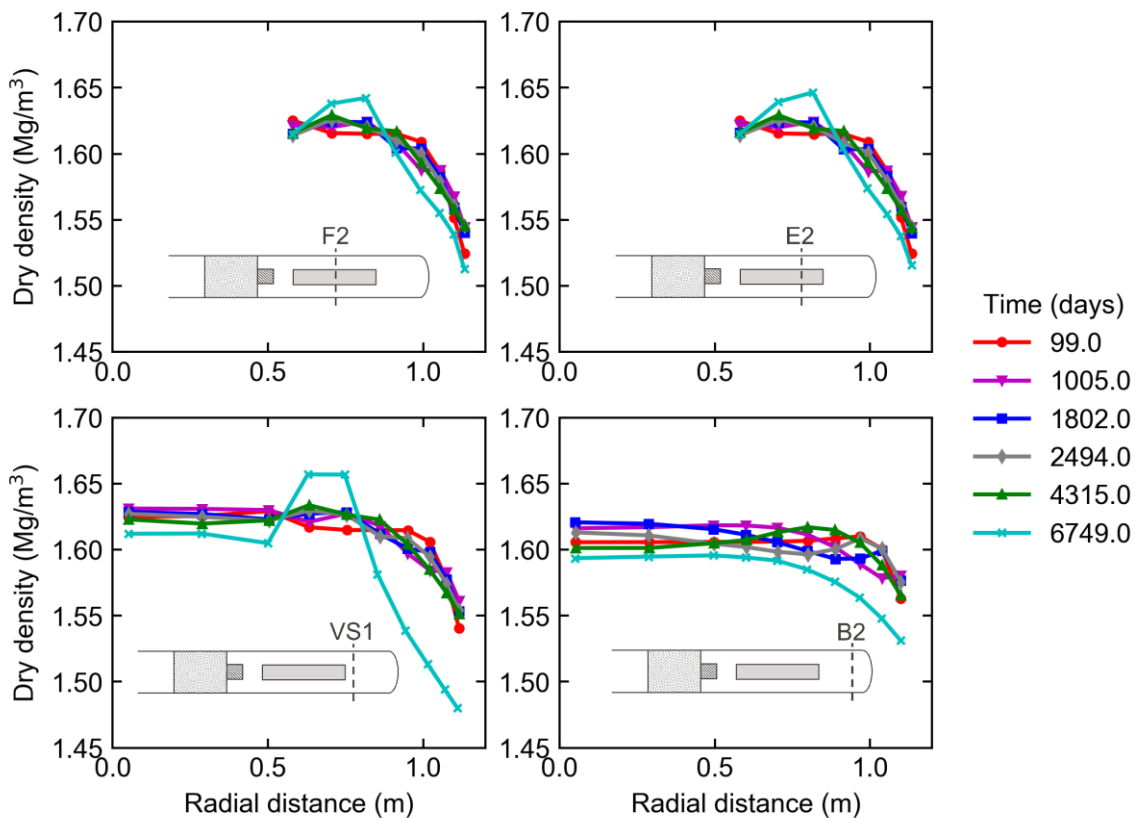


Figure 5-64 Model results of the evolution of dry density distribution in the four sections of interest.

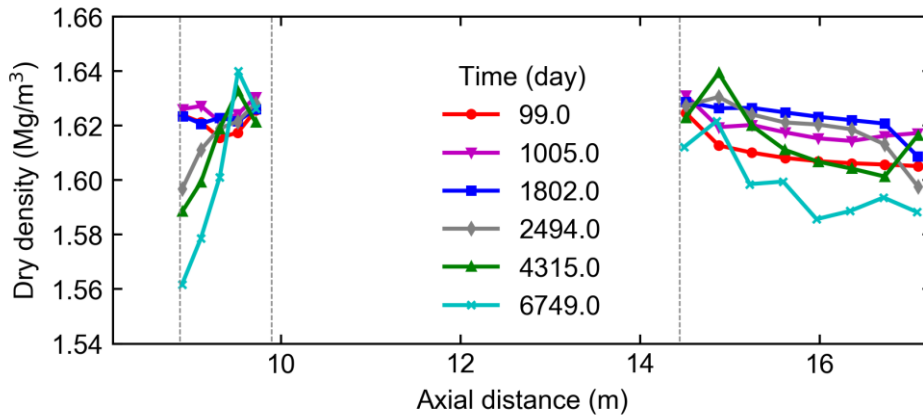


Figure 5-65 Model results of the evolution of dry density distribution in the axial direction (section HS1). The vertical dashed lines represent the heater zone.

Figure 5-66 shows the dry density distribution of the four radial sections before and after dismantling phases. The post-mortem results (Villar et al. 2015) are plotted for comparison purposes. Overall, the gradients of dry density are well reproduced by the model, except perhaps for the locations close to the heater. The comparison of results of section B2 are difficult to assess due to a lower density obtained during the EBS constriction (bentonite blocks did not fit well the tunnel geometry).

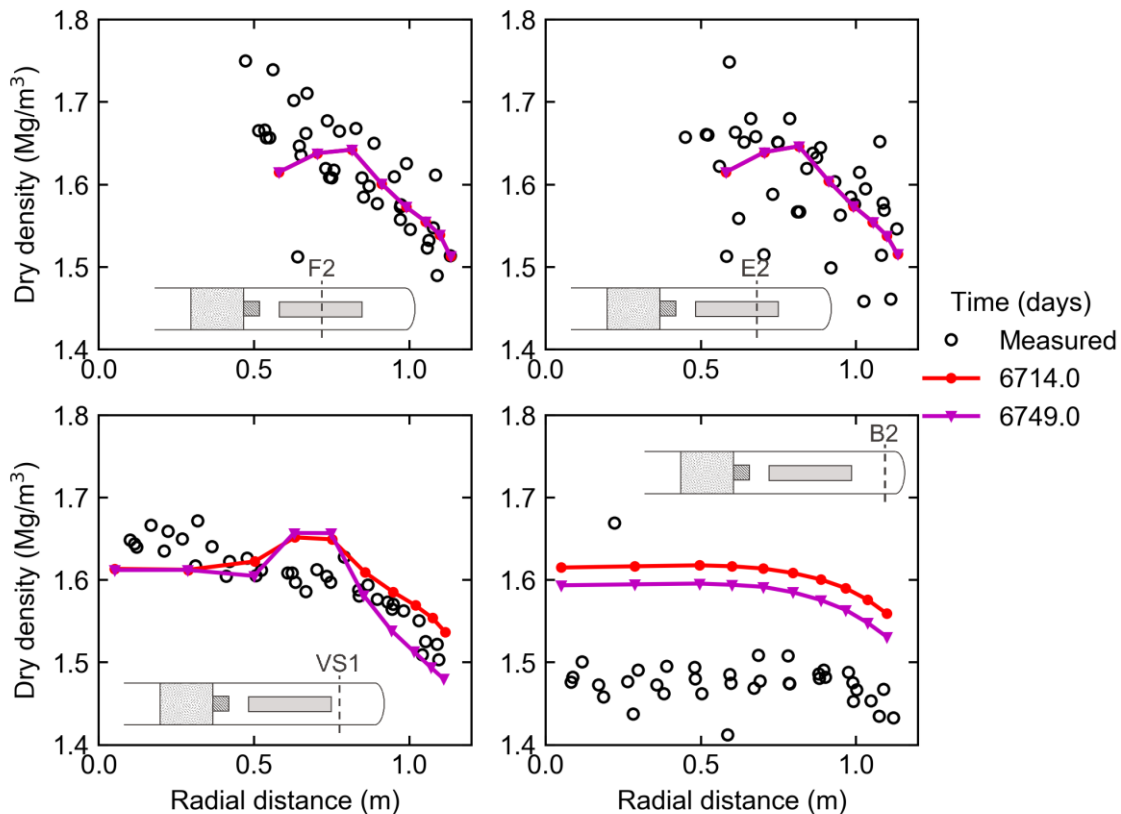


Figure 5-66 Model results of the dry density distribution before (day 6714) and after (day 6749) dismantling in the four sections of interest.

Figure 5-67 shows the evolution of water content predicted by the model in

the four sections requested. The trend is very much related to that of the relative humidity (see Figure 5-60) but influenced by the evolution of the dry density due to the hydro-mechanical coupling component of the water retention model.

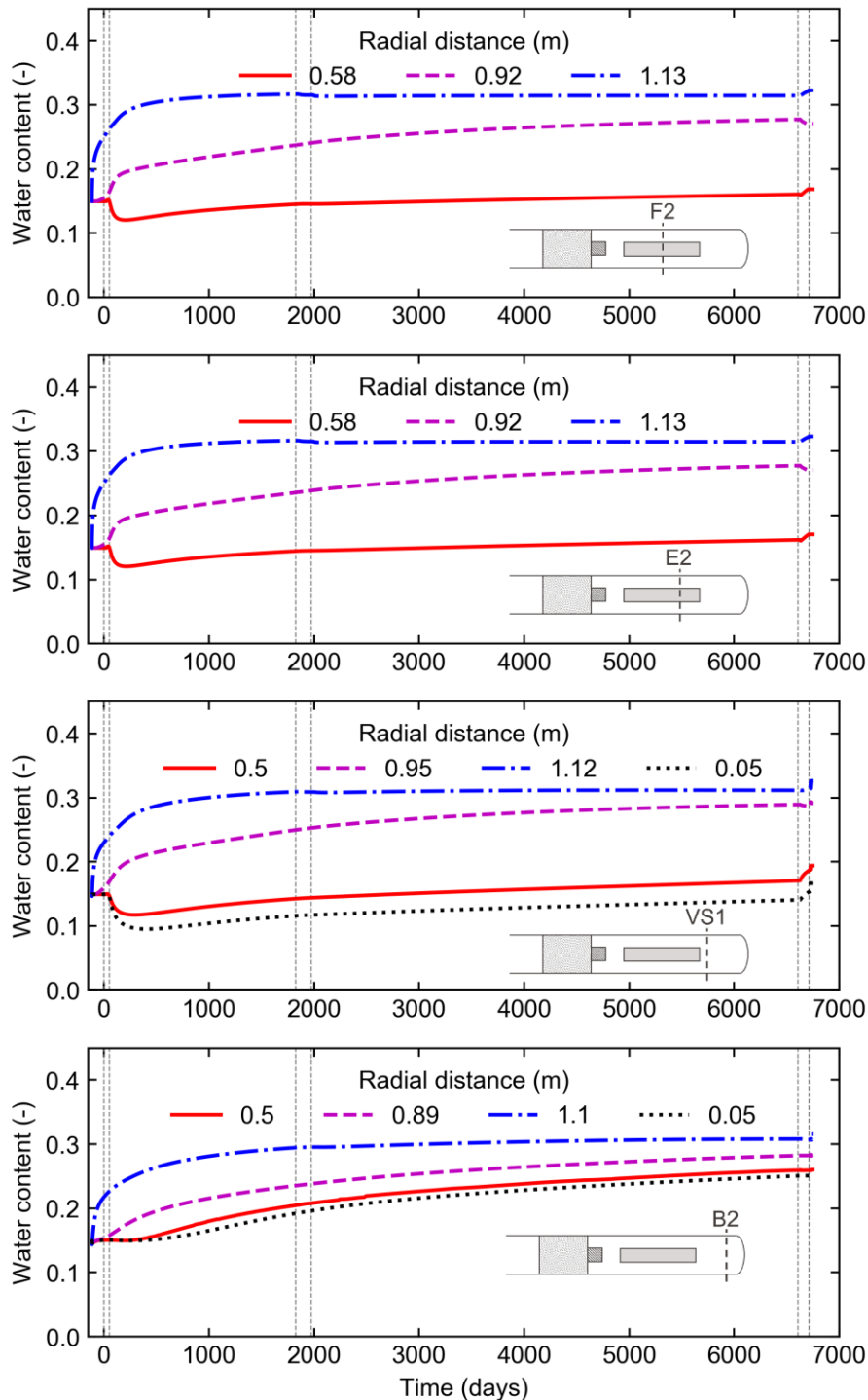


Figure 5-67 Model results of water content evolution at the requested locations corresponding to 4 sections. Grey-dashed vertical lines indicate transition between phases.

This is however not readily observed because phase transitions, mostly involve

temperature changes, which in turn affect the dry density. Likewise, the dismantling operations influence dry density, and if the material is saturated, water content is uniquely related to dry density.

This is also seen in Figure 5-68, which shows the spatial distribution of water content at different times, and Figure 5-69, which shows the distribution of water content in the axial direction in the central axis, at different times. The gradients are very similar to those observed for the relative humidity (Figure 10), while the distribution tends to be aligned with that of the dry density profiles (Figure 13) as time increases.

The water content distribution predicted by the model is compared with the post-mortem measurements in Figure 5-70. The results are generally good for all sections, especially, as already indicated with the dry density, that section B2 had in reality lower density than the other sections, and therefore, a higher water content measured is justified by the lower density that is not accounted in the model.

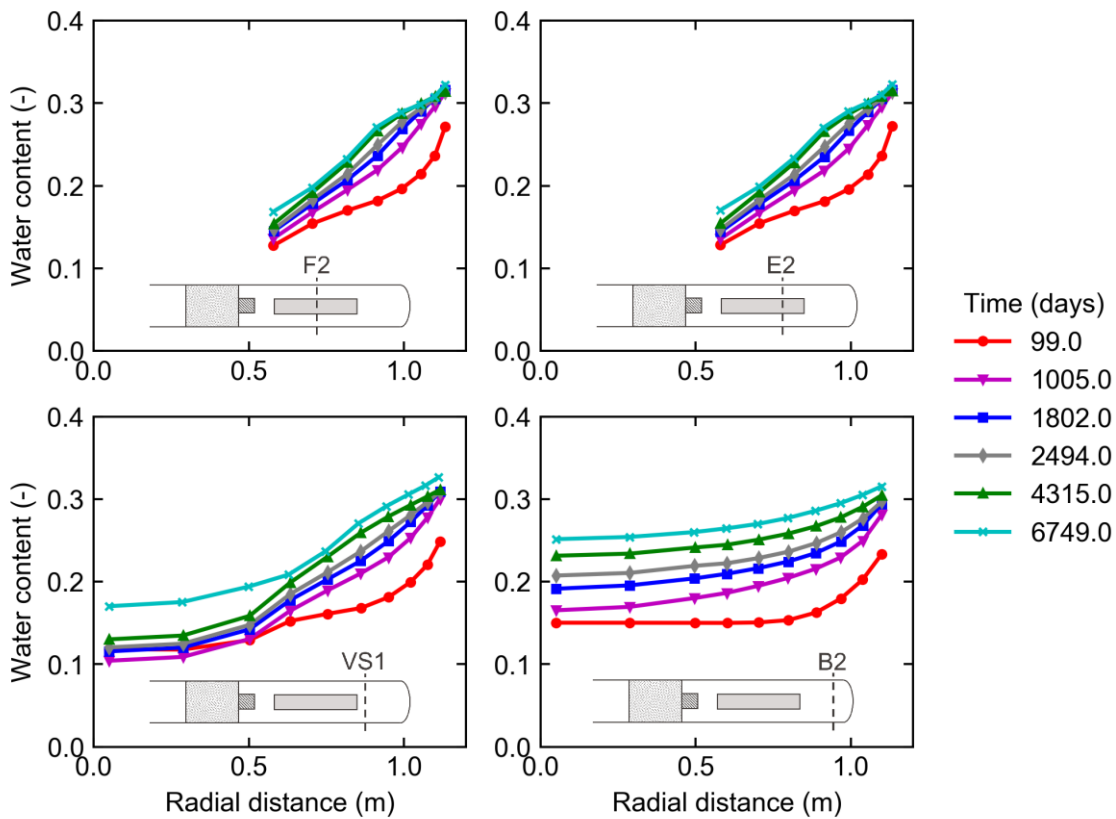


Figure 5-68 Model results of the evolution of water content distribution in the four sections of interest.

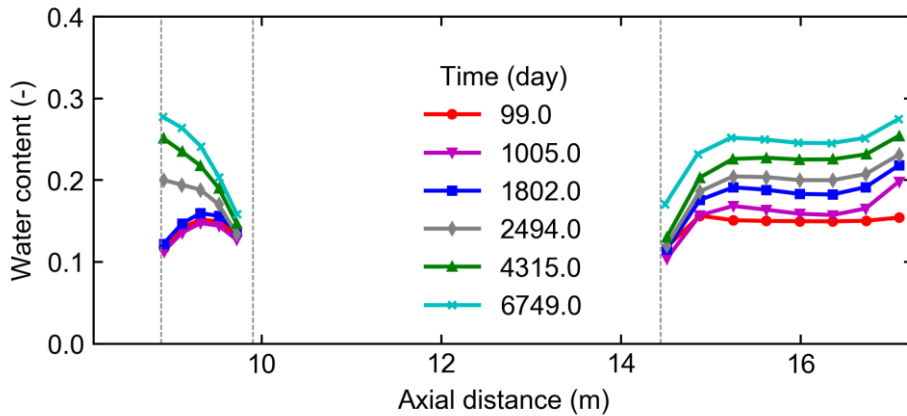


Figure 5-69 Model results of the evolution of water content distribution in the axial direction (section HS1). The vertical dashed lines indicate the heater zone.

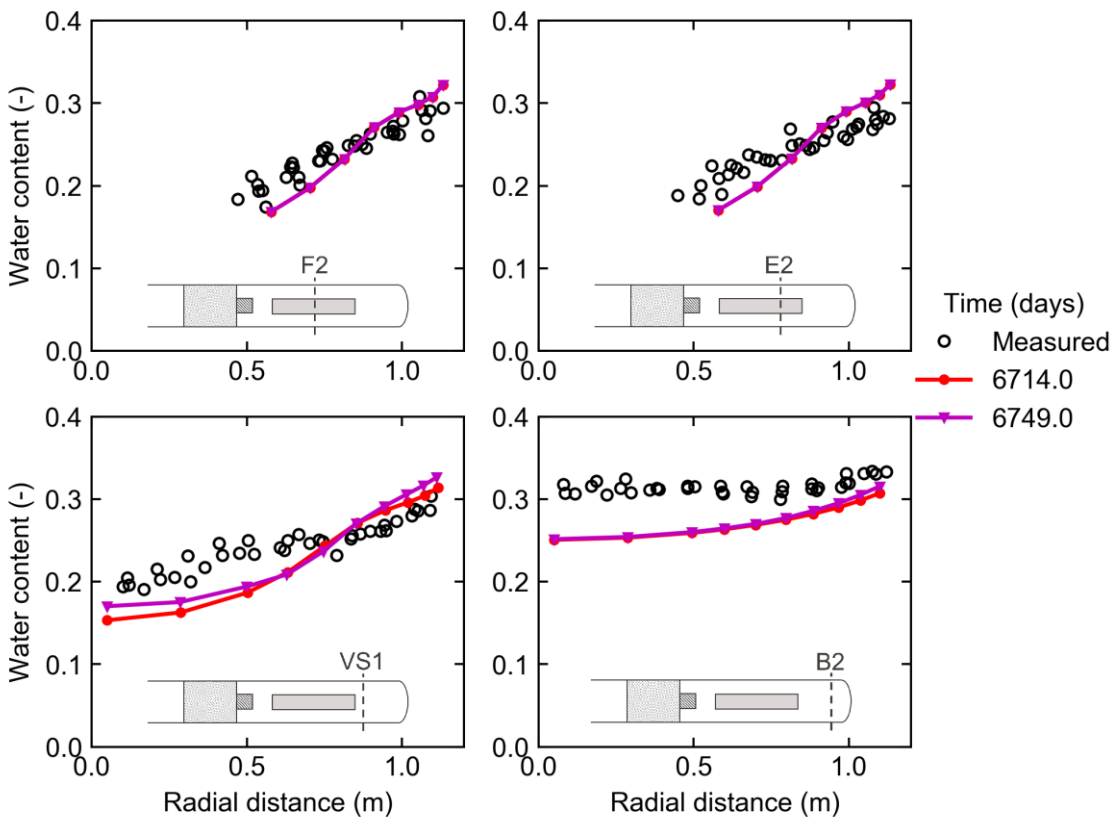


Figure 5-70 Model results of the water content distribution, in the four sections of interest, before (day 6714) and after (day 6749) dismantling. Post-mortem results are included for comparison purposes.

Figure 5-71 shows the evolution of the degree of saturation in the four sections of interest. It is observed that this evolution is very similar to that of the water content, which in turn is strongly correlated to the relative humidity. The degree of saturation is arguably the variable that is most influenced by the multi-physical processes due to its direct dependence on the dry density and water content, while these two latter variables are strongly affected by the temperature field. Therefore, the little variations of dry density after the first

temperature increase, explain why the degree of saturation is mostly correlated with the evolution of water content.

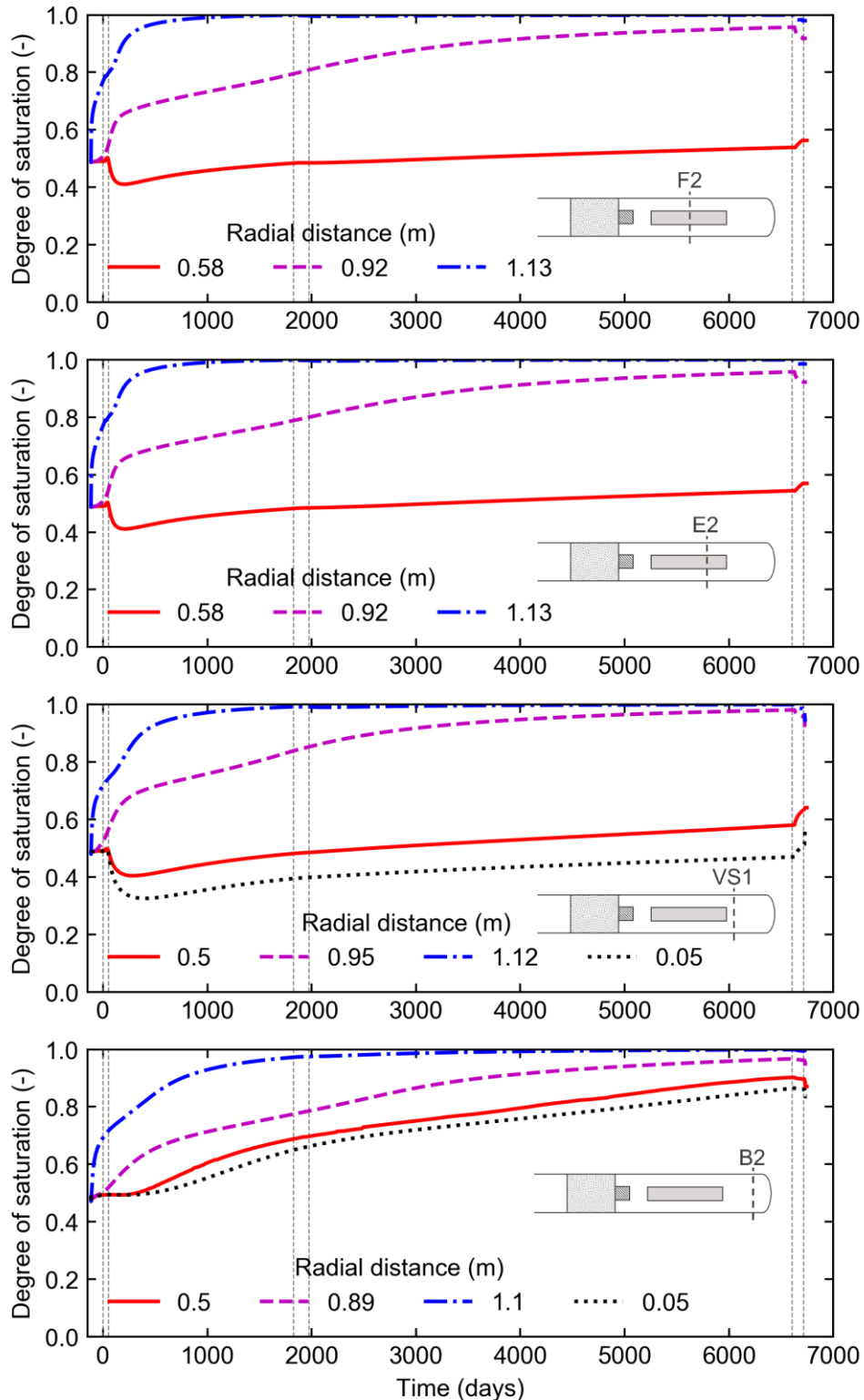


Figure 5-71 Model results of the evolution of the degree of saturation in the four sections of interest at different radial distance from the tunnel axis. Grey-dashed vertical lines indicate transition between phases.

Figure 5-72 shows the evolution of the spatial distribution of the degree of saturation. Similarly to what is observed in Figure 5-71, the main trend is very much related to the evolution of water content, because the dry density does not drastically change after the temperature of the heaters is maintained constant.

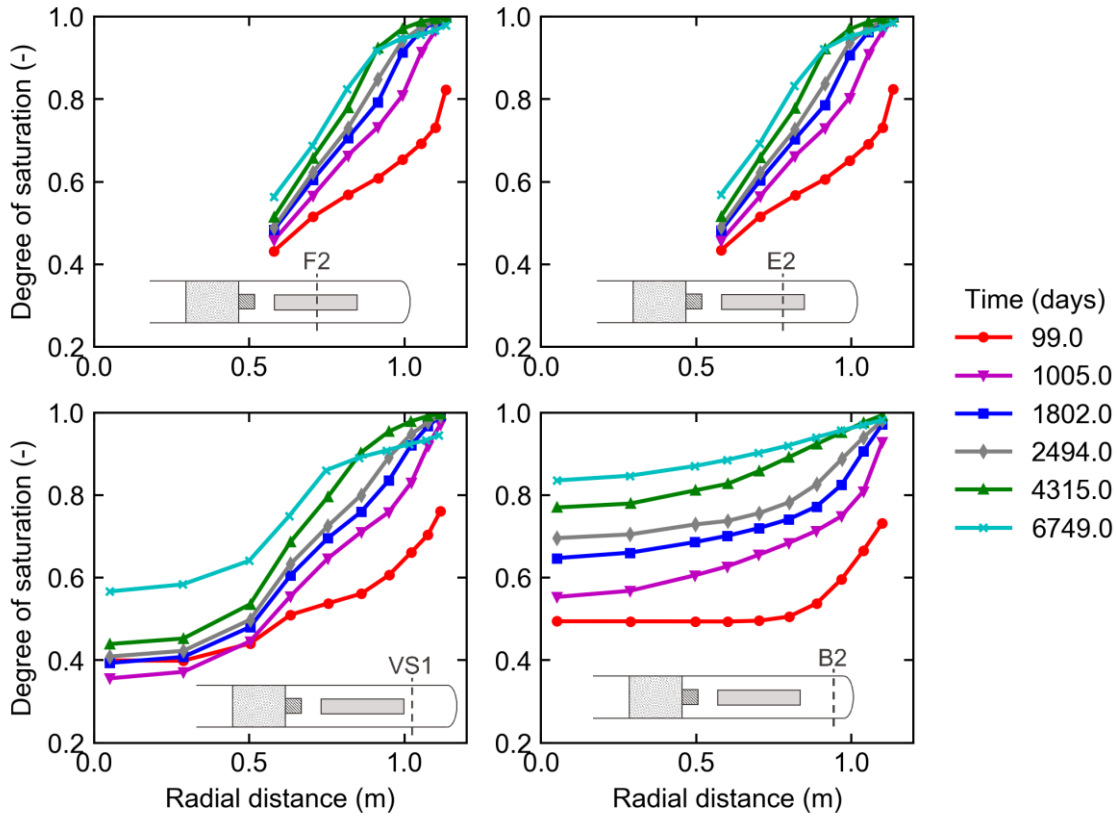


Figure 5-72 Model results of the evolution of the degree of saturation distribution in the four sections of interest.

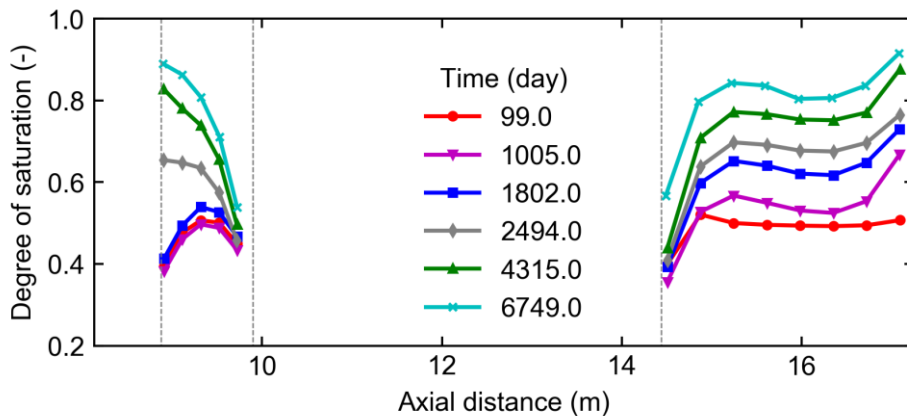


Figure 5-73 Model results of the evolution of the degree of saturation distribution in the axial direction (section HS1). The vertical dashed lines indicate the heater zone.

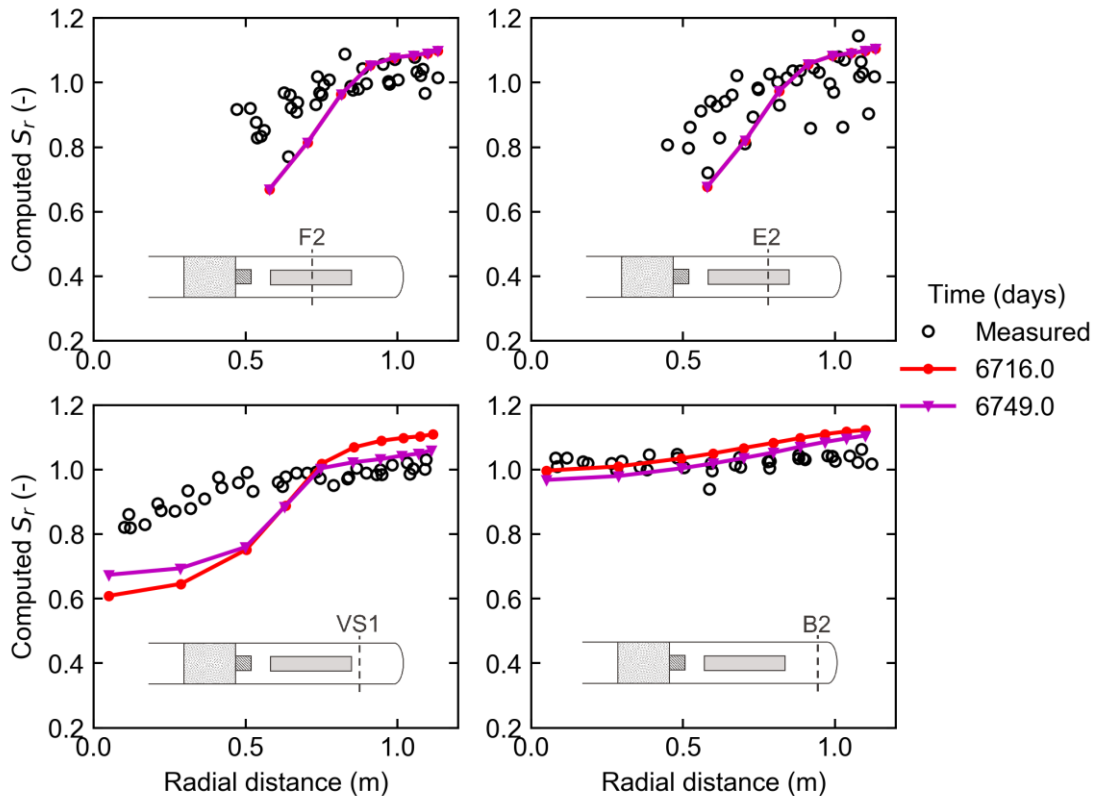


Figure 5-74 Model results of the distribution of computed degree of saturation (i.e. assuming a water density of 1.0 Mg/m^3), in the four sections of interest, before (day 6714) and after (day 6749) dismantling. Post-mortem results are included for comparison.

The comparison of the degree of saturation predicted by the model with the results obtained after the post-mortem analysis is not straightforward. This is because the degree of saturation of the post-mortem analysis was computed assuming water density of 1 Mg/m^3 , which led to values of $S_r > 1$. In the model such anomalous density is taken into account by means of the adsorption model of the water retention curve (Figure 5-53). Therefore, in order to perform a meaningful comparison, a so-called “computed S_r ” is introduced, which results from computing the degree of saturation from the simulated water content assuming water density of 1 Mg/m^3 . Figure 5-74 shows the results of the simulations in terms of the computed S_r , compared to the post-mortem analysis. The results of the model are again in line with those obtained from the measurements. The least satisfactory match is that of the section VS1, because the model slightly underpredicted both dry density and water content, resulting in a more significant underprediction of the computed S_r . In the same line of analysis, although neither the dry density nor water content of section B2 were well predicted due to a lower initial density, the degree of saturation is well predicted because the higher dry density was compensated by a lower water content at saturation. Also of interest, is that the model predicts a computed S_r in line with those measured from the hot sections, in the zones close to the host rock, providing confidence in the value of density assumed for adsorbed water.

5.8 BGR

5.8.1 Geometry and discretization

The model is setup as an axisymmetric model along the axis of the emplacement drift. The model measures 72 m in the axial direction and 58.14 m in the radial direction. Geological features such as the lamprophyre, technical features of the drift such as a disturbed zone and discrete features of the bentonite system such as gaps are not simulated. The end of the drift is simplified to rectangular geometry. The model domain is discretized using an unstructured grid. A 3-stage modelling strategy is chosen. The model domain of stage 1 (heating phase with both heaters 1 and 2) is chosen as the base model and has 11 material groups. They are shown in Figure 5-75.

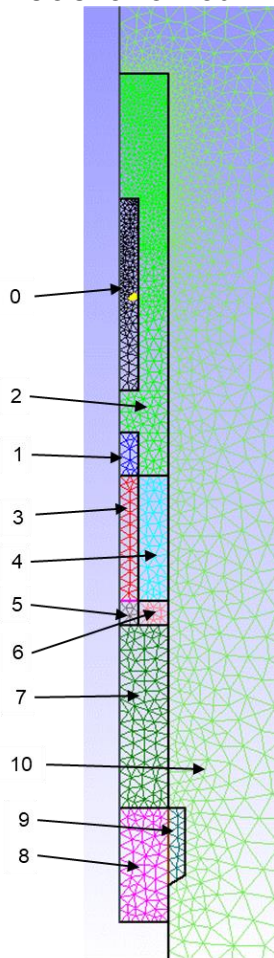


Figure 5-75: Material group numbers of the base model domain of the FEBEX experiment (refer

Table 5-27).

The three stages of the simulation are:

- Stage 0: Desaturation of the host rock
- Stage 1: Heating with both heaters
- Stage 2: Heating with only second heater

Parts of the model geometry are deactivated or reassigned to different materials groups corresponding to the simulated stage:

- Heater 1 (material group no. 1, 3, 4, 5)
- The bentonite barrier around heater 1 (material group no. 4, 5)
- The bentonite barrier between heater 1 and the concrete plug (material group no. 7) and
- The concrete plug (material group no.8)

Accordingly, a part of heater 1 and the bentonite around it is reassigned with the properties of the dummy at the beginning of stage 2. The concrete plug is deactivated. The geometries of the three stages in comparison to each other and to the schematic of the experimental setup is shown in Figure 5-76. An overview of the material groups is given in

Table 5-27.

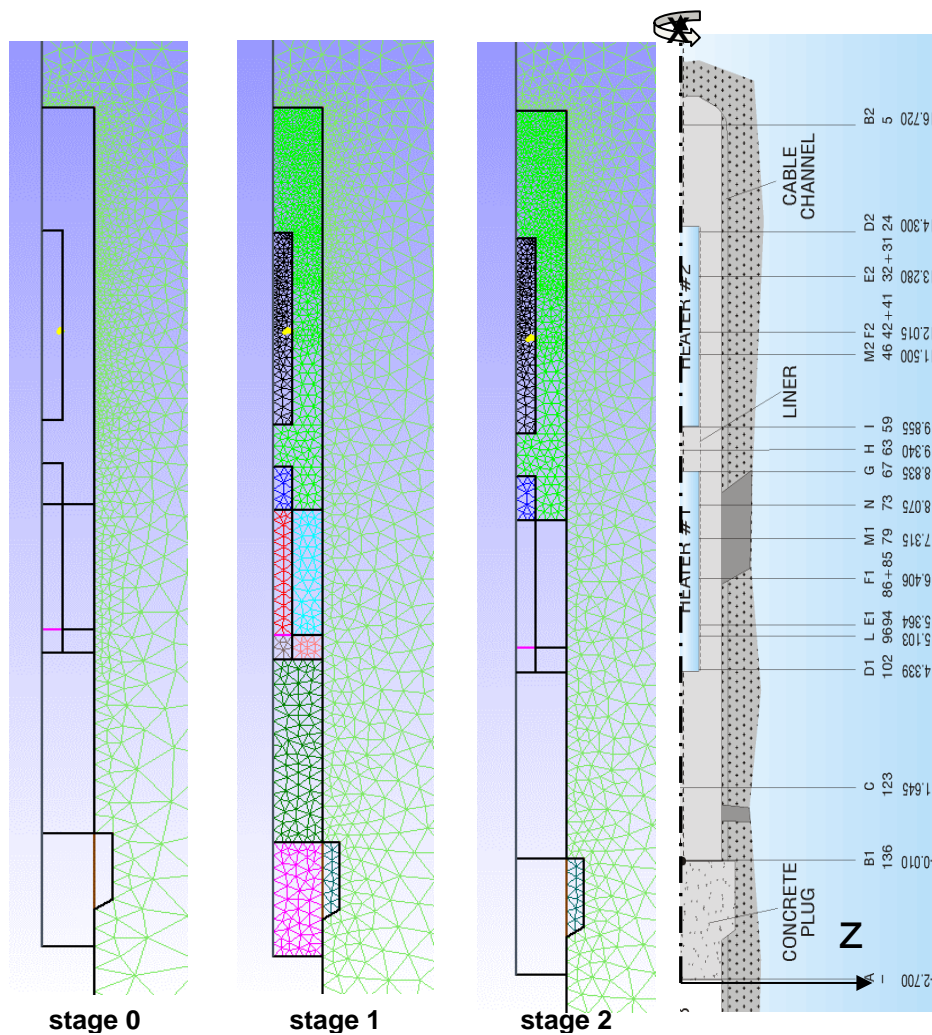


Figure 5-76: The three stages of simulation of the FEBEX experiment and the model domain as given in the specification document,

Table 5-27: Summary of material groups of stages 1 and 2

Material Group No.	Description	
	Stage 1	Stage 2
0	Heater 2	Heater 2
1	Heater 1 (part 1)	Dummy
2	Bentonite	Bentonite
3	Heater 1 (part 2)	Deactivated
4	Heater 1 (part 3)	Deactivated
5	Heater 1 (part 4)	Deactivated
6	Bentonite	Deactivated
7	Bentonite	Deactivated
8	Plug	Deactivated
9	Plug	Deactivated
10	Granite	Granite

The mesh density is higher in the heaters and the bentonite barrier and is gradually coarsened into the granite. A close-up of the mesh around heater 2 and the various output sections perpendicular to the drift axis and output points along these sections are shown in Figure 5-77. Due to rotational symmetry, output is documented only at the points A1, A2 and A3. The state of the system is written out to files at the end of each stage and is read as input for the next stage.

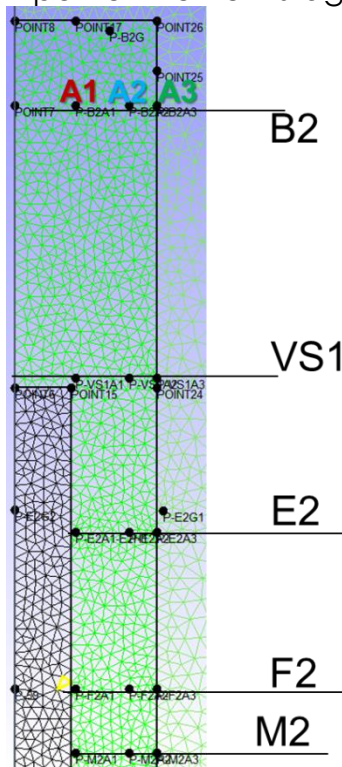


Figure 5-77: Schematic representation of output points and sections around heater 2

5.8.2 Input parameters

The input parameters of the coupled THM model are documented in Table 5-28.

Table 5-28: THM input parameters used in the simulation

Parameter	Value		Unit
	Bentonite	Granite	
Permeability (k)	1.9e-21	8e-17	m ²
Porosity (ϕ)	0.375	0.01	-
Initial saturation (S_{init}^w)			-
Fluid density (ρ^w)	1000		kg/m ³
Grain density (ρ^s)	2780	2780	kg/m ³
Biot coefficient (α_{Biot})	0.1	1	-
Young's modulus (E)	150	12000	MPa
Poisson's ratio (ν)	0.2	0.33	-
Max swelling pressure ($\sigma_{max,sw}$)	7	0	MPa
Sp. Heat capacity	f(T)	920	J/(kg.K)
Thermal conductivity	f(Sw)	2.66	W/(m.K)
Thermal expansion coefficient	1.5e-5	7.8e-6	1/K

The thermal conductivity of water is taken as 0.6 W/(m.K) and its specific heat capacity as 4280 J/(kg.K). The specific heat capacity and thermal conductivity of bentonite are taken as functions of temperature and water saturation respectively as specified in the specification document.

5.8.3 Initial and boundary conditions

In Stage 0 the desaturation of the granite due to the drift excavation is calculated. At this stage, the bentonite and the heaters are not considered. The model is initialized with a fluid pressure of 0.9 MPa and a constant pressure desaturation boundary of -1.6 MPa is applied to the surface of the fully excavated drift at the start of the simulation without considering the various stages of the excavation. Although at this stage, the influence of temperature in the model is minimal, the entire simulation of all the stages are performed with the same non-isothermal Richards' flow model coupled to linear-elastic mechanics. Therefore, a constant temperature boundary of 12 deg. C was applied along the outer boundaries of the granite. The state of the granite at

the end of stage 0 is the initial condition for stage 1 of the simulation.

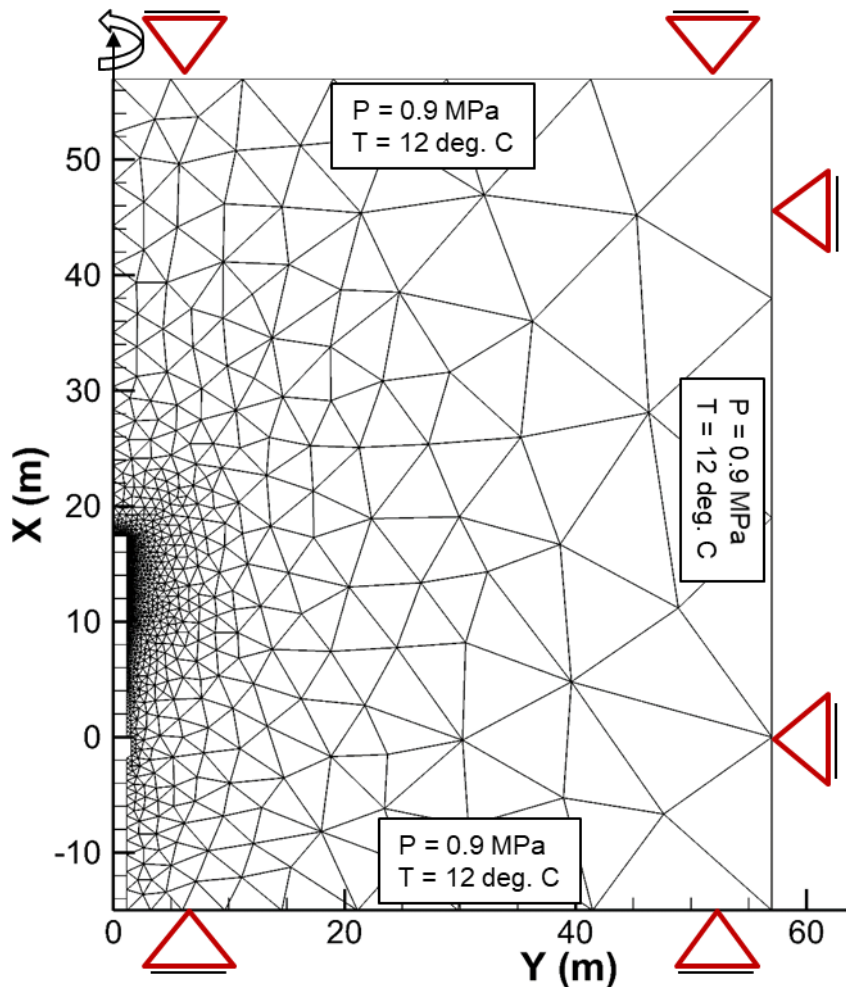


Figure 5-78: Boundary conditions of the model domain.

In stage 1, the sub-domains representing the bentonite, the heaters and the concrete drift plug are active. A constant temperature boundary of 100 deg. C was set along the outer boundaries of both heaters. The bentonite was initialized with a fluid pressure of -138 MPa, corresponding to an initial water content of 17%.

The state of the system after stage 1 formed the initial condition for stage 2. In stage 2 the sub-domains representing the excavation are deactivated and heater 2 remains active. The transition from stage 1 to stage 2 (partial excavation and installation of the new plug) is not modelled.

5.8.4 Results/discussion

Several simulations were performed with this setup changing various parameters to gain a better understanding of their influence on the outcome:

- Thermal power output instead of Dirichlet boundary condition for the

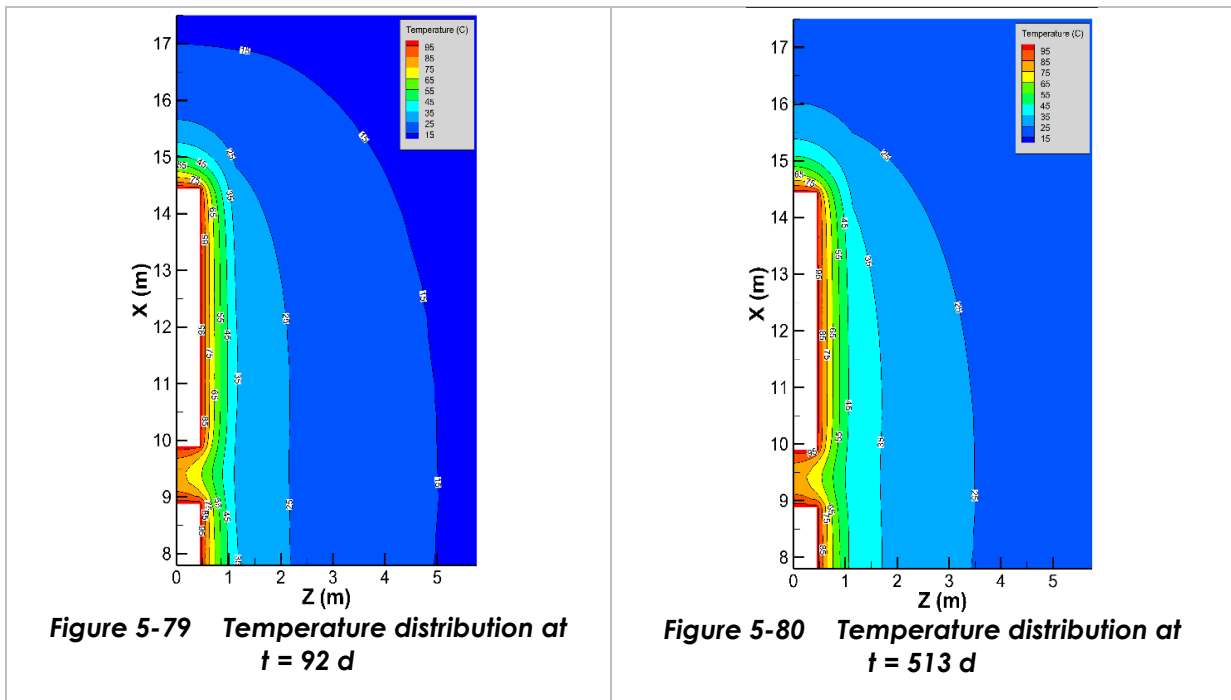
heaters

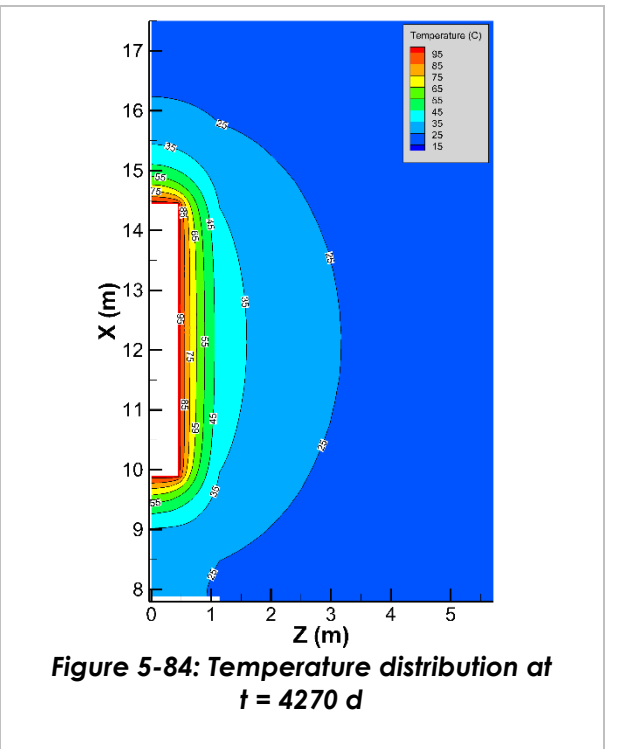
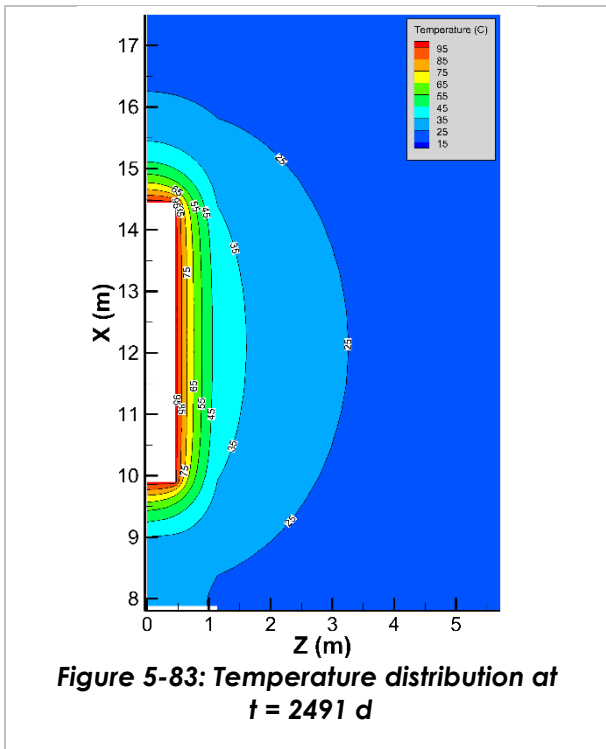
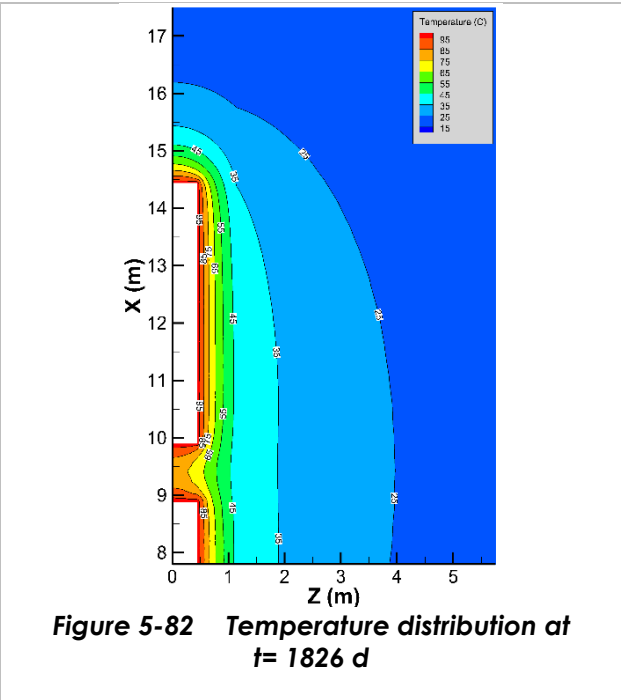
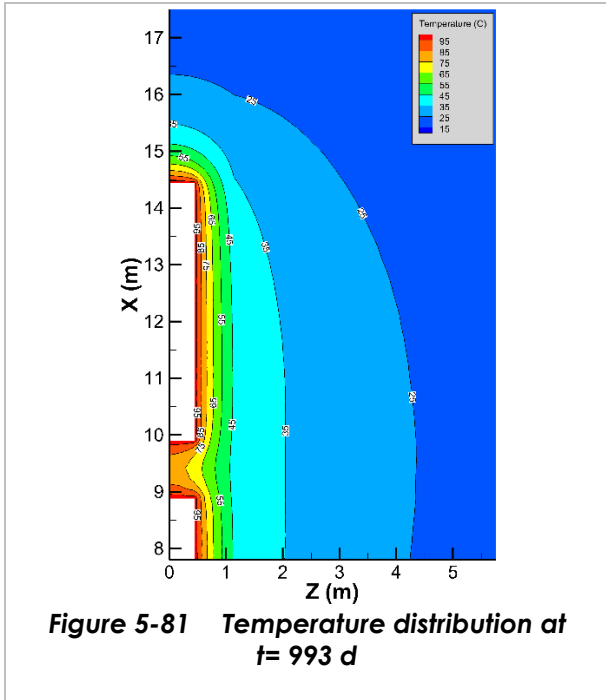
- Arithmetic vs. geometric averaging of the thermal conductivities of the liquid and solid phases for the calculation effective thermal conductivity instead of functions specific to bentonite.
- Constant specific heat capacity for the bentonite instead of a function of temperature.

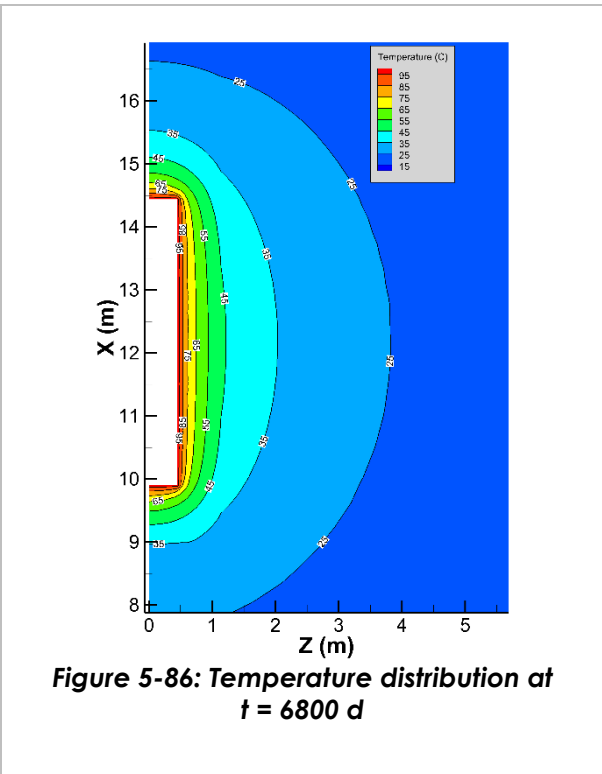
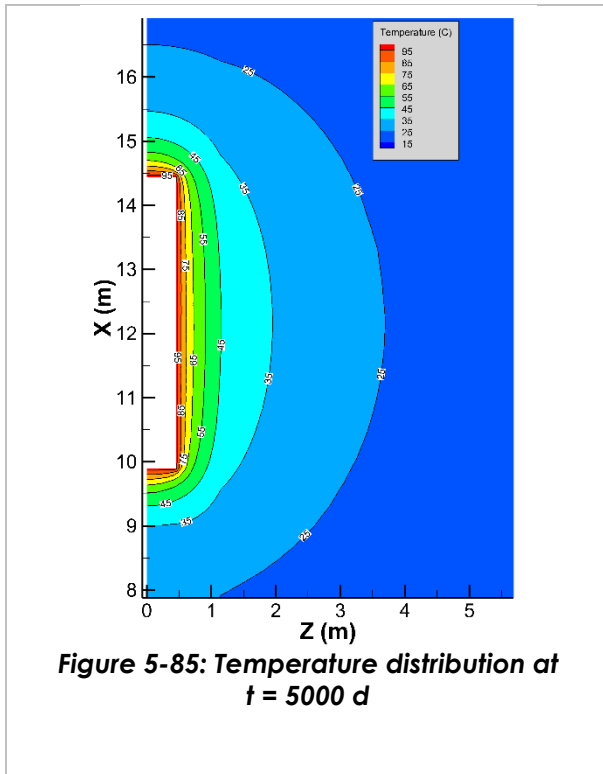
The results documented here are from the simulation that adhered to the parameters given by the test case specifications to the greatest extent. In qualitative comparison of the previously mentioned simulations to the simulation documented here, the following observations were made:

- The simulation using the heater power instead of a Dirichlet temperature boundary was numerically unstable because the power output curve is not smooth. However, the measured temperature on the heater surface suggests that the desired temperature was maintained and therefore the usage of a Dirichlet boundary is justified.
- Both arithmetic and geometric averaging underestimated the temperature evolution behind heater 2 (e.g., sec. B2).

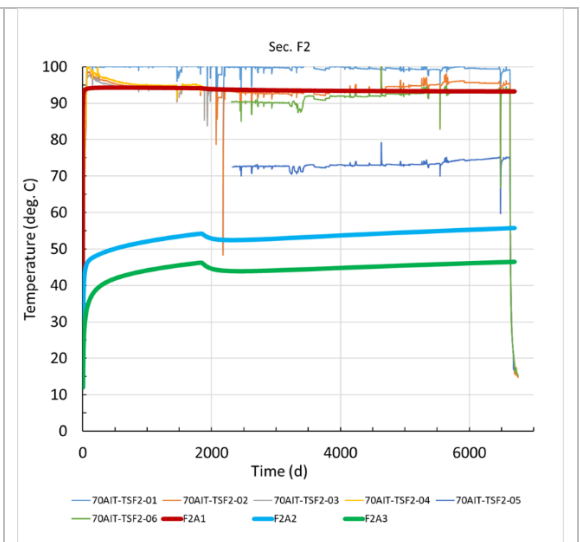
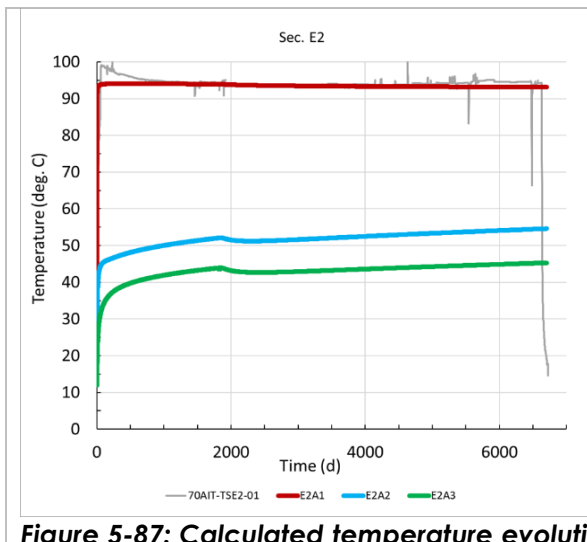
The simulated temperature distributions around heater 2 at various times in stages 1 and 2 is documented by contour plots in Figure 5-79 to Figure 5-86.







The temporal evolution of the temperature and stresses are documented below. In all the figures, a solid red, a solid blue and a solid green line represent the simulation output points A1, A2 and A3 respectively. Thinner lines represent the measurements. The temperature evolutions around (radially) and behind (axially, towards the end of the drift) heater 2 are shown in Figure 5-87 to Figure 5-89.



Sections E2 and F2 have relatively few temperature measurements available over the duration of the experiment. Many of these measurements lie in the proximity of the heater. The point A1 of the simulation output, which lies nearest to the heater, is not of great analytical significance since the calculated temperature here is strongly influenced by the Dirichlet boundary condition prevailing on the heater surface.

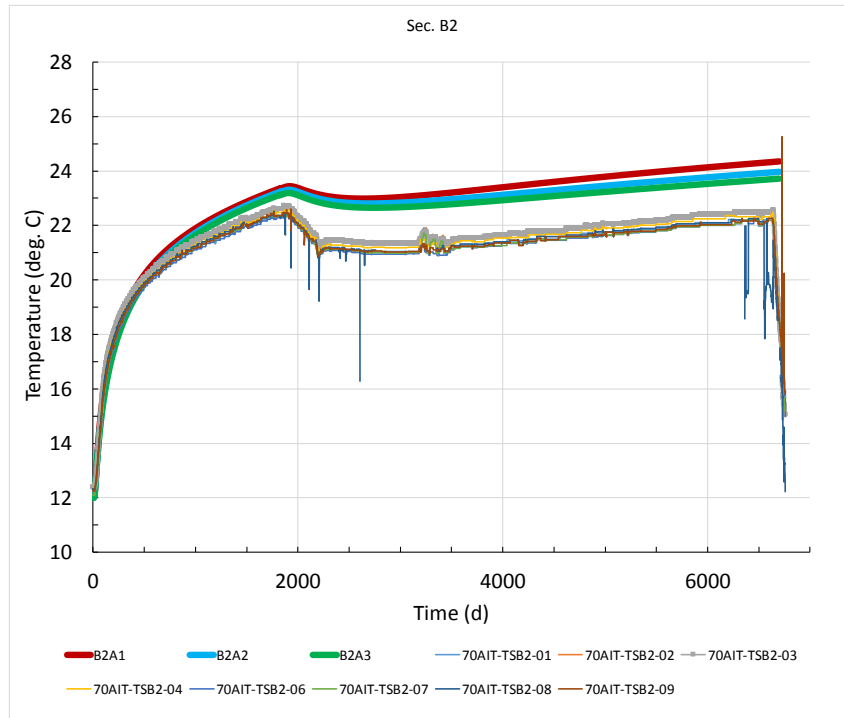


Figure 5-89: Calculated temperature at specified output points at section B2 in comparison to sensor data

The three output points of section B2 show only small differences in the temperature evolution, suggesting that section B2, due to its distance from the heater, gets heated uniformly. The evolution is consistent with the measured data. Near the end of stage 1, the calculated temperature is slightly overestimated. This overestimation consistently continues into stage 2. The absolute overestimation of temperature in stage 2 is about 1 deg. C. A detailed modelling of the partial dismantling and its influence on the prediction of temperature is a scenario that can be further investigated.

Radial stresses were evaluated at two sections around heater 2 and axial stresses were evaluated at one section behind it. The simulation output at these sections follows the general trend of measured data. In the section B2, the measured values suggest that the stresses had not reached steady state. However, the stresses in the model tend towards a steady maximum stress value and therefore underestimates the measured stresses at later times. In the sections E2 and F2 the calculated values are in relatively good agreement with the measurement data.

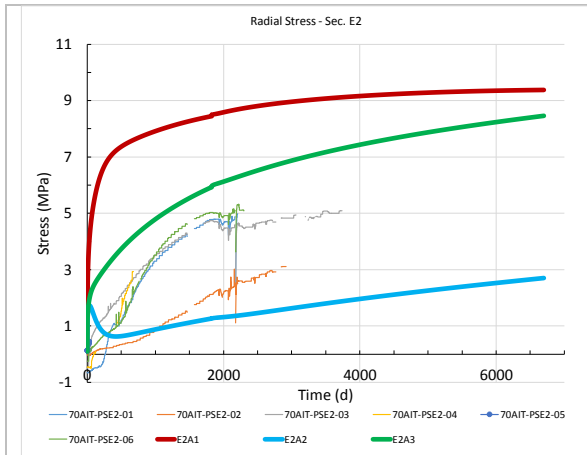


Figure 5-90 Calculated radial stress evolution at specified output points at section E2 in comparison to sensor data

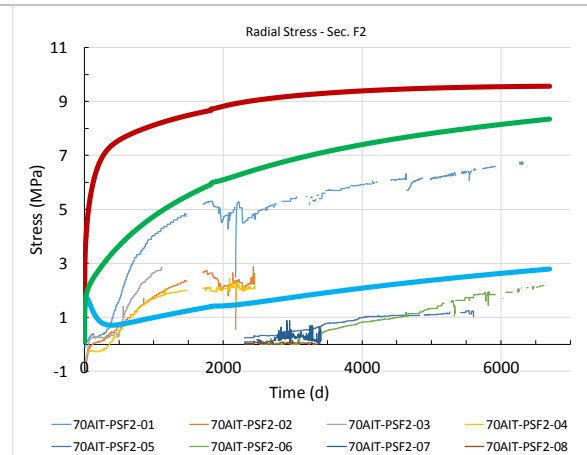


Figure 5-91 Calculated radial stress evolution at specified output points at section F2 in comparison to sensor data

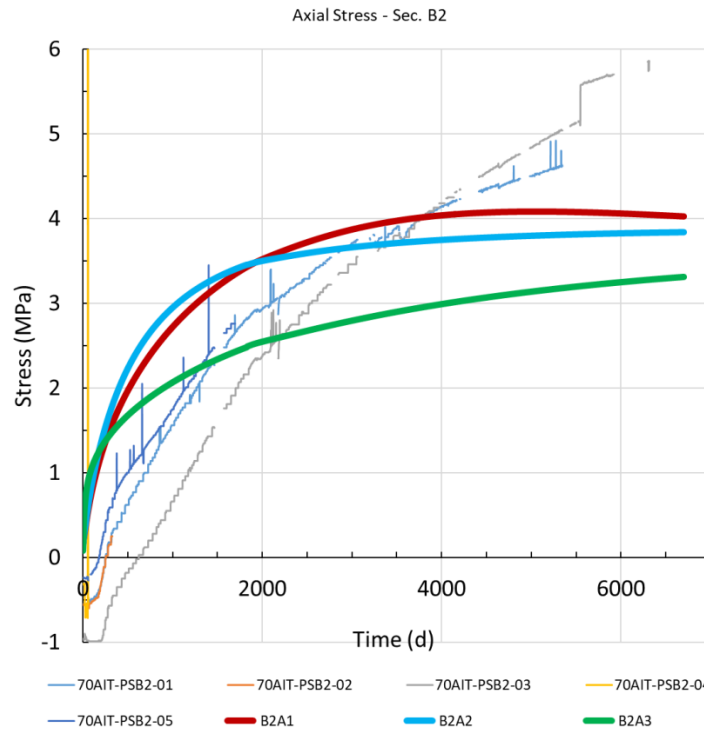


Figure 5-92 Calculated axial stress evolution at specified output points at section B2 in comparison to sensor data

The evolution of the relative humidity at the output sections E2 and F2 show good agreement for the points A2 and A3. Since the Kelvin equation used to calculate the relative humidity is a function of the pressure and temperature, the good agreement with the measured values suggests that the prediction of pressure and temperature was satisfactory.

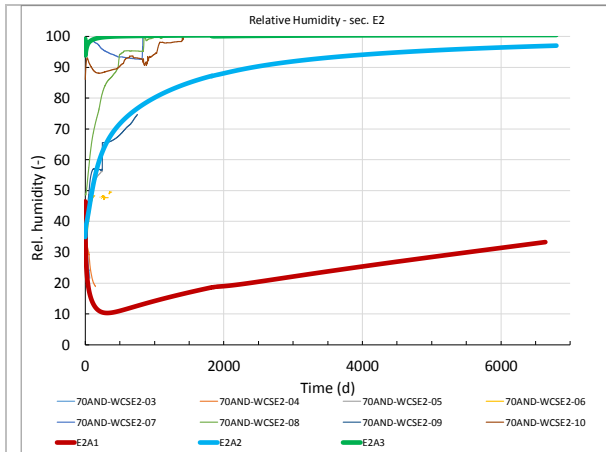


Figure 5-93: Calculated relative humidity evolution at specified output points at section E2

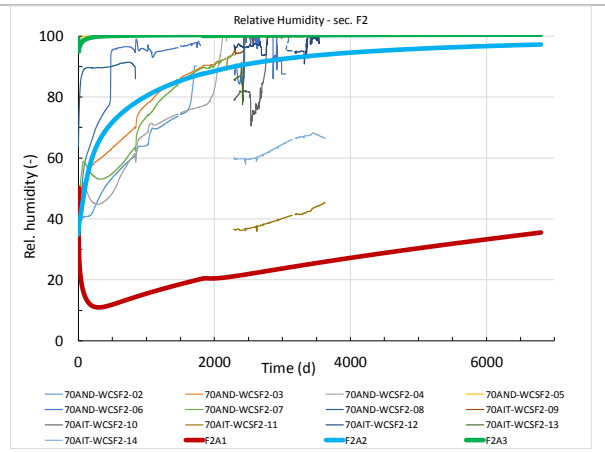


Figure 5-94: Calculated relative humidity evolution at specified output points at section F2

The water content is underestimated (Figure 5-95-Figure 5-99) and the dry density is overestimated. This suggests that the calculation of porosity needs improvement.

Water Content - sec. M2

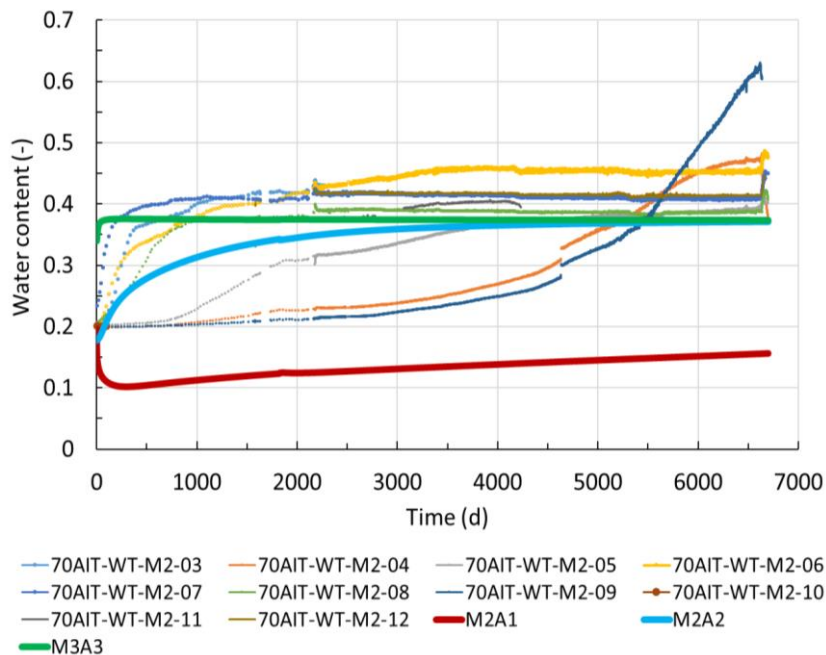


Figure 5-95: Comparison of the evolutions of calculated and measured water contents.

Similar to the temporal evolution, the comparison of the dry density and the water content with the data from the final dismantling indicates a strong over prediction of the water content. These are shown in Figure 5-96 to Figure 5-99. In the following figures, the black points are the calculated and the blue points, the measured values.

Water content sec. 49

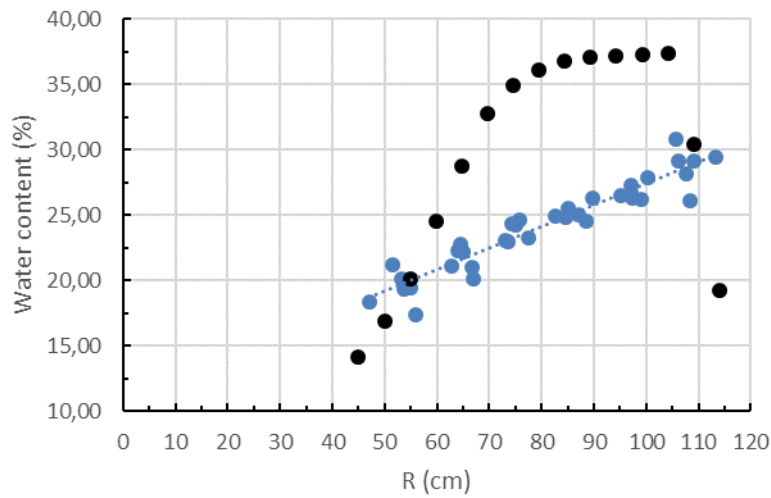


Figure 5-96 Final spatial water content distribution at the section 49

Water content sec. 52

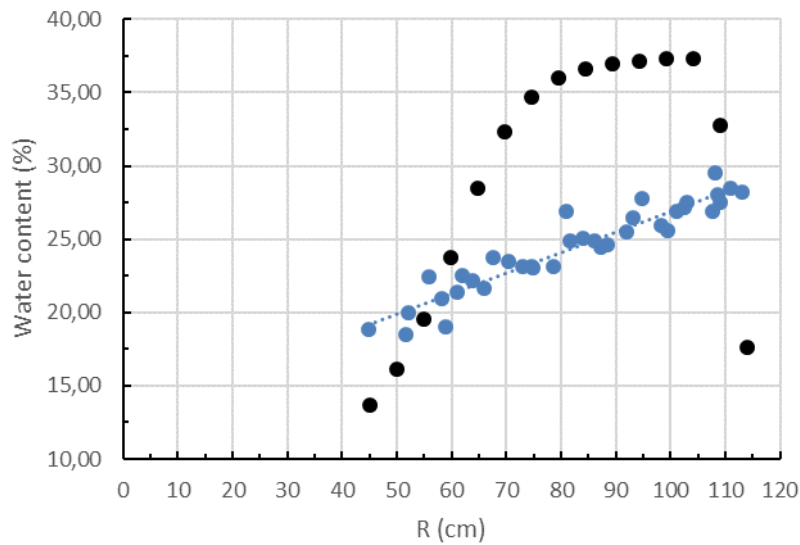


Figure 5-97 Final spatial water content distribution at the section 52

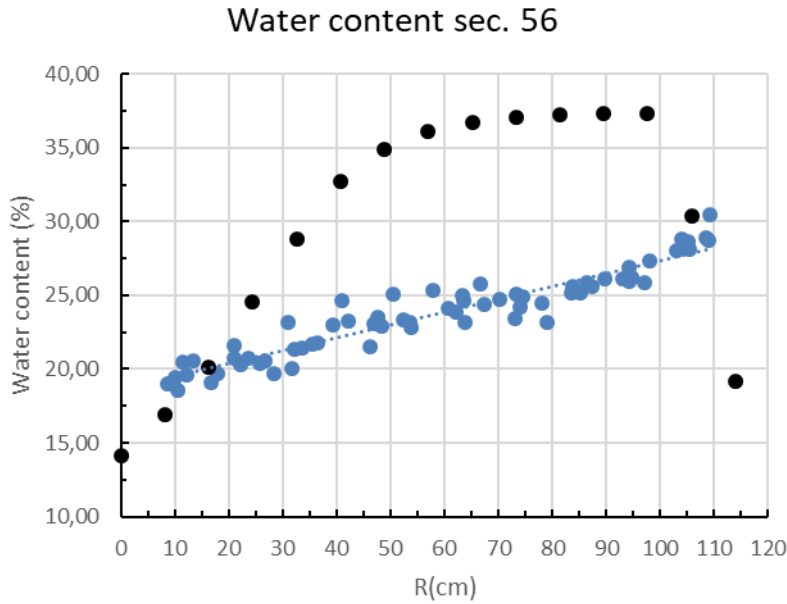


Figure 5-98 Final spatial water content distribution at the section 56

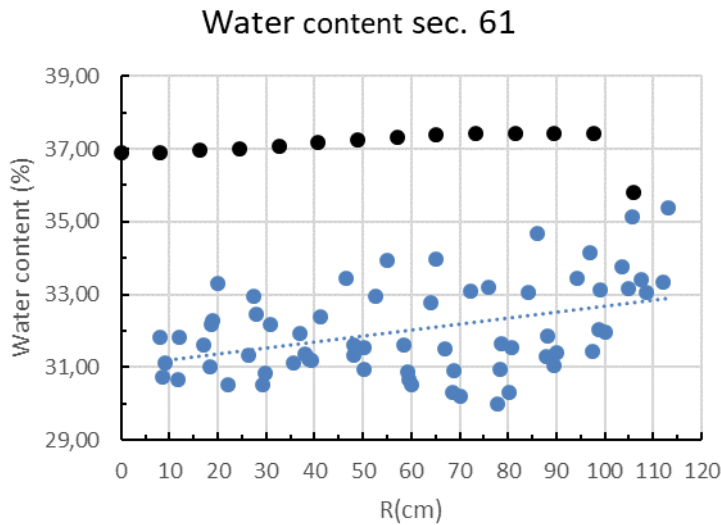


Figure 5-99 Final spatial water content distribution at the section 61

In the current model, the water content calculations are based on both the changes in porosity and saturation whereas the dry density calculations are based on changes in the porosity only. Behind the strong under prediction of the change in porosity lies the assumption of weak hydromechanical coupling. This strongly influences the calculation of the change in porosity thus affecting both the calculated water content and dry density. Improved models for the changes in porosity and dry density are currently being investigated as a part of WP3. Considering the experience gathered from the application of the current porosity model to the FEBEX simulation, a comparison and interpretation of the dry density results were not considered

beneficial and have hence been withheld.

With the exception of the dry density and the water content, both of which are dependent on the porosity, the simulation can reproduce the coupled THM behaviour of the FEBEX experiment. A few deviations were made from the provided parameter set, such as choosing a low swelling pressure and thermal expansion coefficient in order to consider the numerically homogenized model without explicitly modelling gaps. A few other model simplifications were made in the choice of the geometry (simplification of drift end section, neglecting the lamprophyre and the disturbed zone) and in the processes modelled (linear elasticity, simplified excavation and partial dismantling). Despite these, the coupled THM model demonstrates good predictive capability and provides a good basis for investigations in the next step in WP5 involving large scale THM models, namely, the assessment cases.

5.9 Synthesis of results for FEBEX – key lessons (Andra + All)

Due to the large amount of data available and produced by the participants of the Febex exercise, only few curves are presented in this paragraph showing the main lessons. Most of the presented results are coming from the section F2 located in the middle of the canister.

On Figure 5-100 left, temperature evolution is presented at a locations close to the canister where the boundary conditions is applied. Comparing the measurements themselves, it can be seen that differences exist depending on the position of the sensors around the canister leading to temperatures between 90 and 100°C. The numerical models are in this range for all of them and due to the 2D axisymmetric approach can't distinguish this variation of temperature around the canister. Certainly these differences in temperature at the boundary condition are one of the reasons of the numerical prediction level of temperature observed further in the bentonite as it can be seen on Figure 5-100 (right) and that indicate some dispersion. In any cases the trend (rapid increase and stabilisation of temperature) is well catch by the model with levels of temperature consistent with the observations.

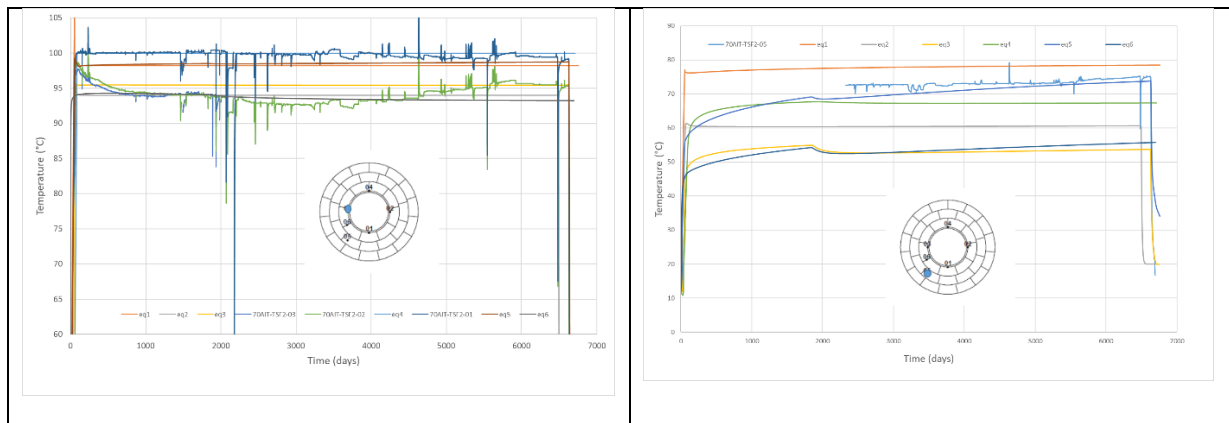


Figure 5-100 Temperature evolution in section F2 at two locations interface bentonite/canister and middle of bentonite ring, comparison between numerical results and quantities measured

A rapid relative humidity increase to around 90-100 % facilitated by the vicinity of the wetting boundary at the rock interface is observed on the sensors in the outer ring of the buffer (close to the rock) – see Figure 5-101. The numerical results show this rapid increase in agreement with the measurements. In the middle ring, the relative humidity evolved more slowly following the invasion front of water. This saturation evolution is influence by the hydro-mechanical evolution of the bentonite and the water retention model. The trend of evolution for relative humidity in the block and the characteristic times seem well reproduced by the models and indicate a good representation of the hydraulic behaviour of the bentonite.

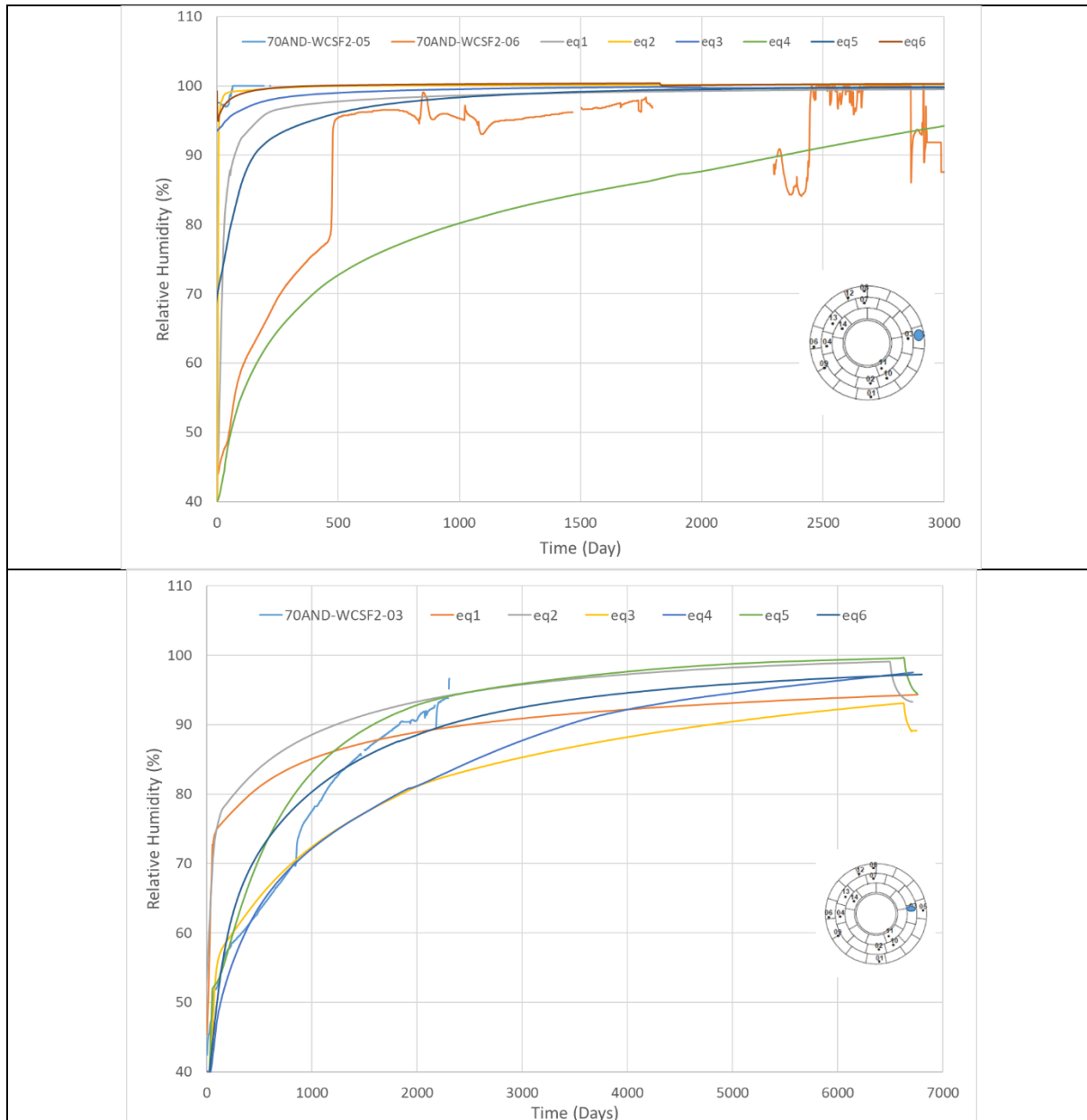


Figure 5-101 Relative humidity evolution in section F2 at two locations middle of the second and third rows of bentonite blocks, comparison between numerical results and quantities measured

The same type of evolution can be observed on the water content in the bentonite rings (Figure 5-102). A rapid increase of water content happened close to the host rock while the evolution is driven by the propagation of the hydration front deeper into the bentonite block. If the trend is well approached by the models as for relative humidity, the importance of the coupling terms between hydraulic parameters and mechanical behaviour explains certainly the larger dispersion observed on the numerical results.

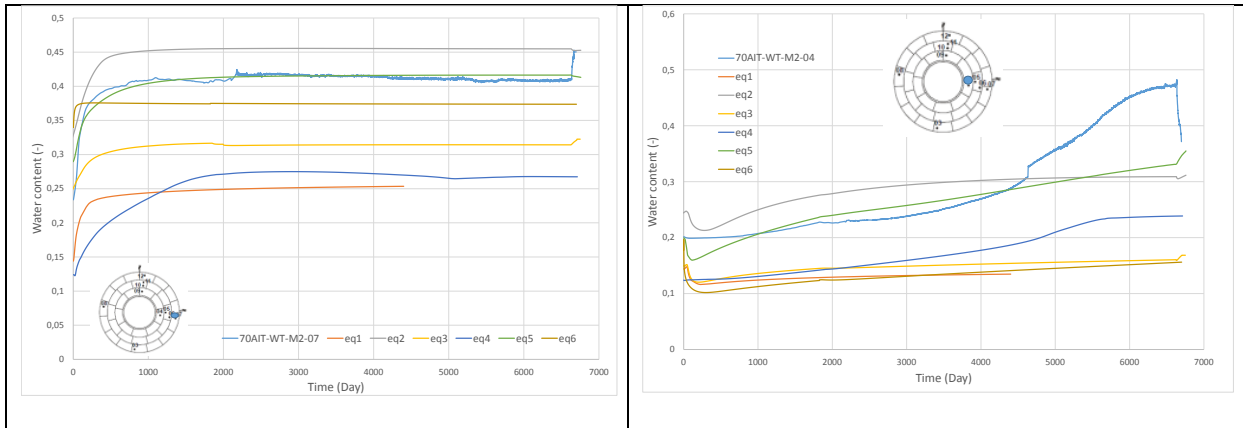


Figure 5-102 Water content evolution in section M2 at two locations interface bentonite/canister and middle of external bentonite ring, comparison between numerical results and quantities measured

The difficulty to introduce this hydro-mechanical coupling in the models can also be observed on some of the radial stress results. Figure 5-103 shows the radial stress evolution close to the host rock (PSF2-01) and in the middle of the second row of bentonite block. If the trend of evolution is in most cases well reproduced by the models, dispersion in the results is observed. In this complex tests the origin of this dispersion can be attributed to the model itself but also to the real knowledge of the initial and the boundary conditions and sometimes also to the information deliver by the sensor.

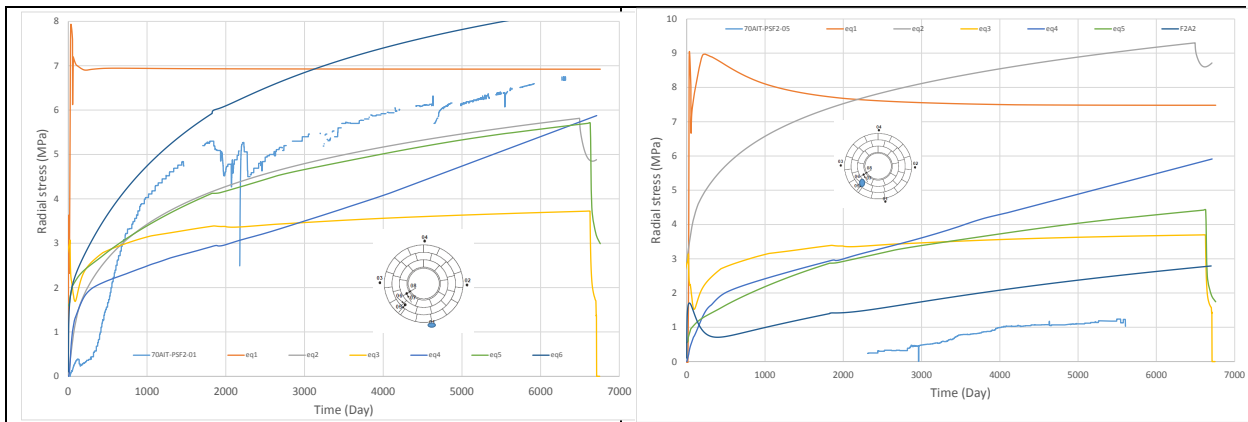


Figure 5-103 Radial stress evolution in section F2 at two locations interface host rock/bentonite and middle of the second row of bentonite blocks, comparison between numerical results and quantities measured

In Figure 5-104, adjustment of radial stress at the location PSF2-05 suggests that the sensor were initialized at a value close to zero at the time when recording begun, 2311 days after switching on the heaters. With this consideration, numerical results coming from three partners fit very well the measured quantities.

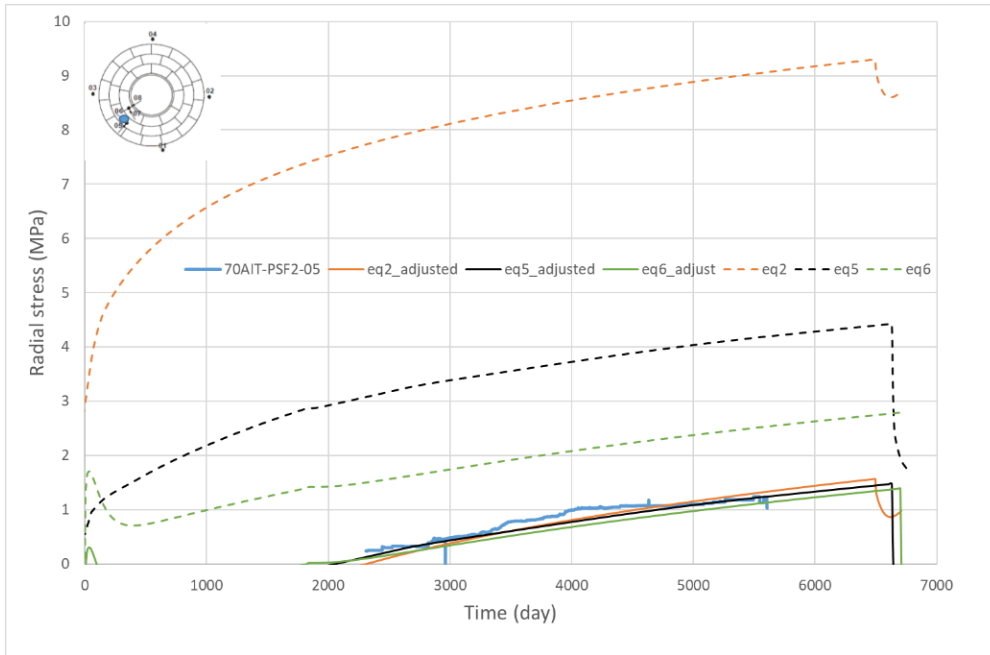


Figure 5-104 Radial stress evolution in section F2, adjustment of the numerical results considering a value close to zero at the time when recording begun, 2311 days after switching on the heaters.

The property distributions at the end are of a great interest for the project in link with the homogenised state. Some post-mortem analysis of the bentonite about after dismantling are compared with the numerical results. Two sections are presented here S49 and S56 (see Figure 5-105), one around the canister and second at the end of the tunnel.

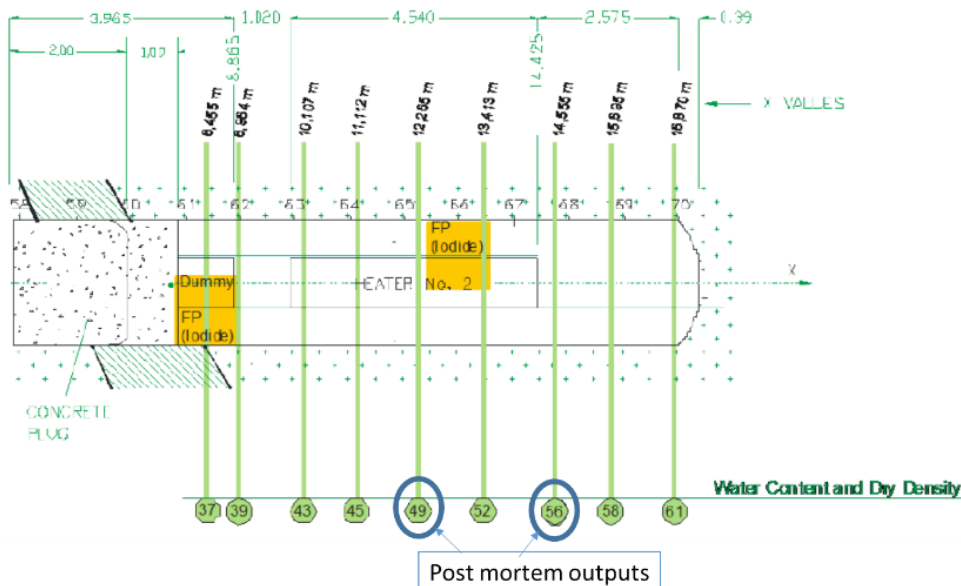


Figure 5-105 Location of the two sections for the post mortem analysis

The comparison between the measured quantities and the numerical results are presented on Figure 5-106 for S49 and on Figure 5-107 for S56. The dry

density, water content and water saturation obtained by models at the final state are in very good agreement with the post-mortem analysis made after dismantling.

As in previous tests (EB and CRT), or in task 5.1 from Beacon project, the models give always a good estimation of final state. Main differences between measurements and numerical results are obtained during the transient phase and on some specific quantities.

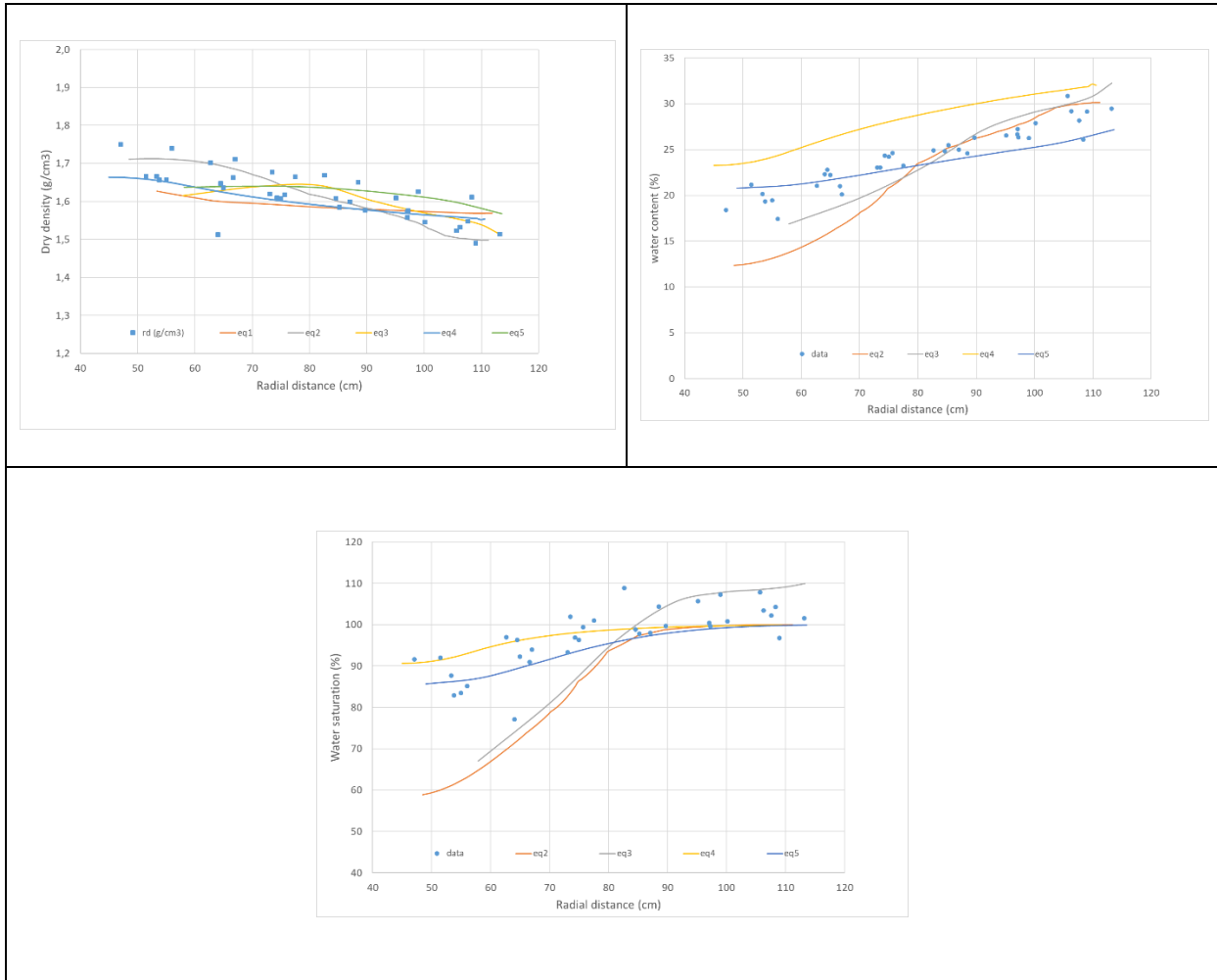


Figure 5-106 Dry density, water content and water saturation profiles after dismantling in section S49 comparison between numerical results and measured quantities

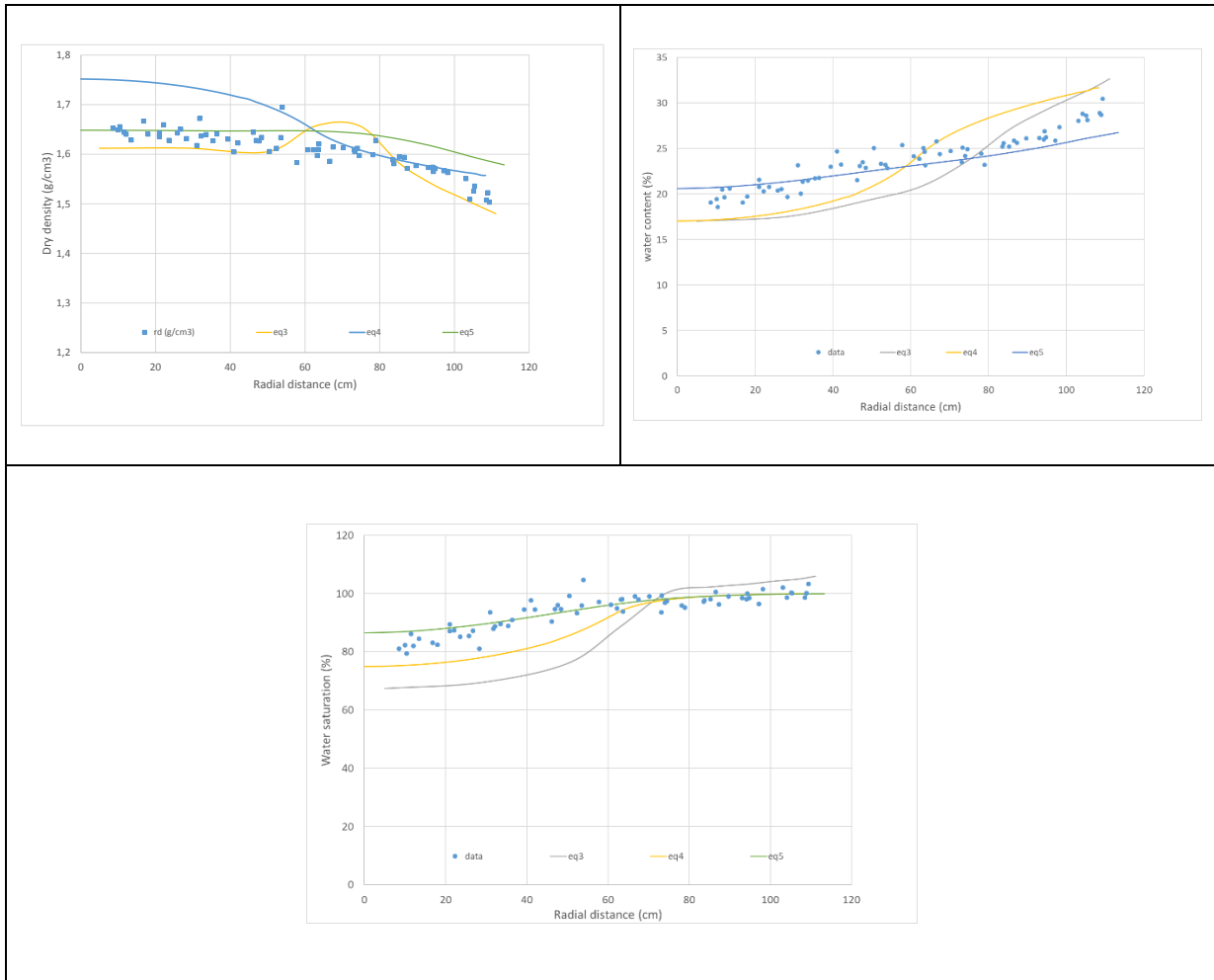


Figure 5-107 Dry density, water content and water saturation profiles after dismantling in section S56 comparison between numerical results and measured quantities

Despite the duration of this experiment, it can be observed as it was previously shown on EB or CRT, that a gradient of density is still persisting in the material. In this case, few heterogeneities are identified in the initial state of the material except the interfaces between blocks and should not explain this gradient of properties at the end. The main origin is due to the way of hydration happened from the periphery of the bentonite blocks. It is really interesting to see that the numerical models are able to follow this evolution.

6 Synthesis of task 5.2

In Task 5.2, the purpose was to model some large scale experiments. The tests were chosen among those listed during the inventory carried out in WP2.

The main criteria of selection were that for the tests chosen the maximum amount of data was available and they have to be relevant for the Beacon project in terms of homogenisation of the components made with bentonite materials.

This task was much more difficult than the previous one due to complexity of the geometry, the uncertainties on the boundary and initial conditions and sometimes in the analysis of the information given by the sensors. As one consequence, this implies to superpose to the complexity of the physical processes to large domain of computation increasing the number of cells in the considering mesh. Moreover, for two of the tests (CRT, Febex), it was necessary to take into account the temperature and the couplings between the thermal part and the hydro-mechanical behaviour.

Till the beginning of the project, a large diversity of approaches and formulations have been retained by the partners. This is one of the strengths of the project and these approaches have been applied to the proposed test cases of task 5.2. It should be noticed that even groups that started the project with few numerical tools available or few experiences have been able to produce some very good results during this stage of the project. This is an important contribution of the project which shows the beneficial returns for all participants. This task is a perfect illustration of the progress made by all partners in terms of improving the models and constituent laws or developing skills.

As it was observed in the previous task, it is necessary to look at two aspects of the tests, the transient phase and the end state.

The transient phase is associated in all the cases with resaturation processes and the couplings between the different THM processes drive the evolution of the system. Models have sometimes difficulties to reproduce all the evolution of physical quantities during this phase even if they reproduced well in most of the cases the trend and the magnitude of the measured quantities.

The comparison with the final state of the barrier provides more discriminating information in a matter that is very much aligned with the aims of the project. Relevant observations are obtained in the dismantling of the tests concerning the homogenization of several quantities of importance such as the dry density or water content. Two types of heterogeneities are considered: (i) initial heterogeneity in the material induces for example by the used of blocks and pellets (EB situation) with consequences on dry densities and the hydromechanical evolution, (ii) heterogeneous state induces by external hydro-mechanical boundary conditions.

It was really interesting to see that the final states with in most cases and for all the test cases proposed in this task despite the complexity of the studied

system were well approached by the models.

These observations concern both dry density distribution that is mainly well captured by the model and the final distribution of water in bentonite materials.

Most of the partners used for this stage, a double porosity constitutive model to represent the mechanical behaviour of bentonite materials. They showed clearly the interest of this type of approach to simulate the bentonite component evolution during hydration and the contribution of such models to predict the final state. The partition between micro and macro porosity needs to introduce the interaction between the two porosity levels. It has been shown that the representation and the choice of the interaction functions in the model plays a significant role in the quality of the results. Experimental determination of the precise shape and magnitude of the interaction functions is therefore an essential issue in order to improve the representativeness of the models.

Some analyses have also shown the sensitivity of the results to some parameters such as retention curve or swelling pressure dry density relationship. These results underline the need to determine more precisely a set of basic but essential data for a better representation of the physical processes that develop within bentonites during hydro mechanical solicitations.

References

- AITEMIN (2013) Engineered Barrier Emplacement Experiment in Opalinus Clay: "EB" Experiment. As-built of dismantling operation. Deliverable n°: D2.1-4. Madrid, Spain.
- Åkesson M, Börgesson L, Kristensson O, 2010. SR-Site Data Report. THM modelling of buffer, backfill and other system components. SKB TR-10-44. Stockholm, Sweden: Svensk Kärnbränslehantering AB.
- Åkesson M, Kristensson O, Malmberg D (2020), D3.2 Annex C: Developments of the HBM model. Clay Tech, D3.2, BEACON.
- Alcoverro J, Alonso E E, 2001. Scientific bases of Code_Bright. 70-UPC-L-Q-001: 1-12. UPC.
- Alonso, E.E., Gens, A., Josa, A. (1990) A constitutive model for partially saturated soils. *Géotechnique* 40, N° 3, 405-430.
- Alonso, E.E., Vaunat, J., Gens, A. (1999) Modelling the mechanical behaviour of expansive clays. *Engineering Geology*, N° 54, 173-183.
- Alonso, E.E., Hoffman, C. (2007) Modelling the field behaviour of a granular expansive barrier. *Physics and Chemistry of the Earth*, N° 32, 850-865.
- Cerfontaine, B., Dieudonne, A., Radu, J., Collin, F., & Charlier, R. (2015). 3-D zero-thickness coupled interface element: Formulation and application. 69.
- Charlier, R. (1987) : Approche unifiée de quelques problèmes non linéaires de mécanique des milieux continus par la méthode des éléments finis. PhD Thesis, Université de Liège in Department ArGEnCo, Liège, Belgium
- Cleall P J, Singh R M and Thomas H R, 2013. Vapour transfer in unsaturated compacted bentonite. *Géotechnique* 63, No. 11, 957-964 [<http://dx.doi.org/10.1680/geot.12.P.147>]
- Collin, F. (2003) : Couplages thermo-hydro-mécaniques dans les sols et les roches tendres partiellement saturés. PhD Thesis, Université de Liège in Department ArGEnCo, Liège, Belgium.
- Collin, F., Li, X.L., Radu, J.P. & Charlier, R. (2002): Thermo-hydro-mechanical coupling in clay barriers. *Engineering Geology*, 64(2-3):179-193.
- Collins, I.F. and Kelly, P.A., 2002. A thermomechanical analysis of a family of soil models. *Geotechnique*, 52(7), pp.507-518.
- Dean J A and Lange N A, 1999. Lange's Handbook of Chemistry, 15th ed. p1199. McGraw-Hill.
- Di Donna, A. and Laloui, L., 2015. Response of soil subjected to thermal cyclic loading: experimental and constitutive study. *Engineering Geology*, 190, pp.65-76.
- Dieudonne, A. C. (2016). Hydromechanical behaviour of compacted

bentonite: from micro-scale analysis to macro-scale modelling. Liege: Universite' de Liege.

Dueck, A., & Nilsson, U. (2010). Thermo-Hydro-Mechanical properties of MX-80. SKB.

Dupray, F., François, B. & Laloui, L. (2013): Analysis of the FEBEX multi-barrier system including thermoplasticity of unsaturated bentonite. *International Journal for Numerical and Analytical Methods in Geomechanics* 37, 399–422. doi:10.1002/nag.

Enresa (1998): FEBEX Pre-Operational Stage Summary Report. Publicaciones Técnicas 01/98, Enresa, Madrid, Spain

Enresa, 2000. FEBEX Project. Full-scale Engineered Barriers Experiment for a Deep Geological Repository for High Level Radioactive Waste in Crystalline Host Rock. Final Report. Enresa Report 1/2000, Enresa, Madrid.

FEBEX. 2017. Stage 2 specifications. EBS Task Force.

FEBEX full-scale engineered barriers experiment in crystalline host rock. Preoperational thermo-hydro-mechanical (THM) modelling of the "in situ" test. Report 9900152, ENRESA, Spain, 1999, 103 p.

Fehlberg, E., 1969. Low-order classical Runge-Kutta formulas with step size control and their application to some heat transfer problems.

Finsterle S, Pruess K (1995). Solving the estimation-identification problem in two phase flow modelling. *Water Resour. Res.*, 31(4), 913-924

Fredlund D G, Rahardjo H, 1993. Soil mechanics for unsaturated soils. New York, NY: John Wiley & Sons, Inc.

Gaus, I., Wieczorek, K., Schuster, K., Garitte, B., Senger, R., Vasconcelos, R. and Mayor, J.C. (2014). EBS behaviour immediately after repository closure in a clay host rock: HE-E experiment (Mont Terri URL). In: *Clays in Natural and Engineered Barriers for Radioactive Waste Confinement*, Geological Society, London, Special Publications, 400, 71-91.

Gens A, Alonso EE, 1992, A framework for the behaviour of unsaturated expansive clays, *Canadian Geotechnical Journal* 29 (6), pp.1013-1032.

Gens, A., Valleján, B., Sánchez, M., Imbert, C., Villar, M.V., Van Geet, M., 2011. Hydromechanical behaviour of a heterogeneous compacted soil: experimental observations and modelling. *Géotechnique* 61, 367–386.

Gens, A., Vasconcelos, R. (2018) HE-E Experiment: Modelling of the HE-E test – 1st Modelling Phase. Technical Note TN 2018-51 – Mont Terri Project (Phase 23).

Georgiadis K, Potts DM, Zdravkovic L. (2005). Three-dimensional constitutive model for partially and fully saturated soils, *Int J Geomech* 5 (3), pp. 244–255

Ghiadistri G.M. (2019). Constitutive modelling of compacted clays for

applications in nuclear waste disposal; PhD Thesis, Imperial College London, UK.

Ghiadistri G.M., Potts D.M., Zdravkovic L., Tsiampousi A. (2018). A new double structure model for expansive clays; 7th Int. Conf. on Unsaturated Soils, UNSAT 2018, 3-5 August, 2018, Hong Kong

Goudarzi R, Börgesson L, Röshoff K, Edelman M, 2006. Äspö Hard Rock Laboratory. Canister Retrieval Test. Sensors data report (Period 001026-060501). Report No: 12. SKB IPR-06-35. Stockholm, Sweden: Svensk Kärnbränslehantering AB.

Gramegna, L., & Charier, R. (2019). Deliverable (D5.1) Third verification case: test 1c. Liege: BEACON project.

Hausmannová, L., Vašíček, R., 2014. Measuring hydraulic conductivity and swelling pressure under high hydraulic gradients. Geological Society, London, Special Publications 400, 293–301.

Hoffman, C. (2005) Caracterización hidromecánica de mezclas de pellets de bentonita. Estudio experimental y constitutivo. Doctoral Thesis, Technical University of Catalonia (UPC), Barcelona, Spain.

Hoffman, C., Alonso, E.E., Romero, E. (2007) Hydro-mechanical behaviour of bentonite pellet mixtures. *Physics and Chemistry of the Earth*, N° 32, 832-849.

Janda, T., Mašín, D., 2017. General method for simulating laboratory tests with constitutive models for geomechanics. *International Journal for Numerical and Analytical Methods in Geomechanics* 41, 304–312.

Kolditz, O.; Bauer, S.; Bilke, L.; Böttcher, N.; Delfs, J. O.; Fischer, T. et al. (2012): OpenGeoSys. An open-source initiative for numerical simulation of thermo-hydro-mechanical/chemical (THM/C) processes in porous media. In: *Environ Earth Sci* 67 (2), S. 589–599. DOI: 10.1007/s12665-012-1546-x.

Koudelka, T., Krejčí, T., Kruis, J., 2018. Time integration of hypoplastic model for expansive clays, in: *AIP Conference Proceedings*. AIP Publishing, p. 080011.

Koudelka, T., Krejčí, T., Kruis, J., 2017. Coupled hydro-mechanical model for expansive clays. *AIP Conference Proceedings* 1863, 290008. <https://doi.org/10.1063/1.4992445>

Koudelka, T., Krejčí, T., Kruis, J., 2011. Modeling of Building constructions in SIFEL Environment.

Kristensson U., Borgesson L. (2015). Canister Retrieval Test: Final Report; Technical Report TR-14-19; Clay Technology AB

Kristensson O, 2019a. EBS TF - THM modelling. Task 4 - Prototype Repository. Simulating the Canister Retrieval Test.

Kristensson O, 2019b. EBS-TF. Task 9: FEBEX in situ test. Final Report from SKB1.

Laloui, L. and Cekerevac, C., 2003. Thermo-plasticity of clays: an isotropic

yield mechanism. *Computers and Geotechnics*, 30(8), pp.649-660.

Laloui, L. & François, B. (2009): ACMEG-T, Soil Thermoplasticity Model. *Journal of Engineering Mechanics*, 135(9):932-944

Lanyon, Gaus, 2013. Main outcomes and review of the FEBEX in situ test (GTS) and Mock-up after 15 years of operation. *Arbeitsbericht NAB 13-96*. Wettingen, Switzerland: Nagra.

Lloret A, Romero E and Villar M V, 2005. FEBEX II Project Final report on thermo-hydro-mechanical laboratory tests. ENRESA report ISSN: 1134-380X.

loret, A., Villar, M. V., & Pintado, X. (2002). *Ensayos THM: Informe de síntesis*. Internal report. CIEMAT.

Lloret, A., Villar, M. V., Sánchez, M., Gens, A., Pintado, X. & Alonso, E. E. (2003). Mechanical behaviour of heavily compacted bentonite under high suction changes. *Géotechnique* 53, No. 1, 27–40

Marcial D, Delage P, Cui YJ, (2008). Hydromechanical couplings in confined MX80 bentonite during hydration, 1st European Conference on Unsaturated Soils, E-UNSAT 2008, 249-255. CRC Press, Durham, UK.

Martínez V, Abós H, García-Siñeriz J L, 2016. FEBEXe: Final Sensor Data Report (FEBEX "in situ" Experiment). *Arbeitsbericht NAB 16-19*. Wettingen, Switzerland: Nagra.

Mašín, D., 2018. *Modelling of Soil Behaviour with Hypoplasticity: Another Approach to Soil Constitutive Modelling*. Springer.

Mašín, D., 2017. Coupled thermohydromechanical double-structure model for expansive soils. *Journal of Engineering Mechanics* 143, 04017067.

Mašín, D., 2014. Clay hypoplasticity model including stiffness anisotropy. *Géotechnique* 64, 232–238.

Mašín, D., 2013a. Double structure hydromechanical coupling formalism and a model for unsaturated expansive clays. *Engineering Geology* 165, 73–88.

Mašín, D., 2013b. Clay hypoplasticity with explicitly defined asymptotic states. *Acta Geotechnica* 8, 481–496.

Mašín, D., 2010. Predicting the dependency of a degree of saturation on void ratio and suction using effective stress principle for unsaturated soils. *International Journal for Numerical and Analytical Methods in Geomechanics* 34, 73–90.

Mašín, D., Khalili, N., 2015. Swelling phenomena and effective stress in compacted expansive clays. *Canadian Geotechnical Journal* 53, 134–147.

Melgarejo Corredor MM (2004). Laboratory and numerical investigations of soil retention curves. PhD Thesis, Imperial College, University of London, UK.

Navarro V, Asensio L, Alonso J, Yustres Á, Pintado X (2014) Multiphysics implementation of advanced soil mechanics models. *Computers and*

Geotechnics, 60, 20-28.

Nuth, M. & Laloui, L. (2008). Effective stress concept in unsaturated soils: Clarification and validation of a unified framework. *International Journal for Numerical and Analytical Methods in Geomechanics* 32, 771–801. doi:10.1002/nag.645

Nyambayo VP., Potts DM (2010). Numerical simulation of evapotranspiration using root water uptake model. *Computers & Geotechnics* 37, pp 175-186.

Papafotiou A, Li C, Kober F, 2017. Pre-dismantling THM modelling of the FEBEX in situ experiment. *Arbeitsbericht NAB 16-22*. Wettingen, Switzerland: Nagra.

Philip J R and De Vries D A, 1957. Moisture movement in porous materials under temperature gradients. *Transactions, American Geophysical Union* 38.

Pintado X, Lloret A (1997). THM laboratory tests in FEBEX Phase 3. UPC, 70- UPC-L-3-01

Pintado X, Ledesma A, Lloret A, 2002. Backanalysis of thermohydraulic bentonite properties from laboratory tests. *Engineering Geology* 64 (2–3), 91–115, doi:10.1016/S0013-7952(01)00110-7.

Potts D.M. & Zdravkovic L. (1999). *Finite element analysis in geotechnical engineering: theory*. Thomas Telford Publishing, London, UK.

Pusch, R., 1982. Mineral–water interactions and their influence on the physical behavior of highly compacted Na bentonite. *Canadian Geotechnical Journal* 19, 381–387.

Richards, L. A. (1931): *Capillary Conduction of Liquids Through Porous Mediums*. In: *Physics* 1 (5), S. 318–333. DOI: 10.1063/1.1745010.

Romero, E., Villar, M.V. & Lloret, A. (2005): Thermo-hydro-mechanical behaviour of two heavily overconsolidated clays. *Engineering Geology*, 81(3):255-268

Roscoe, K.H., Schofield, A. and Wroth, A.P., 1958. On the yielding of soils. *Geotechnique*, 8(1), pp.22-53.

Rodriguez-Dono A., S. Olivella and N. Mokni. 2018 Assessment of a high-level spent nuclear fuel disposal model. *Environmental Geotechnics*, paper 1800017, 17 p.

Rutqvist, J.; Börgesson, L.; Chijimatsu, M.; Kobayashi, A.; Jing, L.; Nguyen, T. S. et al. (2001): Thermohydromechanics of partially saturated geological media. Governing equations and formulation of four finite element models. In: *International Journal of Rock Mechanics and Mining Sciences* 38 (1), S. 105–127. DOI: 10.1016/S1365-1609(00)00068-X.

Sánchez, M. and Gens, A. (2006) FEBEX Project: Final report on thermo-hydro-mechanical modelling. ENRESA Technical Report 05-2/2006, Madrid, Spain.

Sánchez, M., Gens, A., Guimaraes, L. do N., Olivella, S. (2005) A double

structure generalized plasticity model for expansive materials. *International Journal for Numerical and Analytical Methods in Geomechanics*, N° 29, 751-787.

Seiphoori A, Ferrari A, Laloui L, (2014). Water retention behaviour and microstructural evolution of MX-80 bentonite during wetting and drying cycles", *Géotechnique* Vol. 64, No. 9, pp. 721–734

Sun, H., Mašín, D., Najser, J., 2018a. Thermal Water Retention Characteristics of Compacted Bentonite, in: Hu, L., Gu, X., Tao, J., Zhou, A. (Eds.), *Proceedings of GeoShanghai 2018 International Conference: Multi-Physics Processes in Soil Mechanics and Advances in Geotechnical Testing*. Springer, Singapore, pp. 71–78. https://doi.org/10.1007/978-981-13-0095-0_8

Sun, H., Mašín, D., Najser, J., 2018b. Investigation of the mechanical behavior of compacted bentonite. *Proceedings of the 7th International Conference on Unsaturated Soils (UNSAT2018)*, 3-5.8.2018, Hong Kong.

Sun, H., Mašín, D., Najser, J., Neděla, V., Navrátilová, E., 2018c. Bentonite microstructure and saturation evolution in wetting–drying cycles evaluated using ESEM, MIP and WRC measurements. *Géotechnique* 69, 713–726.

Svensson D, Dueck A, Nilsson U, Olsson S, Sandén T, Lydmark S, Jägerwall S, Pedersen K, Hansen S, 2011. Alternative buffer material. Status of the ongoing laboratory investigation of reference materials and test package 1. SKB TR-11-06. Stockholm, Sweden: Svensk Kärnbränslehantering AB.

Talandier J, 2018. Specifications for Beacon WP5: Testing, verification and validation of models step 2 - large scale experiments. Deliverable (D5.2.1). Report.

Tang, A.-M., Cui, Y.-J., 2005. Controlling suction by the vapour equilibrium technique at different temperatures and its application in determining the water retention properties of MX80 clay. *Can. Geotech. J.* 42, 287–296.

Tang, A.-M., Cui, Y.-J., Barnel, N., 2008. Thermo-mechanical behaviour of a compacted swelling clay. *Géotechnique* 58, 45–54.

Thatcher, 2017. FEBEX-DP: THM modelling. Quintessa's contribution on behalf of RWM. Contractor Report to RWM QRS-1713A-R2, V1.8.

Tsiampousi A, Zdravkovic L, Potts DM. (2013). A new Hvorslev surface for critical state type unsaturated and saturated constitutive models, *Computers & Geotechnics* 48, pp. 156–166.

UPC. CODE-BRIGHT users guide. Version 9. Universitat Politècnica de Catalunya, Barcelona, Spain, 2019.

Van Eekelen, H.A.M., 1980. Isotropic yield surfaces in three dimensions for use in soil mechanics. *International Journal for Numerical and Analytical Methods in Geomechanics*, 4(1), pp.89-101.

Van Genuchten, MT (1980). A closed-form equation for predicting the

hydraulic conductivity of unsaturated soils. *Soil Sci. Soc. Am. J.*, 44, pp. 892-898.

Villar, M.V., Lloret, A., 2004. Influence of temperature on the hydro-mechanical behaviour of a compacted bentonite. *Applied Clay Science* 26, 337–350.

Villar M, Fernández A M, Romero E, Dueck A, Cuevas J, Plötze M, Kaufhold S, Dohrmann R, Iglesias R, Sakaki T, Voltolini M, Zheng L, Kawamoto K and Kober F (2018), FEBEX-DP Post-mortem THM/THG Analysis Report, NAB 16-17 Rev.1, Nagra.

Villar, M. (2008). Report on Thermo-Hydro-Mechanical Laboratory Tests Performed by CIEMAT on Febex Bentonite 2004-2008. CIEMAT.

Villar MV (2005). MX-80 Bentonite. Thermo-Hydro-Mechanical characterisation performed at CIEMAT in the context of the Prototype Project, CIEMAT Technical Report: CIEMAT/DIAE/54540/2/04

Villar M.V., M. Sánchez, A. Gens. 2008 Behaviour of a bentonite barrier in the laboratory: Experimental results up to 8 years and numerical simulation. *Physics and Chemistry of the Earth*. Vol. 33, p. 476–485

Villar, M. V., Iglesias, R. J., Abós, H., Martínez, V., De la Rosa, C. & Manchon, M. (2016): FEBEX-DP on-site analyses report. Nagra Arbeitsbericht NAB 16-12.

Vilarrasa, V., Parisio, F. and Laloui, L., 2017. Strength evolution of geomaterials in the octahedral plane under nonisothermal and unsaturated conditions. *International Journal of Geomechanics*, 17(7), p.04016152.

VII Tutorial example - THM "Mock-up test" problem. CODE_BRIGHT tutorial manual. UPC, Spain, 2019, 404 p.

Zheng L., et al. 2020. The hydration of bentonite buffer material revealed by modelling analysis of a long-term in situ test. *Applied Clay Science*. Vol. 185, paper 105360, 10 p.

Zhou, A.N., Sheng, D., Sloan, S.W. and Gens, A., 2012a. Interpretation of unsaturated soil behaviour in the stress–saturation space, I: volume change and water retention behaviour. *Computers and Geotechnics*, 43, pp.178-187